ALMA MATER STUDIORUM
UNIVERSITÀ DI BOLOGNA

DOTTORATO DI RICERCA IN
ASTROFISICA

CICLO XXXVII

Settore Concorsuale: 02/C1 - ASTRONOMIA, ASTROFISICA, FISICA DELLA TERRA E DEI PIANETI

Settore Scientifico Disciplinare: FIS/05 - ASTRONOMIA E ASTROFISICA

MAGNETIC FIELDS AND COSMIC RAYS IN THE LARGE-SCALE FILAMENTS

Presentata da
Giada Venusta Pignataro

Coordinatore Dottorato
Prof. Andrea Miglio

Supervisore
Prof.ssa Annalisa Bonafede

Co-supervisore
Dott. Gianni Bernardi

Esame Finale Anno 2025

To Lorenzo.

Abstract

The large-scale structure of the Universe forms a web-like pattern, where low-density filaments of gas and dark matter connect the densest nodes, where galaxy clusters are located. Recent low-frequency radio observations have revealed the presence of diffuse radio emission on megaparsec scales, along the densest regions of these cosmic-web filaments. The discovery of these bridges has triggered the development of theoretical models to explain the emission. These models can be tested with multifrequency studies, that are able to shed light on the particle acceleration mechanisms and the properties of magnetic fields in these previously unexplored regions of the Universe.

The primary aim of this Thesis is to investigate, for the first time, the properties of cosmic-web bridges and filaments, focusing on their spectral characterisation, magnetic field properties, and occurrence.

In particular, in this Thesis I will focus on the multifrequency study of the most prominent and first discovered example of a radio bridge, located between the galaxy clusters Abell 0399 and Abell 0401. For the first time, I characterize the radio spectrum of the bridge analysing high-sensitivity observations at 60, 144, and 400 MHz. Additionally, I have expanded the sample of radio bridges by studying other promising systems, such as the merger between Abell 2061 and Abell 2067 in the Corona Borealis Supercluster, where I find extended diffuse emission reaching beyond the radio halo in Abell 2061 towards Abell 2067. The only two intercluster bridges confirmed thus far are associated with highly dynamic regions between merging galaxy clusters, but fainter, more extended filaments on scales of tens of megaparsecs remain undetected. A promising method for locating these cosmic filaments is through the study of galaxy superclusters, which increase the probability of detecting filamentary structures. To gain a comprehensive understanding of magnetic fields in these poorly explored environments, I employed the Faraday rotation measure of linearly polarised sources along the line of sight to magnetised plasma in three rich superclusters: Corona Borealis, Leo, and Hercules. With this method, I detected the presence of magnetic fields at levels higher that what is predicted solely by the adiabatic compression of a primordial seed in cosmic filaments. These results indicate that in superclusters of galaxies different mechanisms of magnetic field amplification may be at play, such as dynamo amplification or AGN and galaxy feedback. This work is a step toward constraining theoretical models of cosmic magnetogenesis and particle-acceleration mechanisms on the largest scales.

Overall, the work presented in this Thesis highlights the importance of radio observations as probe of the non-thermal emissions and magnetic fields in cosmic filaments, advancing our understanding of their physical nature and role in large-scale structure formation.

Thesis Outline

This Thesis is structured as follows:

- In Chapter 1, I provide an overview of the hierarchical structure formation of the Universe, that brings to the formation of the Cosmic web, with a particular focus on interacting galaxy clusters and the synchrotron emission detected in the intercluster filaments.

- In Chapter 2, I introduce the physics of polarization and focus on the methods used in practice to measure the Faraday rotation in radio observations and infer the origin of cosmic magnetic fields.

- In Chapter 3, I highlight the importance and the challenges of wide-field radio interferometry for the detection of the diffuse emission in the large-scale structure of the Universe, introducing the two instruments used in this Thesis: the LOw Frequency ARray (LOFAR) and the upgraded Giant Metrewave Radio Telescope (uGMRT).

- In Chapter 4, I present the work conducted to investigate the properties of the non-thermal emission in the interacting clusters pairs Abell 0399-Abell 0401 and Abell 21-PSZ2 G114.9 with uGMRT observations at the central frequency of 400 MHz. In both system the diffuse emission between the clusters remain undetected at the observing frequency. I develop a method to place limits on the emission of radio bridges, and derive an upper limit to the steep spectral index of the radio bridge in Abell 0399-Abell 0401, already detected at 140 MHz.

- In Chapter 5, I present the follow-up work on the radio bridge in Abell 0399-Abell 0401, where I conduct a multifrequency study with very low frequency observations with LOFAR at 60 MHz. I detect the radio bridge with high significance and I am able to measure a spectral index, for the first time, between 60 and 144 MHz. I also produce spectral index maps and, with the limits derived with the previous uGMRT observations, I am able to constrain a radio spectrum for the bridge. The comparison with the synchrotron spectrum from theoretical models predictions allows us to set some constrain on the particle accelerations mechanism at play and the magnetic field strength in these regions.

- In Chapter 6, I report the results on the study performed on the merging system Abell 2061-Abell 2067 in the Corona Borealis Supercluster. I analysed deep LOFAR observations at 144 MHz to follow up on the possible inter-cluster filament suggested by previous 1.4 GHz observations. I investigated thermal-non thermal relations to describe the nature of the diffuse emission. I detect diffuse radio emission on an 800 kpc scale, which is more extended than previously

known, reaching beyond the radio halo in Abell 2061 towards Abell 2067. I explored three different dynamical scenarios to explain the nature of the diffuse emission, which could be an unique candidate radio bridge.

- In Chapter 7, I present the work I conducted to constrain the magnetic field strength in low-density environments inside the boundaries of superclusters of galaxies using the Faraday rotation measure of polarized sources detected at 1.4 GHz and 144 MHz. I constructed a catalog of 4497 polarized sources in the background of three rich superclusters of galaxies, with the literature NVSS and LoTSS data and additional non released LoTSS DR3 data. I constrain the magnetic fields in the low-density regions of superclusters, and the detected value suggests that the adiabatic amplification of the magnetic field detected in filaments of the cosmic web can not account for the magnetic field detected in superclusters. Hence, I conclude that different mechanisms of magnetic field amplification may be at play in filaments, such as dynamo amplification or AGN and galaxy feedback.

- In Chapter 8, I summarize the results achieved in this Thesis and I provide an outlook on future work.

The results obtained during the PhD project and detailed in this Thesis are reported in the following publications:

- *Probing diffuse radio emission in bridges between galaxy clusters with uGMRT*
  G. V. Pignataro, A. Bonafede; G. Bernardi ; C. J. Riseley ; D. Dallacasa ; T. Venturi
  A&A, 682, A105 (2024)
  DOI: 10.1051/0004-6361/202346243

- *Abell 0399-Abell 0401 radio bridge spectral index: First multi-frequency detection*
  G. V. Pignataro, A. Bonafede, G. Bernardi, F. de Gasperin, G. Brunetti, T. Pasini, F. Vazza, N. Biava, J. M. G. H. J. de Jong, R. Cassano, A. Botteon, M. Bruggen, H. J. A. Rottgering, R. J. van Weeren and T. W. Shimwell
  A&A, 685, L10 (2024), Letter to the Editor
  DOI: 10.1051/0004-6361/202450051

- *Mind the gap between A2061 and A2067: Unveiling new diffuse, large-scale radio emission*
  G.V. Pignataro, A. Bonafede, G. Bernardi, M. Balboni, F. Vazza, R.J. van Weeren, F. Ubertosi, R. Cassano, G. Brunetti, A. Botteon, T. Venturi, H. Akamatsu, A. Drabent, M. Hoeft
  A&A, 691, A99 (2024)
  DOI: 10.1051/0004-6361/202451529

- *Detection of magnetic fields in superclusters of galaxies*
  G.V Pignataro, S.P. O'Sullivan, A. Bonafede, G. Bernardi, F. Vazza, E. Carretti; (Submitted to A&A)

Contents

List of Figures

List of Tables

List of Abbreviations

ACT	**A**tacama **C**osmology **T**elescope
AGN	**A**ctive **G**alactic **N**ucleus
BCG	**B**rightest **C**luster **G**alaxy
CC	**C**ool **C**ore
CDM	**C**old **D**ark **M**atter
CIE	**C**ollisional **I**onization **E**quilibrium
CfA2	**C**enter for **A**strophysics galaxy redshift survey
CMB	**C**osmic **M**icrowave **B**ackground
CR	**C**osmic **R**ay
CS	**C**ore **S**tation
DDE	**D**irection **D**ependent **E**ffects
DDF	**DD F**acet
DIE	**D**irection **I**ndependent **E**ffects
DM	**D**ark **M**atter
DR	**D**ata **R**elease
DSA	**D**iffusive **S**hock **A**cceleration
FFT	**F**ast **F**ourier **T**ransform
FDF	**F**araday **D**ispersion **F**unction
FoF	**F**riends-**o**f-**F**riends
FWHM	**F**ull **W**idth at **H**alf **M**aximum
FT	**F**ourier **T**ransform
GRM	**G**alactic **R**otation **M**easure
HBA	**H**igh **B**and **A**ntenna
IC	**I**nverse **C**ompton
ICM	**I**ntra**C**luster **M**edium
IGM	**I**nter**G**alactic **M**edium
IS	**I**nternational **S**tation
ISM	**I**nter**S**tellar **M**edium
KMS	**K**ill **MS**
KSP	**K**ey **S**cience **P**roject
LBA	**L**ow **B**and **A**ntenna
LILF	**L**ibrary for **L**ow **F**requencies
LLS	**L**argest **L**inear **S**cale
LOFAR	**LO**w **F**requency **AR**ray
LOTSS	**LO**FAR **T**wo-**M**etre **S**ky **S**urvey

LSS	**L**arge **S**cale **S**tructure
MHD	**M**agneto**H**ydro**D**ynamic
NCC	**N**on-**C**ool **C**ore
NCRA	**N**ational **C**entre for **R**adio **A**strophysics
NVSS	**N**RAO **V**LA **S**ky **S**urvey
POSSUM	**P**olarization **S**ky **S**urvey of the **U**niverse's **M**agnetism
RFI	**R**adio **F**requency **I**nterference
RM	**R**otation **M**easure
RMSF	**R**otation **M**easure **S**pread **F**unction
RS	**R**emote **S**tation
RRM	**R**esidual **R**otation **M**easure
SDSS	**S**loan **D**igital **S**ky **S**urvey
SKA	**S**quare **K**ilometre **A**rray
SMBH	**S**uper**m**assive **B**lack **H**ole
SPAM	**S**ource **P**eeling and **A**tmospheric **M**odeling
SPH	**S**mooth-**P**article **H**ydrodynamic
SSD	**S**ub **S**pace **D**econvolution
SZ	**S**unyaev-**Z**el'dovich
TTD	**T**ransit **T**ime **D**amping
UGMRT	**U**pgraded **G**iant **M**etre**w**ave **R**adio **T**elescope
2dFRS	**T**wo **D**egree **F**ield **R**edshift **S**urvey
2MASS	**T**wo **M**icron **A**ll **S**ky **S**urvey
VLASS	**V**ery **L**arge **A**rray **S**ky **S**urvey
WSRT	**W**esterbrok **S**ynthesis **R**adio **T**elescope

Chapter 1

The Hierarchical Structure of the Universe

1.1 Introduction to the Cosmic Web

The large-scale structure (LSS) we observe in our Universe is the result of a hierarchical process rooted in a cold dark matter (CDM) cosmology, where small density fluctuations grow under the influence of gravity on a homogeneous and isotropic background, leading to the formation of galaxies, galaxy groups, and ultimately massive clusters and superclusters of galaxies (e.g., White and Rees 1978). It now can be described as an intricate web-like pattern, where galaxies are distributed along filaments in an orderly way.

This so-called 'Cosmic Web' (Bond, Kofman, and Pogosyan, 1996) is composed of three main building blocks: densest condensations of groups and clusters of galaxies, connected by less dense filaments and sheets (Einasto, Joeveer, and Saar, 1980; Vogelsberger et al., 2014), that extends through large underdense voids (Einasto et al., 1975). The formation of large-scale structure follows a bottom-up scenario, galaxies and smaller objects form first, and progressively larger structures emerge over time through gravitational merging and accretion (Kravtsov and Borgani, 2012). Understanding the details of this process, along with the role of gas dynamics in the physical processes governing galaxy formation and evolution, is key to unraveling the mechanisms that characterize both the thermal and non-thermal properties of the Cosmic Web, including the origin and nature of magnetic fields in the largest structure of the Universe. In fact, the presence of primordial magnetic fields in the Cosmic Web is one of the principal fundamental questions being investigated today (Vazza et al., 2015; Vazza et al., 2017). While the dark-matter skeleton of the cosmic web is closely traced by galaxies and galaxy clusters, the particle counterpart of filaments is more difficult to investigate, given the low signal and densities involved. Since relativistic particles and magnetic fields are thought to have a spatial distribution more extended than that of thermal baryons, we focus current observations on the outskirts of galaxy clusters and beyond.

Recently, significant progress has been achieved with radio, X-ray and Sunyaev–Zeldovich (SZ) effect observations, alongside polarisation studies that trace interactions between baryons, magnetic fields, and relativistic particles in these vast structures.

1.2 The Cosmic Web and Galaxy Clusters

Galaxy clusters are the largest structures in the Universe bounded by the gravitational force and are found at the nodes of the Cosmic Web. Their masses range between 10^{14} $M_\odot$ and 10^{15} $M_\odot$, with $\sim 100 - 1000$ galaxy members inside typical radii of $1 - 3$ megaparsecs (Mpc). While clusters can be highly populated, galaxies only represent the $\sim 5\%$ of the total mass, and the dark matter (DM) component is dominant ($\sim 80\%$). The remaining $\sim 15\%$ of the mass is in the form of hot (T$\sim 10^7 - 10^8$ K) rarified ($n_e \sim 10^{-3}$ cm^{-3}) plasma that fills the space in-between galaxies, called the intracluster medium (ICM) (Sarazin, 1986). Galaxy clusters are ideal subjects for investigating structure formation processes from various perspectives, starting from their unique physical and environmental properties, to their interactions on larger scales. In particular, for the aims of this Thesis, galaxy clusters serve as crucial probes for studying the presence of bridges and filaments of gas that connect them, as well as the magnetic fields in these structures.

1.2.1 Formation and Evolution of Galaxy Clusters

In the hierarchical structure formation model that is at the basis of standard cosmologies such as the ΛCDM galaxy clusters are the last formed structures. In this Thesis, we adopt a ΛCDM cosmology (Allen, Evrard, and Mantz, 2011), with matter content parameter $\Omega_M = 0.30$, dark energy content parameter $\Omega_\Lambda = 0.70$, and Hubble constant $H_0 = 70$ km s^{-1} Mpc^{-1}.

The history of galaxy clusters can be traced back to temperature anisotropies now observable in the Cosmic Microwave Background (CMB, Planck Collaboration et al. 2020); these are the consequence of primordial, randomly distributed, density fluctuations. Overdensities naturally evolved in at a slower rate with respect to the Hubble flow expansion, until their own gravitational field reached the point of instability. The collapse of the overdensities in an initial halo of dark matter is then followed by accretion of smaller halos, which in time evolves to present day galaxy clusters (e.g., Coles and Lucchin 2002). The linear and non-linear evolution of the instabilities that leads to the formation of the Cosmic Web can be followed with large and computationally-expensive cosmological simulations, of which prime examples are the Millennium simulation (Springel et al., 2005), the Bolshoi simulation (Klypin, Trujillo-Gomez, and Primack, 2011), and the Illustris (Vogelsberger et al., 2014) and Illustris TNG (Springel et al., 2018) simulations (see Fig. 1.1). In particular, the new Illustris TNG-Cluster simulation (Nelson et al., 2024) is a project that resimulates ~ 350 galaxy clusters and enables the study of the ICM properties, the central supermassive black holes (SMBHs) and brightest cluster galaxies (BCGs), as well as

cooling and active galactive nuclei (AGN) feedback to compare against current and upcoming observations.

Cluster formation is a process that has an enormous dynamic range, and the formation and evolution of galaxies in clusters is still not fully understood since cluster member galaxies show many differences with respect to field galaxies. Most differences are attributed to the dense environment that can affect the galaxy interstellar medium (ISM) through ram pressure stripping (Gunn and Gott, 1972), evaporation (Cowie and Songaila, 1977), merging and other dynamical processes (e.g. Gorkom 2003). Galaxies are important components of the cluster system, however the stellar component in clusters is not the dominant one, not even among baryonic matter: in fact, while massive galaxy clusters have a baryon fraction approaching the cosmic baryon fraction ($\rho_b/\rho_{tot} \sim 0.17$, Spergel et al. 2003), stars in cluster make up only $\rho_s/\rho_{tot} \sim 0.02$ (Lin, Mohr, and Stanford, 2003). Therefore, baryons must be present in a different component. Considering that clusters potential wells are extremely deep, it is reasonable to assume that baryons can not escape. Most baryons must be in form of gas, with a fraction of $\rho_{gas}/\rho_{tot} \sim 0.15$.

1.2.2 The Intracluster Medium

The ICM makes up the largest part of the baryonic matter in galaxy clusters. It is described as a weakly collisional plasma at high temperatures of $T \sim 10^7 - 10^8$ K, mostly consisting of thermal electrons with low density of $n_e \sim 10^{-2} - 10^{-4}$ cm^{-3} and typical metallicity of $Z \sim 0.2 - 0.3\ Z_\odot$. The ICM emits in the X-ray through optically thin bremsstrahlung emission, which is a key instrument for the identification of their dynamical state (e.g. Lovisari et al. 2017). Additionally, a fraction of galaxy clusters show diffuse radio emission from synchrotron radiation of relativistic electrons accelerated in magnetic fields over scales that, in some cases, are comparable with the extension of the thermal gas (van Weeren et al., 2019).

Thermal Components

Due to the high temperature ($T \sim 10^8$K) of the gas, galaxy clusters are luminous X-ray sources and this emission is primarly caused by thermal bremsstrahlung from the ICM. Sarazin (1988) reviewed the physical properties of hot diffuse plasma: the particles are assumed to have a Maxwell-Boltzmann distribution at the temperature T; the particles mean free paths are generally much shorter than the length scales of clusters ($\sim$ 1 Mpc) so the ICM can be well approximated as a collisional fluid. At the characteristic low densities of the ICM, excitation and de-excitation processes are described in the framework of collisional ionization equilibrium (CIE) (Smith and Hughes, 2010). The emissivity of the bremsstrahlung process (ϵ_ν), at frequency ν is

$$\epsilon_\nu = aZ^2 n_e n_i T^{-1/2} g_{ff} e^{\frac{h\nu}{kT}}, \tag{1.1}$$

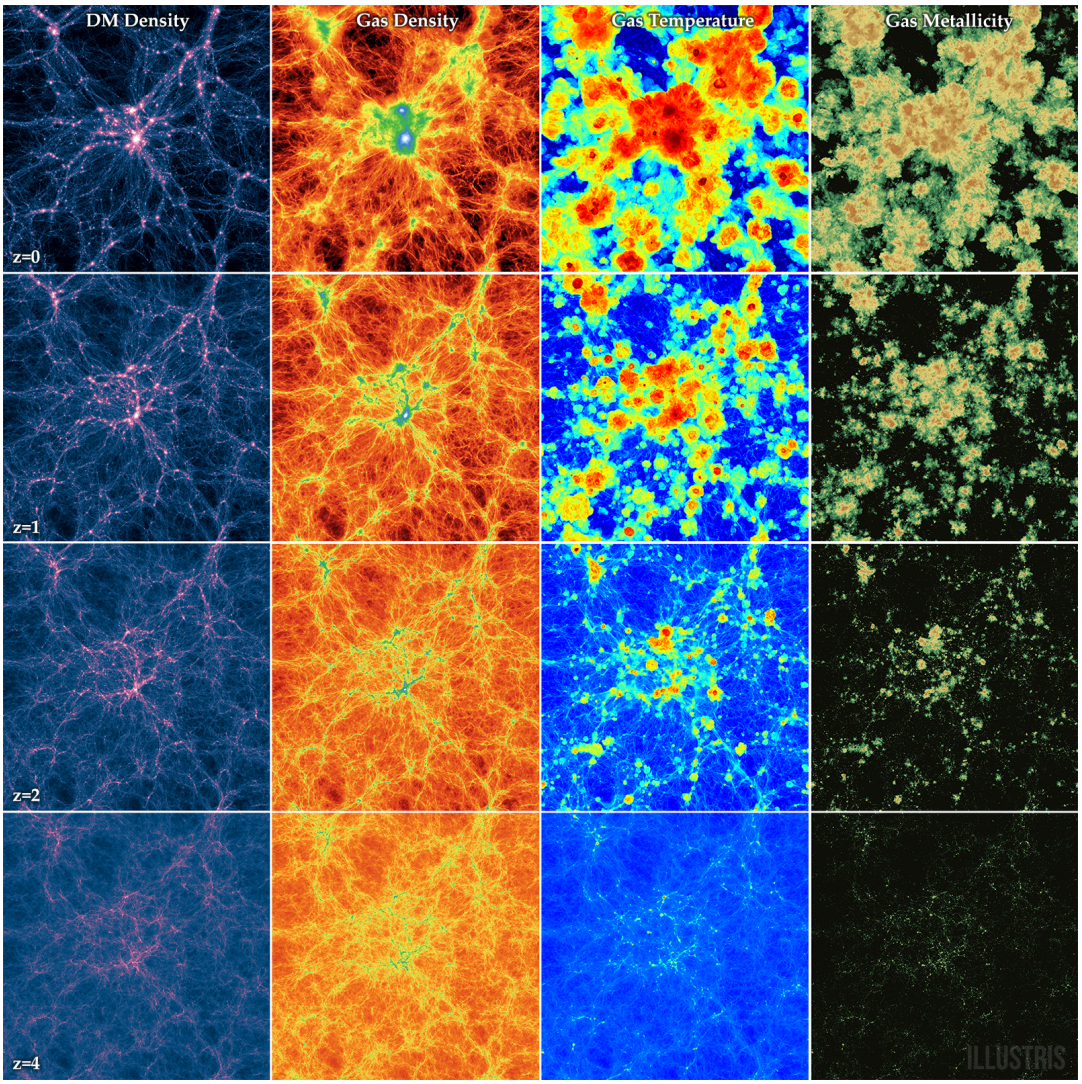

FIGURE 1.1: Illustris cosmological simulation of the Cosmic Web (Vogelsberger et al., 2014). Redshift evolution of a whole box slice from z=4 to z=0, showing four projections: dark matter density, gas density, gas temperature, and gas metallicity.

where T is K, h is the Planck constant, k is the Boltzmann constant, $a = 5.4 \times 10^{-39}$ erg s^{-1}Hz^{-1}cm^{-3}, Z in the ions charge, n_e and n_i is the number density of electrons and ions, and g_{ff} is the Gaunt factor (Sarazin, 1986). From the exponential dependence on frequency, it follows that the peak of the emission is in the 0.1-2 keV X-ray band. This allows the determination of the temperature and density of the gas from the X-ray spectrum - typically, galaxy clusters have a bolometric X-ray luminosity of $L_X \sim 10^{43} - 10^{45}$ erg s^{-1}.

The gas is generally thought to be in hydrostatic equilibrium in the potential well of the cluster, so under the assumption that the ICM is locally homogeneous and the cluster is spherically symmetric, the hydrostatic equilibrium equation can be written as (Gitti, Brighenti, and McNamara, 2012):

$$\frac{1}{\rho}\frac{dp}{dr} = -\frac{d\phi}{dr} = -\frac{GM(r)}{r^2}, \tag{1.2}$$

where $p = \rho kT/\mu m_p$ is the gas pressure, ρ is the gas density, ϕ is the gravitational potential of the cluster and $M(r)$ is the total cluster mass enclosed in the radius r from the cluster center. Neglecting the gas self-gravity, its distribution can be fully determined by the potential $\phi(r)$ and the temperature $T(r)$ radial profiles. The galaxy cluster's total the gravitational mass M_{tot} is:

$$M_{\rm tot}(< r) = -\frac{kTr}{G\mu m_p}\left[\frac{d\ln\rho}{d\ln r} + \frac{d\ln T}{d\ln r}\right]. \tag{1.3}$$

Thus, by measuring the density and the temperature profiles, $\rho(r)$ and $T(r)$, it is possible to estimate the gravitational mass of the cluster (see e.g. Gitti, Piffaretti, and Schindler 2007; Voigt and Fabian 2006).

An important and extensively used model for the density profile is the $\beta-model$, derived by Cavaliere and Fusco-Femiano (1976). They assume that both ICM and galaxies are in equilibrium in the cluster potential well and that the galaxy distribution is described by a King profile (King, 1962); moreover, both gas and galaxies are considered "isothermal", namely the gas temperature is constant and the galaxies' velocity dispersion is isotropic. Under these assumptions the density profile can be written as

$$\rho(r) = \rho_0\left[1 + \left(\frac{r}{r_{\rm c}}\right)^2\right]^{-(3/2)\beta}, \tag{1.4}$$

where r_c is the core radius of the galaxy cluster, and the parameter β is

$$\beta = \frac{\sigma_r^2}{kT/\mu m_p}. \tag{1.5}$$

In the last equation σ_r is the line-of-sight velocity dispersion. The great advantage of this model is that one can recover an analytical expression for the total mass:

$$M_{\rm tot}(<r) = \frac{kr^2}{G\mu m_p}\left[\frac{3\beta rT}{r^2+r_c^2} - \frac{dT}{dr}\right]. \tag{1.6}$$

Since the gas density increases in the central regions and the bremsstrahlung emission depends on the square of the gas density, the X-ray emissivity increase in those regions causing the gas to cool and flow towards the center: the cooling flows (see e.g. McNamara and Nulsen 2007; Ettori and Brighenti 2008). The presence or absence of a prominent X-ray peak of emission in their centre, where the gas has lower temperature, result in a dynamical distinction between 'cool core' (CC) and 'non-cool core' (NCC) clusters (Sanderson, O'Sullivan, and Ponman, 2009). While CCs are relaxed and regular clusters that have not undergone a recent major merger (within the last $\sim$ 3 Gyr), NCCs are disturbed and irregular merging systems. In cool-core clusters the central regions are not well described by a single $\beta-$model, but a second $\beta-$model is needed (Lovisari, Reiprich, and Schellenberger, 2015). The contribution of current facilities such as *Chandra* and *XMM-Newton* to high-resolution and large-scale mapping of the X-ray surface brightness in galaxy clusters makes it one of the most accurate tool to dynamical studies.

Sunyaev-Zeldovich Effect

The ICM is a hot plasma that interacts with the CMB photons, causing a distortion in the spectrum called the Sunyaev-Zeldovich (SZ) effect (Sunyaev and Zeldovich, 1972). It occurs due to the Inverse Compton (IC) scattering of CMB photons with free electrons in the plasma. The change in the background CMB intensity is given by

$$\frac{\Delta I_{CMB}}{I_{CMB}} = f(\nu)y_e, \tag{1.7}$$

where $f(\nu)$ is the frequency-dependent spectral shape function (e.g. Carlstrom, Holder, and Reese 2002) and y_e is the Comptonization parameter, defined as

$$y_e = \frac{\sigma_T}{m_e c^2}\int n_e T_e {\rm d}l, \tag{1.8}$$

where σ_T is the Thomson cross-section, m_e is the electron mass and c is the speed of light. From this definition it follows that the SZ effect can be used to detect galaxy clusters and measure their mass because intensity variation of the CMB is proportional to the density and temperature of the gas along the line of sight. Unlike other methods, the SZ effect is independent of redshift, allowing for the study of clusters' evolution over cosmic time. The *Planck* survey (Planck Collaboration et al., 2011) provides SZ maps over all the extragalactic sky (Planck Collaboration et al., 2016). From the *Planck* data maps, a cluster appears as an increment (decrement) of emission at frequencies above (below) 218 GHz allowing the creation of large samples

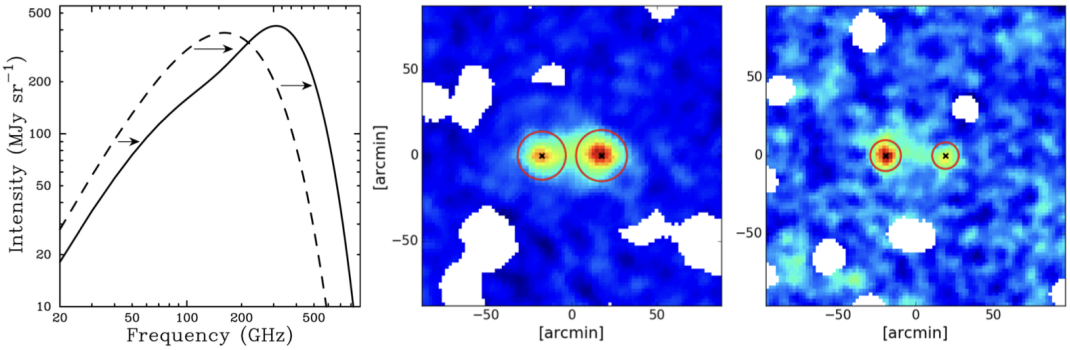

FIGURE 1.2: *Left:* CMB spectrum, the SZ effect distortion (solid line) compared to the original undistorted profile (dashed line) (Carlstrom, Holder, and Reese, 2002). *Right:* Planck satellite SZ-effect maps that show two galaxy clusters pairs (Abell 399-Abell 401 and Abell 21-PSZ2 G114.90-34.35) and the inter-cluster gas between them as excess emission (Bonjean et al., 2018).

of galaxy clusters in a most efficient way. By combining X-ray observations and SZ measurements, the density and pressure profiles of galaxy clusters can be obtained. This information can be used to calculate the entropy profile, which provides insights into the thermodynamic properties of the plasma both within and beyond the virial radius of the cluster. In the case of pairs of galaxy clusters, the inter-cluster filament is expected to be denser with a hotter gas and thus, in principle, easier to detect in particular in the X-rays and SZ effect (Dolag et al., 2006). This has driven some recent studies on the inter-cluster filaments (Fig. 1.2) from SZ data (e.g. Planck Collaboration et al. 2013; Bonjean et al. 2018; Hincks et al. 2022).

Non-thermal Components

Some galaxy clusters are observable in the radio band, revealing the presence of non-thermal components, i.e. relativistic particles ($\sim$ GeV energy) and magnetic fields ($\sim$ μG strength) spread over different scales, that can be linked to individual radio galaxies or to a diffuse component in the ICM (for a review, van Weeren et al. 2019). The synchrotron radiation from a relativistic particle moving with velocity v in a magnetic field B has power

$$P_s \propto \beta^2 \gamma^2 B^2 sin^2 \theta \tag{1.9}$$

where $\beta = v/c$, $\gamma = (1-\beta^2)^{-\frac{1}{2}}$ is the Lorentz factor, and θ is the pitch angle between the direction of v and B. In clusters a population of electron can be described with a power-law distribution in the form $N(p) \propto p^{-\delta}$, where δ is the injection index. The flux density of the synchrotron emission is $S(\nu) \propto \nu^{-\alpha}$[1], where the spectral index α is

$$\alpha = \frac{\delta - 1}{2}. \tag{1.10}$$

[1] In recent studies it is common to adopt the form $S(\nu) \propto \nu^{\alpha}$.

The spectral index can be derived by flux density measurements at two different frequencies, and it is used to compute the $k-$corrected radio power as

$$P_\nu = 4\pi S_\nu D_L^2 (1+z)^{\alpha-1} \tag{1.11}$$

where D_L is the luminosity distance to the source at redshift z (Condon, 1988). The same electron population emitting with synchrotron experiences further energy losses due to non-thermal IC interaction with the CMB photons. By introducing an equivalent CMB magnetic field at the cluster redshift, $B_{CMB} = 3.25(1+z)^2\ \mu$G (Murgia et al., 1999), the characteristic radiative age of relativistic electrons experiencing synchrotron and IC energy losses is

$$t_{age} \approx 3.2 \frac{\sqrt{B}}{B^2 + B_{CMB}^2} [(1+z)\nu]^{-\frac{1}{2}} \times 10^{10}\ \text{yr}, \tag{1.12}$$

where ν is the observing frequency in MHz (van Weeren et al., 2019).

There is a variety of radio sources that can be found in galaxy clusters that can give insights on various aspects of the non-thermal properties of ICM. In particular, the origin and evolution of magnetic fields within galaxy clusters can be investigated with a combination of radio observations and Faraday rotation studies (e.g., Bonafede et al. 2010; Ryu et al. 2012; Bonafede et al. 2013) and through two types of radio sources (see Fig. 1.3):

- Compact sources, often associated with individual galaxies, are primarily linked to radio galaxies powered by active galactic nuclei (AGN). In the common model of radio galaxy emission (Urry and Padovani, 1995), the AGN, fueled by gas accreting onto a supermassive black hole, produces radio emission from an unresolved core, typically aligned with the host galaxy, and a pair of jets that extend outwards for tens to hundreds of kiloparsecs (kpc). The interaction of these jets with the external medium results in a variety of radio galaxy morphologies, which can be bent or distorted, as demonstrated by the increasing evidence of environmental interactions (e.g., Hardcastle et al. 2019; Hardcastle and Croston 2020). Radio galaxies are valuable tools for studying magnetic fields in both the intra-cluster medium (ICM) and the intergalactic medium (IGM) (Vernstrom et al., 2019; O'Sullivan et al., 2019; Stuardi et al., 2020). In particular, Faraday rotation measurements and catalogs can provide insights into the properties and existence of large-scale magnetic fields, a method discussed further in Chapter 2 and in 7.

- Diffuse radio sources on larger scales, from $\sim$ 500 kpc to Mpc, have also been found in galaxy clusters. For the first time, Willson (1970) proposed that these 'halos' were not associated with individual point sources but were instead widespread features of rich galaxy clusters. Since then, numerous diffuse sources have been observed and categorized into three main classes: radio

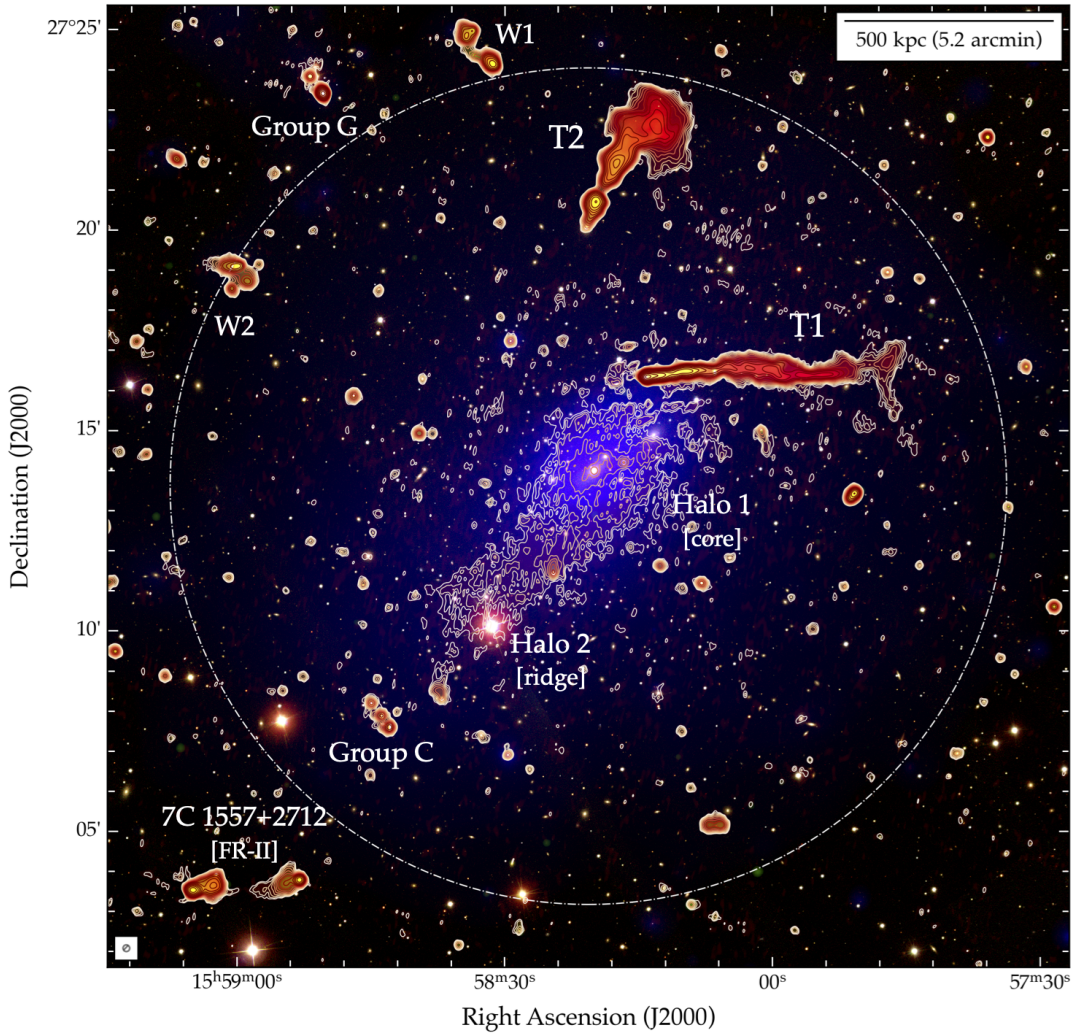

FIGURE 1.3: Colour-composite image of the galaxy cluster Abell 2142, showing both compact and diffuse emission sources. Optical from the SDSS. Yellow-through-red colours trace the radio surface brightness measured by LOFAR at 143 MHz and MeerKAT at 1283 MHz. Blue colours trace the thermal ICM plasma measured by XMM-Newton. Credits: Riseley et al. (2024).

halos, mini-halos, and relics, based on their morphology and location within clusters (Feretti and Giovannini, 1996; van Weeren et al., 2019). The detection of these diffuse sources proves directly the presence of magnetic fields on cluster-wide scales, offering insight into the interactions between cosmic rays, magnetic fields, and turbulent motions in the ICM. These sources are described in detail in Sec.1.2.4.

Both numerical simulations and observations reveal that the magnetic field strength is not uniform across the ICM, but rather decreases with distance from the cluster center (Murgia et al., 2004; Bonafede et al., 2010b; Osinga et al., 2024). The magnetic field strength, $(B(r))$, scales with the thermal particle density profile, $(n_e(r))$, according to a power-law relation:

$$B(r) = B_0 \left(\frac{n_e(r)}{n_{e,0}} \right)^{\eta}, \tag{1.13}$$

where B_0 and $n_{e,0}$ are the central magnetic field and gas density, respectively, and $\eta = 0.4 - 0.7$ are likely slope values for this relation - as it is the case of the Coma Cluster (Bonafede et al., 2010b).

On the other hand, the origin of cosmic magnetic fields on large scales remains an open question. Probing magnetic fields in low-density environments such as cosmic filaments may provide better insights into their primordial origins, as suggested by simulations and theoretical studies (e.g., Vazza et al. 2014; Vazza et al. 2017).This aspect will be further discussed in Sec. 2.3.1.

1.2.3 Mergers of Galaxy Clusters

Galaxy clusters grow and evolve through mergers, which are the most energetic events in the Universe. Vast amounts of kinetic energy is released, approximately $\sim 10^{63} - 10^{64}$ ergs, over time scales of 1 to 2 billion years (Gyr). These cluster mergers have strong impacts on the ICM, and X-ray observations allow to infer the dynamical state of the cluster. In particular, X-ray spectroscopy and high-resolution imaging offer a powerful tool to investigate the temperature distribution of clusters, revealing shocks and cold fronts (e.g., Markevitch and Vikhlinin 2007), which are now well-recognized as common signatures of merging events. The complex interactions between gravitational (i.e. adiabatic compression and heating) and non-gravitational (i.e. AGN, supernovae, turbulence) processes during cluster mergers have been studied in recent years through a combination of semi-analytical models and numerical simulations. These models incorporate various physical phenomena such as shocks, magnetic fields, cosmic ray (CR) particles, and turbulence to better reproduce the merger dynamics (e.g., Arieli, Rephaeli, and Norman 2010; Martin-Alvarez, Planelles, and Quilis 2017; Chisari et al. 2019). These merger-induced effects are key to understanding both the evolution of galaxy clusters and the underlying physical processes governing large-scale cosmic structure formation. In fact,

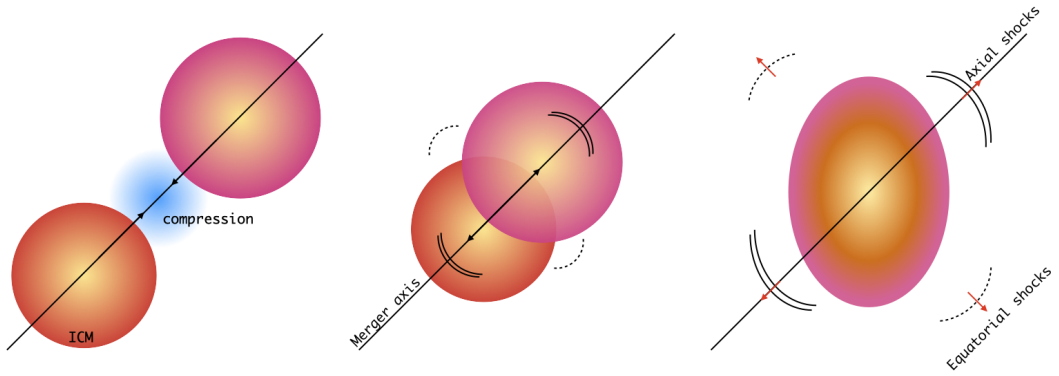

FIGURE 1.4: Schematic representation of an idealized binary merger of two galaxy clusters. In the first phase, the two gas halos approach along the merger axis, compressing the medium of the intercluster filament. In the second phase, the two gas halos start merging, and equatorial shocks are launched first perpendicular to the merger direction, while axial shocks are formed ahead of each DM halo. In the last phase, the merger of the two gas halos left one single gas core at the center.

all significant mergers should experience a phase where the filament connecting the two clusters is compressed and processed by gas dynamics, prior to their collision (Brunetti and Vazza, 2020).

Shocks

During cluster mergers, shock waves are driven in the ICM. A general overview of an idealized binary merger is shown in Fig. 1.4. In the first phase, two gas halos approach along the merger axis, causing a compression of the intercluster medium between them; equatorial shocks are expected to form first and move outward perpendicular to the merger axis; later, two axial shocks launch in opposite directions, ahead of each DM clump, along the merger axis, leaving a single gas core in the middle (see e.g. Ha, Ryu, and Kang 2018). The shock strength is characterized by its Mach number, defined as:

$$M = \frac{V_{sh}}{c_s}, \tag{1.14}$$

where V_{sh} is the velocity of the shock and c_s is the sound speed in the pre-shock medium. For cluster mergers, we expect to find low Mach numbers $M \sim 3-5$, since the sound speed in the ICM is comparable to the infall velocity (i.e. the shock velocity) of a virialized system(Roettiger, Burns, and Stone, 1999; Ricker and Sarazin, 2001). These weak shocks dissipate a significant portion of the merger energy through gas heating, and their strength, along with the dissipated energy, tends to increase with distance from the cluster center (e.g. Ryu et al. 2003; Vazza et al. 2012). In contrast, much stronger shocks ($M \gg 10$) occur externally in the IGM during the accretion of cold gas onto massive cosmic structures, but in turn, they dissipate less energy into the ICM due to their slower propagation in lower density

environments (Vazza, Brunetti, and Gheller, 2009). Merger shocks are strictly related to the formation of radio relics, diffuse synchrotron sources found in the peripheries of disturbed clusters (see Sec. 1.2.4).

Turbulence

Mergers between galaxy clusters, as well as the accretion of smaller substructures along cosmic filaments, are known to inject significant turbulence into the ICM. Turbulent mechanisms have been extensively studied through numerical simulations (e.g., Vazza et al. 2009; Iapichino et al. 2011; Miniati 2014; Vallés-Pérez, Planelles, and Quilis 2021). The Reynolds number (R_e), which measures the ratio between inertial and viscous forces in a fluid, is defined as

$$R_e = \frac{v\rho L}{\mu}, \tag{1.15}$$

where v is the flow velocity, *rho* is the fluid density, L is the characteristic scale of the motions, and μ is the dynamic viscosity of the fluid (e.g Brunetti and Lazarian 2007). When $R_e \gg 1$, the fluid is considered to be turbulent, and this condition is often met during cluster mergers.

Simulations of cluster mergers show that turbulent motions produced by these energetic events can contribute up to 20% of the ICM total thermal energy (e.g., Sunyaev, Norman, and Bryan 2003; Vazza et al. 2006; Vazza et al. 2012; Vazza et al. 2018). The turbulence in the ICM is typically subsonic, with $M \sim 0.2 - 0.5$, but super-Alfvénic, meaning the turbulence speed is higher than the Alfvén speed (V_A):

$$V_A = \frac{B}{\sqrt{\mu_0 \rho}}, \tag{1.16}$$

where B is the magnetic field strength, μ_0 is the permeability of the vacuum and ρ is total mass density of the charged plasma particles. The turbulent energy injected in the ICM is transferred from large to small scales, down to the Alfvén scale. Below this scale, the turbulent eddy velocity becomes comparable to the Alfvén speed, marking the transition from hydrodynamic to magneto-hydrodynamic (MHD) turbulence. The turbulent motions on small-scale are critical for processes like particle acceleration, which contribute to the formation of diffuse radio emission observed in clusters (e.g. Brunetti and Jones 2014).

Particle Acceleration Mechanisms

Turbulence and shocks generated by the merger process in galaxy clusters play a crucial role in accelerating particles over a range of scales, through several physical mechanisms. In this section, we review the main mechanism that are currently accepted to explain the diffuse radio emission observed in galaxy clusters and their outskirts:

- *Adiabatic compression*: a process in which a sub- or supersonic wave compresses a bubble of fossil relativistic plasma, often remnants of earlier AGN activity. Due to the high sound speed within the relativistic bubble (Enßlin and Vogt, 2003), the wave may have the only effect of compressing the plasma adiabatically. The fossil electrons, that have experienced significant synchrotron and inverse Compton (IC) losses, are detectable primarily at very low frequencies (tens of MHz). Although adiabatic compression re-energizes the electrons, it just boosts their emission and their steep and curved original spectral slope remains unchanged due to their earlier energy losses. During this process, the energy density of the magnetic field within the bubble is also increased, amplifying the field by a factor of around 2 for shocks with $M \sim 2-3$ (Iapichino and Brüggen, 2012). If the magnetic field in the bubble is not too strong (few μG), the compression along the direction of the shock motion results in an expansion in the perperdicular direction, leaving the cloud with the typically elongated shape of radio relics (Sec. 1.2.4). However, for adiabatic compression to occur, the relativistic plasma should remain confined within the ICM to maintain its high internal sound speed, which is not the case when mixing with the thermal ICM takes place. As a result, shock (re-)acceleration, rather than adiabatic compression, becomes the dominant mechanism responsible for generating relativistic electrons in clusters (as discussed below).

- *Diffusive shock acceleration (DSA)*: particle acceleration at shocks is well described DSA theory (e.g., Krymskii 1977; Malkov and Drury 2001). DSA is a Fermi Type I acceleration mechanism, where thermal particles are repeatedly scattered across a shock front due to magnetic inhomogeneities (Fermi, 1949). In the classic theory of Fermi, when a particle with velocity $v \sim c$ is reflected by a cloud with random velocity $V \ll v$, and L is the mean free path between clouds, its energy changes: it increases for head-on collisions (e.g. shocks) and decreases for overtaking collisions. For head-on collisions only, the rate at which the average energy E per particle increases can be derived as

$$\frac{\mathrm{d}E}{\mathrm{d}t} \approx \frac{V}{L}E, \tag{1.17}$$

yielding an energy growth linearly proportional to the shock velocity. During each crossing of the shock, the particles gain additional energy, resulting in a power-law momentum spectrum. The injection index, δ_{inj}, which describes the slope of this distribution, is determined by the shock's Mach number, following the relationship (Blandford and Eichler, 1987):

$$\delta_{inj} = 2\frac{M^2+1}{M^2-1.} \tag{1.18}$$

As the particles are moving in the downstream region of the shock, radiative cooling, primarily due to inverse Compton (IC) scattering and synchrotron

losses (Eq.1.12), reduces their maximum energy. As a result, the integrated electron energy spectrum steepens, leading to a shift in the power-law index of the spectrum by one as

$$\delta = \delta_{inj} + 1, \tag{1.19}$$

provided that there are not any other mechanism at play other than the shock (Ensslin et al., 1998). Consequently, the synchrotron spectral index follows Eq.1.10 and can be linked to the Mach number as

$$\alpha = \frac{M^2 + 1}{M^2 - 1} = \alpha_{inj} + \frac{1}{2}. \tag{1.20}$$

Therefore, the DSA predicts that for strong shocks ($M \rightarrow \infty$), the injection index $\delta_{inj} \rightarrow 2$ and $\alpha \rightarrow 1$, otherwise for weak shocks ($M \approx 2-5$), $\delta_{inj} > 2$ and $\alpha > 1$ (Brunetti and Jones, 2014).

Merger shocks in galaxy clusters typically have low Mach numbers ($M \sim$2-5). This creates a challenge, as the high radio power and steep spectra observed in radio relics cannot be easily explained if particles are accelerated solely from the thermal pool (e.g., Botteon et al. 2016; Eckert et al. 2016; Hoang et al. 2017; Botteon et al. 2020). To address this, it has been proposed that a population of pre-existing mildly-relativistic electrons may be re-accelerated by the shock wave (e.g., Markevitch et al. 2005; Kang, Ryu, and Jones 2012; Kang et al. 2014; Vazza et al. 2014; Caprioli, Zhang, and Spitkovsky 2018). Indeed, the tails of radio galaxies have been found to supply seed cosmic-ray electrons (CRe), which can then be re-energized by weak merger shocks for a more efficient particle re-acceleration process (e.g., Bonafede et al. 2014; Botteon et al. 2016; van Weeren et al. 2017; Hoang et al. 2018). However, direct observational link between AGN as the source of seed CRe and the formation of radio relics is not always found.

Another issue to explain radio relics with DSA is the absence of the expected γ-ray emission from galaxy clusters. In fact, even considering a small fraction of protons in the ICM ($e/p \sim 0.01$, e.g. Schlickeiser 2002), the inelastic nuclear collisions between relativistic protons and the nuclei of the thermal ICM would generate pions π^0. The decay of π^0 would result in $\gamma-$ray emission which should be detected given current limits from the Fermi satellite (Ackermann et al., 2010; Ackermann et al., 2014; Ackermann et al., 2016). To systematically investigate the limitations of the DSA theory, large samples of radio relics having available spectral, polarisation, and X-ray information are necessary.

- *Turbulent acceleration*: particle re-acceleration can be triggered by turbulence inhomogeneities on small scales, which are responsible for the Fermi II acceleration process in the ICM (Brunetti et al., 2001; Petrosian, 2001). In this stochastic process, particles gain energy only in head-on collisions, which have a higher

probability than inverse collisions, but the re-energization is relatively slow. From the classic Fermi theory (Fermi, 1949), in this case the combination of head-on and overtaking collisions results in an average energy increase rate of

$$\frac{\mathrm{d}E}{\mathrm{d}t} \approx \frac{V^2}{Lc}E, \tag{1.21}$$

with a quadratic dependence on V. In particular, directly accelerating electrons from the thermal pool is highly inefficient, so a pre-existing population of mildly relativistic electrons is required to explain the observed large-scale diffuse radio emission (Brunetti and Jones, 2014; Brunetti and Vazza, 2020).

The turbulent spectrum produced by the merger event have a wide range, from large (∼500 kpc) to small ($\sim r_L$, i.e. the Larmor giroradius) scales. In particular, particles and magnetic fields in a turbulent medium can experience compressive and incompressive (i.e. solenoidal) turbulence on small scales. Up to 10% of the total energy in the compressive turbulence of magnetosonic waves, which is the most effective process in the ICM, is expected to be converted in CR re-acceleration via the Transit Time Damping (TTD) resonance (Brunetti and Lazarian, 2007; Brunetti and Lazarian, 2011). In this model, a particle resonates with the magnetic field fluctuations in these waves, and it experiences a periodic acceleration as it passes through regions of varying magnetic field strength. Moreover, solenoidal turbulence, which is a key component in amplifying magnetic fields via the small-scale dynamo mechanism (Ryu et al., 2008; Miniati, 2015), is seen in the central regions of galaxy clusters in MHD simulations (e.g. Domínguez-Fernández et al. 2019). For the large-scales, recently Brunetti and Lazarian (2016) proposed a different mechanism, where large-scale super-Alfvénic solenoidal turbulence in the ICM allows for particle re-acceleration as they diffuse stochastically across regions of magnetic reconnection and dynamo processes. In the case of prevalence of solenoidal component and strongly super-Alfvénic turbulence, this acceleration mechanism may be more efficient than TTD (Brunetti and Vazza, 2020).

1.2.4 Diffuse Radio Sources in Galaxy Clusters

In the past decades, low frequency observations of galaxy clusters revealed the presence of diffuse radio sources in a fraction of dynamically disturbed galaxy clusters (e.g. van Weeren et al. 2019 for a recent review). The connection between diffuse radio emission in the ICM and dynamically disturbed systems (e.g. Buote 2001; Cassano et al. 2010; Cassano et al. 2013; Cuciti et al. 2015) indicates that the merger activity is a key ingredient for the formation of non-thermal components in galaxy clusters. In fact, these sources revealed the presence of relativistic CRs and magnetic fields in the ICM, and opened up several questions on their origin, and the particle acceleration mechanism that allow diffuse emission on large scales (Brunetti and

Jones, 2014). The detection of extended diffuse emission is observationally challenging, as these sources are characterized by steep synchrotron spectra ($\alpha > 1$) and low surface brightness (few μJy arcsec^{-2} at 1.4 GHz). In the following, we will focus on the main properties of *radio relics* and *radio halos*, as well as the newest discovered classes of steep spectrum diffuse sources revealed by low-frequency observations.

Radio Relics

Radio relics are Mpc-scale structures typically observed in the outskirts of galaxy clusters. They are characterized by distinct elongated, arc-like morphologies with sharp emission edges, and by steep radio spectral index ($\alpha = 1 - 1.3$) and significant linear polarization, usually reaching up to 30%. Spectral index maps show clear spectral steepening, indicative of particle aging, toward the cluster center (e.g. Bonafede et al. 2009; Bonafede et al. 2012; van Weeren et al. 2010; de Gasperin et al. 2015; Hoang et al. 2018). Prime examples of this class of sources are the relic in the Coma cluster (Giovannini, Feretti, and Stanghellini, 1991; Bonafede et al., 2021) and the Sausage relic, in the cluster CIZA J2242.8+5301 (van Weeren et al., 2010). Among other notable and well studied relics there are those in the Toothbrush (e.g. van Weeren et al. 2012; Rajpurohit et al. 2020), Bullet (Shimwell et al., 2015), Abell 2256 (van Weeren et al., 2012a; Rajpurohit et al., 2022), and Abell 3667 (Rottgering et al., 1997; Johnston-Hollitt, 2003; Hindson et al., 2014; de Gasperin et al., 2022) clusters. The latter (see Fig. 1.5) is one of the remarkable cases where symmetric double relics appear on opposite sides of galaxy clusters (e.g. de Gasperin et al. 2014; Bonafede et al. 2017), as consequence of shock waves that propagate outward along the merger axis (Fig. 1.4) (Brüggen, van Weeren, and Röttgering, 2012; Ha, Ryu, and Kang, 2018). Currently, around 60 radio relics have been documented across a wide range of cluster masses (van Weeren et al., 2019). The occurrence of radio relics was estimated at $\sim$ 5% in the GMRT Radio Halo Survey (Kale et al., 2015), while the second Planck cluster catalog, overlapping with the LoTSS, reported a $\sim$ 10% fraction of clusters hosting radio relics (Jones et al., 2023). Radio relics probe the magnetic field properties in cluster peripheries, as they can be located at significant distances, often up to a large fraction of the cluster's virial radius. Furthermore, the high polarization of these relics (often exceeding 20% and up to 70% in some regions) reveals that the magnetic field is aligned with their major axis (Ensslin et al., 1998; van Weeren et al., 2010; Bonafede et al., 2012; Pearce et al., 2017). While it is widely accepted that radio relics are connected with shocks, from their arc-shaped morphology, spectral index gradients or spectral curvature, and high-degree of polarisation, the details of the mechanism responsible for the particle acceleration is still being investigated (Sec.1.2.3).

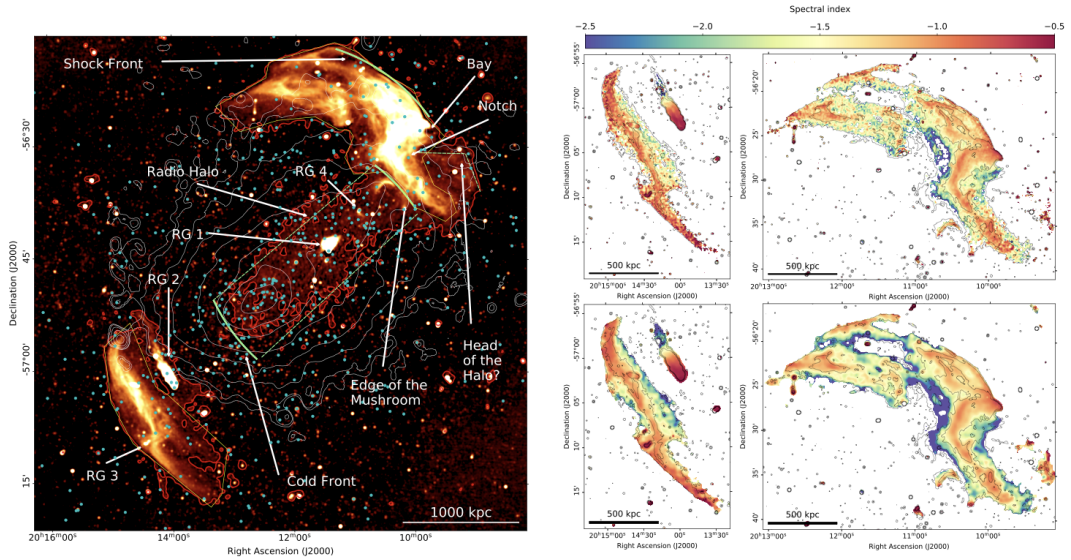

FIGURE 1.5: *Left panel:* Abell 3667 observed with MeerKAT as an example of double-relic system. White contours trace the X-ray emission from XMM-Newton. Light blue dots mark the positions of spectroscopically identified cluster members. Right panel: Spectral index maps of the radio relic regions, from high-resolution images (top) and low-resolution images (bottom), showing a clear gradiet from the spectral ageing of the relativistic particles. Credits: de Gasperin et al. (2022).

Radio Halos

Radio halos are large-scale diffuse radio sources located at the centers of galaxy clusters, permeating the ICM with a distribution similar to the thermal gas. They are generally circular in shape and have regular morphology, with sizes extending beyond 1 Mpc, and their radio surface brightness peak is usually cospatial with the X-ray centroid of the cluster. Unlike radio relics, their emission is unpolarized, typically down to a few percent. The radio halo in the Coma cluster (Fig. 1.6), first detected by Large, Mathewson, and Haslam (1959), serves as the prototype for this class of objects. Currently, around 80 radio halos have been observed (van Weeren et al., 2019), and are found to be more common in massive galaxy clusters. The occurrence of radio halos is approximately 60–70% in clusters with masses greater than $6 \times 10^{14} M_{\odot}$, but this fraction decreases to 10–30% in lower-mass clusters (Cassano et al., 2023). One of the key parameters for understanding the origin and evolution of radio halos is their spectral index, as highlighted by Brunetti and Jones (2014). The spectral characterization of extended emission is not always straightforward, since the flux density could be contaminated by embedded discrete sources and could suffer from the missing uv-coverage at short spacings. The uncertainties on the measurement of the spectral index should also consider the possible different uv-coverage between different instruments observations. Despite these issues, several robust spectral index determinations indicate that a single power-law is appropriate to fit the radio halos flux density across a wide frequency range, from tens of

FIGURE 1.6: The Coma Cluster radio halo and radio relic as seen by LOFAR at 144MHz. Credits: Bonafede et al. (2022).

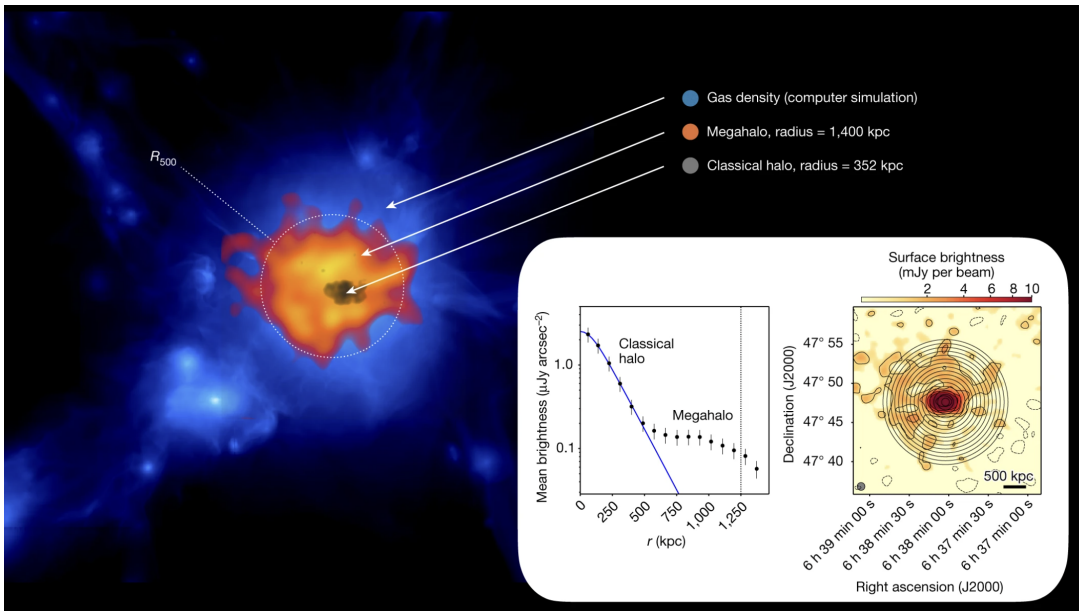

FIGURE 1.7: Megahalo (orange) in the galaxy cluster ZwCl 0634.1+4750, embedding the classical radio halo (black). The thermal ICM (blue) is obtained from a numerical simulation. In the bottom inset, the surface brightness profiles of the radio halo and megahalo for comparison. Credits: Cuciti et al. (2022)

MHz to a few GHz. The real spectrum is expected to deviate from the single power-law at GHz frequencies as result of energy losses and inefficient acceleration, as it is seen for Coma (Thierbach, Klein, and Wielebinski, 2003) and few other systems (Rajpurohit et al., 2021c; Xie et al., 2020). Recent low-frequency radio observations, made possible by instruments like the upgraded Giant Metrewave Radio Telescope (uGMRT) and the LOw Frequency Array (LOFAR), have also led to the discovery of an increasing number of radio halos with very steep spectral indices ($\alpha \geq 1.5$), known as *ultra-steep spectrum* radio halos (USSRHs) (Brunetti et al., 2008; Dallacasa et al., 2009; Macario et al., 2010; Bonafede et al., 2012; Venturi et al., 2017; Wilber et al., 2018; Di Gennaro et al., 2021; Bruno et al., 2023).

The origin of radio halos is closely tied to the turbulence generated by cluster mergers. As seen in Sec.1.2.3, a portion of the kinetic energy from the merger event dissipates through a cascade of turbulence, transferring energy to non-thermal components of the ICM via Fermi II re-acceleration processes (Brunetti and Jones, 2014). In this turbulent re-acceleration scenario, the more massive the merging cluster, the more energy is channeled into non-thermal components, which explains the observed radio power-mass correlation (Cassano et al., 2013; Cuciti et al., 2021). In contrast, relaxed clusters that have not experienced a recent merger (within the past $\sim$ 1 Gyr) tend to be radio quiet, as they lack the turbulence necessary to generate significant radio halo activity.

While the origin and evolutionary phases of radio halos are still being investigated with several studies, the classification of radio diffuse sources is quickly evolving thanks to new sensitive radio observations at low frequencies. Cuciti et al. (2022)

reported the detection of diffuse emission beyond the scales of classical radio halo in four disturbed galaxy clusters—ZwCl 0634.1+4750, A665, A697, and A2218. These newly identified sources, classified as *megahalos* , extend up to the galaxy cluster $\sim R_{500}$ and encompass the existing radio halos (Fig. 1.7). For two of these megahalos, the authors could estimate the spectral index, which resulted to be very steep ($\alpha_{50MHz}^{150MHz} \approx 1.6$) and in general they show a shallower radio surface brightness profile compared to classical radio halos, indicating that different physical processes may be responsible for the two types of emissions. It has been proposed that megahalos may trace particle re-acceleration from turbulence generated by the accretion of matter in the outskirts of the cluster, an area where the conditions of the ICM are not well understood.

On even larger scales, the discovery of bridges of radio diffuse emission connecting two pre-merger galaxy clusters (Govoni et al., 2019; Botteon et al., 2020) has challenged the current understanding of relativistic particles and magnetic field components in the large-scale structure of the Universe (see next Section).

1.3 Cosmic Filaments

In the previous Sections, we have explained the importance of galaxy clusters and their internal environment to the study of the mechanisms of particle acceleration and magnetic field amplification. While galaxy clusters are nowadays well-studied, the larger-scale filamentary structure they inhabit remain poorly explored. Therefore, recently galaxy clusters have been exploited as probes in tracing the diffuse component of the large-scale structure of the Universe, particularly in identifying bridges and filaments between merging systems. In the next Sections, we focus on these under-investigated regions, particularly intercluster radio bridges, which are the main subject of study for the aims of this Thesis.

1.3.1 Radio Bridges between Merging Clusters

Recent low-frequency observations have shown the presence of diffuse radio emission on scales never probed before, along the filaments of the cosmic web between interacting cluster pairs (Govoni et al., 2019; Botteon et al., 2020). Radio bridges are a new class of diffuse emission, and their characteristics are being defined with new focused studies. Observations of the two confirmed cases, detected between the pre-merging galaxy clusters Abell 0399 - Abell 0401 (Govoni et al., 2019) (hereafter, A399-A401) and in Abell 1758N- Abell 1758S (Botteon et al., 2020), show that radio bridges can extend over scales ≥ 1 Mpc beyond the clusters R_{500}, and have a homogeneous diffuse morphology at low frequencies (Fig. 1.8).

The most spectacular case of radio bridge is the one in A399-A401, which is also further analysed in this Thesis (see Chapter 4 and Chapter 5). The galaxy clusters A399-A401 are a local ($z \sim 0.07$, Oegerle and Hill 2001) pair found in a pre-merger

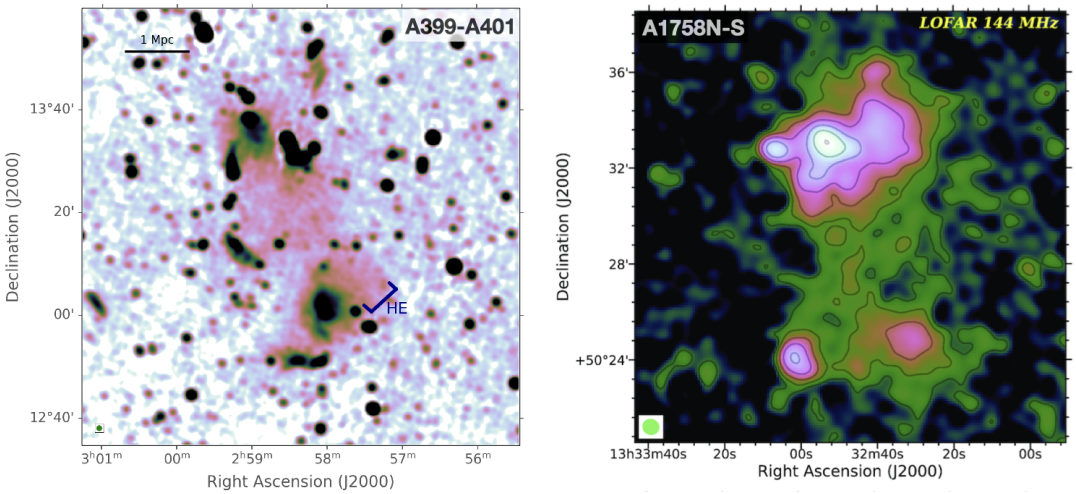

FIGURE 1.8: Two spectacular cases of radio bridges. *Left panel:* A399-A401 radio bridge ($\sim$ 3 Mpc) observed with LOFAR at 144 MHz and resolution of $70''$ (de Jong et al., 2022). Right panel: A1758N-A1758S radio bridge ($\sim$ 2 Mpc) observed with LOFAR at 144 MHz (Botteon et al., 2020).

state (Bonjean et al., 2018) where X-ray observations (Fujita et al., 1996; Fujita et al., 2008; Akamatsu et al., 2017) revealed the presence of $6-7$ keV ionised plasma in the region between the clusters. The gas in this region is also detected via the Sunyaev-Zeldovich (SZ) effect by *Planck* (Planck Collaboration et al., 2013; Planck Collaboration et al., 2016; Bonjean et al., 2018) and the Atacama Cosmology Telescope (ACT) (Hincks et al., 2022; Radiconi et al., 2022). The two clusters show their own history of merger, having both radio halos, that have been studied through multifrequency observations (Murgia et al., 2010; Govoni et al., 2019). With LOFAR observations at 140 MHz, they measure a surface brightness of $I = 0.38$ μJy arcsec^{-2} for the bridge, which is extended for approximately 3 Mpc, i.e. the entire projected separation between the two clusters centers. More recently, de Jong et al. (2022) presented a 40-hour, deep LOFAR observation at 144 MHz and investigated further the properties of the diffuse emission in the bridge. They were able to detect the bridge at high significance, and measure a flux density of $S_{144} = 550 \pm 60$ mJy over 2.7 Mpc^2. Other examples of radio bridges are also being discovered between clusters and groups of galaxies, as in the cases of the Coma cluster, detected at a low frequency (Bonafede et al., 2021), and, for the first time at a high frequency, in the Shapley Supercluster (Venturi et al., 2022). Moreover, a candidate bridge is reported in Abell 1430 (Hoeft et al., 2021), and a bridge between relic and halo in A1550 (Pasini et al., 2022). A peculiar bridge, where the absence of one radio halo makes the classification non-trivial, has also been observed between Abell 2061 and Abell 2067 (Pignataro et al., 2024b) and is presented in Chapter 6.

The discovery of such bridges stressed the need to find a theoretical model that can explain this emission, which is different than radio relics and halos. Govoni et al. (2019) explored different possibilities to explain their observations, since the

synchrotron and inverse Compton losses (Sec.1.2.2) make the lifetime of the particles ($\sim 10^8$ years at 140 MHz) too short to travel from the centre of the cluster and cover the bridge extension. This points to an in situ mechanism for particle acceleration, such as diffuse shock re-acceleration of a pre-existing population of mildly relativistic electrons. This process would plausibly result in a spectral index of $\alpha \sim 1.2 - 1.3$ for the bridge, as often observed in relics (van Weeren et al., 2019). Alternatively, Brunetti and Vazza (2020) showed how this emission could also be explained by a Fermi-II re-acceleration process (see Sec.1.2.3). In this scenario, the fossil relativistic particles are re-accelerated by turbulence in amplified magnetic fields over Mpc-scales. This would result in steep observed synchrotron spectra between 150 MHz and 1.5 GHz ($\alpha < -1.5$). Therefore, following the discovery of the bridge, the A399-A401 system was extensively studied at radio frequencies. Recently, Nunhokee et al. (2023) presented WSRT observations at 346 MHz that were not sufficiently deep to observe the bridge, and therefore place a limit on the bridge spectral index ($\alpha_{140}^{346} < -1.5$). A similar procedure to place limits on the emission of radio bridges is defined in Pignataro et al. (2024). As discussed in depth in Chapter 4, the non-detection of bridge emission in high sensitivity uGMRT data at 400 MHz results in a more stringent constraint on the steep bridge spectral index ($\alpha_{140}^{400} < -2.2$), disfavouring the Fermi-I acceleration scenario.

In Chapter 5, we present the spectral characterization of the radio bridge in A399-A401 that, with observations at 60 MHz, are able to constrain the particle acceleration mechanism involved, and allow us to constrain the magnetic fields in this region (Pignataro et al., 2024c).

Multi-frequency studies of synchrotron emission from radio-bridges between clusters are fundamental to shed light on mechanisms of particle acceleration and properties of the magnetic fields on such large scales.

1.3.2 Filaments in Superclusters of Galaxies

Recent studies have investigated the possibility of detecting the radio and X-ray emission associated with the filaments of the cosmic web (Vacca et al., 2018; Vazza et al., 2019), and it was proven by the discovery of two radio bridges of diffuse synchrotron emission between clusters (Govoni et al., 2019; Botteon et al., 2020), that resulted in an estimate of magnetic field of $\sim 0.3\mu$G in the intercluster region (Pignataro et al., 2024c). With LOFAR HBA observations, the non-detection of diffuse emission in filaments between galaxy clusters resulted in upper limits of $\leq 0.2\mu$G (Locatelli et al., 2021). However, these detections represent the densest regions of filaments, compressed by the high level of dynamical activity between two merging clusters, and fainter filaments on several tens of Mpc scale remain mostly undetected.

The presence of non-thermal emission on the cosmic large-scale (1-15 Mpc) is reported in Vernstrom et al. (2021), where they find a robust detection of stacked radio signal from the filaments between luminous red galaxies. Several studies tried

to constrain the strength of magnetic fields in filaments with different approaches: direct detections are now beyond the capabilities of current instruments, but cross-correlation (Vernstrom et al., 2017; Brown et al., 2017) and X-ray and radio images stacking studies (Tanimura et al., 2020; Vernstrom et al., 2021) have found equipartition magnetic field estimates and limits for B ranging from 30 to 60 nG. Finally, another approach is to use the Faraday rotation of linearly polarized sources in the line of sight of magnetised plasma (see Chapter 2).

Vernstrom et al. (2023) recently reported a high polarisation fraction for filaments, which implies a significant ordered magnetic field component in these environments, consistent with the detection of an RM signal from them. Carretti et al. (2022); Carretti et al. (2023) estimated magnetic fields of 40–80 nG with extragalactic background RMs at low frequencies. At higher frequencies, RM studies reported limits between 40nG (Vernstrom et al., 2019) for extragalactic magnetic fields and 0.3μG in superclusters of galaxies (Xu et al., 2006; Sankhyayan and Dabhade, 2024). These studies suggest that magnetic fields and relativistic particles are a component of the large scale structure, and to detect them at radio wavelengths the process of major merger can produce a favourable environment, where turbulence and shocks trigger particle re-acceleration on very large scale. Therefore, the conditions to generate diffuse radio emission on very large scales are expected to be particularly favourable in superclusters of galaxies, where rich clusters in their core may be dynamically active (Einasto et al., 2021): these are nested within the Cosmic Web, creating a coherent structure of galaxy clusters embedded in a network of filaments spanning up to hundreds of Mpc (Lietzen et al., 2016; Bagchi et al., 2017). Superclusters of galaxies are the ideal laboratory to identify and study cosmic filaments. In fact, the possibility of finding filamentary structure increases within superclusters (Tanaka et al., 2007).

Several different ways exist to map superclusters in the sky, which makes it convenient when researching the large-scale structure of filaments. One frequently used approach is to exploit the galaxy distribution to trace filamentary structures connecting clusters and groups. This is supported by the vast availability of sky area survers such as the Sloan Digital Sky Survey (SDSS, Almeida et al. 2023), the Two Micron All Sky Survey (2MASS, Skrutskie et al. 2006), and Two Degree Field Redshift Survey (2dFRS, Huchra et al. 2012) or the Center for Astrophysics galaxy redshift survey (CfA2, Huchra, Vogeley, and Geller 1999). Superclusters of galaxies are frequently identified using the Friends-of-Friends (FoF, e.g. Zeldovich, Einasto, and Shandarin, 1982; Einasto et al., 1984; Chow-Martínez et al., 2014; Bagchi et al., 2017; Sankhyayan and Dabhade, 2024) algorithm, which is used to find and group points (in this case, galaxies) with unknown distribution in a simulation. Other methods are also used, such as applying a threshold cut on the luminosity density field of the galaxy distribution (Einasto et al., 2007; Lietzen et al., 2016), or on the number density field constructed by Voronoi tassellation (Neyrinck, 2008; Nadathur and Crittenden, 2016). Santiago-Bautista et al. (2020) developed an identification methodology based on

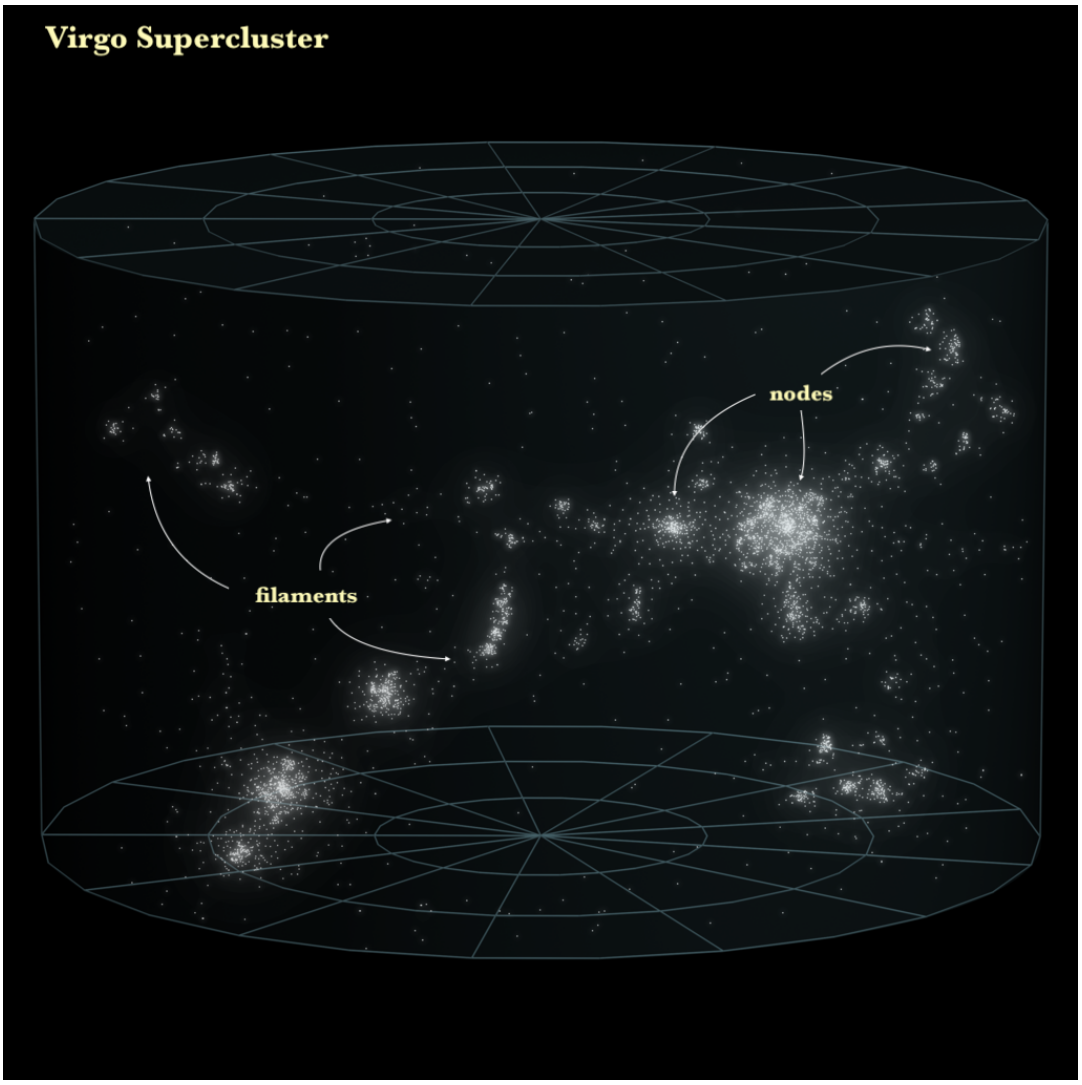

FIGURE 1.9: Virgo Supercluster representation, with filaments and nodes.

geometrical information of the galaxy distribution. This process of identification resulted in several different catalogs of known superclusters of galaxies that can be used in combination with Faraday Rotation measures catalogs of sources behind superclusters, to probe the magnetic field of the plasma crossed by the polarised emission of the distant radio sources (Xu et al., 2006; Sankhyayan and Dabhade, 2024). This approach will be presented in Chapter 7.

Chapter 2

The Magnetized Cosmic Web with Polarization

2.1 Polarization of Synchrotron Emission

Synchrotron radiation is linearly polarized. The electric field vector of the radiation emitted by the relativistic electron oscillates mainly in the plane perpendicular to the electron's acceleration, resulting in linearly polarized light. The degree of polarization depends mainly on the observer's angle relative to the magnetic field and the energy of the electrons. In ideal conditions, synchrotron radiation can exhibit a high ($\sim 70-75\%$) degree of linear polarization, making it a powerful tool to directly probe the structure of astrophysical magnetic fields at the source, as it is the case for radio relics (e.g. van Weeren et al. 2010). In reality, observations show low polarization fraction ($\leq 10\%$ at cm or mm wavelengths, e.g. Taylor et al. 2007; Murphy et al. 2010) for many radio sources, which further decreases rapidly with wavelength.

Extensive studies conducted by Burn (1966) and Sokoloff et al. (1998) investigated the origins of wavelength-dependent depolarization effects. They demonstrated that such depolarization can arise from fluctuations in the magnetic field structure, both of the orientation and strength of the field either along the line of sight through the source or across the angular size of the observing beam. The primary mechanism responsible for the observed depolarization is Faraday rotation, which is actually a powerful tool to probe the magnetic field embedded in the crossed medium.

In this Chapter, we review the basic physics of polarization and describe the techniques relative to the Faraday rotation used in this Thesis to derive an estimate of magnetic fields in cosmic filaments.

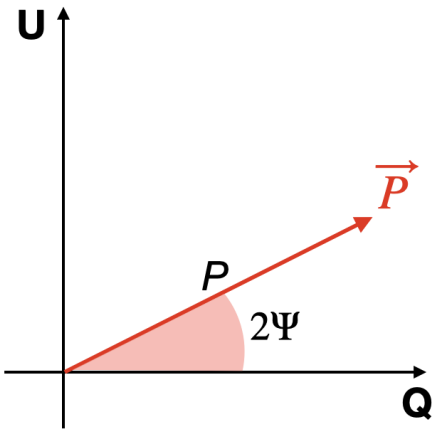

FIGURE 2.1: Representation of the $\vec{P}$ polarization vector in the complex QU plane.

2.1.1 The Physics of Polarization

The polarization of an electromagnetic wave can be described with the Stokes parameters: I, Q, U, and V (Stokes, 1851). The fractional polarization of linearly polarised emission ($V = 0$) can be written as function of the total intensity I:

$$p = \frac{P}{I} = \frac{\sqrt{Q^2 + U^2}}{I}, \tag{2.1}$$

or integrating over the energy spectrum of the electrons (Sec.1.2.2) (Le Roux 1961):

$$p = \frac{3\delta + 3}{3\delta + 7} = \frac{3\alpha + 3}{3\alpha + 5} \tag{2.2}$$

(see Eq.1.10). It follows, that from the observed spectrum of the radiation, we can infer the expected degree of polarization. Typical observed values of $\alpha \sim 0.7$ imply a maximum $p \sim 70\%$, with uniform magnetic field and no depolarizing effects. The degree of polarization can also be enhanced if the magnetic field is preferentially ordered along one direction.

The polarization can also be written as a pseudo-vector in the complex plane defined by the Stokes parameters Q and U (Burn, 1966):

$$\vec{P} = Pe^{2i\Psi} = pIe^{2i\Psi} = Q + iU, \tag{2.3}$$

where Ψ is the polarization angle (see Fig. 2.1), defined as

$$\Psi = \frac{1}{2}\arctan\frac{U}{Q}. \tag{2.4}$$

2.1.2 Faraday Rotation

The Faraday rotation is an effect that occurs when a linearly polarised wave passes through a medium with free thermal electrons of density n_e and magnetic field $\vec{B}$, and the intrinsic polarisation angle Ψ_0 is rotated by a quantity that is dependent on the squared observing wavelength (λ):

$$\Psi(\lambda^2) = \Psi_0 + \phi\lambda^2, \tag{2.5}$$

where ϕ is the Faraday depth, defined as (Burn, 1966)

$$\phi = 0.812 \int_{source}^{obs} n_e B_{||} \mathrm{d}l \ [\mathrm{rad\ m^{-2}}] \tag{2.6}$$

with n_e in $\mathrm{cm^{-3}}$, $B_{||}$ is the magnetic field component parallel to the line-of-sight in μG, and dl is the infinitesimal path length in parsecs (pc). The Faraday depth is taken positive when the magnetic field is pointing towards the observer. An additional correction is needed for the observed Faraday depth, ϕ_{obs}, that is reduced by a factor $(1+z)^2$ with respect to the intrinsic ϕ for a source at redshift z. The integral becomes:

$$\phi_{obs} = 0.812 \int_{z}^{0} \frac{n_e(z') B_{||}(z')}{(1+z')^2} \frac{\mathrm{d}l}{\mathrm{d}z'} \ [\mathrm{rad\ m^{-2}}]. \tag{2.7}$$

Sources can be more or less extended in Faraday depth, and the extension ($\Delta\phi$) depends on the wavelength. They can be separated in Faraday-thin (or Faraday simple) and Faraday-thick (or Faraday complex) sources, for which $\lambda^2\Delta\phi \ll 1$ and $\lambda^2\Delta\phi \gg 1$, respectively (see Fig. 2.2). In Faraday depth space, Faraday-thin sources can be described by a Dirac δ-function, while Faraday-thick sources appear as a convolution of multiple δ-functions and, thus, with a larger extension (Brentjens and de Bruyn, 2005).

In the simplest case, for a Faraday-thin source where only one non-emitting screen lies along the line-of-sight and does not suffer from depolarization, the Faraday depth of that source is equal to its Rotation Measure (RM) at all wavelengths, defined as the coefficient of the linear relation between the polarization angle and λ^2:

$$RM = \frac{\mathrm{d}\Psi(\lambda^2)}{\mathrm{d}\lambda^2}. \tag{2.8}$$

We can therefore approximate the average Faraday rotation of a screen of physical depth L as

$$\langle RM \rangle = 0.812\, n_e B_{||} L \ [\mathrm{rad\ m^{-2}}], \tag{2.9}$$

and it is possible to solve the equation for the magnetic field strength if the gas density distribution is known (Fig. 2.3).

A number of detailed images of polarized radio sources reveal how the RM can fluctuate down to linear scales $\leq$ 10 kpc (e.g. Carilli and Taylor 2002). As the RM can have both positive and negative values, also for strong magnetic fields a source can

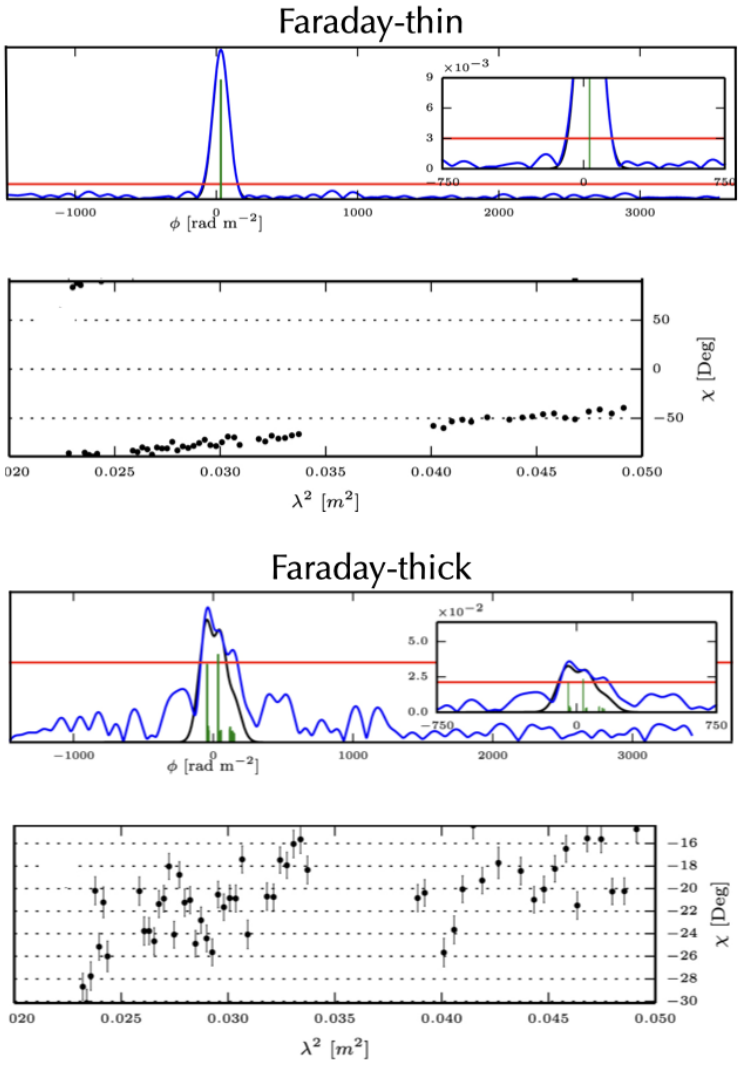

FIGURE 2.2: A Faraday-thin (top panel) and Faraday-thick (bottom panel) source. The Faraday simple source appears as a δ-function in the Faraday depth space, and there exists a linear relation between the polarization angle (Ψ) and λ^2. Conversely, the Faraday-thick source shows complex structure in the Faraday depth space, a larger $\Delta\Psi$, and a non-linear relation in the $\Psi - \lambda^2$ plane.

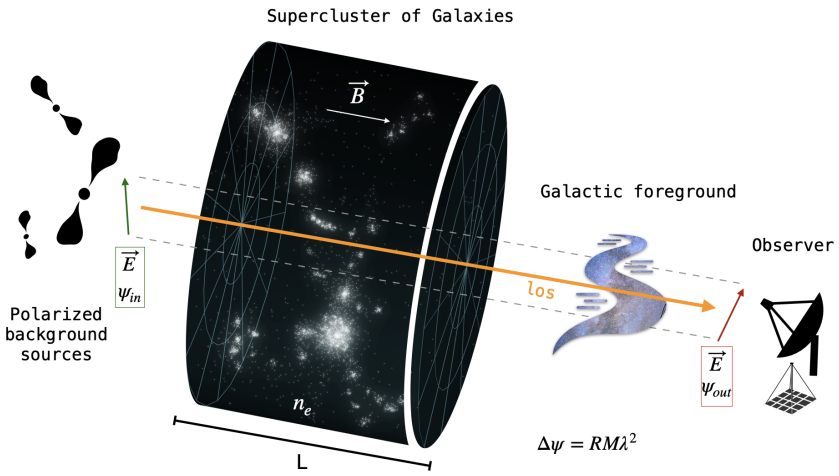

FIGURE 2.3: Schematic representation of the Faraday rotation effect for linearly polarized radiation of background sources passing through a magnetoionic medium in a supercluster of galaxies.

have $\langle RM \rangle = 0$. Hence, the dispersion, σ_{RM} of the RM fluctuations is a very informative tool to constrain the magnetic field of the intervening medium (see Chapter 7). If we assume a single-scale magnetic field model, i.e. the screen is made of cells of uniform size (Λ_c), electron density and magnetic field strength, but with a field orientation at random angles in each cell, the observed RM distribution from background sources is Gaussian with zero mean and variance given by (Lawler and Dennison, 1982; Tribble, 1991; Murgia et al., 2004):

$$\sigma^2_{RM} = \langle RM^2 \rangle = 0.812^2 \Lambda_c \int (n_e B_{||})^2 \mathrm{d}l \ [\mathrm{rad}^2\ \mathrm{m}^{-4}]. \tag{2.10}$$

If the gas density profile of a galaxy cluster is determined through X-ray observations or modeled (e.g. a β-model as shown in Eq.1.4), and assuming Λ_c, the magnetic field strength of the cluster can be estimated by measuring the RM dispersion from resolved RM images of background or embedded radio sources. Although from observations the RM distribution often appears nearly Gaussian, indicating a random magnetic field structure at small scales, the presence of a non-zero mean RM ($\langle RM \rangle$) in galaxy clusters suggests large-scale magnetic field fluctuations extending over hundreds of kpc (Murgia et al., 2004). This same approach can be used to infer the magnetic fields in the large-scale structure, investigating the properties of the medium in filaments of superclusters of galaxies.

2.1.3 Depolarization effects

The expected value of fractional polarization (Eq.2.2) is never observed because a number of depolarising effects play a role in decreasing the amount of polarization. Depolarization towards longer wavelengths can occur due to the mixing of the emitting and rotating media (i.e. an intrinsic effect) (Arshakian and Beck, 2011), as well as from the finite spatial resolution of our observations (i.e. an instrumental effect)

(O'Sullivan et al., 2012). Here we present the main depolarization mechanism (e.g. De Rubeis et al. 2024):

- *Differential Faraday rotation*: this effect is caused by co-spatial emitting and rotating regions in a regular magnetic field. The polarization angle of the radiation emitted from the layer farthest to the observed is more rotated than that from the nearest layer. Since the observed emission results from the superposition of the different components along the line of sight, this causes depolarization. The observed polarization becomes:

$$P_{obs} = P_{int} \frac{sin\phi\lambda^2}{\phi\lambda^2} e^{2i(\Psi_0 + \frac{1}{2}\phi\lambda^2)} \tag{2.11}$$

- *Internal Faraday rotation*: this effect occurs when the emitting and rotating regions contain turbulent and/or filamentary magnetic fields therefore the emission from turbulent layers is mixed together. Assuming that the components of the magneto-ionic medium have the same distribution along the line of sight, we can write

$$P_{obs} = P_{int} e^{2i\Psi_0} \left(\frac{1 - e^{2i\phi\lambda^2 - 2\xi^2_{RM}\lambda^4}}{2\xi^2_{RM}\lambda^4 - 2i\phi\lambda^2} \right), \tag{2.12}$$

  where ξ_{RM} is the internal Faraday dispersion of the medium.

- *External Faraday dispersion/beam depolarization*: this an instrumental effect caused by an external non emitting (i.e. no relativistic electrons) screen. If the magnetic field is turbulent and the synthesized observing beam is larger than the typical scales of RM variations, the different paths mixed together in the beam cause depolarization (Burn, 1966; Sokoloff et al., 1998). This effect can be described with

$$P_{obs} = P_{int} e^{-2\sigma^2_{RM}\lambda^4} e^{2i(\Psi_0 + RM\lambda^2)}. \tag{2.13}$$

  This effect is stronger with larger observing beam sizes.

  In the case of a regular magnetic, then any strength or direction variation (e.g. a strong gradient of gas density) within the beam will lead to depolarization. This is more generally called beam depolarization, and it is an instrumental effect that can be reduced with higher angular resolution observations.

- *Bandwidth depolarization*: if the observing bandwidth is limited between two wavelegths λ_1 and λ_2, with $\lambda_2 \approx \lambda_1$, the polarization angle is rotated across the band according to

$$\Delta\Psi = RM(\lambda_1^2 - \lambda_2^2) = RM(\lambda_1 + \lambda_2)(\lambda_1 - \lambda_2) \approx 2\lambda_0 \Delta\lambda RM, \tag{2.14}$$

  where λ_0 is the central wavelength. The measured value of $\vec{P}$ is averaged over the bandwidth, causing depolarization.

2.2 RM Synthesis

The conventional term RM is ordinarily used to describe all Faraday effects. This is because it is assumed that most sources are Faraday-simple, meaning they can be characterized by a single value of ϕ which, only in this simple case, coincides with the RM. However, in galaxy clusters and large-scale structure, the magnetic field is expected to be turbulent and filamentary, and the emitting and rotating medium can easily be co-spatial. As a result, a single ϕ value is revealed insufficient to describe these Faraday-complex sources. Additionally, different polarized sources could be aligned along the same line of sight, leading to multiple ϕ values contributing to the observed emission.

To accurately describe Faraday-complex sources, the RM synthesis technique was developed by Brentjens and de Bruyn (2005), following Burn (1966). Starting from the observed polarization vector $\vec{P}(\lambda^2)$, they introduce the Faraday dispersion function (FDF) $\vec{F}(\phi)$ (also called Faraday spectrum), which describes the intrinsic polarized flux as a function of the Faraday depth

$$\vec{P}(\lambda^2) = \int_{-\infty}^{+\infty} \vec{F}(\phi) e^{2i\phi\lambda^2} \mathrm{d}\phi, \tag{2.15}$$

which has the form of a Fourier Transform (FT), and in principle could be inverted to express the intrinsic polarization in terms of the observable quantities:

$$\vec{F}(\phi) = \int_{-\infty}^{+\infty} \vec{P}(\lambda^2) e^{-2i\phi\lambda^2} \mathrm{d}\lambda^2. \tag{2.16}$$

The knowledge of the Faraday spectrum along a line-of-sight allows to recover the different Faraday depths relative to all the sources and layers present. However, we do not observe for $\lambda^2 < 0$ and neither for all positive λ^2. The limited sampling in λ^2 space is solved in Brentjens and de Bruyn (2005), by introducing a weight function $W(\lambda^2)$ (also called window function) that is non-zero only where the λ^2 space is sampled by the observation. Therefore, the observed polarized flux is the product of the polarized flux density and the weight function, and the reconstructed Faraday spectrum becomes:

$$\tilde{\vec{F}}(\phi) = \vec{F}(\phi) \otimes \vec{R}(\phi) = K \int_{-\infty}^{+\infty} \vec{P}(\lambda^2) W(\lambda^2) e^{-2i\phi\lambda^2} \mathrm{d}\lambda^2, \tag{2.17}$$

where $\otimes$ denotes convolution, K is a normalization factor, and $\vec{R}(\phi)$ is the Rotation Measure Sampling Function (RMSF) defined as

$$\vec{R}(\phi) \equiv K \int_{-\infty}^{+\infty} W(\lambda^2) e^{-2i\phi\lambda^2} \mathrm{d}\lambda^2. \tag{2.18}$$

The RMSF can be thought of as the observing beam of an interferometric observation, which depends on the *(u,v)*-coverage. The RMSF depends on the λ^2-coverage of the data in the Faraday space. A more complete coverage of the λ^2 space will

improve the reconstruction, hence the final quality of the reconstructed $\vec{F}(\phi)$ will depend strongly on the weight function which controls the shape of the RMSF; a larger range of wavelengths increases the resolution, and closer λ^2 sampling reduces the side lobes of the RMSF. The full width half maximum (FWHM) of the RMSF defines the resolution for an observation of total width $\Delta\lambda^2$:

$$\delta\phi \approx \frac{2\sqrt{3}}{\Delta\lambda^2}. \tag{2.19}$$

The largest scale observable in ϕ space, i.e. observable at 50% sensitivity is linked to the minimum sampled λ^2:

$$\Delta\phi_{max} \approx \frac{\pi}{\lambda^2_{min}}, \tag{2.20}$$

and the maximum observable Faraday depth, at which the sensitivity of the observations drops to 50%, is linked to the channel width $\delta\lambda^2$:

$$\mid \phi_{max} \mid \approx \frac{\sqrt{3}}{\delta\lambda^2}. \tag{2.21}$$

Brentjens and de Bruyn (2005) introduced the quantity λ_0^2, which represent the mean of the sampled λ^2 weighted by $W(\lambda^2)$:

$$\lambda_0^2 = \frac{\int_{-\infty}^{+\infty} W(\lambda^2)\lambda^2 \mathrm{d}\lambda^2}{\int_{-\infty}^{+\infty} W(\lambda^2)\mathrm{d}\lambda^2}. \tag{2.22}$$

They have shown that the RMSF is better behaved when all polarization vectors are rotated back to their position at λ_0^2, and this rotation can be performed without any loss of generality for the Fourier shift theorem. Finally, Eq.2.17 and Eq.2.18 can be approximated with a sum if $\phi\delta\lambda^2 \ll 1$ for each of the N channels of width $\delta\lambda^2$ and central frequency λ_i^2:

$$\tilde{\vec{F}}(\phi) \approx K \sum_{i=1}^{N} \vec{P}(\lambda_i^2) W(\lambda_i^2) e^{-2i\phi(\lambda_i^2 - \lambda_0^2)}, \tag{2.23}$$

$$\vec{R}(\phi) \approx K \sum_{i=1}^{N} W(\lambda_i^2) e^{-2i\phi(\lambda_i^2 - \lambda_0^2)}. \tag{2.24}$$

The equations in this form are implemented in practice in order to perform the RM Synthesis.

2.2.1 FDF deconvolution

The RM synthesis provides the reconstructed FDF, i.e. the convolution between the true Faraday spectrum and the RMSF. RM synthesis can be summarized as a trial-and-error technique, which explores a range of Faraday depths to identify the one that maximizes the polarized flux signal across all observed wavelength channels. The Faraday depth at which this flux is maximum corresponds to the actual RM

of the source. In cases where multiple sources are observed along the same line of sight, the RM synthesis process can resolve these sources as distinct peaks, unlike traditional methods, such as $\Psi - \lambda^2$ fitting, which would likely produce a non-linear relationship between Ψ and λ^2, as shown in Fig. .2.2.

However, when multiple features emerge in the reconstructed function, it can be challenging to distinguish between actual astrophysical signals and the sidelobes of the RMSF. To mitigate this issue, deconvolution methods, specifically the `RM-CLEAN` algorithm (Heald, 2009), can be employed to remove the RMSF from the reconstructed Faraday spectrum. This deconvolution process is conceptually similar to the `CLEAN` algorithm (Clark, 1980; Högbom, 1974), used in aperture synthesis imaging, with the distinction of taking place in one dimension and dealing with complex quantities. An example of cleaned FDF is shown in Fig. 2.4.

A limitation of the `RM-CLEAN` is the assumption that each detected feature in the Faraday spectrum is a perfect Dirac δ-function, which can lead to issues when analyzing Faraday-complex sources, particularly at low signal-to-noise ratios, where the algorithm may diverge. When interpreting the resulting spectrum, it is necessary to consider that different combinations of magnetic field distributions, thermal electron densities, and path lengths can produce identical Faraday spectra. Thus, this degeneracy complicates the interpretation of the reconstructed spectrum, as multiple physical models could explain the same observed data. Beam depolarization further adds to this complexity by introducing spatially varying ϕ components. For sources with more intricate Faraday dispersion functions, alternative techniques have been developed to address these shortcomings (Frick et al., 2010; Bell et al., 2013; Cooray et al., 2021) but their reliability is still being investigated (e.g. Schnitzeler 2018; Ideguchi, Miyashita, and Heald 2018). Generally, to describe a Faraday-complex source, it is assumed that the value of ϕ corresponding to the peak in the Faraday spectrum can be considered to be representative for the Faraday depth of the source, while in reality the peak value represents only the main component of the spectrum. Therefore, polarization quantities computed in this way should be considered as a lower limit.

2.2.2 Detection threshold and Rician bias

Brentjens and de Bruyn (2005) provided the statistical error on the peak Faraday depth computation (σ_ϕ). If the rms noise in the Stokes Q and U single frequency channels is approximately the same, (i.e. $\sigma_{Q,ch} \sim \sigma_{U,ch} \sim \sigma_{ch}$), assuming s source with no intrinsic emission, and a uniform coverage in λ^2, we have

$$\sigma_\phi = \frac{\delta\phi}{2(P/\sigma_{QU})}, \tag{2.25}$$

where $\delta\phi$ is the FWHM of the RMSF (Eq.2.19), and $\sigma_{QU} = (\sigma_Q + \sigma_U)/2$ is the rms noise derived from the reconstructed $\tilde{Q}$ and $\tilde{U}$ spectra from the RM synthesis (Hales et al., 2012).

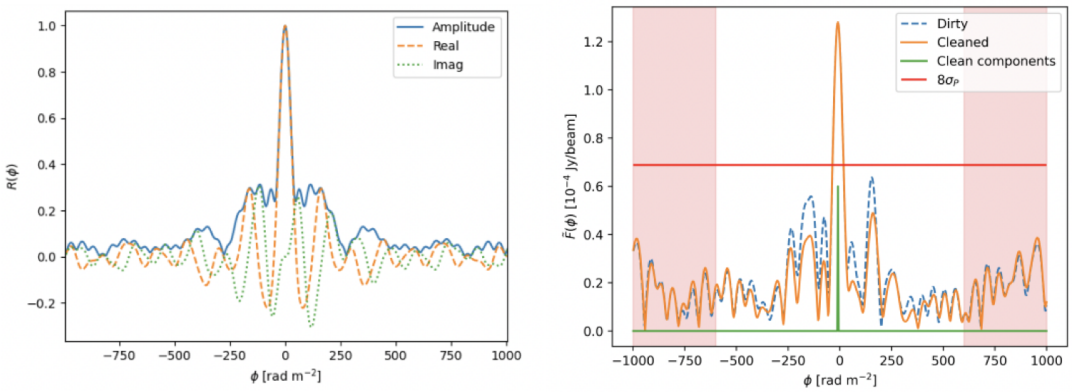

FIGURE 2.4: *Left panel*: Example of an observations RMSF, with real and imoaginary components in orange and green dashed lines, respectively, and the total amplitude in blue. *Right panel*: Faraday spectrum of one pixel for the same observation. The dirty spectrum is shown in blue, and the clean one is shown in orange. The horizontal line show the $8\sigma_{QU}$ threshold. Credits: De Rubeis et al. (2024)

The simplified assumptions for this estimate can lead to either an over- or an underestimation of the true errors (Schnitzeler and Lee, 2017). Hales et al. (2012) derived a relationship between Gaussian statistic and the statistical error on the polarization measured with RM synthesis, finding that at least a detection threshold of $P/\sigma_{QU} = 6$ is necessary to achieve a 5σ corresponding Gaussian significance. After studies conducted on surveys where the RM is derived with the RM synthesis, George, Stil, and Keller (2012) recommended a more conservative detection threshold of $8\sigma_{QU}$, which corresponds to a false detection rate of just 0.06% and a Gaussian 7σ significance.

When working at $\sigma_{QU} \leq 5$, an over-estimation of P, called the Ricean bias, becomes particularly important (Simmons and Stewart, 1985). Following Eq.2.1, P is obtained by summing in quadrature Q and U, thus the noise in Q and U results in a positive P even in the absence of signal. The statistics of P noise follows the Rice distribution, which assumes Gaussian noise in Q and U. However, real observations from sky surveys can present non-Gaussian tails in the noise distribution. In addition to the bias from the Gaussian noise, the actual Faraday depth of the source is not known, and we solve for this by finding the peak of the Faraday spectrum. This additional bias is particularly strong for RM synthesis images, since there is an uncertainty term in determination of the Faraday depth of the peak (ϕ_{peak}). In this case, a better estimator of the true polarized intensity is given by (George, Stil, and Keller, 2012)

$$P = \sqrt{|\,\tilde{\tilde{F}}(\phi_{peak})\,|^2 - 2.3\sigma_{QU}^2}, \tag{2.26}$$

and this correction is now commonly applied.

2.3 RM Grids

In the previous Sections, we have reviewed the properties of the polarized emission, and how it is affected by several effects, focusing mainly on the Faraday rotation. We have shown that the observed RM and the dispersion of the RM distribution of a sample of background sources can give very insightful information on the magnetoionic medium field strength and structure, also over large scales (Sec. 2.1.2). To exploit the full potential of RM studies, large samples of polarized sources are needed; the compilation of RM catalogues (or grids) covering the entire or large portions of sky is one of the key objective of recent radio sky surveys (see Fig. 2.5), Heald et al. 2020). With this tool, we can detect the small variations induced in the RM distribution of distant sources by the large-scale structure, but the RM grids can also be employed to map a high-quality foreground model of the Galaxy (to obtain the galactic RM; GRM) and to interpret the extragalactic objects contribution along the line-of-sight (e.g. Vernstrom et al. 2019; O'Sullivan et al. 2019; Hutschenreuter et al. 2022).

For the aims of this Thesis, we will make use of mainly the LOFAR Two-metre Sky Survey (LoTSS) DR2 and the NRAO VLA Sky Survey (NVSS) RM grids. The NVSS RM Grid (Condon et al., 1998; Taylor, Stil, and Sunstrum, 2009) is composed by 37 543 sources produced from observations at 1.4 GHz with $45''$ resolution, and has been widely used to characterize the Milky-Way properties (e.g. Purcell et al., 2015; Hutschenreuter and Enßlin, 2020; Hutschenreuter et al., 2022), as well as to isolate the RM dispersion contribution local to the source itself (Rudnick and Blundell, 2003; O'Sullivan et al., 2013; Anderson et al., 2018; Banfield et al., 2019; Knuettel et al., 2019).

RM studies at metre wavelengths offer a significant advantage over centimetre wavelength observations, due to the improvement in the precision of individual RM values. The accuracy of Faraday rotation measurements is directly related to the wavelength-squared coverage, thus RM studies at metre wavelengths provide substantially higher accuracy for individual RM measurements (~ 6 rad m^{-2} vs. ~ 0.06 rad m^{-2} at 1.4 GHz and 144 MHz, respectively) (Neld et al., 2018; O'Sullivan et al., 2018; Van Eck et al., 2018). Despite this, identifying linearly polarized sources at long wavelengths presents its challenges, primarily requiring high angular resolution and high sensitivity to counteract the significant effects of Faraday depolarization which results in a smaller fraction of radio sources exhibiting detectable polarization levels and the generally lower polarization fraction caused by the intrinsic depolarization (e.g. Farnsworth, Rudnick, and Brown 2011). LOFAR is addressing these challenges effectively with its capability to produce high-fidelity images at high angular resolution (Morabito et al., 2016; Jackson et al., 2016; Harris et al., 2019; Sweijen et al., 2022). Additionally, LOFAR broad field of view and extensive frequency bandwidth facilitate the efficient surveying of large sky areas, aiding in the detection of numerous linearly polarized sources and their RM values. The ionospheric Faraday rotation,

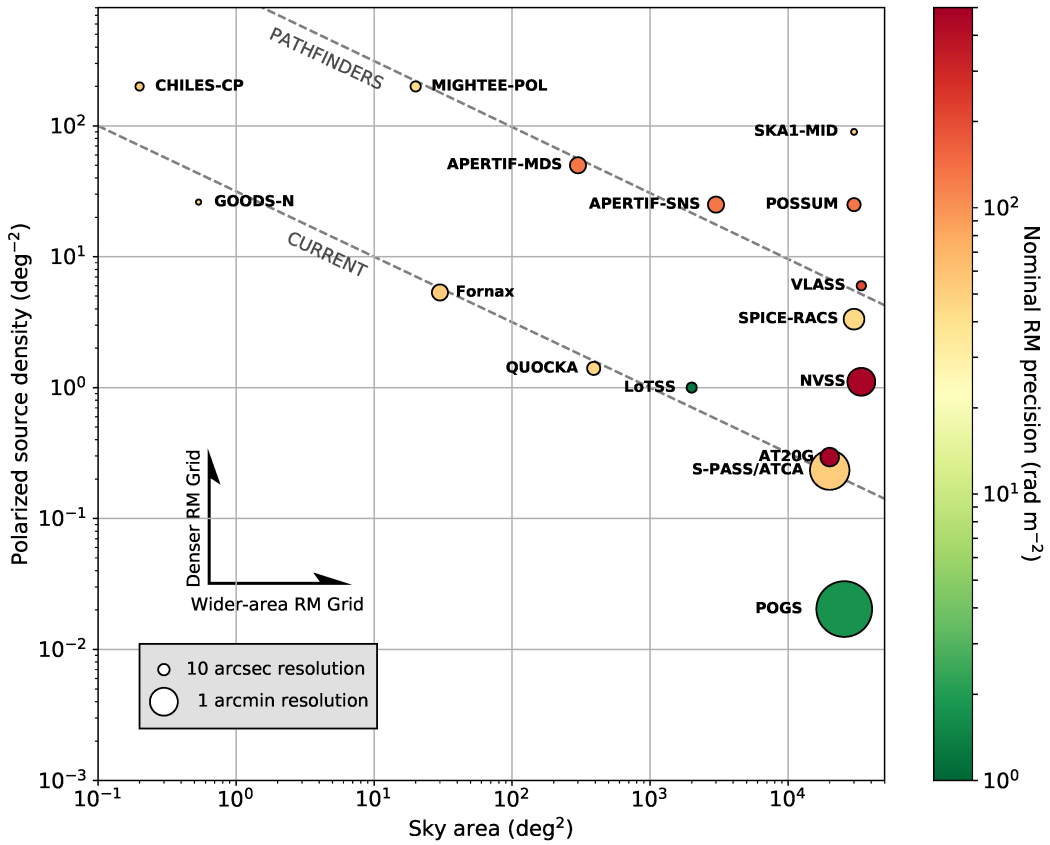

FIGURE 2.5: Illustration of the RM Grid survey strengths of various existing and future radio surveys. The size of each marker reflects the angular resolution of the survey, and the colour indicates the nominal RM precision that can be reached. Diagonal dashed lines are intended to highlight the locus of "current" (lower) and "pathfinder" (upper) survey capability. Credits: Heald et al. (2020)

which varies with time and direction, must be accounted for in low-frequency observations. LOFAR addresses this using the `RMEXTRACT` tool (Mevius, 2018), where the ionospheric Faraday rotation is modeled using a thin-shell approximation that incorporates measurements of the total electron content (TEC) in the ionosphere and the geomagnetic field's projection along a specific line of sight. The residual systematic error after the ionospheric RM correction, for a typical LoTSS pointing, is estimated to range from approximately 0.1 to 0.3 rad m^{-2} (Sotomayor-Beltran et al., 2013). The LoTSS-DR2 RM Grid (O'Sullivan et al., 2023) have produced a catalogue of 2461 extragalactic high-precision ($\sim$ 0.06 rad m^{-2}, although up to 0.3 rad m^{-2} is possible, after the ionosphere RM correction) RM values at 144 MHz and 20″ resolution.

The combined analysis of RM Grid catalogues from both metre and centimetre wavelengths is crucial for a more comprehensive understanding of the various contributors to Faraday rotation along the line-of-sight.

2.3.1 Origin and Evolution of Cosmic Magnetic Fields

In Sec. 1.3.1 and Sec. 1.3.2, we have reported the current status of estimates on the magnetic field strength found in studies that focus on the large-scale structure, with different approaches. Despite it is widely accepted that magnetic fields play a crucial role in cosmic structure formation and evolution, their origin remains a major unresolved question.

One prevailing hypothesis suggests that extremely weak ($\ll$ nG) magnetic fields were seeded early in the Universe history (i.e. during inflation, phase transitions, or even during the baryogenesis) and later amplified by turbulent dynamo mechanisms or by shock compression during structure formation and galaxy mergers (Ryu et al., 2012; Iapichino and Brüggen, 2012; Subramanian, 2016; Vazza et al., 2018). This class of magneto-genesis models, often referred to as "primordial models," has been the subject of various theoretical investigations (Harrison, 1973; Kahniashvili et al., 2010; Kahniashvili, Tevzadze, and Ratra, 2011; Kahniashvili, Brandenburg, and Tevzadze, 2016; Widrow et al., 2012; Durrer and Neronov, 2013). Alternatively, magnetic fields may have been injected during the processes of star and galaxy formation. In this "astrophysical" scenarios, magnetic fields are thought to have affected the transport of heat and entropy, as well as the distribution of heavy elements and cosmic rays in the cosmic structure (Planelles, Schleicher, and Bykov, 2016). The combination of the two scenarios is also often investigated.

The specific interest on cosmic filaments lies in the fact that in rarefied and unprocessed environments the information on the original magnetic field seed might have survived. In fact, the structure and strength of the magnetic fields we measure in the structures formed in the latest stages of the Universe evolution are believe to be the result of amplification of an earlier seed. For example, during cluster environment development, feedback from AGN, supernovae, and galactic winds may also contribute to an additional injection and amplification of magnetic fields (e.g., Bertone, Vogt, and Enßlin 2006; Donnert et al. 2009; Xu et al. 2009). As a consequence

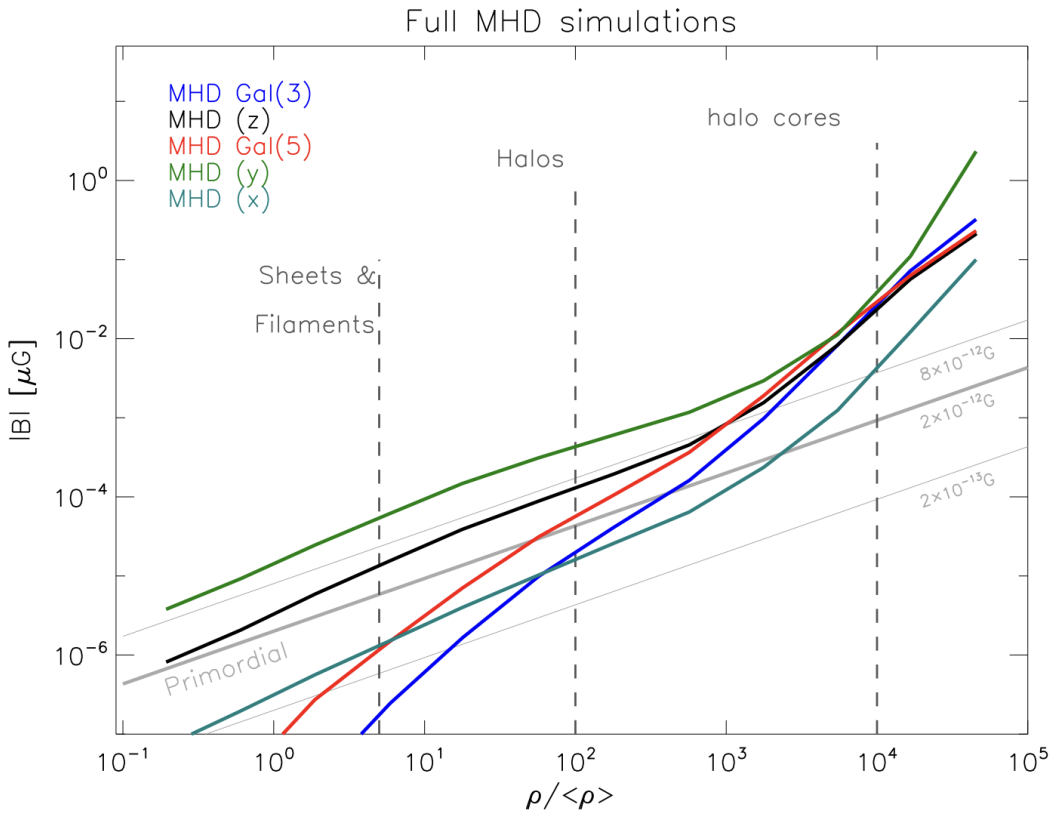

FIGURE 2.6: Magnetic field strength as a function of overdensity in cosmological SPH simulations. The solid lines represent different evolution starting from 3 different different cosmological seed field strengths: 2×10^{-13} G (dark green), 2×10^{-12} G (black), 8×10^{-12} G (green) (Dolag et al., 2004; Dolag, Bykov, and Diaferio, 2008). Additionally, 2 different galactic seeds are shown in red and blue. The adiabatic evolution solely by compression is shown in grey. Credits: Donnert et al. (2018).

of multiple feedback and processes involved, the initial seed field information is lost inside clusters, but it remains in filaments and voids, as shown in Fig. 2.6: from early cosmological smooth-particle hydrodynamic (SPH) simulations, the magnetic field reaches μG strength at central cluster over-densities, and different seeding models are indistinguishable (Donnert et al., 2018).

Therefore, we can distinguish between magnetogenesis scenarios comparing observations with MHD cosmological simulations (e.g., Vazza et al. 2017) where, starting from different initial conditions, the magnetic field evolves together with the structure formation. The amplification of the initial seed at all scales is driven by adiabatic expansion (Marinacci et al., 2015), thus the structures growth as

$$B = B_0 \left(\frac{n}{n_0} \right)^{\frac{2}{3}}, \tag{2.27}$$

where B_0 is the seed magnetic field intensity, and (n/n_0) is the local overdensity of the plasma with respect the critical value. The seed information is completely lost in the ICM due to the small scale dynamo acting in addition to the adiabatic compression of the field lines. The small scale dynamo is an MHD process of magnetic field amplification driven by turbulence and shear motions in the plasma (Ryu et al., 2008). While the small scale dynamo enables the growth of the magnetic intensity to levels detectable through synchrotron, in turn rapidly erases information on the initial value B_0.

A few works explored the evolution of magnetic fields in cosmic environments to infer the value of the initial seed and the most favorable scenarios to match observations. Observations of the non-detection of synchrotron radio emission from the cosmic web (e.g. Vernstrom et al. 2017; Locatelli et al. 2021) or more local analysis of the residual RM (RRM=RM-GRM; e.g. O'Sullivan et al. 2019) resulted in a comoving uniform seed field of $\approx 0.1 - 0.5$ nG. However, recent redshift-dependent analysis refined these estimates. Carretti et al. (2022) used 144 MHz observations to measure the evolution with redshift of the extragalactic RM, which is an extremely powerful probe of cosmic magnetism on cosmic scales. In Carretti et al. (2023), they explore several different magnetogenesis scenarios, (e.g. primordial uniform, stochastic, dynamo, astrophysical, and mixed models) to obtain a first estimate of the evolution of the magnetic field in filaments. They find magnetic fields at $z = 0$ in the range $39 - 84$ nG, which is in agreement both with previous upper limits (Brown et al., 2017; Vernstrom et al., 2017; O'Sullivan et al., 2019; Amaral, Vernstrom, and Gaensler, 2021; Locatelli et al., 2021) and the estimate of $30 - 60$ nG obtained from stacked synchrotron emission from filaments of the cosmic web (Vernstrom et al., 2021). The observed redshift trend of RRM rms leads to the dynamo and primordial stochastic models being favoured, mainly because of the flat RRM rms they predict (Fig. 2.7). A seed field of $0.04 - 0.11$ nG, comoving, best matches a primordial stochastic scenario, also consistent with previous upper limits of $0.12 - 0.13$ nG derived from CMB observations with the same scenario (Paoletti et al., 2022).

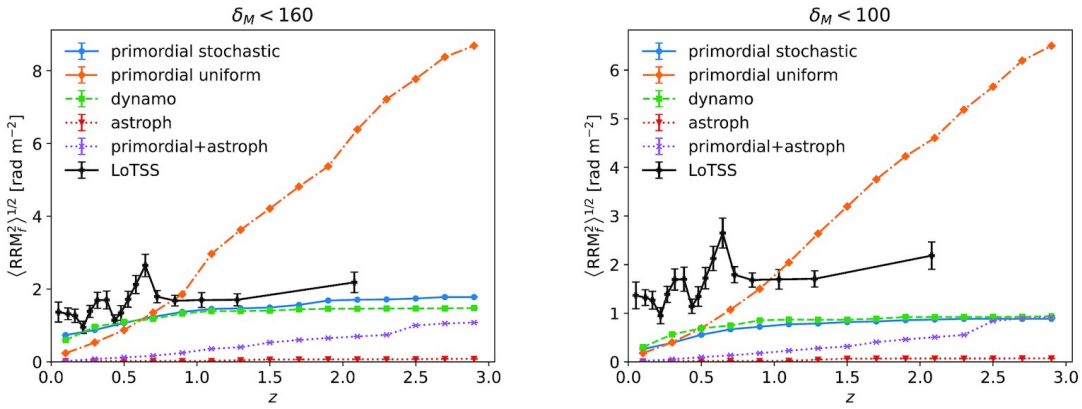

FIGURE 2.7: The RRM rms from the LoTSS RM catalogue measured in 60-source redshift bins compared with the one computed using density and magnetic field from simulations, for different magnetogenesis models. Two cases differing by the overdensity limit are shown: $\delta_M < 160$ (left panel) and $\delta_M < 100$ (right panel). Credits: Carretti et al. (2023)

Chapter 3

Wide-Field Radio Interferometry

3.1 Overview

The LSS of the Universe can be probed by cutting-edge radio interferometric observations. The next-generation of radio interferometers are currently undertaking wide-field continuum surveys to cover the majority of the sky, including the LOFAR Surveys (Sec. 3.3.2). The results of these surveys are dependent on the quality and accuracy of wide-field imaging methods, as well as the correct modeling of ionospheric structure when working at low frequency (i.e. below 1 GHz). In this Chapter, we review the main methods that are currently being used to calibrate and image large fields of view in radiastronomy. We also present the LOFAR and uGMRT facilities, and their data reduction recipes that are used throughout this Thesis.

3.2 Imaging techniques

One of the main problems of wide-field imaging is that different observed directions will have different diffraction of the wavefront between elements of the interferometer. This is called the 'w-effect'. This term follows from the definition of baseline (u, v, w), where w is directed along the line-of-sight to the phase centre of the observation. The visibility on this baseline is denoted V(u, v, w) and can be written as:

$$V(u,v,w) = \int\int \mathrm{d}l\mathrm{d}m \frac{I(l,m)}{n} e^{-i2\pi[ul+vm+w(n-1)]}, \tag{3.1}$$

where $I(l, m)$ represents the sky brightness distribution and l, m and $n = \sqrt{1-l^2-m^2}$ are direction cosines to the far-field source from the point of observation. In the approximation of a small field of view $n \approx 1$ and $w(n-1) \approx 0$, so the equation reduces to a 2D FT of visibilities on the (u, v) plane. However, in the wide-field case the w-term can not be neglected, and imaging methods capable of reconstructing the true sky brightness with the extra w-terms are required. Algorithms such as the w-projection (Cornwell, Golap, and Bhatnagar, 2005), the w-snapshot (Cornwell, Voronkov, and Humphreys, 2012), and the w-stacking (Humphreys and Cornwell,

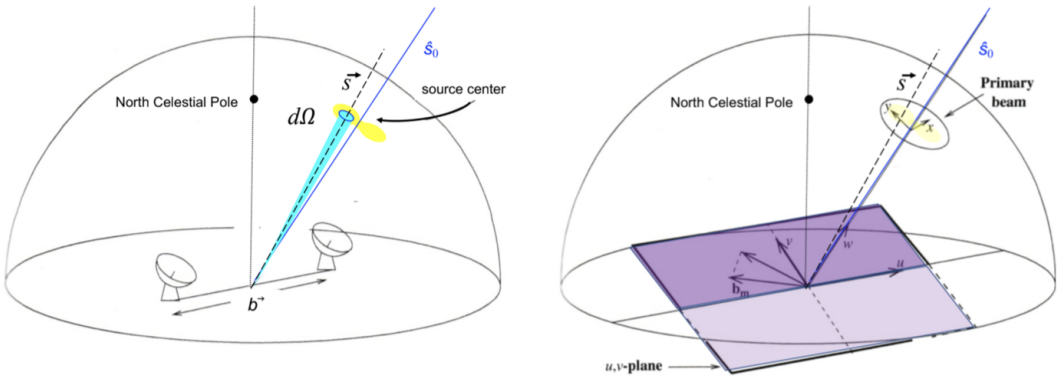

FIGURE 3.1: Schematic reprentation of the (u, v, w) space. *Left*: Contribution of radiation received from a small element of an extended radio source of brightness I(S), subtending a solid angle dΩ in direction $\vec{S}$, to the response of an interferometer. *Right*: The baseline vector $\vec{b}$ is specified by (u, v, w) where w is chosen to be in the direction of the source (known as the phase center), normal to the u,v plane.

2011; Offringa, McKinley, Hurley-Walker, et al., 2014) methods have been proposed. The w-projection method is implemented in the Common Astronomy Software Applications (CASA; McMullin et al. 2007), and the w-stacking and $w-$snapshot methods are implemented in WSClean[1] (Offringa, McKinley, Hurley-Walker, et al., 2014), which is the main tool we use in this Thesis to produce our scientific images. Hybrid methods, for example combining w-projection and facet-based imaging (i.e. it divides the sky into smaller patches, each of which is imaged separately with the assumption that the w-term is negligible for small areas) are also commonly employed in LOFAR wide-field data reduction.

3.2.1 W-projection and W-stacking

The w-projection exploits the fact that the w-term is a convolution in Fourier space. Thus, we can re-project visibilities from any position (u, v, w) to the $w = 0$ plane using a convolution with a known kernel. We can rewrite Eq.3.1:

$$V(u, v, w) = \int\int \mathrm{d}l\mathrm{d}m \frac{I(l, m)}{n} G(l, m, w) e^{-i2\pi[ul+vm]}, \tag{3.2}$$

with,

$$G(l, m, w) = e^{-i2\pi[w(\sqrt{1-l^2-m^2}-1)]}. \tag{3.3}$$

For the convolution theorem, we can write:

$$V(u, v, w) = \tilde{G}(u, v, w) \otimes V(u, v, w = 0), \tag{3.4}$$

[1] https://gitlab.com/aroffringa/wsclean

where $\tilde{G}(u,v,w)$ is the Fourier transform of $G(l,m,w)$. This show that we can derive the three-dimensional function $V(u,v,w)$ from the two-dimensional function $V(u,v,w=0)$ with the known function $\tilde{G}$ (Cornwell, Golap, and Bhatnagar, 2005).

Instead, the w-stacking method expresses the w-term as a multiplicative factor in the image domain. The w-correction is done after the inverse FT. In this case, we can rewrite Eq.3.1 (Offringa, McKinley, Hurley-Walker, et al., 2014):

$$V(u,v,w) = \int\int \mathrm{d}l\mathrm{d}m \frac{I(l,m)e^{-i2\pi[w(\sqrt{1-l^2-m^2}-1)]}}{\sqrt{1-l^2-m^2}} \times e^{-i2\pi[ul+vm]}, \tag{3.5}$$

that can be inverted and then both side integrated over w_{min} to w_{max}, into

$$\frac{I(l,m)(w_{max}-w_{min})}{\sqrt{1-l^2-m^2}} = \int_{w_{min}}^{w_{max}} e^{i2\pi[w(\sqrt{1-l^2-m^2}-1)]} \times \int\int V(u,v,w)e^{i2\pi(ul+vm)}\mathrm{d}u\mathrm{d}v\mathrm{d}w. \tag{3.6}$$

By making u,v,w parameters discrete, the integration over u,v can become an inverse Fast FT (FFT) and the integration over w is a summation. Therefore, the sky brightness can be reconstructed by:

i. gridding the visibility data with equal w-terms;

ii. calculate the inverse FFT;

iii. multiply by the direction-dependent phase shift $e^{i2\pi[w(\sqrt{1-l^2-m^2}-1)]}$;

iv. repeat the previous steps for all w-terms and add the results together;

v. apply the final scaling factor $\frac{(w_{max}-w_{min})}{\sqrt{1-l^2-m^2}}$.

W-stacking have been proven to be faster than w-projection when the gridding step is the dominating cost, while when the inverse FFT step is more important the w-projection is faster. Both methods are suitable for parallelism and multicore implementation, however w-stacking is more easily adapted to parallelism given the data are partitioned in w. An in-depth discussion of the main advantages and disadvantages of the w-stacking method can be found in Offringa, McKinley, Hurley-Walker, et al. (2014).

These methods can be applied in combination with facet-based imaging. In this case, each facet is imaged in a two-dimensional plane tangent to the celestial sphere at the point corresponding to the phase center of the individual facet. The small facet are deconvolved separately, and then the phases and the (u,v,w) coordinates of each facet are shifted to a common phase center (Cornwell and Perley, 1992). Within each facet, is possible to implement w-projection to improve the imaging of sources far from the phase center. This is implemented in the DDFacet algorithm (Tasse et al., 2018), which takes into account generic direction-dependent effects in each facet

by applying a variation of the classical w-projection kernels (see Sec. 3.3.3), and has parallel multicore support.

3.2.2 Mosaicking

In radio interferometry, mosaicking is a technique that allows to recover fields larger that the primary beam of the observation, and therefore requires multiple pointings of the sky. In general it is more practical to tile the sky with discrete pointings organized in a rectangular or hexagonal grid. If the sampling is dense enough, the effect of the layout are modest, however the hexagonal grid is usually preferred (Cornwell, 1988).

There are two main techniques for observing a region of the sky that is larger than the telescope field of view. The traditional method is called *linear mosaicking*, and involves stitching together individual fields from separate pointings of the telescope. In linear mosaicking each pointing is imaged and deconvolved separately and then combined together with optimal weights from noise and primary beam (Holdaway 1999, see also Chapter 4). While this method has the disadvantage of not being very effective in recovering the shorter spacings (Ekers and Rots, 1979), at low-frequency can be convenient to treat each pointing with their calibration effects. We use this technique in the data analysis in Chapter 4.

Alternatively, wide-field imaging combines data from different pointings in the *uv* domain and then deconvolve one single dirty map. In this way, called *joint mosaicking*, all *uv* informations are used and can be used with on-the-fly interferometry data (i.e. the gathering of data while the telescope continuously moves across the sky, rather than pausing at specific positions).

Mosaicking is particularly useful for large-scale observations because it allows to achieve high resolution and sensitivity across the entire observed field, which would not be possible with a single pointing. This technique ensures that even regions far from the center of individual pointings retain image fidelity and sensitivity, avoiding the significant drop-off in signal that occurs at the edges of the primary beam. Moreover, the overlapping regions between pointings in a mosaic improve the overall sensitivity, as these areas receive multiple observations, reducing noise and increasing the significance of the detection for diffuse emission, that is recovered from the short baselines.

3.3 LOFAR

The LOw Frequency ARray (LOFAR, van Haarlem et al. 2013) is a new generation radio interferometer centered in the Netherlands and with stations across 10 European countries. LOFAR covers the low-frequency range from 10 to 240 MHz (i.e. wavelengths 30-1.2 meters) with unprecedented sensitivity and angular resolution. During its initial phase, the design, development, and construction of the LOFAR

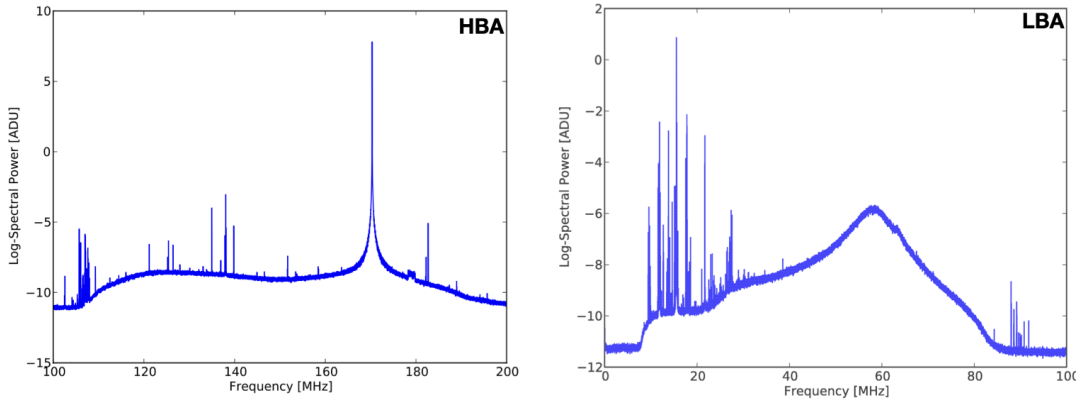

FIGURE 3.2: Median averaged spectrum for all LOFAR HBA tiles (left) and LBA dipoles (right) of a single station.

telescope were driven by six Key Science Projects (KSPs): the Cosmic magnetism, Solar physics and space weather, Epoch of Reionization, Ultra High Energy Cosmic Rays, and Transient events.

3.3.1 Array configuration

At present LOFAR consists of 52 total stations all over Europe. The Netherlands host 38 stations, of which 24 Core Stations (CS) are found in a 2 km radius, and among them 6 CS are concentrated at the very center constituting the 'Superterp' for very short baselines. The remaining 14 Remote Stations (RS) are spread within a 90 km radius. The distribution of the CSs and RSs optimises the density of the *uv*-coverage, especially at the shortest baselines. Additionally, 14 International Stations (IS) are located in European facilities and allow to reach sub-arcsecond resolution.

To meet the need for covering a wide frequency range while being sensitive to Radio Frequency Interference (RFI) from various origins, LOFAR employs two distinct antenna designs:

- *High Band Antenna* (HBA): they operate in the frequency range 110-250 MHz. Due to the heavy instrumental RFI contamination above 240 MHz, the actual usable bandwidth is typically limited to 110-240 MHz.

- *Low Band Antenna* (LBA): they operate in the frequency range 10-90 MHz. Due to the high levels of RFI at the lowest frequencies, primarily associated with the Earth's ionosphere variability, the observtion range is typically limited to 30-80 MHz.

Depending on the scientific aims, different combinations of the antennas can be employed, and the choice of the configuration will impact the shape of the main lobe of the primary beam and on the positions and amplitudes of the side lobes. Each antenna has its observing strategies and calibration algorithms of the corresponding data.

3.3.2 The Surveys

Among the KSPs there is the Surveys KSP, whose aim is to conduct wide and deep surveys of the northern sky. There are currently four surveys ongoing with LOFAR:

- *LOFAR Two metre Sky Survey* (LoTSS): it is a wide-area survey performed in the HBA frequency range 120-168 MHz (Shimwell et al., 2017; Shimwell et al., 2019a; Shimwell et al., 2022a). Its goal is to observe the whole northern sky at a resolution of $6''$ and a sensitivity $\sim$ 0.1 mJy beam^{-1} at the nominal frequency of 144 MHz. The first data release (LoTSS-DR1; Shimwell et al. 2019) has covered an area of 424 deg^2 (2% of the Northern Sky) in the direction of the Hobby-Eberly Dark Energy Experiment (HETDEX; Hill et al. 2008) field. The second data release (LoTSS-DR2; (Shimwell et al., 2022a)) includes two areas (including the HETDEX field) for a total coverage of 5635 deg^2 (27% of the Northern Sky). In the near future, the International LOFAR Two-metre Sky Survey (ILoTSS) will extend and build on the LoTSS survey to be the first wide-area, sensitive (30μJy beam^{-1}), high resolution ($0.3''$) extragalactic radio survey.

- *LOFAR LBA Sky Survey* (LoLSS): it plans to cover the entire northern sky in the frequency range 42-66 MHz, with a resolution of $15''$ and an average sensitivity of 1 mJy beam^{-1}. The first data release, compared to the preliminary release (de Gasperin et al., 2021), takes into account direction-dependent errors, that have been corrected for during the calibration process. This results in a typical sensitivity of 1.55 mJy beam^{-1} at the target resolution. The LoLSS-DR1 covers 650 deg^2 in the HETDEX spring field (de Gasperin et al., 2023).

- *LoTSS Deep Fields*: from LoTSS, some fields have been selected for deep ($\sim$ 100 hours) observations with the goal of a final noise $\sim$ 10μJy beam^{-1} at their completion. The first data release of the LoTSS deep fields includes the Bootes (Tasse et al., 2021), Lockman Hole (Tasse et al., 2021), and Elais-N1 (Sabater et al., 2021) fields. From LoLSS, deep observations of the Bootes field have been carried out as well (Williams et al., 2021).

- *WEAVE-LOFAR*: is a spectroscopic survey of the LOTSS sky with the WEAVE fibre spectrograph on the William Herschel Telescope. It will provide redshifts for the wide and deep tiers of LoTSS.

3.3.3 Data reduction

HBA data reduction

HBA data are processed with the standard Surveys KSP `ddf-pipeline`[2] (see Shimwell et al. 2019; Tasse et al. 2021), which perform the direction-independent (DI) and

[2] `https://github.com/mhardcastle/ddf-pipeline`

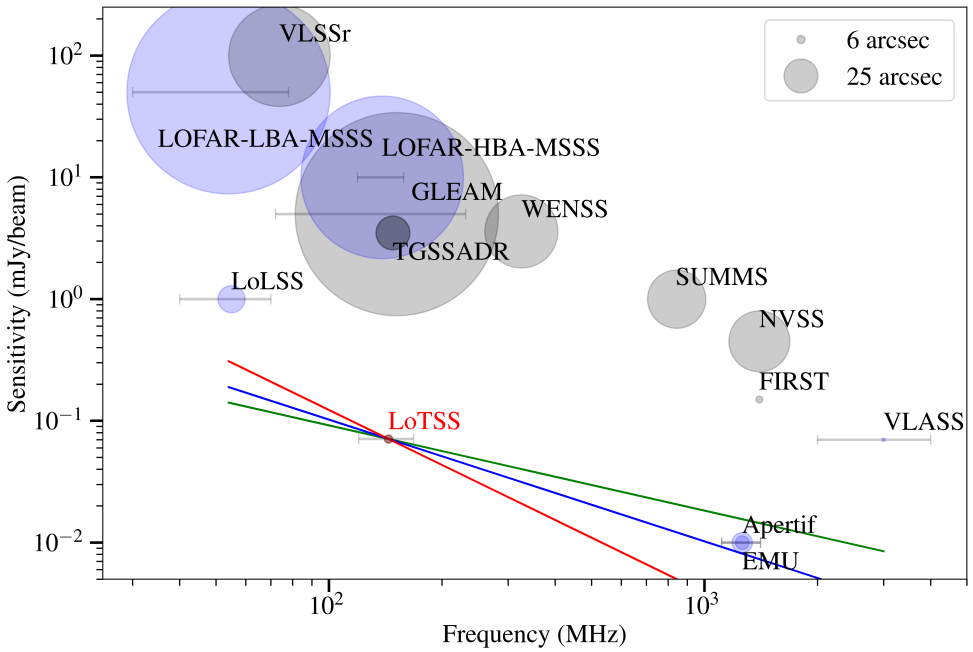

FIGURE 3.3: Comparison of LoTSS and LoLSS rms, frequency and angular resolution with other wide-area completed (grey) and upcoming (blue) radio surveys. The green, blue and red lines show an equivalent sensitivity to LoTSS for compact radio sources with spectral indices of 0.7, 1.0 and 1.5, respectively. Credits: Shimwell et al. (2019)

direction-dependent (DD) calibration. Here we outline the main steps of the calibration:

1. The *DI calibration* (see Shimwell et al. 2017) starts from the target data ($\sim$ 8 hr) and the calibrator data (2 $\times$ 10 min), recorded with 1 sec sampling and 64 channels per 0.195 MHz sub-band. These data were flagged for interference by the observatory using the `AOFLAGGER`[3] (Offringa, van de Gronde, and Roerdink, 2012) before they were averaged to 4 channels per 0.195 MHz sub-band and 4 s and flagged again for interference. The model used for the calibrator uses the flux density scale provided by Scaife and Heald (2012). The time independent clock values and amplitude solutions that were derived from the calibrator observations are then applied to the target data, which is further averaged by a factor 2 in both time an frequency. An additional correction for very bright sources (i.e. Cygnus A, Cassiopeia A, Virgo A, Taurus A, and Hercules A) whose distant side lobes, for the wide LOFAR field of view, contribute significant artefacts across the main lobe of the beam. In the final step of the DI calibration pipeline, the data are phase calibrated against a sky model for the target field, generated from the TGSS-ADR1 catalogue (Intema et al., 2017).

2. The *DD calibration* is performed on the DI calibrated target data. The direction-dependent effects (DDE) can be described in terms of Jones matrices (Hamaker,

[3] https://gitlab.com/aroffringa/aoflagger

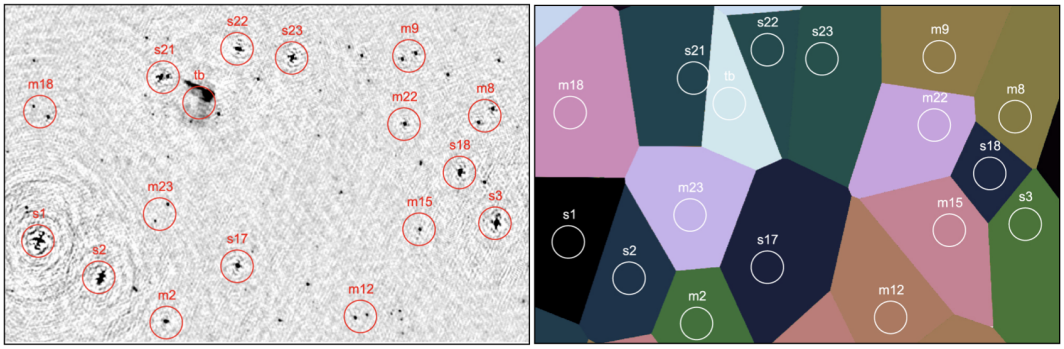

FIGURE 3.4: Direction-Dependent calibration. *Left panel*: Example of bright sources in the field selected as DD-calibrators. *Right panel*: Faceting of the field based on the position of the DD-calibrators. Credits: van Weeren et al. (2016).

Bregman, and Sault, 1996) and to correct for these matrices, which depend on direction, time, frequency, and antenna, they must be derived from the visibilities and applied during imaging. For this, `KillMS`[4] (KMS; Tasse 2014; Smirnov and Tasse 2015) to calculate the Jones matrices and `DDFacet`[5] (DDF; Tasse et al. 2018) to apply these during the imaging were developed. To rapidly image the DI calibrated data, DDF uses the subspace deconvolution (SSD) algorithm (Tasse et al., 2018). From this image, a refined deconvolution mask is created and from the resulting sky model 45 facets for DD calibration are defined. The calibration is done with KMS, which creates an amplitude and phase solution for each of the 45 facets every 60 s and 1.95 MHz of bandwidth, and the data are re-imaged. Several steps of DD calibration, spectral deconvolution and imaging are performed to find phase and amplitude solutions which are then used to calibrate the entire dataset. Finally, the high-resolution imaging with full bandwidth is performed with a resolution of 6″.

3. To produce an improved calibrated target field and allow flexible re-imaging, the so-called *extraction* procedure (van Weeren et al., 2021) is performed, where the DD solutions are used to subtract all sources outside a small box around the target. Then, additional cycles of phase and amplitude self-calibration are performed in the extracted region using DPPP[6] and WSclean (Offringa, McKinley, Hurley-Walker, et al., 2014; van Diepen, Dijkema, and Offringa, 2018).

LBA data reduction

LBA observations are characterized by strong ionospheric-induced phase variations, therefore the flux density calibrator is observed simultaneously to the target, with half of the available bandwidth on the target field and half on the calibrator. The cal-

[4] `https://github.com/saopicc/killMS`
[5] `https://github.com/saopicc/DDFacet`
[6] `https://github.com/lofar-astron/DP3`

ibration procedure in this case requires some steps that differ from the HBA strategy. The pipeline is called Library for Low-Frequencies (LiLF[7]; de Gasperin et al. 2019; de Gasperin et al. 2020), and we outline here the main steps:

1. For the calibration of very low frequency data, it is important to isolate systematic effects in the calibrator, such as: the *clock drift/total electron content* (TEC), caused by the timestamps made by the stations clocks that are periodically realigned using GPS signals introducing a time-dependent delay between the CSs which is not separable from the TEC delay; the *polarization alignment*, caused by the two separate streams of X and Y polarizations to which different station calibration tables are applied, imprinting an artificial constant delay between the two streams; the *bandpass*, caused by the frequency dependency of the LBA dipole beam that has a peak efficieny near the resonance frequency of the dipole, introducing a time-dependent effect that affects the visibility amplitudes in the same way for both polarizations. The procedure is pipelined in the so-called `PREFACTOR`[8]. The three solutions are applied to the target, and since it is not easy to isolate the TEC ionospheric delay, the raw scalar phase solutions are transferred to the target.

2. The target data still require calibration to correct for the remaining systematic effects. A DI calibration step solves for the direction-averaged ionospheric delay, the Faraday rotation and beam variations with time and frequency on top of the LOFAR beam model. After removing these effects, all sources outside a primary beam null at mid-frequency are removed after corrupting their signal with all systematic effects isolated before. A second self-calibration cycle uses this model to produce a final image at 40″ resolution to use for the DD calibration.

3. At this point, the target data is primarly affected by ionospheric differential effects. To identify different DD-calibrators, sources in the model are grouped together by proximity to find aggregate apparent flux density higher than 2 Jy. Each DD-calibrator is used to estimate the differential ionosperic effect in that direction. The field is then divided in facets given by the Voronoi-tesselation of the positions of the DD-calibrators. For each facet, the visibilities are corrected with the phases correction estimated from the corresponding DD-calibrator during imaging with DDF (Tasse et al., 2018). Each facet is separately imaged at full resolution (15″). Finally, they are combined to form a wide-field mosaic.

4. As for the HBA pipeline, the last step is the extraction of the target field. Sources outside 0.5° around the target of interest are subtracted, and a few cycles of scalar phase self-calibration was then performed with phase solutions obtained at increasing time-resolution, from 32s to 8 s.

[7] `https://github.com/revoltek/LiLF`
[8] `https://github.com/lofar-astron/prefactor`

Both the HBA and LBA data reduction pipelines are used in this Thesis to process LOFAR data.

3.4 uGMRT

The Giant Metrewave Radio Telescope (GMRT), located near Pune, India, is one of the world's largest radio interferometers operating at low frequencies. The uGMRT (upgraded GMRT) offers a seamless frequency coverage, replacing the limited bandwidth of the original GMRT, a maximum instantaneous bandwidth of 400MHz, better dynamic range, and sophisticated next-generation instruments and controls (Gupta et al., 2017). The telescope now covers a broader frequency range, from 120 MHz to 1.5 GHz, enhancing its sensitivity and expanding its scientific reach. Operating under the National Centre for Radio Astrophysics (NCRA), the uGMRT plays a critical role in addressing key questions in astrophysics, including galaxy evolution, the early Universe, and transient radio phenomena.

3.4.1 Array configuration

The uGMRT array consists of 30 parabolic antennas, each with a diameter of 45 meters, distributed across a Y-shaped pattern. This configuration offers good *uv*-coverage with a combination of high angular resolution and sensitivity to both compact and extended sources. The antennas are spread over an area with a maximum baseline of about 25 km. Of the total, 12 antennas are located in a central array of about 1 km in diameter. The remaining 18 antennas are distributed along three arms, extending out from the central region. The antennas are fully steerable and each dish is equipped with receivers that can be switched between the four observing bands. In fact, the uGMRT operates across four distinct observing bands:

- *Band 2* (120-250 MHz) is the lowest frequency band and is ideal for studying diffuse radio sources. However, it is more susceptible to RFI, particularly from Earth sources, which requires careful calibration.
- *Band 3* (250-500 MHz) provides a middle range between the low and higher frequencies. It is useful for studying pulsars, AGN, and emission from radio galaxies. Band 3 offers better resolution and sensitivity compared to Band 2 and is less affected by RFI.
- *Band 4* (550-850 MHz) is optimized for higher sensitivity and angular resolution. This band is used for detailed imaging of nearby galaxies, galaxy clusters, and investigations of neutral hydrogen (HI) emission in the local Universe.
- *Band 5* (1000-1450 MHz) is the highest frequency range and the high-resolution is particularly well-suited for observing fine-scale structures and high-redshift galaxies.

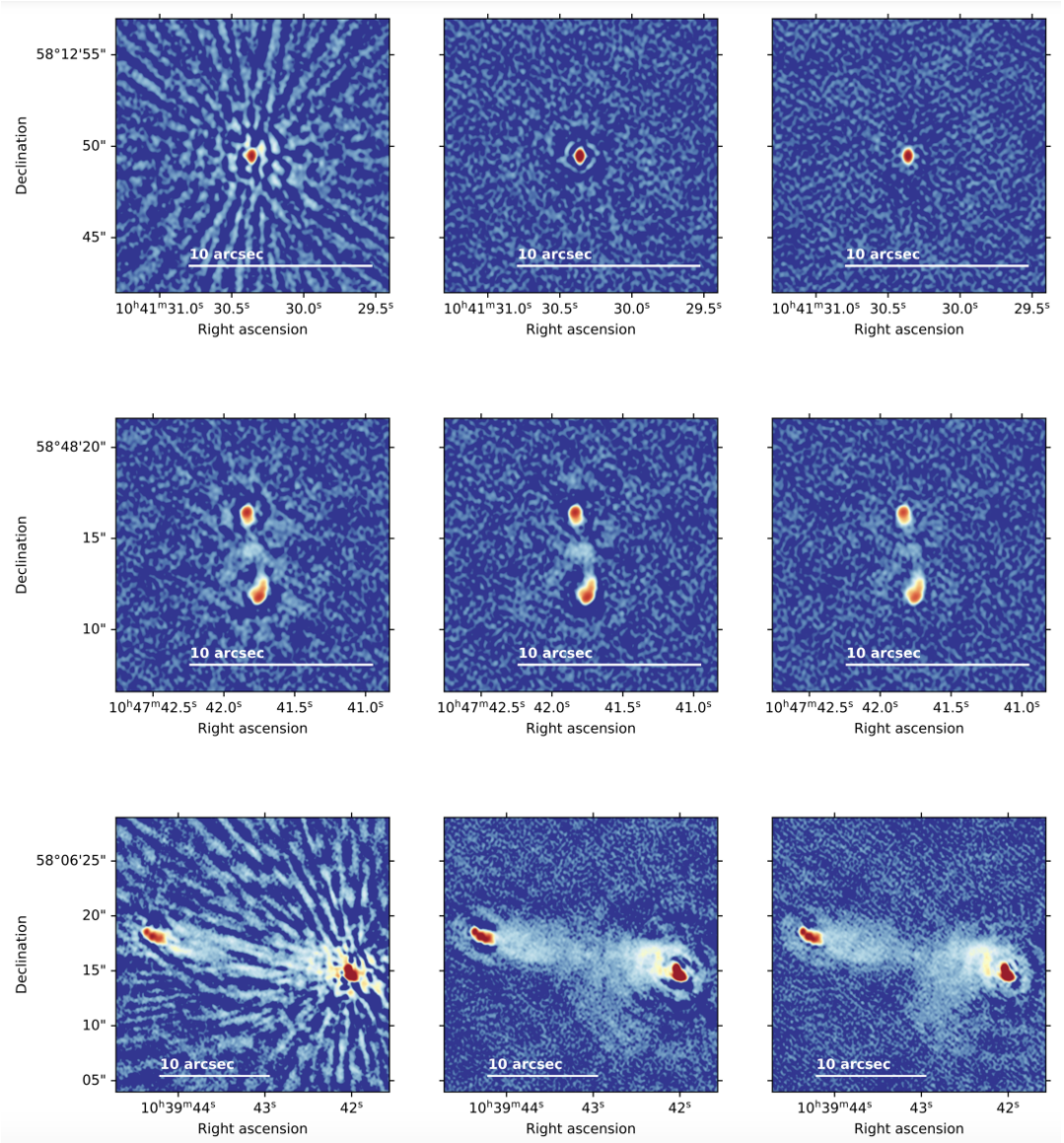

FIGURE 3.5: Example of the direction-dependent calibration process for different sources, carried out with DDF. Initial image with only direction-independent corrections applied (left), image after directional ionospheric corrections have been applied (centre) and image after amplitude corrections have been applied (right). Credits: Sweijen et al. 2022

The gaps in the frequency coverage in this choice of bands is due to constraints of very strong radio frequency interference (RFI) such as the FM band, TV channels and mobile communication bands.

3.4.2 Data reduction

The data reduction of uGMRT data faces similar challenges to LOFAR data, especially in the lower frequency bands (i.e. Band 2 and 3). The Source Peeling and Atmospheric Modeling (SPAM[9]; Intema et al. 2009; Intema 2014) pipeline was designed primarily for the uGMRT to mitigate the effects of the ionosphere and instrumental errors. The pipeline approaches the differential ionospheric effects by 'peeling' bright sources in the field, that are subtracted from the data by solving for their specific direction-dependent calibration.

SPAM calibration can be summired in the following steps (see Intema et al. 2009 for more details):

1. Find and apply instrumental calibration solutions for phase: each antenna in the array adds instrumental phase offset to the signal before correlation; antenna-based phase corrections are obtained on the highest possible time resolution by calibration on a very bright source, and are split into instrumental and ionospheric parts to be estimated.

2. Construct an initial model of the sky and perform a first ionospheric phase calibration: the instrumentally corrected target field data is phase calibrated against an apparent sky model, followed by wide-field imaging and several rounds of phase only self-calibration yielding the initial sky model and initial phase calibration. SPAM uses facet-based imaging to deal with the w-term, using the polyhedron method (Perley, Schwab, and Bridle, 1989; Cornwell and Perley, 1992) to divide the large field-of-view into overlapping facets. Additional facets are centered on relatively bright sources inside and outside the primary beam area to reduce image artefacts due to pixellation (Perley, 1989; Briggs and Cornwell, 1992; Briggs, 1995a; Voronkov and Wieringa, 2004; Cotton and Uson, 2008).

3. Peel bright sources: SPAM uses the peeling technique (Noordam, 2004) to obtain phase corrections in different directions over the field-of-view. Peeling consists of self-calibration on each individual sources, finding a set of time-variable antenna-based phase corrections and a source model, after which the source model is subtracted from the visibility data set while temporarily applying the phase corrections. In particular, sources are peeled in decreasing flux order.

[9] https://www.intema.nl/doku.php?id=huibintema:spam:pipeline

4. Fit an ionospheric phase screen model to the peeling solutions: SPAM constructs a quasi-physical phase screen model that attempts to accurately reproduce and interpolate the measured peeling phase corrections found in the different facets.

5. Apply model phases to each facet during re-imaging: with the ionospheric screen model, SPAM calculates and applies the appropriate model phase corrections during imaging and deconvolving for different parts of the field-of-view. The image produces in this last step can be used as an improved apparent sky model to repeat the calibration.

The SPAM pipeline is used to calibrate uGMRT data analyzed in this Thesis (see Chapter 4).

Chapter 4

Probing Diffuse Emission in Radio Bridges with uGMRT

4.1 Introduction

Recent low-frequency observations have shown the presence of diffuse radio emission on even larger scales, along the filaments of the cosmic web between interacting cluster pairs (Govoni et al., 2019; Botteon et al., 2020; Hoeft et al., 2021). We have presented the main systems in Sec. 1.3.1, and here we make a brief overview of the A399-A401 system.

Multi-frequency studies of synchrotron emission from radio-bridges between clusters are fundamental to shed light on mechanisms of particle acceleration and properties of the magnetic fields on scales never probed before (Vazza et al., 2019). The discovery of such bridges stressed the need to find a theoretical model that can explain this emission, which is different than radio relics and halos. Govoni et al. (2019) explored different possibilities to explain their observations, since the synchrotron and inverse Compton losses make the lifetime of the particles ($\sim 10^8$ years at 140 MHz) too short to travel from the centre of the cluster and cover the bridge extension. This points to an in situ mechanism for particle acceleration, such as diffuse shock re-acceleration of a pre-existing population of mildly relativistic electrons. This process would plausibly result in a spectral index[1] of $\alpha \sim 1.2 - 1.3$ for the bridge, as often observed in relics (van Weeren et al., 2019). Recently, Brunetti and Vazza (2020) presented a model that could explain the origin of radio bridges as synchrotron emission from fossil seed particles (from past AGN or star-formation activity) re-accelerated in turbulence generated along the filament of accreting compressed matter. The resulting emission should be characterised by a steep spectrum ($\alpha > 1.3$). Therefore, to test the models, it is important to characterise the spectral properties of these structures.

[1] Hereafter, we adopt $S \propto \nu^{-\alpha}$.

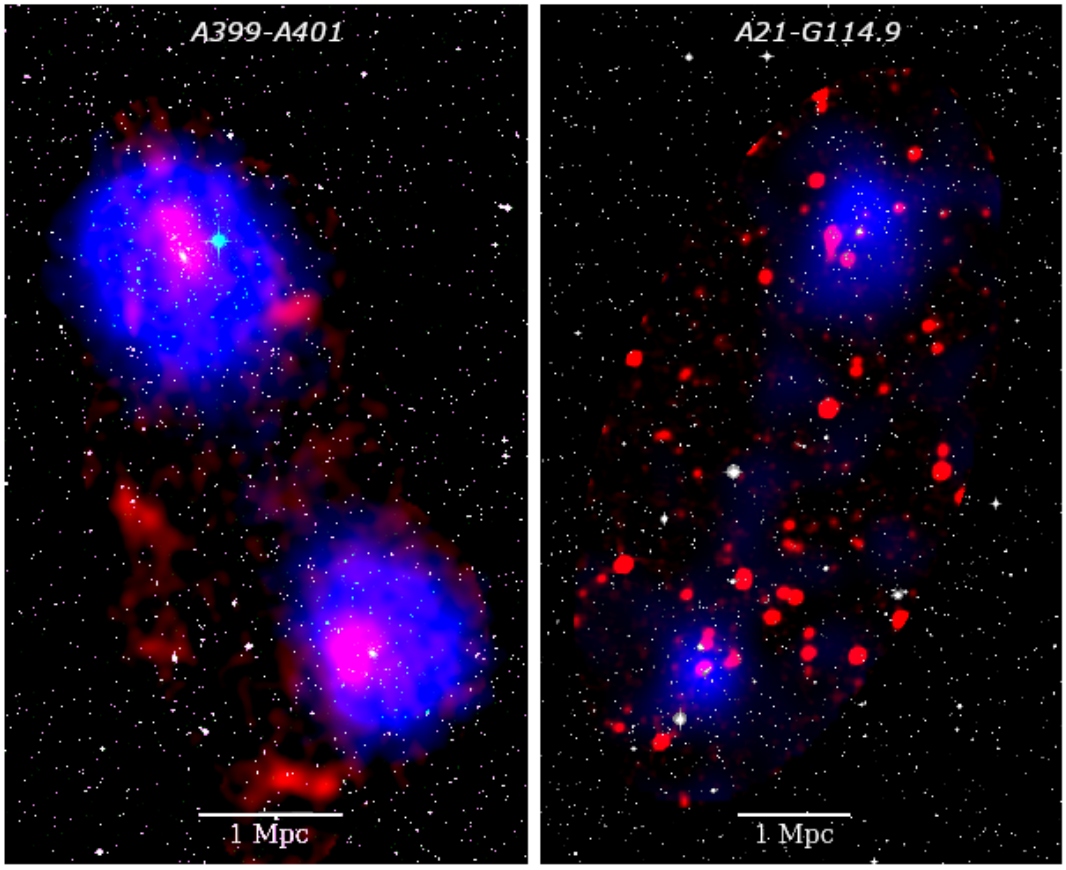

FIGURE 4.1: Composite image of the A399-A401 (*left*) and A21-G114.9 (*right*) cluster pairs. Optical data are recovered from the DSS, while X-ray data (ASCA for A399-A401, ROSAT for A21-G114.9) are shown in blue, and uGMRT data from this work are overlaid in red.

Target	Right Ascension (J2000)	Declination (J2000)	Redshift	Mass ($M_\odot$)
A399	02h 57m 56s	+13°00′ 59″	0.072	$\sim 5.7 \times 10^{14}$
A401	02h 58m 57s	+13°34′ 46″	0.074	$\sim 9.3 \times 10^{14}$
A21	00h 20m 52s	+28°30′ 30″	0.094	$\sim 3.8 \times 10^{14}$
G114.9	00h 21m 13s	+28°15′ 00″	0.095	$\sim 2.5 \times 10^{14}$

TABLE 4.1: Position, redshift, and mass of the two pairs of target galaxy clusters analysed in this work. For the A399-A401 pair, the mass was X-ray derived by *Chandra* (Vikhlinin et al., 2009), while for A21-G114.9 it is the SZ-derived value (as defined in Planck Collaboration et al., 2013).

The first example of a radio bridge is the detection reported in Govoni et al. (2019) between the galaxy clusters A399-A401 (see Sec. 1.3.1). This local (see Table 4.1, Oegerle and Hill 2001) system is rich in examples of diffuse emission: both clusters host a radio halo, detected at high (1.4 GHz, Murgia et al. 2010) and low frequencies, and some diffuse features possibly classified as radio relics (Govoni et al., 2019). The pair is in a pre-merger state (Bonjean et al., 2018) and X-ray observations

(Fujita et al., 1996; Fujita et al., 2008; Akamatsu et al., 2017) revealed the presence of a $6-7$ keV ionised plasma in the region between the clusters. This connection is further supported by the detection of the Sunyaev-Zeldovich (SZ) effect with *Planck* (Planck Collaboration et al., 2013; Planck Collaboration et al., 2016; Bonjean et al., 2018) and the Atacama Cosmology Telescope (ATC) (Hincks et al., 2022; Radiconi et al., 2022) from the gas in the bridge with a density of $\sim 10^{-4}$ cm^{-3}.

Low-frequency radio observations of this cluster pair were carried out with the Westerbork Synthesis Radio Telescope (WSRT) at 346 MHz, but they were not sufficiently deep to detect the radio halo in A401 and the bridge diffuse emission, placing a lower limit on its spectral index at $\alpha > 1.5$ (Nunhokee et al., 2023).

Bonjean et al. (2018) also reported an SZ detection in between another pair of galaxy clusters, Abell 21 and PSZ2 G114.9 (hereafter, A21 and G114.9), separated by a projected distance of approximately 4 Mpc. The morphology of the SZ emission suggests that this nearby pair (see Table 4.1 for details) is found in the interacting, early stage of a merger as well. So far, these two galaxy cluster pairs are unique systems where the *Planck* satellite (Planck Collaboration et al., 2013; Planck Collaboration et al., 2016) has shown a significant SZ detection in their inter-cluster region.

Here we present high-sensitivity observations with the upgraded Giant Meterwave Radio Telescope (uGMRT) in Band 3 (250-500 MHz) of the A399-A401 and A21-G114.9 pairs to investigate the non-thermal properties of their connecting filaments. This work is organised as follows: in Sec. 4.2 we describe the data reduction and imaging parameters; in Sec. 4.3 we present the results and discussion on the A399-A401 pair; and in Sec. 4.4.1 we show the results for the A21-G114.9 pair. Throughout this work we assume a ΛCDM cosmology, with $H_0 = 70$ km s^{-1} Mpc^{-1}, $\Omega_m = 0.3$, and $\Omega_\Lambda = 0.7$. With these assumptions, at the average distance of the A399-A401 system, $1'$ corresponds to 83 kpc and the luminosity distance is $D_L = 329$ Mpc, while at the average distance of the A21-G114.9 system $1' = 105$ kpc and the luminosity distance is $D_L = 360$ Mpc.

4.2 Observations and data reduction

4.2.1 uGMRT

Observations of A399-A401 and A21-G114.9 were carried out with the uGMRT in Band 3 (proposal code: 36_043, P.I.: Bernardi). The total length of the observation was ten hours per pair, including the time spent on calibration sources. Each cluster pair was observed with two distinct pointings, one centred on each galaxy cluster (this pointing strategy was chosen to maximize the sensitivity also to the individual radio halos of A399 and A401, ensuring an unambiguous detection). This results in approximately four hours of on-source time for each target galaxy cluster, and approximately one hour in total spent on calibrators - see Table 4.2 for observational details.

Data reduction was carried out with SPAM (Intema, 2014) pipeline (as described in Intema et al., 2017). The pipeline is explained in Sec. 3.4.2, and here we outline the main steps. The pipeline started with a pre-processing part that converted the data into a pre-calibrated visibility dataset by performing several rounds of flagging visibilities affected by RFI and then transferring the calibration solutions derived from the primary calibrator to the data. This was followed by direction-independent calibration on the pre-processed visibilities, with several rounds of phase self-calibration, amplitude self-calibration, and more RFI flagging. Finally, from the resulting self-calibration gain table and the final wide-field image, started the direction-dependent (DD) calibration, which determines the DD gain phases from the peeling of the brightest-appearing sources in the field. The gain phases from the peeled sources were spatially fit to constrain a model of the ionosphere, used to predict ionospheric phase delays for arbitrary positions within the field of view. The total bandwidth was reduced at the start of the data calibration with RFI flagging that includes the first and last channels of the band. Then, the remaining wide-band (200 MHz) observations were split into six sub-bands, 33.3 MHz each, and the pipeline ran independently on each sub-band. The calibrated data of each sub-band were then jointly imaged with `WSClean v3.1` (Offringa, McKinley, Hurley-Walker, et al., 2014). For the A399-A401 pair, the central frequency of the images was 400 MHz. For the A21-G114.9 pair, we excluded the high frequency (467-500 MHz) sub-band, where SPAM could not find enough sources to fit the ionospheric model. This resulted in an image with rms noise five times higher than that of the other sub-bands. After excluding this sub-band, the remaining calibrated data were imaged at the central frequency of 383 MHz.

Date	24-25 Aug 2019
Frequency band	$250 - 500$ MHz
N.o. channels	2048
Channel width	97.7 kHz
Integration time	16.1 s
Time on source	4 hrs
Calibrators	3C48, 3C147, 3C468.1, 2310+110, 0321+123
Correlations	RR, LL

TABLE 4.2: uGMRT observation details for A399-A401 and A21-G114.9 target cluster pairs. Each observation is comprised of two different pointings, one centred on each galaxy cluster of the pair. The on-source time refers to the single-pointing time spent on each galaxy cluster.

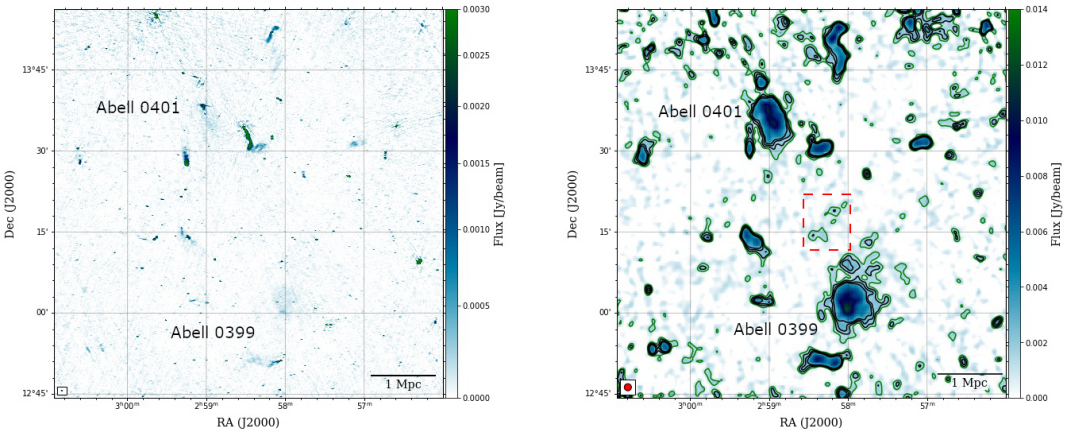

FIGURE 4.2: Mosaic radio images at 400 MHz of the A399-A401 cluster pair. *Left panel:* High-resolution ($12'' \times 5''$) mosaic image with $\sigma_{\rm rms} = 50$ μJy beam^{-1} produced with `Briggs robust = 0` and primary-beam-corrected. A hint of diffuse emission from the radio halos is visible, but no emission is detected in the bridge area. *Right panel:* Low-resolution ($80'' \times 80''$), compact source-subtracted image with $\sigma_{\rm rms} = 600$ μJy beam^{-1}. It is generated by `Briggs robust=-0.5` and a Gaussian *uv*-taper of $60''$. Contour levels start at $2\sigma_{\rm rms}$ (in green) and increase up to $5\sigma_{\rm rms}$ (black). The red-dashed box denotes the region where we find a $2\sigma_{\rm rms}$ detection of a patch of the bridge.

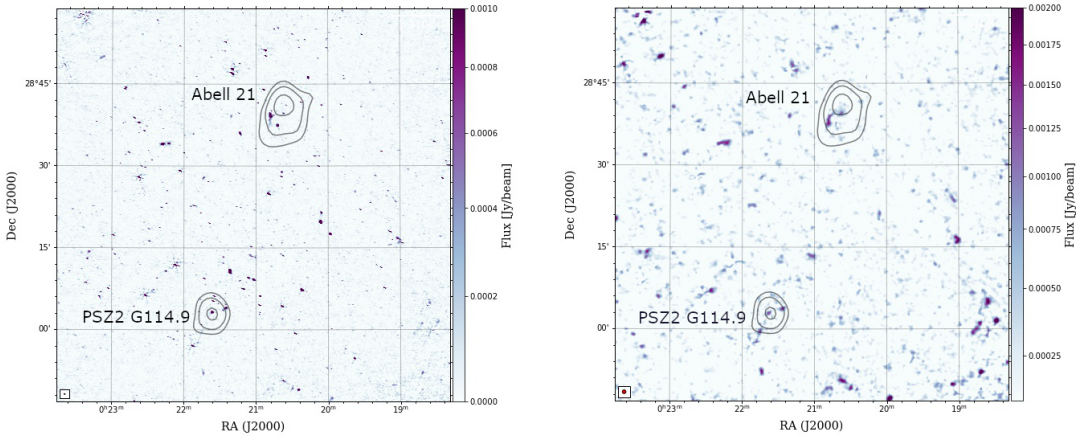

FIGURE 4.3: Mosaic radio images at 383 MHz of the A21-G114.9 clusters pair, with overlaid X-ray ROSAT contours. *Left panel:* High-resolution ($15'' \times 5''$) mosaic image with $\sigma_{\rm rms} = 40$ μJy beam^{-1} produced with `Briggs robust = 0`, showing the compact sources in the field. *Right panel:* Low-resolution ($40'' \times 40''$), compact source-subtracted image with $\sigma_{\rm rms} = 230$ μJy beam^{-1}. It is generated by `Briggs robust=0` and a Gaussian *uv*-taper. No diffuse emission is revealed.

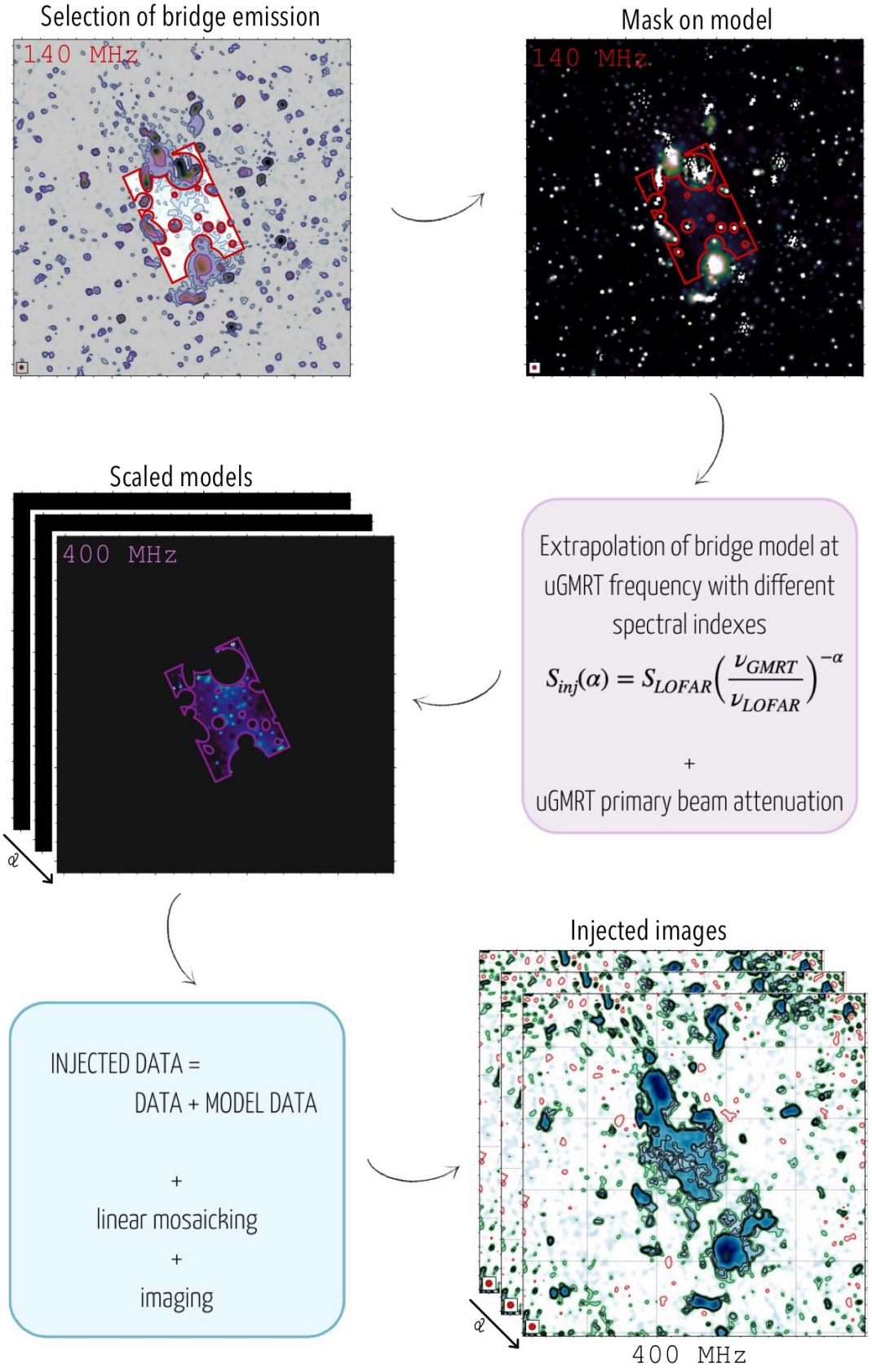

FIGURE 4.4: Schematic flowchart of the injection method, described in Sec. 4.3.1.

4.2.2 Imaging and linear mosaicking

Before imaging, each pointing of the A399-A401 observation was phase-shifted to a common phase centre (RA $= 02^{h}\,58^{m}\,28^{s}$, Dec $= +13^{\circ}\,20'\,18''$) and individually deconvolved. We then produced a high-resolution ($12'' \times 5''$, p.a. 79°) image for each pointing with the same parameters. We adopted a weighting scheme, `Briggs robust=0` (Briggs, 1995b), resulting in an rms noise, $\sigma_{\rm rms} \sim 70$ μJy beam^{-1}, similar in both images, which shows a hint of the radio halos' diffuse emission. The choice of this weighting parameter was motivated by the necessity of recovering the diffuse components of the sources in the field. In order to enhance the sensitivity on Mpc scales, we chose to subtract all compact sources in the field, but, as shown in Fig. 4.3, we needed to consider also the presence of more extended sources that could contaminate the bridge emission. Thus, we decided to subtract physical scales smaller than 600 kpc: the choice of a 600 kpc scale was a trade-off between the best subtraction of all the compact emission, including the tail of the tailed-radio galaxy in A401 that extends towards the bridge region, and retaining the emission from the radio halos, which extends on scales of approximately 700 kpc. With WSClean, we imaged the field with a *uvmin* of 464λ to recover only the compact sources, and then subtracted their components from the visibilities. After producing the high-resolution image with the uv-cut, we carefully inspected the model image to ensure that no components of diffuse emission from the bridge area would be subtracted. For each pointing, we then imaged the source-subtracted data with `Briggs robust=-0.5` and a Gaussian *uv*-taper to obtain a $80'' \times 80''$ resolution image with an rms noise, $\sigma_{\rm rms} \sim 800$ μJy beam^{-1}. At this point, we could further enhance the diffuse emission present in each pointing by combining the individual high- and low-resolution images produced with the same parameters into a mosaic (see 3.2.2). This approach is referred to as linear mosaicking (see, e.g., Holdaway, 1999); in other words, the value, $\tilde{I}$, of a pixel, $\mathbf{x}$, is the average value among all the i pointings, weighted by the primary beam, P:

$$I(\mathbf{x}) = \frac{\sum_i P_i(\mathbf{x})\, I_i(\mathbf{x})}{\sum_i P_i^2(\mathbf{x})}. \tag{4.1}$$

Here, the summation, i, is over the pointing centres, $\mathbf{x_i}$, $I_i(\mathbf{x})$ is the image produced from the i-th pointing, and $P(\mathbf{x})$ is the uGMRT primary beam pattern[2]. The results of the linear mosaicking procedure are shown in Fig. 4.2 both for the high- and low-resolution image, with a final rms noise of $\sigma_{\rm rms} \sim 50$ μJy beam^{-1} and $\sigma_{\rm rms} \sim 600$ μJy beam^{-1}, respectively.

The same general procedure was followed for the A21-G114.9 observation. Each pointing is shifted to a common phase centre (RA $= 00^{h}\,21^{m}\,02^{s}$, Dec $= +28^{\circ}\,22'\,51''$), deconvolved and imaged individually. For each pointing, we produced a high-resolution ($15'' \times 5''$, p.a. 68°) image with a weighting scheme, `Briggs robust=0`,

[2]The uGMRT primary beam shape parameters can be found here

and a resulting rms noise, $\sigma_{\rm rms} \sim 50$ μJy beam^{-1}. In the high-resolution images there is no evidence of diffuse emission; only compact sources are visible. To investigate the presence of diffuse radio emission corresponding to the SZ detection of the filament reported in Bonjean et al. (2018), we subtracted all compact sources in the field, and then proceeded with low-resolution imaging. For each pointing, we imaged the source-subtracted data with `Briggs robust=0`, and a Gaussian uv-taper to have a $40'' \times 40''$ resolution image with an rms noise, $\sigma_{\rm rms} \sim 300$ μJy beam^{-1}. In this case, since the diffuse emission is not revealed, we adopted a moderate weighting scheme and tapering to have a quality image showing the features in the field. Finally, we combined the high- and low-resolution individual images of each pointing in two final mosaics, following the same approach as that for the A399-A401 pointings. The resulting images with their final rms noise are shown in Fig. 4.3, where we can notice how there is no visible detection of diffuse emission in the field.

4.3 Results for the A399-A401 pair

4.3.1 Limit to the bridge spectral index

The presence of a bridge of low-surface-brightness radio emission is reported in Govoni et al. (2019), where they detected the diffuse emission between the two galaxy clusters at 140 MHz with LOFAR. We are not able to detect the full extension of bridge emission in our 400 MHz uGMRT observations, except for a small patch of emission that we discuss in Sec. 4.3.3. Through the non-detection we can however place a lower limit on the spectral index of the bridge. The simplest approach would be to use the classical lack-of-detectability criterion, whereby one places a limit at $3\sigma^b_{rms}$, where σ^b_{rms} is the image rms noise multiplied by the square root of the number of synthesised beams covering bridge area; in this way, we would find a lower limit on the spectral index, $\alpha > 3$. However, this procedure is only appropriate for point sources, as the noise in interferometric images generally does not simply scale with the area but depends on the baseline distribution, the weighting scheme, and the image fidelity. Therefore, here we followed a similar procedure to the one first introduced in Venturi et al. (2008) for radio halos (see also Kale et al., 2013; Bernardi et al., 2016; Bonafede et al., 2017; Duchesne et al., 2022).In particular, we based our method on the work by Nunhokee et al. (2023) on the A399-A401 pair at 346 MHz, in order to produce comparable results. They found a lower limit for the spectral index, $\alpha > 1.5$ at a 96% confidence level, and given that our observations were more sensitive than the WSRT and we were still unable to detect the bridge emission, we expected to place an even more stringent constraint.

We refer to this method as "injection", and a schematic representation of the process is show in Fig. 4.4. We proceeded as follows:

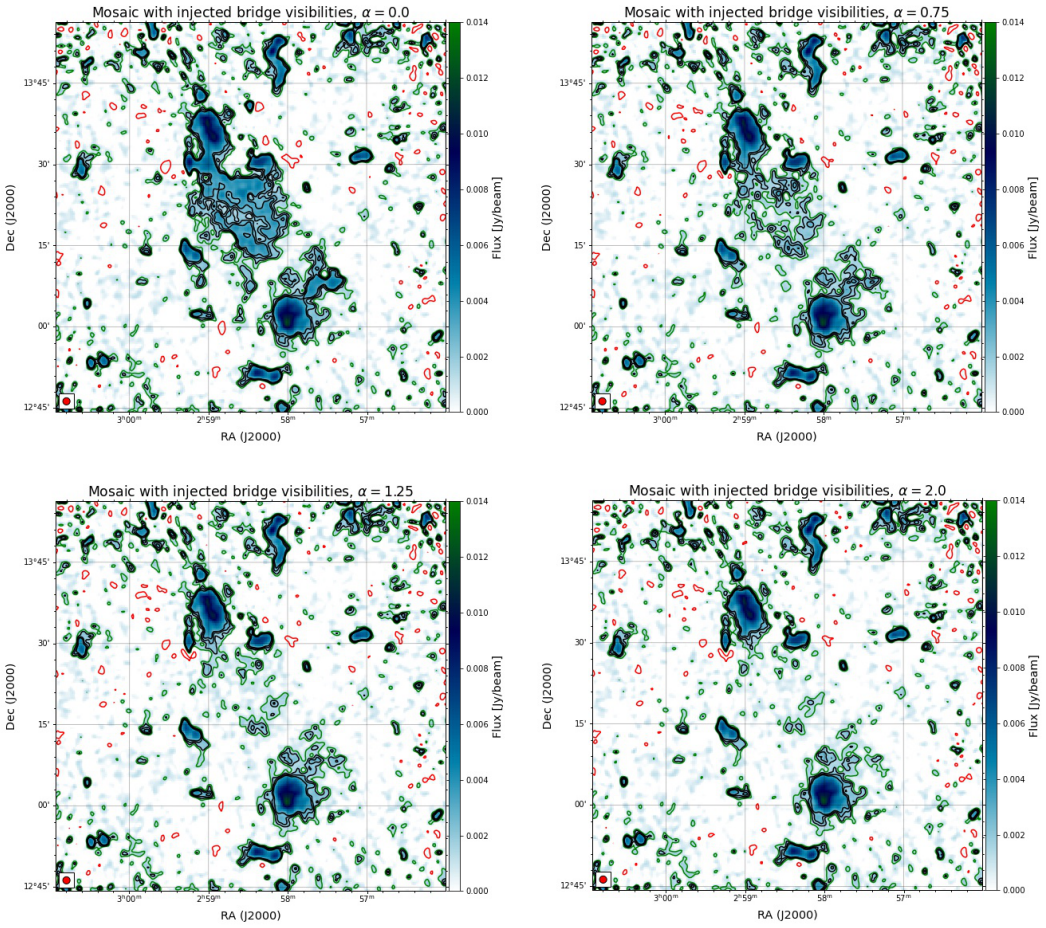

FIGURE 4.5: Examples of 400 MHz, uGMRT images where the A399-A401 bridge visibilities were injected, as a function of the spectral index. In particular, we show the different contributions of the bridge when its spectral index steepens, from $\alpha = 0$ to $\alpha = 2.0$. In the first two top panels, the bridge is clearly detectable, while approaching the lower limit for the spectral index (left-bottom panel) the emission is less visible, until there is no significant change with respect the image without any injected visibilities. Contour levels are drawn from $2\sigma_{\rm rms}$ (in green) and increase up to $5\sigma_{\rm rms}$ (black). A negative contour level at $-3\sigma_{\rm rms}$ is shown in red.

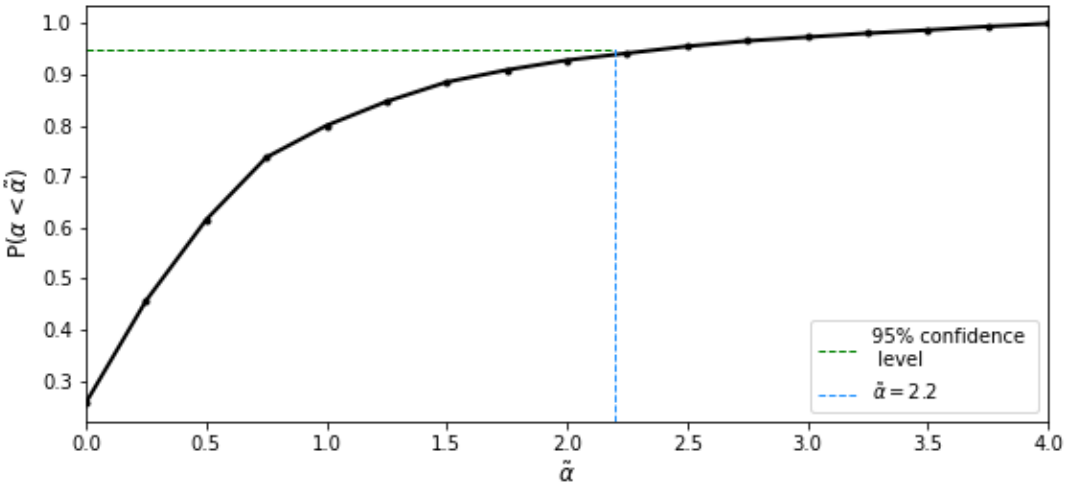

FIGURE 4.6: Cumulative distribution function of $R(\alpha)$, normalised to unit area over the interval $0 \leq \alpha \leq 4$. The horizontal green line marks the 95% probability that the spectral index of the bridge in A399-A401 takes on a value smaller than $\alpha \sim 2.2$ (vertical blue line) if the bridge were detected in our uGMRT observations. The non-detection sets a lower limit for the spectral index at $\alpha_l > 2.2$ with a 95% confidence level.

1. From the model image of the LOFAR detection at 140 MHz, we created a mask by including only the emission from the bridge. This region was selected to include the emission above the 3σ contour in the $80''$ resolution LOFAR image, inside a 2×3 Mpc box, centred on the bridge (RA $= 02^{h}58^{m}26^{s}$, Dec $= +13°18'17''$, with a position angle of 25° E of the vertical axis), as defined in Govoni et al. (2019). To make sure we were not including the contribution from compact sources in the LOFAR detection, we also masked all sources with emission above the 6σ contour inside the defined box;

2. As mentioned in Sec. 4.2.1, our data was divided in six sub-bands of 33.3 MHz each, so we needed to extrapolate the bridge model image to each sub-band central frequency, $\nu_n = [316, 348, 385, 416, 449, 481]$ MHz, with

$$S_{n,\nu_n}(x, y, \alpha) = S_{140}(x, y) \left(\frac{\nu_n}{140\ \text{MHz}}\right)^{-\alpha}, \tag{4.2}$$

where $S_{n,\nu_n}(x, y, \alpha)$ is the flux density of the model image at the frequency, ν_n, at the pixels (x, y), $S_{140}(x, y)$ is the flux density of the LOFAR model image, and the spectral index varies between $0 \leq \alpha \leq 4$ with steps of $\Delta\alpha = 0.25$, assuming a uniform spectral index distribution over the source. We discuss the choice of spectral index range in Sec. 4.3.2.

3. Each extrapolated model image of the bridge was then multiplied with the uGMRT primary beam model to take into account the attenuation of the primary beam in our observation. The final bridge model images were then transformed into visibilities that were injected into our uGMRT source-subtracted,

calibrated visibilities of each pointing. We then deconvolved and imaged each pointing separately and linearly combined them, following the same procedure described in Sec. 4.2.2. In particular, we produced an 80″ resolution mosaic image at the central frequency of 400 MHz for each spectral index, α, with the same parameters used to produce the 80″ image from our observations. An example of such images for different spectral indexes is shown in Fig. 4.5. As expected, as the spectral index steepens from $\alpha = 0$ to $\alpha = 2.0$, the emission of the bridge becomes less and less visible, until it is not detectable above the noise level.

4. We wanted to construct a statistical criterion to determine when the bridge was no longer considered detected; in other words, to determine a lower limit to the spectral index of the bridge. In this sense, the spectral index could be treated as a random variable in the interval $0 \leq \alpha \leq 4$, even if we sampled it at given values for simplicity. We then defined the ratio, $R(\alpha)$, as

$$R(\alpha) = \frac{\sum_{x=1}^{N}\sum_{y=1}^{N} S_{400}\,(x,y) + S_{n,400}\,(x,y,\alpha)}{\sum_{x=1}^{N}\sum_{y=1}^{N} S_{400}(x,y)} = \frac{S_{400}^{\mathrm{inj}}(\alpha)}{S_{400}}, \tag{4.3}$$

where $S_{400}^{\mathrm{inj}}(\alpha)$ defines the flux density of the 400 MHz image with the contribution of the injected visibilities, and S_{400}, is the flux density from the 400 MHz image from the uGMRT observations. Both quantities were measured by summing over the N pixels covering the bridge area (see Fig. 4.4), masking only the area covered by the small patch of emission (dashed red box in Fig. 4.2, right panel) that we treated separately in Sec. 4.3.3. The ratio, $R(\alpha)$, is a decreasing function of α, and has its maximum value when $\alpha = 0$ and approaches unity for increasing spectral index values, that is, when the bridge spectrum is steeper and the emission is therefore less visible in our injected images. In other words, the ratio, $R(\alpha)$, measures how bright, given a certain spectral index value, α, the injected bridge emission is with respect to the image background. While the definition of $R(\alpha)$ is not the formal definition of a distribution function and does not converge for $\alpha \to -\infty$, it does converge when $\alpha \to \infty$. We then normalised the integral of $R(\alpha)$ to unity over the spectral index range, so that $R(\alpha)$ effectively represents a probability to detect a spectral index value given our observations.

5. We then constructed the cumulative distribution function ($P(\alpha < \tilde{\alpha})$) of $R(\alpha)$, defined as

$$P(\alpha < \tilde{\alpha}) = F(\tilde{\alpha}) = \sum_{0}^{\tilde{\alpha}} R(\alpha)\,\Delta\alpha. \tag{4.4}$$

The cumulative distribution function of α evaluated at $\tilde{\alpha}$ gives us the probability of observing an emission with a spectral index, $\alpha < \tilde{\alpha}$ in our observations.

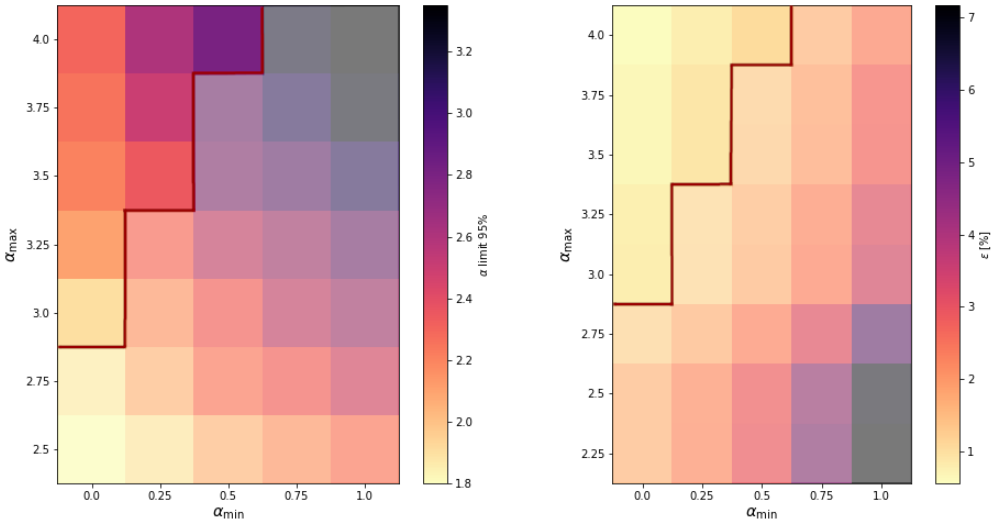

FIGURE 4.7: The effect of the spectral index range on the limit result. *Left:* Lower limits at 95% confidence level as a function of spectral index range. The lower and upper bounds of the range can vary between $0 \leq \alpha_{min} \leq 1$ and $0 \leq \alpha_{max} \leq 4$, respectively. Values above the red line satisfy the criterion of convergence of the cumulative distribution (see right panel). We adopted a lower limit, $\alpha > 2.2$, obtained using the $\alpha_{min} = 0 \leq \alpha \leq 4 = \alpha_{max}$ range. *Right:* Convergence of the cumulative probability function with varying spectral index ranges. Values above the red line have $\epsilon < 1\%$, which we used as an acceptance criterion (see Eq. 4.5).

As shown in Fig. 4.6, we find that the bridge should be detected in our observations with a probability, $P(\alpha < \tilde{\alpha}) = 95\%$ if $\tilde{\alpha} < 2.2$. The non-detection in our observations implies that the spectral index of the bridge has a lower limit of $\alpha_l > 2.2$ with a 95% confidence level. It should be noted that the limit value is dependent on the chosen interval range for α, as discussed in Sec. 4.3.2.

This result represents an improvement over the constraints from Nunhokee et al. (2023), due to the higher sensitivity of our observations. Our lower limit disfavours the shock re-acceleration processes proposed in Govoni et al. (2019) as the main mechanism responsible for the bridge emission and is consistent with the predictions from Brunetti and Vazza (2020), where the origin of radio bridges is explained by second-order Fermi acceleration of electrons interacting with turbulence on above-Mpc scales, resulting in rather steep spectra.

4.3.2 The effect of the spectral index range on limit estimates

As presented in Sec. 4.3.1, we defined the injection procedure to derive the lower limit on the A399-A401 bridge spectral index, by extrapolating the bridge model image from the LOFAR detection to the uGMRT frequency with different spectral index values. We note that the limit value is dependent on the chosen interval range for α, and thus we tested different ranges to investigate the resulting limit. We evaluated

the α_l value corresponding to the 95% value of the cumulative distribution (as described in the main text, Eq. 4.4) as a function of $[\alpha_{min}, \alpha_{max}]$, with $0 < \alpha_{min} < 1$ and $2.25 < \alpha_{max} < 4$, in steps of $\Delta\alpha = 0.25$ (Fig. 4.7, left panel). The $\alpha_{min} > 0$ boundary is motivated by the fact that an inverted spectral index is not expected for synchrotron emission from a bridge-like source. To investigate the convergence of the cumulative distribution, we defined A as the area under the curve $R(\alpha)$ (Eq. 4.3) calculated between α_{min} and α_{max}, before normalisation. We then defined the ratio, ϵ_i:

$$\epsilon_i = \frac{(A_{i+1} - A_i) \times 100}{A_i}, \tag{4.5}$$

where i runs over the number of α steps. For each α_{min}, ϵ_i evaluates the percentage difference between the area, A_i, in the interval $\alpha_{min} \leq \alpha \leq \alpha_{max,i}$ and A_{i+1} in the interval $\alpha_{min} \leq \alpha \leq \alpha_{max,i+1}$, where $\alpha_{max,i+1} = \alpha_{max,i} + 0.25$. In other words, when we fixed the value of α_{min}, we started with the initial area value, A_i, calculated within the interval defined by α_{min} and $\alpha_{max,i}$. Then, we calculated the area value, A_{i+1}, within an extended interval that includes α_{min} and an increased upper bound, $\alpha_{max,i} + 0.25$. This allowed us to compare the percentage difference, ϵ, between the area values at each step. We considered the cumulative distribution converging if $\epsilon < 1\%$. This was computed for each combination range with $0 \leq \alpha_{min} \leq 1$, and $2.25 \leq \alpha_{max} \leq 4$. The results are shown in Fig. 4.7 (right panel), which shows that ϵ decreases with increasing α_{max} values. This is somewhat expected, as the cumulative distribution function converges for increasing α_{max} values. We notice that A has the strongest dependence upon α_{min}, and ϵ changes up to $\sim$ 6% across the $0 < \alpha_{min} < 1$ - a small variation anyway. We assumed that estimates of the spectral index lower limit would begin to converge if $\epsilon < 1\%$; in other words, if the relative variation between the area under the curve $R(\alpha)$ were smaller than 1% (values above the red line in Fig. 4.7, left panel). We choose to report the case where the convergence is strongest, with $\epsilon \sim 0.5\%$, leading to $\alpha > 2.2$ for $0 \leq \alpha \leq 4$.

4.3.3 Detection of a patch of bridge emission

As mentioned in Sec. 4.2.2, we observe a $2\sigma_{\rm rms}$ level patch of emission in the bridge area in the 80″ resolution image, encompassed by the dashed red box shown in Fig. 4.2. There were no compact sources in the location corresponding to this region prior to the source subtraction process. Under the assumption that this patch represents a part of the bridge, and that the spectral index is likely variable across the bridge area, this region could present a spectral index flat enough to be detectable in our observations.

Within the $2\sigma_{\rm rms}$ level contours of the uGMRT image, we measure flux densities of $S_{400\ \rm MHz} = 8.7 \pm 1.7$ mJy and $S_{140\ \rm MHz} = 26.7 \pm 3.7$ mJy, leading to a spectral index value for the patch of $\alpha_p = 1.07 \pm 0.23$.

The uncertainty on the flux density measurements is estimated as

$$\sigma_S = \sqrt{(S \times f)^2 + N_b \times (\sigma_{\rm rms})^2}, \tag{4.6}$$

where $f = 0.1$ is the absolute flux-scale uncertainty (Chandra, Ray, and Bhatnagar, 2004), N_b the number of beams covering the source, $\sigma_{\rm rms}$ the rms noise sensitivity of the map, and S the measured flux density of the source.
As expected, the spectral index of this emission is significantly flatter than our lower limit, and thus could be revealing a small part of the bridge in our observations.
The interpretation of this $2\sigma_{\rm rms}$ level patch of emission is not definitive at this time, but it is possible to make some considerations based on the models and detections available in the literature. A physical scenario that could explain the presence of flatter emission patches is one of the predictions from the turbulent re-acceleration model proposed in Brunetti and Vazza (2020). In fact, with their simulations they show how the volume filling factor of the bridge emission should be larger at LOFAR frequencies, resulting in a smoother emission, but at higher frequencies the emission is predicted to be dominated by a clumpy contribution from smaller, more turbulent regions. Moreover, they show that, even during the early stages of a merger between two systems, the dynamics of the collapse can drive weak shocks into the ICM, resulting in an additional compression of the population of turbulent re-accelerated electrons, increasing the radio brightness in these locations.

4.4 Results for the A21-G114.9 pair

4.4.1 Injection procedure

In this case, we need to assess how deep our observation should be to detect possible diffuse emission from the filament. This is the first time the A21-G114.9 pair has been observed at radio frequencies, and therefore as opposed to A399-A401 we can only place a limit on the bridge flux density assuming a model for the bridge emission. We defined the morphology and the profile of the mock radio bridge to fit the observations of the most in-depth bridge study Govoni et al. (2019), and to follow the elongated shape of filamentary emission that we would expect from the SZ detection. We detail below the steps we have followed:

1. For the mock bridge brightness profile, we assumed a two-dimensional elliptical Gaussian profile:

$$\begin{aligned} I(x,y) = A \exp[(-(a(x-x_0)^2 + \\ 2b(x-x_0)(y-y_0) + c(y-y_0)^2)], \end{aligned} \tag{4.7}$$

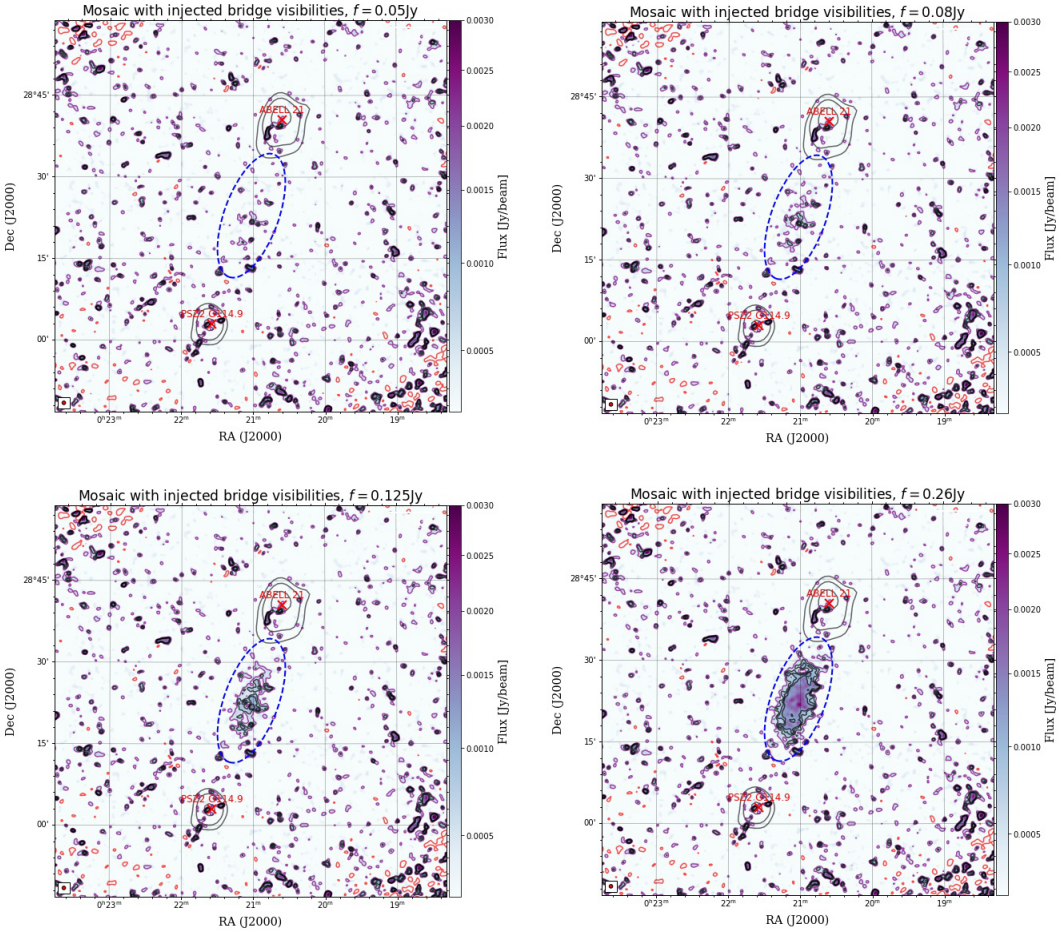

FIGURE 4.8: Examples of 383 MHz uGMRT images of A21-G114.9 where the bridge visibilities are injected, as a function-integrated flux density, f. X-ray ROSAT contours are shown in grey and the location of the X-ray peak is marked with yellow crosses. In particular, we show the different contribution of the injected bridge emission when increasing its flux density, from $f = 50$mJy to $f = 260$mJy. The visibilities are injected inside a 2D model Gaussian (dashed blue ellipse) with a semi-major axis of $12'$ ($\sim$ 2.5Mpc) and a semi-minor axis of $5'$ ($\sim$ 500kpc). We note how in the first two top panels the bridge emission is not significantly detected, while approaching the two values found for the upper limit on the flux density (bottom panels) the emission is continuous and detected over $2\sigma_{rms}$.Contour levels are drawn from $2\sigma_{\rm rms}$ (in purple) to $5\sigma_{\rm rms}$ (in black). A negative contour level at $-3\sigma_{\rm rms}$ is shown in red.

where

$$
\begin{aligned}
a &= \frac{cos^2\theta}{2\sigma_x^2} + \frac{sin^2\theta}{2\sigma_y^2}, \\
b &= -\frac{sin2\theta}{4\sigma_x^2} + \frac{sin2\theta}{4\sigma_y^2}, \\
c &= \frac{sin^2\theta}{2\sigma_x^2} + \frac{cos^2\theta}{2\sigma_y^2},
\end{aligned}
\tag{4.8}
$$

and where σ is the Gaussian standard deviation and θ is the rotation angle. The 2D Gaussian model was centred on (x_0, y_0)=(RA,Dec)=($00^h\,21^m\,02^s$, $+28^\circ\,22'\,51''$). The semi-major axis was $\sigma_y = 12'$, the semi-minor axis was $\sigma_x = 5'$, and the ellipse was rotated to $\theta = 20^\circ$ W of the vertical axis. We scaled the amplitude, A, so that the integrated flux density of the injected mock bridge varied between 5 mJy $-$ 300 mJy with increasing steps of 5 mJy, and between 300 mJy $-$ 1 Jy with increasing steps of 50 mJy.

2. Each Gaussian model was then multiplied with the uGMRT primary beam model to take into account the attenuation of the primary beam in our observations.

3. The final mock bridge models were transformed into visibilities and injected into our uGMRT source-subtracted calibrated data of each pointing. Then we followed the same procedure described in Sec. 4.2.2 to produce 40″ resolution mosaic images at the central frequency of 383 MHz for each model flux density, f. Examples of the resulting injected images with different injected flux densities are shown in Fig. 4.8.

4. We defined the ratio, $R(f)$, as

$$
R(f) = \frac{\sum_{x=1}^{N}\sum_{y=1}^{N} S_{383}(x,y)}{\sum_{x=1}^{N}\sum_{y=1}^{N} S_{383}\,(x,y) + S_{n,383}\,(x,y,f)} = \frac{S_{383}}{S_{383}^{\rm inj}(f)},
\tag{4.9}
$$

where S_{383} defines the flux density of the 383 MHz image with no injected visibilities, and $S_{383}^{\rm inj}(f)$ is the flux density from the 383 MHz image with the contribution of the injected visibilities. Both quantities are measured by summing over the N pixels covering the bridge area within the Gaussian ellipse. The ratio, $R(f)$, is a decreasing function of the injected flux density, f, and hence in the limit, $f \to \infty$ (increasing injected flux), $R(f) \to 0$. This implies that there is a value of the injected flux, f, for which the bridge emission should be significantly detected in our 383 MHz observation (i.e. $S_{383}^{\rm inj}(\geq f_u) > S_{383}$). Since the bridge is not detected, this sets an upper limit on its flux density at f_u.

5. Following the same procedure of the A399-A401 case, we determined the flux density upper limit by constructing the cumulative distribution function, $P(f <$

$\tilde{f}$), as defined in Eq. 4.4) of $R(f)$, normalised to the unit area over the defined interval for f. As shown in Fig. 4.9 (top panel), we find that $P(f < \tilde{f}) = 95\%$ for $\tilde{f} \sim 260$mJy. This means that there is a 95% probability that the bridge emission is lower than 260 mJy, otherwise it would be clearly detected in our uGMRT observations. This sets an upper limit on the bridge flux density at $f_u^1 < 260$mJy with a 95% ($\sim 2\sigma$) confidence level. However, a visual inspection of the image with a 260 mJy injected flux (see Fig. 4.8) shows that the bridge would be detected at $5\sigma_{\rm rms}$. As we were assessing for the first time a procedure to place upper limits on the bridge emission, we evaluated a second criterion for detection, based on the extension and continuity of the injected diffuse emission, as has already been done for radio halos (see, e.g., Bonafede et al. 2017).

6. We measure $L_f^{2\sigma}$, the largest detectable size of continuous injected emission above $2\sigma_{\rm rms}$, for each image of the injected flux density, f. We consider the bridge to be detected when the emission above $2\sigma_{\rm rms}$ is continuous for at least the extent of the semi-major axis of the model Gaussian ellipse ($L_f^{2\sigma} \geq \sigma_y$). With this criterion, we find that we would consider the bridge to be detected when $f \geq 125$mJy. If we define $A_{\rm tot}$ as the total area of the model Gaussian ellipse over which we performed the injection, the area covered by the emission above $2\sigma_{\rm rms}$ in the $f = 125$mJy image corresponds to the 28% of $A_{\rm tot}$. This second method sets a lower value for the upper limit, $f_u^2 < 125$mJy. This result is in agreement with the visual inspection of the images, and would be equivalent to the 80% confidence level from the cumulative probability function (see Fig. 4.9, left panel).

This procedure represents the first attempt to adapt to radio bridges the pre-existing injection method introduced in Venturi et al. (2008) for upper limits on radio halos. These results are dependent on the model we adopted to describe the possible bridge emission. Moreover, given the very few detections of radio bridges so far, the modelling of the morphology and surface brightness of mock emission on such large scales is subject to some arbitrary choices. In comparison with the previous methods, this process presents an improvement by associating a confidence level with the upper limit value, and we are able to compare the results from a second criterion based on the continuity of the recovered emission.

4.4.2 Fractional recovered flux density

As already noticed when the injection procedure was first introduced for radio halos (Venturi et al., 2008), we expect that the measured flux density of the mock bridge can be different than the injected flux density, as the faintest components may not be found during the imaging process.
As a final consideration, to report the measured value of the flux density upper limit, we evaluated how much of the injected model flux density is effectively recovered

in the images we produced. In Fig. 4.9 (right panel) we plot the fractional recovered flux density with the injected flux density (i.e. the ratio of the measured flux over the injected flux). We can see that the percentage of flux lost in the injection procedure is always smaller than the 23% of the injected flux. In particular, for the upper limits found using the two different methods explained above, we find that the measured value of flux is

$$\begin{aligned} f^{\mathrm{meas},1} &= f^{1} * 0.88 = 229\mathrm{mJy} \\ f^{\mathrm{meas},2} &= f^{2} * 0.85 = 106\mathrm{mJy}, \end{aligned} \tag{4.10}$$

as shown in Fig. 4.9 (right panel) with green and red crosses, respectively. Hence, the resulting upper limits on the measured flux density are

$$\begin{aligned} f_u^{\mathrm{meas},1} &< 229\mathrm{mJy}, \\ f_u^{\mathrm{meas},2} &< 106\mathrm{mJy}. \end{aligned} \tag{4.11}$$

As expected, the loss effect is generally more important at lower flux densities, where the faintest components of the mock bridge on larger scales can result below the noise level. At increasing flux densities, the effect is less severe, and the fractional recovered flux converges around $\sim 92\%$.

4.5 Conclusions

In this work, we analysed uGMRT data of two unique systems of early-stage merging galaxy clusters, where their connection along a filament of the cosmic web is supported by a significant SZ effect detection by the Planck satellite (Bonjean et al., 2018; Planck Collaboration et al., 2013; Planck Collaboration et al., 2016). The A399-A401 pair was already studied with LOFAR, detecting extended diffuse emission in the inter-cluster region (Govoni et al., 2019); the A21-G114.9 pair was unexplored at radio frequencies. Our results can be summarised as follows:

1. For the A399-A401 system we are not able to detect the full extension of the bridge emission in our 400 MHz observations. We followed the injection method (Venturi et al. 2008; Nunhokee et al. 2023) to inject the model visibilities of the detected bridge emission at 140 MHz (Govoni et al., 2019) into our observations, scaling the flux density with different values of spectral indices. We find that the bridge would be detected in our observations if its spectral index were flatter than 2.2 with a 95% confidence level, setting a lower limit at $\alpha_l > 2.2$. This result allows us to test the theoretical models for the bridge origin, disfavouring the shock scenario proposed in Govoni et al. (2019), and is instead consistent with the global predictions of the turbulent (re-)acceleration model of electrons of Brunetti and Vazza (2020).

2. We observed a $2\sigma_{\rm rms}$ significance patch of emission in the bridge area. Under the assumption that this could represent a part of the bridge emission, for this patch we find a spectral index value of $\alpha_p = 1.07 \pm 0.23$, significantly flatter than our limit. This result could indicate a variable spectral index distribution across the bridge area.

3. For the A21-G114.9 system, we do not recover any diffuse emission in our 383 MHz observations. We followed a similar injection procedure, but in this case we placed an upper limit on the flux density of the bridge emission by assuming an elliptical Gaussian model for the description of the mock bridge surface brightness profile. From the injection, we find a flux density upper limit at $f_u^1 < 260$mJy with a 95% confidence level.

4. We propose a second criterion for placing the upper limit, based on the morphology and continuity of the injected emission recovered in the images. In particular, we consider the bridge detected when the emission is above $2\sigma_{\rm rms}$ to be continuous for at least the extent of the semi-major axis of the model Gaussian ellipse that defines the injected mock bridge. With this criterion, we find that the upper limit can be placed at $f_u^2 < 125$mJy, in agreement with the visual inspection of the images and equivalent to an 80% confidence level from the cumulative probability function.

5. We investigated how much of the injected flux is effectively recovered at the end of the injection procedure. We find that the percentage of recovered flux increases with the injected flux and converges around 92%, and with our methodology we consider it unlikely that more than 23% of the injected flux is lost.

The limits that we have derived represent an important constraint on the spectral characterisation of the emission in radio bridges. The large-scale extension, low surface brightness, and steep spectra that we expect from the theoretical models and from the few present observations pose a challenge for multi-frequency detection. However, we have defined in this work a procedure to derive upper limits on their flux density that can be applied to more systems in future observations, which will lead to a more comprehensive view of the radio bridges' properties and a statistical assessment of their occurrence. The limits and methods derived here are used in the multifrequency study presented in Chapter 5.

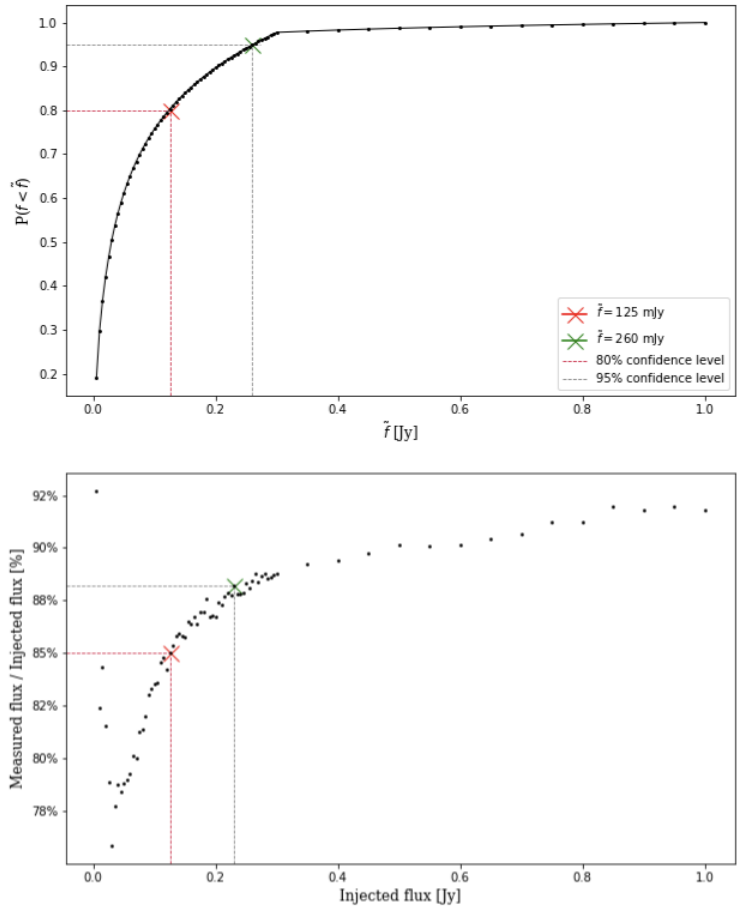

FIGURE 4.9: Cumulative distribution function and recovered flux percentage in the injection procedure for A21-G114.9. *Top panel:* Cumulative distribution function of $R(f)$, normalised to unit area over the interval 5mJy $\leq f \leq$ 1Jy. The horizontal grey line marks the 95% probability that the bridge in A21-G114.9 has a flux density lower than $\tilde{f} =$ 260mJy (green cross), since it is not detected in our observations. This sets an upper limit on its flux density at $f_u^1 <$ 260 with a 95% confidence level. With a second criterion based on the extension and continuity of the bridge emission (see Sec. 4.4.1), we find a lower value for the upper limit at $f_u^2 <$ 125mJy. From the cumulative function, there is an 80% probability that the bridge emission is lower than 125 mJy (red cross). *Bottom panel:* Plot of the ratio (as a percentage) between the measured flux density and the injected flux density, with a varying injected flux density. The green cross corresponds to the recovered percentage of the 260mJy injected bridge emission ($\sim$ 88%), and the red cross corresponds to the recovered percentage of the 125mJy injected bridge emission (85%). We notice that the fractional recovered flux increases at increasing injected flux density, converging around $\sim$ 92%. The injected flux density lost in this procedure is never higher than $\sim$ 23%.

Chapter 5

Abell 0399–Abell 0401 Radio Bridge Spectral Index

5.1 Introduction

The work presented in Chapter 4 represents an important constraint on the spectral characterisation of the emission in radio bridges. We follow up with a multifrequency study with LOFAR and uGMRT data to derive the spectrum of the radio bridge in A399-A401.

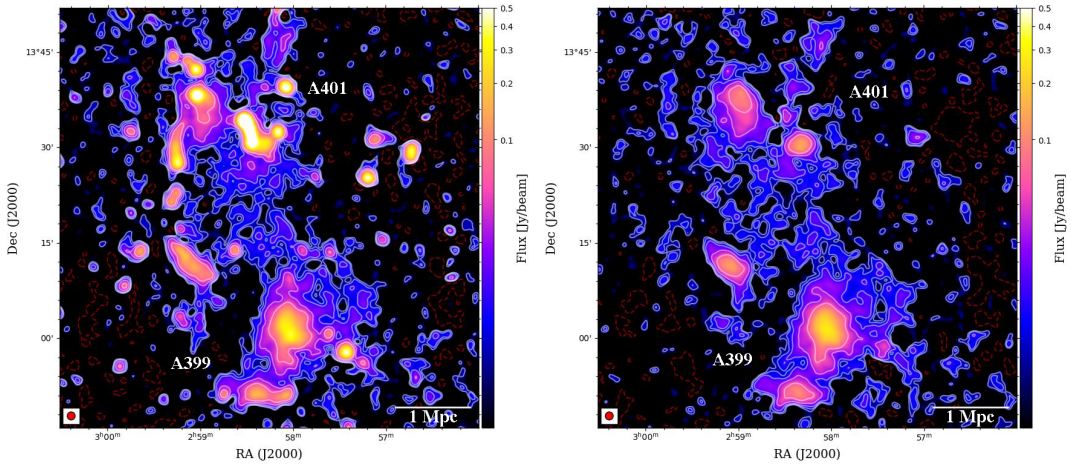

FIGURE 5.1: Radio images at 60 MHz of the A399-A401 clusters pair. *Left panel:* Low-resolution (75″, beam-size in bottom-left corner) image with compact sources and $\sigma_{\rm rms} = 3$mJy beam^{-1} produced with the parameters listed in Table 5.1. *Right panel:* Same as left panel, but after compact source subtraction. Contour levels (in white) start at $2\sigma_{\rm rms}$, $3\sigma_{\rm rms}$, $5\sigma_{\rm rms}$, and then increase to $20\sigma_{\rm rms}$ with factors of 2. A negative contour at $-3\sigma_{\rm rms}$ is shown in red.

The origin of radio bridges is widely discussed. In fact, to cause diffuse emission on such scales, electrons would need to be generated or re-accelerated in situ because of their short synchrotron life-times. Govoni et al. (2019) proposed the model of Fermi-I re-acceleration of fossil electrons by weak shocks crossing the region, which

would result in spectral indices similar to those of radio relics ($\alpha \sim 1.3$). Alternatively, Brunetti and Vazza (2020) showed how this emission could also be explained by a Fermi-II re-acceleration process. In this scenario, the fossil relativistic particles are re-accelerated by turbulence in amplified magnetic fields over Mpc-scales. This would result in steep observed synchrotron spectra between 150 MHz and 1.5 GHz ($\alpha > 1.5$). Recently, Nunhokee et al. (2023) presented WSRT observations at 346 MHz that were not sufficiently deep to observe the bridge, and therefore place a limit on the bridge spectral index ($\alpha_{140}^{346} > 1.5$). A similar procedure to place limits on the emission of radio bridges is defined in Pignataro et al. (2024). The non-detection of bridge emission in high sensitivity uGMRT data at 400 MHz results in a more stringent constraint on the steep bridge spectral index ($\alpha_{140}^{400} > 2.2$), disfavouring the Fermi-I acceleration scenario.

Other than the detection in A399-A401, only a few other radio bridges associated with merging clusters are known. Botteon et al. (2018); Botteon et al. (2020) report the bridge in Abell 1758N-S where they are also able to measure a spectral index for a patch of emission. Moreover, a candidate bridge is reported in Abell 1430 (Hoeft et al., 2021), and the bridge between relic and halo in A1550 (Pasini et al., 2022). Recently, a few more bridges between clusters and groups have been discovered (see Bonafede et al., 2021; Venturi et al., 2022). However, for none of these objects has it been possible to determine the spectral index of the extended diffuse emission.

Here we present a multifrequency study conducted with new LOFAR Low Band Antenna (LBA) data at 60 MHz that allows, for the first time, the determination of the spectral index of the radio bridge in the A399-A401 bridge between 60 and 144 MHz. Here, we assume a ΛCDM cosmology, with $H_0 = 70$ km s^{-1} Mpc^{-1}, $\Omega_m = 0.3$, and $\Omega_\Lambda = 0.7$. With these assumptions, at the average distance of the A399-A401 system (z$\sim$ 0.07), $1' = 83$ kpc and the luminosity distance is $D_L = 329$ Mpc.

5.2 Observations and data reduction

The observations of A399-A401 lasted for 18 hours and were carried out using the LOFAR LBA system in the frequency range of $30 - 77$ MHz (proposal code: LC13_022, P.I.: Bonafede). The correlated data were initially pre-processed for RFI and demix procedure (Van der Tol, 2009; de Gasperin et al., 2020a). In this case, both Cygnus A and Cassiopia A were demixed. The data were also averaged from 1 to 4 s integration time and from 64 to 8 channels per subband to reduce memory and computational load. The data were then calibrated with the pipeline LiLF (Sec. 3.3.3). We briefly summarise its main steps here, and a full description can be found in de Gasperin et al. (2019); de Gasperin et al. (2020). The pipeline obtains solutions from the calibrator (3C196) and applies them to correct the target data. In this part,

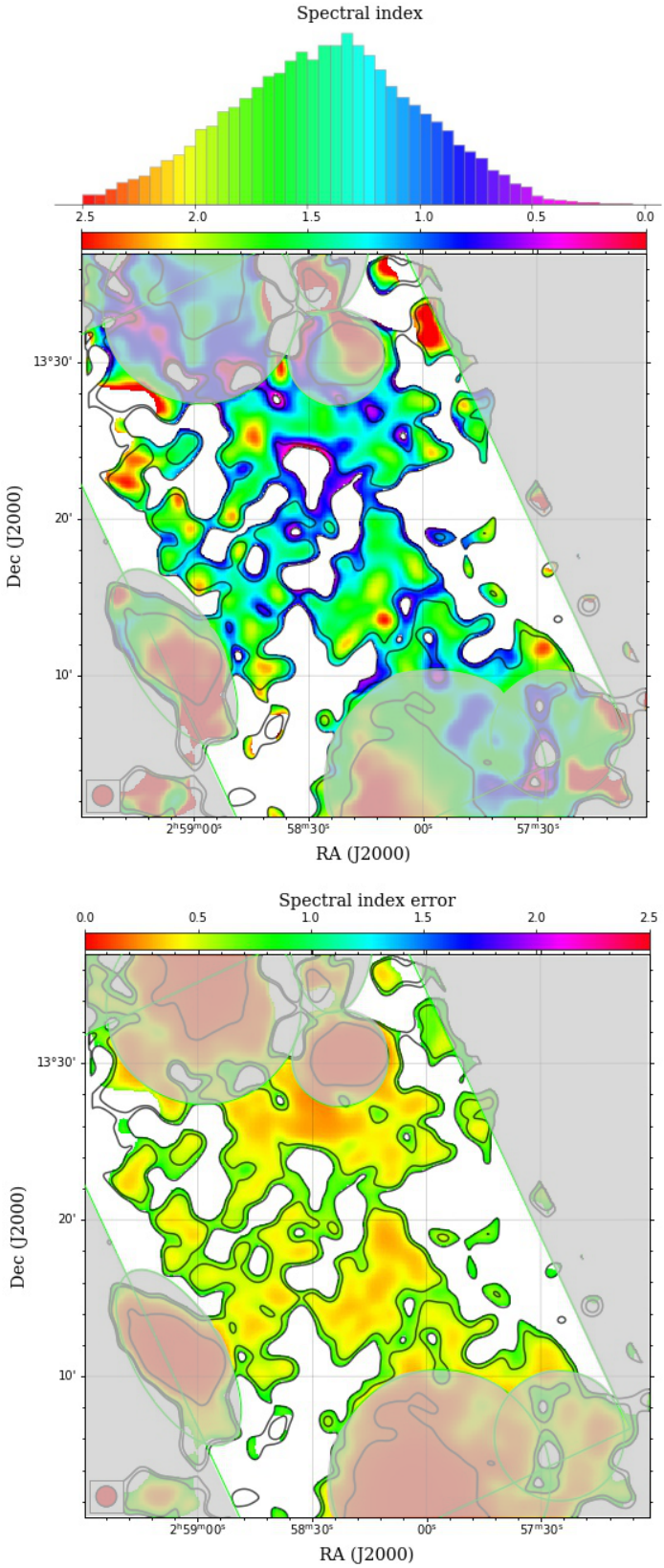

FIGURE 5.2: Spectral index maps. *Top panel:* Spectral index map of the emission in the radio bridge in A399-A401 between 60 and 144 MHz, with a resolution of 80″. The distribution of the spectral index values (histogram at the top) only refers to the bridge emission inside the $2\sigma_{\rm rms}$ level, which is not covered by the grey mask over the radio haloes. *Bottom panel:* Associated spectral index error map. The LOFAR LBA contours at $2\sigma_{\rm rms}$ and $3\sigma_{\rm rms}$ are overlaid in black.

the pipeline isolates the systematic effects of the polarisation alignment, the bandpass, and Faraday rotation well. The clock drift is left mixed with the total electron content (TEC), and both are transferred to the target. Additional calibration is then needed to correct for the differential ionospheric effects that strongly affect the lower frequencies (de Gasperin et al., 2018), especially for observations at low elevation, as is the case of this target (Dec +13°). This is done for the target field with direction-independent (DI) self-calibration and then with a direction-dependent (DD) calibration. After a round of calibration, we inspected the data and found very strong artefacts produced by a radio galaxy (3C79) outside the first primary beam null. To mitigate this effect, we reduced the observation bandwidth to eliminate the frequencies at which the source is brightest and the primary beam is largest. This reduced the frequency range to $44 - 77$ MHz, with the central frequency at 60 MHz. Then, we proceeded with a new round of DI phase and amplitude self-calibration, which performs two cycles and corrects for the systematic errors in the target field. From the sky model produced in the last round of DI calibration, the bright sources were selected as calibrators for the DD calibration, which removed the differential ionospheric errors in the direction of each calibrator within the field of view. Both steps are described in detail in de Gasperin et al. (2019). Finally, the pipeline performs the target extraction (van Weeren et al., 2021; Biava et al., 2021; Pasini et al., 2022), where the DD solutions found are used to subtract all sources outside a radius of approximately 0.5° around the target system. To refine the calibration towards the target, a few cycles of phase self-calibration at an increasing time resolution are performed on the extracted field. At this point, we can use the final calibrated extracted visibilities of the target to image at different resolutions with `WSClean v3.1` (Offringa, McKinley, Hurley-Walker, et al., 2014).

We produced a final primary-beam-corrected image at the central frequency of 60 MHz at a resolution of 75″ with an rms noise of $\sigma_{\rm rms} = 3$ mJy beam^{-1}. This is shown in Fig. 6.2 (left panel). We then produced a high-resolution image excluding baselines shorter than 900λ (i.e. emission on scales more extended than $\sim 4'$) to recover only the compact sources, and we then subtracted their components from the visibilities. The 75″ resolution source-subtracted image of the target field is shown in Fig. 6.2 (right panel). The radio bridge is detected at $2\sigma_{\rm rms}$ and continuously connects the two radio haloes. Its morphology is patchier at the $3\sigma_{\rm rms}$ level.

5.3 Results and discussion

5.3.1 Spectral analysis

In order to understand the origin and properties of the large-scale emission, we investigate the integrated spectral index and spectral index distribution of the bridge emission. To perform the spectral index analysis, the LBA data were imaged with the same parameters as the HBA data at 144 MHz presented in de Jong et al. (2022). The

	LBA	**HBA***
Image size (pixels)	1500	1500
Cell size (arcsec)	6	6
Weighting	Briggs robust -0.5	Briggs robust -0.5
min-uv (λ)	24	24
max-uv (λ)	3500	-
Taper gaussian (arcsec)	70	60
$\sigma_{\rm rms}$ (mJy beam^{-1})	3	0.5

TABLE 5.1: `WSClean` imaging parameters used to produce the low-resolution source-subtracted images for spectral index analysis. In the last line, we report the image rms noise $\sigma_{\rm rms}$. *The HBA low-resolution images at 144 MHz made with these parameters are presented in de Jong et al. (2022).

imaging parameters are listed in Table 5.1. In particular, we matched the *uv*-min and weighting scheme to recover the same angular scales and reach a similar resolution between LBA and HBA observations. To ensure that we corrected for possible shifts introduced by the phase self-calibration, we checked that the locations of the peaks of some point-sources in the field matched in both images. We then convolved the images to the same restoring beam (80″ resolution). Additionally, we performed a flux density alignment on the uv-subtracted image HBA maps presented in de Jong et al. (2022), as is usually done for LoTSS pointings (Shimwell et al., 2019b; Shimwell et al., 2022b), and applied a scale factor of 0.9 to the data. Finally, we only considered the emission above the $2\sigma_{\rm rms}$ contour in both images and computed the spectral index map with the associated error map, assuming a flux calibration error of 10% (as done for LoLSS, de Gasperin et al., 2021).

We show the resulting spectral index and spectral index error maps between 60 and 144 MHz with a resolution of 80″ in Fig. 5.2. We only considered the emission outside the grey mask as part of the radio bridge, while we masked the radio haloes and other features of diffuse emission that are unrelated to the bridge emission. Fig. 5.2 (top panel) shows the distribution of the spectral index along the bridge, and the occurrence of each value is represented in the histogram. The distribution appears uniform overall. Most values lie between $1.2 \leq \alpha \leq 1.5$. The error map (Fig. 5.2, bottom panel) shows the associated errors, which are mostly around $\Delta\alpha \sim 0.2$.

Within the $2\sigma_{\rm rms}$ level contours of the LBA image, we measure a flux density of $S_{60\ \rm MHz} = 1.77 \pm 0.18$ Jy and $S_{144\ \rm MHz} = 0.50 \pm 0.05$ Jy[1], leading to an integrated spectral index value for the radio bridge of $\alpha_{60}^{144} = 1.44 \pm 0.16$. This is the first estimate of a radio bridge spectral index, and it provides important information on

[1]This is in agreement with the flux density measured in de Jong et al. (2022), the difference is due only to different areas.

the models of magnetic field amplification and particle re-acceleration processes on megaparsec-scales.

5.3.2 Theoretical models

The origin of the radio emission from radio bridges is still being investigated. The megaparsec-scale size of the bridge requires an in situ mechanism that accelerates the relativistic particles so that they travel over these scales (Brunetti and Jones, 2014). Govoni et al. (2019) suggested a shock-driven emission model, where multiple weak shocks re-accelerate a pre-existing population of electrons. However, they showed that it is difficult to account for the extension and strength of the bridge emission only via a shock prior to the collision between A399 and A401. Moreover, the high-sensitivity study of de Jong et al. (2022) reported no filamentary structures or shock surfaces in the bridge region, which disfavours the shock origin. We wished to investigate the spectrum of the bridge emission with the measured flux densities at LOFAR frequencies. Additionally, we wished to incorporate data from the uGMRT observations at a central frequency of 400 MHz presented in Pignataro et al. (2024), where the bridge emission was undetected. This also allows for a comprehensive comparison of the radio spectrum with the synchrotron spectrum predicted by theoretical models. In Pignataro et al. (2024), we found a limit on the bridge emission by following the injection procedure (see e.g. Venturi et al., 2008; Bernardi et al., 2016; Bonafede et al., 2017; Duchesne et al., 2022; Nunhokee et al., 2023). In order to incorporate the limit in the radio spectrum produced in this work, we again performed the procedure by injecting the 60 MHz emission model, where the emission appears to be less extended than the 144 MHz detection. We extended the procedure presented in Pignataro et al. (2024) and took the spatial variations in the noise pattern in the uGMRT image into account. This follows from a generalisation of the injection approach, where we do not only inject at the centre of the image (i.e. the location at which the bridge is detected at lower frequencies), but also in different locations in the field. Analysing the noise pattern in the final uGMRT image over which the injection is performed, we find a non-uniform distribution. Therefore, to place a more conservative limit on the flux density of the bridge, we injected the visibilities three times: once at the known location of the bridge in the centre of the image, once north-east of the centre, and once south-west of the centre. The final limit is the result of an average of the three injections.
The injection procedure can be summarised as follows (see Pignataro et al. 2024 for an extensive description):

- From the model image of the LOFAR detection at 60 MHz, we created a mask that only included the emission from the bridge.

- The bridge model image was extrapolated to the central frequency of the uGMRT observation with a varying spectral index between $0 \leq \alpha \leq 4$ with steps of $\Delta\alpha = 0.25$. The model images were additionally multiplied with the uGMRT

Telescope	ν **[MHz]**	$P(\nu)$ **[W Hz^{-1}]**	$S(\nu)$ **[Jy]**
LOFAR LBA	60	$(2.2 \pm 0.2) \times 10^{25}$	1.77 ± 0.18
LOFAR HBA	144	$(6.1 \pm 0.6) \times 10^{24}$	0.50 ± 0.05
uGMRT Band3	400	$< 7.6 \times 10^{23}$	< 0.06

TABLE 5.2: Radio quantities for the bridge emission at the three frequencies. The columns list (1) the telescope, (2) the central frequency in MHz, (3) the radio luminosity in W Hz^{-1} at given frequency, and (4) the integrated flux density in Jy at given frequency.

primary beam model to take the attenuation of the primary beam in the uGMRT observation into account.

- The final bridge model images were then Fourier transformed into visibilities (`WSClean -predict`, Offringa, McKinley, Hurley-Walker, et al., 2014) that were injected into the uGMRT source-subtracted calibrated visibilities. The prediction of the model visibilities in the original dataset takes into account the missing short baselines or flagged data of the uGMRT observation. We then deconvolved and imaged with the same parameters, uv sampling, and image and visibility weighting as for the non-injected data images. In this way, we produced a mosaic with a resolution of 80″ as the injected image at the central frequency of 400 MHz for each spectral index, α.

- We defined the ratio $R(\alpha) = S^{\rm inj}_{400}(\alpha)/S_{400}$, which measures how bright, given a certain spectral index value, α, the injected bridge emission is (i.e. the flux density $S^{\rm inj}_{400}(\alpha)$) with respect to the image background (S_{400}). We computed the ratio $R(\alpha)$ each time we performed the injection in a different location. We then computed the average of the three ratios, $\langle R(\alpha) \rangle$.

- We finally evaluated the cumulative probability distribution function of $\langle R(\alpha) \rangle$. We find that the spectral index of the bridge has a limit of $\alpha_l > 1.75$ with a 95% confidence level. This is different from the confidence level presented in (Pignataro et al., 2024c) because we started from a different injected model and followed a more robust procedure.

The limit on the spectral index translates into an upper limit on the bridge-integrated flux density that is $S_{400} < 60$ mJy.

The radio spectrum of the bridge is shown in Fig. 5.3 (top panel), and the plotted values are listed in Table 5.2. The observations at 60 and 140 MHz and the upper

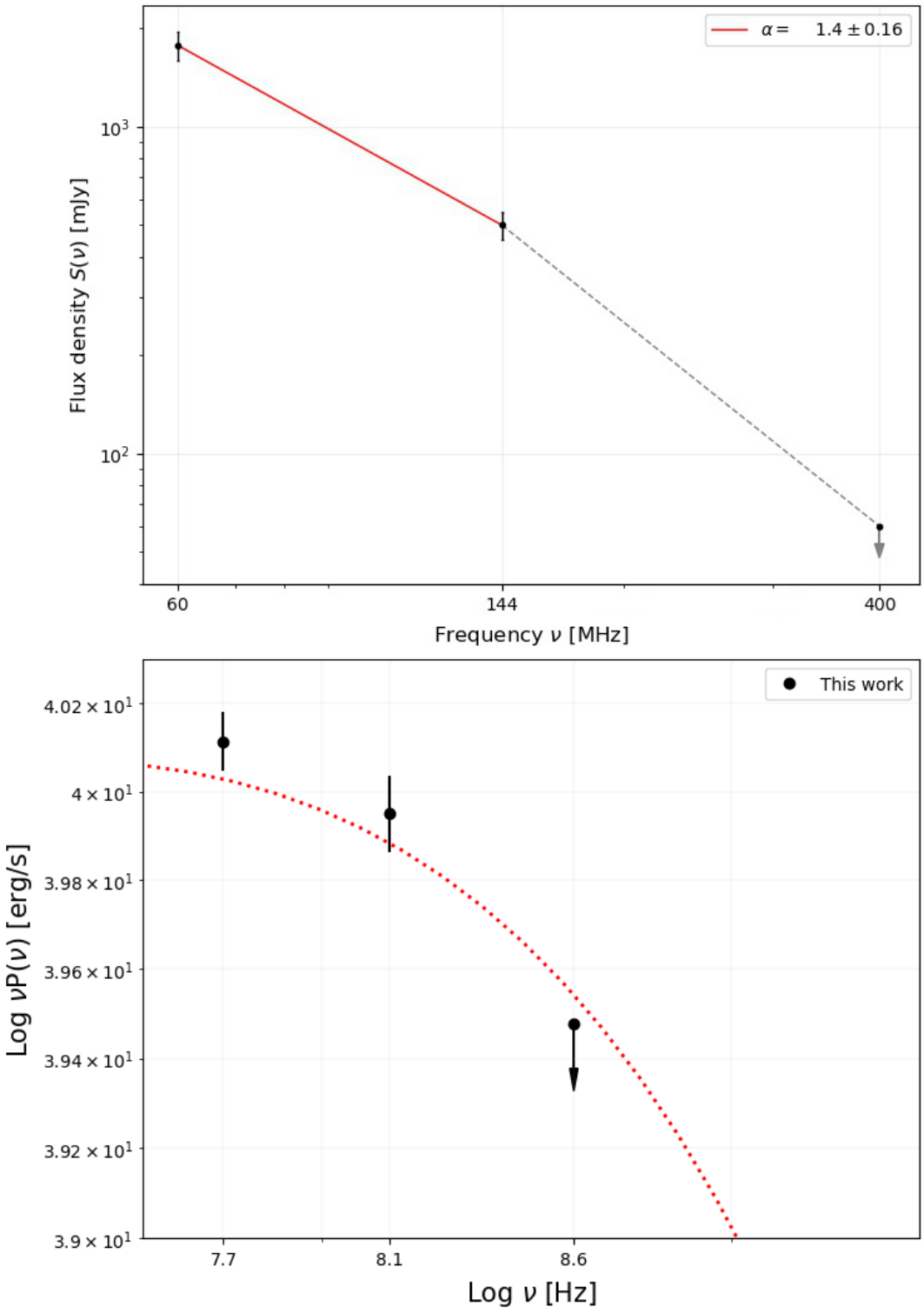

FIGURE 5.3: Radio spectra. *Top panel:* Bridge emission radio spectra in integrated flux density. The grey arrow represents the uGMRT limit. *Bottom panel:* Radio luminosity of the bridge emission compared to a synchrotron theoretical model (red curve) produced by the relativistic particle populations with acceleration times τ_{acc} >200 Myr.

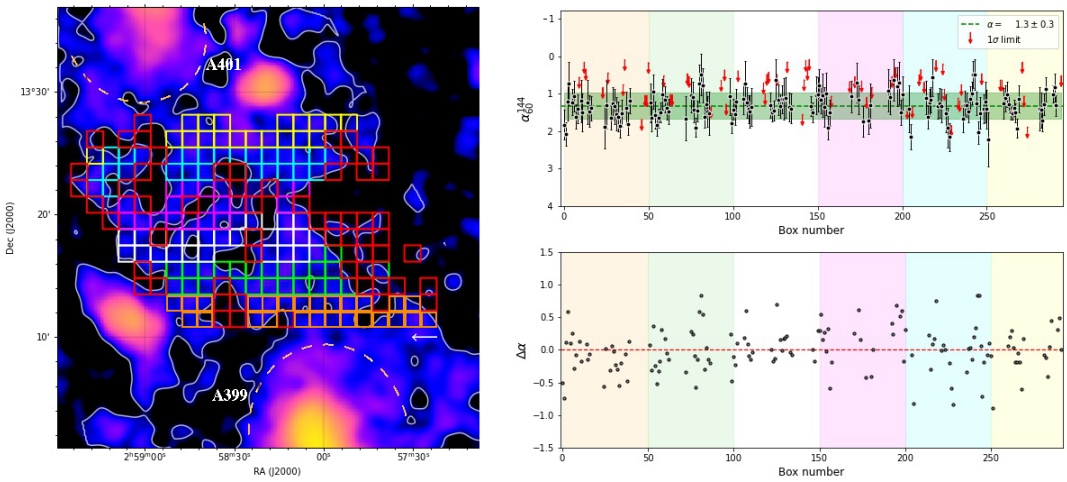

FIGURE 5.4: Spectral index distribution. *Left panel:* LBA radio image at 60 MHz and resolution of 80″. The $2\sigma_{\rm rms}$ contours and the grid to extract the spectral index between 60 and 144 MHz are overlaid. Different areas of the bridge are covered by differently coloured cells. The coloured cells cover the LBA emission above $2\sigma_{\rm rms}$, and the red cells cover the $1\sigma_{\rm rms}$ LBA emission and $2\sigma_{\rm rms}$ HBA emission. *Top right:* Spectral index distribution across the bridge. The black points show values extracted from each cell, separated by colour, and the red arrows indicate $1\sigma_{\rm rms}$ limits extracted from the red cells. The dashed horizontal green line shows the mean spectral index, and the filled horizontal green region represents the standard deviation. *Bottom right:* Distribution of residuals ($\Delta\alpha$) of α with respect to the mean spectral index.

limit derived at 400 MHz show a steepening towards increasing frequency. This feature, as well as the steep spectrum found between 144 and 400 MHz, is hard to reconcile with a shock-origin scenario. However, spectral steeping is a key prediction of the turbulent re-acceleration model presented in Brunetti and Vazza (2020). These authors investigated several re-acceleration scenarios coupled with the result of a cosmological simulation and showed that the steepening changes as a function of the magnetic field amplification efficiency (η_B) and particle acceleration times ($\tau_{\rm acc}$). In particular, they identified for their analysis a simulated system that resembles the A399-A401 bridge (Govoni et al., 2019; Domínguez-Fernández et al., 2019). The initial spectrum of relativistic electrons was evolved by solving the Fokker-Planck equations assuming a single-zone model, that is, assuming average quantities, such as thermal densities and magnetic fields, which are measured in each cell in the simulated bridge region at a fixed time. This was done for different values of particle acceleration times ($\tau_{\rm acc}$), from ∼10 Myr up to ∼10 Gyr (see Brunetti and Vazza 2020, Fig. 2). The spectrum shown in Fig. 5.3 (bottom panel) was obtained from the spectrum presented in Brunetti and Vazza (2020) (see Fig. 3, for $\eta_B \sim 0.05$). To reproduce our observed data, we re-scaled the spectrum from a surface of ~ 3.9 Mpc^2 to ~ 2.2 Mpc^2, which is the area covered by the LBA detection, excluding the radio haloes. Additionally, it was necessary to exclude all cells with a generated $\tau_{\rm acc} < 200$ Myr,

which make up ∼3% of the volume of the simulated bridge. Therefore, the observed LOFAR luminosities and the uGMRT limit set a constraint on the particles acceleration times to values longer than 200 Myr, which are generated in the majority of the cells in the simulation.

Finally, we investigated how the spectral index value could vary in different areas of the bridge. The distribution of the spectral index is likely related to the contribution of turbulence and re-acceleration processes across the extended emission. We created a grid covering the emission inside the $2\sigma_{\rm rms}$ contours in the 60 MHz image (Fig. 5.4, left panel). Each grid cell was one beam size ($80'' \times 80''$). We extracted a value of the spectral index between 60 and 144 MHz in each coloured cell. We computed the spectral index over the $2\sigma_{\rm rms}$ LBA detection and therefore considered the emission component with steepest spectra and/or weakest surface brightness. To check this bias, we extracted the $1\sigma_{\rm rms}$ emission in the red cell and evaluated a limit on the spectral index with the $2\sigma_{\rm rms}$ emission in the 144 MHz image. The distribution of the spectral index in the bridge is shown in the top right panel of Fig. 5.4, and in the bottom right panel we show the distribution of the residuals, $\Delta\alpha$, between each value of the spectral index we extracted and the mean α value. The values of each cell are consistent around the mean value inside the standard deviation for most points. Even though a larger scatter is observed for some cells ($0.5 < \Delta\alpha < 0.9$), they do not appear to be spatially correlated. The red arrows represent the limits extracted from the red cells, which are generally flatter than the mean value. However, we also note the limits at the level of the measured spectral index, or steeper. The spectral index is consistent with being constant throughout the region, and there is no evidence for any systematic trend in the bridge region.

5.4 Conclusions

For the first time, we have determined the spectral index for the emission of a radio bridge that connects the two pre-merging galaxy clusters A399 and A401. The radio bridge was only detected at 144 MHz before, and therefore, we analysed new LOFAR LBA data at 60 MHz to constrain the spectral index of the emission.

We measured an integrated spectral index for the bridge between 60 and 144 MHz of $\alpha_{60}^{144} = 1.44 \pm 0.16$. We also investigated the spectral index distribution, which gives insights into the contribution of turbulence and re-acceleration processes causing the extended emission. In the spectral index and associated errors maps, the distribution shows no systematic gradients in the bridge regions.

Combining the two LOFAR detections and the uGMRT limit found at 400 MHz, we produced a comprehensive comparison of the obtained radio spectrum of the bridge with the synchrotron spectrum predicted by theoretical models. The steepening of the spectrum between 144 and 400 MHz is hardly reconcilable with a scenario of a shock acceleration origin (as proposed in Govoni et al., 2019), but it can be

explained by the turbulent acceleration models investigated by Brunetti and Vazza (2020). Our observations allowed us to constrain the particle acceleration time and in turn the volume-filling factor of the particle distribution in the turbulent re-acceleration model. Short acceleration times (corresponding to re-acceleration in regions that occupy a small fraction of the bridge volume) generate shallower spectra, which are disfavoured by our observations. Conversely, a long acceleration time ($\tau_{\rm acc} > 200$ Myr) for particles that occupy most of the bridge volume is consistent with our data. The fact that the emission in the 60 MHz image appears to be less volume-filling than at 144 MHz is likely related to the sensitivity limitations of the LBA observations. The Fermi-II origin scenario suggested by these observations requires significant turbulent motions in most of the bridge volume. Moreover, the aforementioned scenario assumes a volume-filling reservoir of low-energy electrons ($\gamma \leq 10^3$), whose existence requires further observational evidence and is not yet quantitatively predicted by simulations either. Finally, the $B \geq 0.3\,\mu$G magnetic field required by this model is large for a peripheral region like this, and it might be detected by the next generation of polarization surveys through RM grid (Heald et al., 2020).

Chapter 6

Mind the Gap between Abell 2061 and Abell 2067

6.1 Introduction

In this Chapter we explore an interesting merging system that host a unique extended diffuse feature. The two clusters are Abell 2061 and Abell 2067, in the Corona Borealis Supercluster.

The conditions to generate diffuse radio emission on very large scales are expected to be particularly favourable in superclusters of galaxies, the largest coherent structures in the Universe, where rich clusters in their core may be dynamically active (Einasto et al., 2021). The Corona Borealis supercluster (CSC) is the most prominent and dense supercluster in the Northern Sky, at an average redshift of $z \sim 0.07$. It is composed of ten galaxy clusters, including which Abell 2056, Abell 2061, Abell 2065, Abell 2067, and Abell 2089 comprise a gravitationally-bound supercluster core that is collapsing (Pearson, Batiste, and Batuski, 2014). The dominant cluster of the CSC is Abell 2065 (Markevitch, Sarazin, and Vikhlinin, 1999), and recent studies have found Abell 2061-Abell 2067 (hereafter, A2061 and A2067) to be a gravitationally-bound pair, in a pre-merger state (Marini et al., 2004; Batiste and Batuski, 2013; Pearson, Batiste, and Batuski, 2014). This system closely resembles the cluster pairs A399-A401 and A1758N-S, where radio bridges have been observed at low frequency (Govoni et al., 2019; Botteon et al., 2020; de Jong et al., 2022; Pignataro et al., 2024a).

The two cluster centres are separated by a projected distance of ∼2.5 Mpc (Rines and Diaferio, 2006), and A2061 is the main cluster of this pair. It has a R_{500}^{SZ} ∼1 Mpc radius, (Planck Collaboration et al., 2016) and an X-ray luminosity of $L_X^{0.1-2.4keV} \sim 3.95 \times 10^{44}$ erg s^{-1} (Ebeling et al., 1998). Its X-ray disturbed morphology suggests it is undergoing mergers with the surrounding, smaller halos (Marini et al., 2004). In particular, it contains an X-ray extension (dubbed *plume* in Marini et al. 2004) visible with ROSAT-Position Sensitive Proportional Counters (PSPC) extending towards A2067 in the North-East (NE) direction. However, since the interaction between the

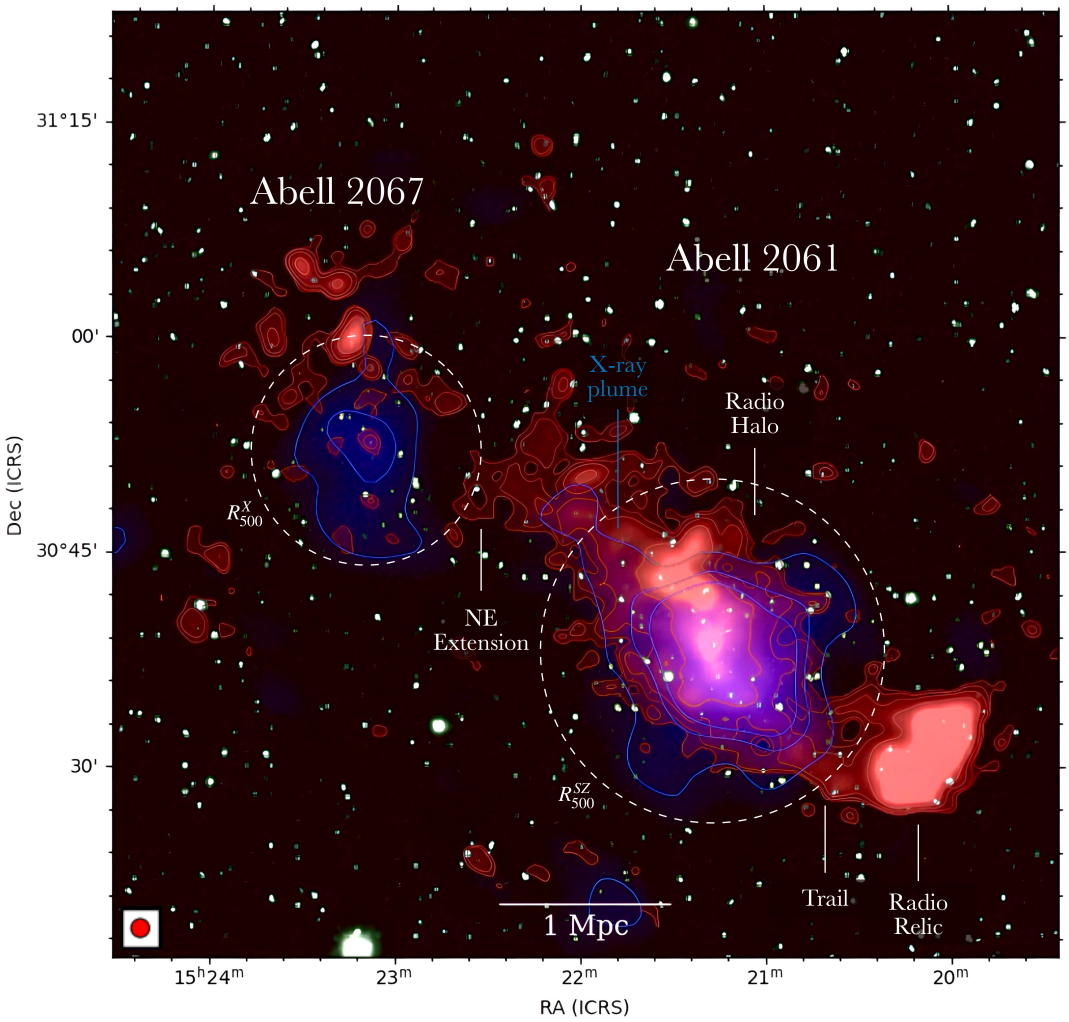

FIGURE 6.1: Composite image of the galaxy clusters system Abell 2061 - Abell 2067 in the Corona Borealis Supercluster. The radio emission from LOFAR observations at 144 MHz and 80″ resolution is shown in red. The diffuse emission sources presented in this work are highlighted in white. The X-ray, ROSAT emission is shown in blue, overlaid on the optical, Pan-STARRS1 image.

two clusters appears to be in early stages (Marini et al., 2004), the plume is likely related to a third substructure that is currently interacting or has already interacted in the past with A2061. Marini et al. (2004) suggested the interaction of the two clusters could be an indication of the existence of an underlying filament, along which also the group merged into A2061.

A2067 is, in turn, a relatively low X-ray luminosity cluster ($L_X^{0.1-2.4keV} \sim 4 \times 10^{43}$ erg s^{-1}), which also shows an elongated morphology in the ROSAT All Sky-Survey (RASS) image. The X-ray peak coordinates differ by $\sim 8'$ from the ACO center, and the measured X-ray radius R^X_{500} is $\sim$ 0.7 Mpc (Piffaretti et al., 2011). The quantities related to the two clusters are summarized in Table 6.1.

Radio observations of this system have been carried out at different frequencies to investigate evidence of diffuse emission. For A2061, Kempner and Sarazin (2001) and Rudnick and Lemmerman (2009) reported a possible relic, detected at 1.4 GHz

	RA [J2000]	Dec [J2000]	z	R_{500} [Mpc]	M_{500} [$10^{14} M_{\odot}$]
A2061	15h 21m 08s	+30°38′08″	0.0783	1.0	3.5
A2067	15h 23m 07s	+30°50′42″	0.0756	0.7	1.2

TABLE 6.1: Coordinates, redshift, radius and mass of the two clusters analysed in this work. The reported coordinates are referring to the X-ray centers, from XMM observations for A2061 (Bartalucci et al., 2023), and ROSAT for A2067 (Piffaretti et al., 2011). The quantities R_{500} and M_{500} are measured from SZ (Planck Collaboration et al., 2016) and X-ray (Piffaretti et al., 2011) observations for A2061 and A2067, respectively.

with the NRAO VLA Sky Survey (NVSS, Condon et al., 1998) and 327 MHz with the Westerbork Northern Sky Survey (WENSS, Rengelink et al., 1997). The presence of the relic is then confirmed with WSRT observations at 1.38 and 1.7 GHz, which results in a $\alpha = 1.03 \pm 0.09$ spectral index (van Weeren et al., 2011). Additionally, Rudnick and Lemmerman (2009) reported a tentatively detected radio halo at 327 MHz at the center of the cluster. The radio halo is also tentatively detected by GBT-NVSS observations at 1.4 GHz reported in Farnsworth et al. (2013), where they derive a preliminary spectral index for the halo of $\alpha = 1.8 \pm 0.3$ between 0.3 and 1.4 GHz. In the GBT-NVSS and WENSS images, the radio halo appears elongated, displaying an extension towards the NE likely associated with the X-ray plume. Farnsworth et al. (2013) also reported the presence of a possible bridge of emission, joining the radio halo and the relic, and a possible inter-cluster filament between A2061 and A2067, seen at a limited statistical significance in images with 11′ angular resolution at 1.4 GHz. However, the very poor resolution of GBT does not allow a firm conclusion on this classification. A2067 is also observed with GBT-NVSS at 1.4 GHz, where they detect a marginally resolved emission $\sim 12'$ north of the X-ray peak. However, there appears to be a blending of unresolved emission and they classify this emission as a possible relic (Farnsworth et al., 2013). Recently, A2061 was observed with the LOFAR Two-Metre Sky Survey (LoTSS, Shimwell et al., 2017; Shimwell et al., 2019a; Shimwell et al., 2022a) and was studied as part of the Planck (Planck Collaboration et al., 2016) clusters sample covered by the LoTSS-DR2 (Botteon et al., 2022). They were able to confirm the presence of the radio halo, the radio relic, and the trail between them at 144 MHz.

Here we present 16 hours new LOFAR High Band Antenna (HBA) observations at 144 MHz of the A2061-A2067 system, following up the LoTSS observations that already suggested the presence of a bridge of emission to the region of the X-ray plume. Here, we report the discovery of further extended diffuse emission between the two clusters (see Fig. 6.1) that might be related to the filament connecting the two clusters (Einasto et al., 2021). This work is organized as follows: in Sec. 6.2

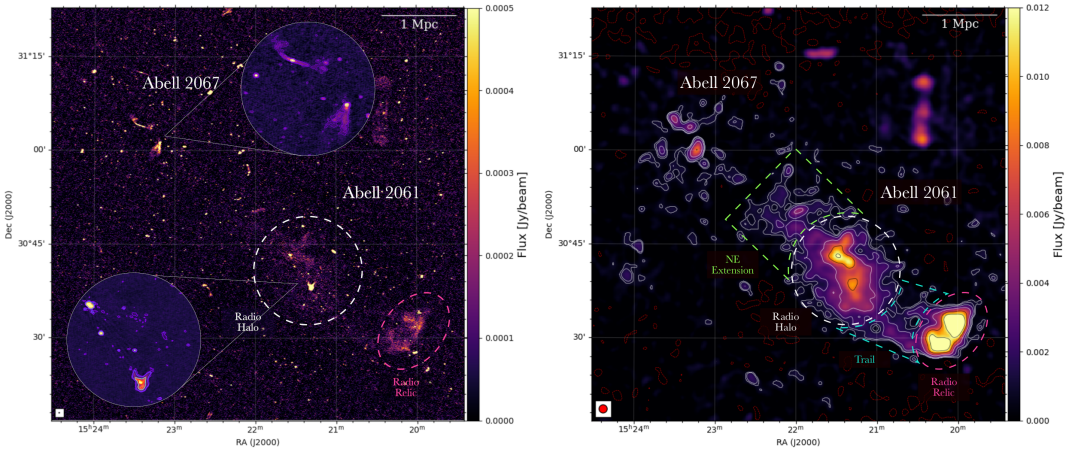

FIGURE 6.2: Radio maps of A2061-A2067. *Left panel*: Image of A2061-A2067 at a resolution of $8'' \times 5''$ (p.a. 90°). The imaging was done adopting a briggs weighting scheme (Briggs, 1995b) with `robust=`-0.5, and the resulting rms noise is $\sigma_{rms} = 80$ μJy beam^{-1}. The radio halo (white dashed circle) and the radio relic (magenta dashed circle) are already visibile at high resolution and without compact source subtraction. The most interesting radio sources in the field are highlighted in the circles. *Right panel*: Image of A2061-A2067 at a resolution of $80''$, after subtraction of compact sources. The imaging was made adopting a briggs weighting scheme with `robust=`-0.5 and applying a Gaussian *uv*-taper of $70''$. We show the $2, 3, 5, 10 - \sigma_{rms}$ contour levels in white, and the $20, 30 - \sigma_{rms}$ contours level in black ($\sigma_{rms} = 0.4$ mJy beam^{-1}.) The $-2\sigma_{rms}$ contours are shown in dashed red. Additionally to the radio halo and relic in A2061, we now detect diffuse emission in the NE extension (green dashed region) and trail (cyan dashed region).

we describe the radio and X-ray data reduction; in Sec. 6.3.1 we compare radio and X-ray radial profiles in the direction of the extended radio feature; in Sec. 6.3.2 we investigate the radio/X-ray correlation for A2061; finally, in Sec. 7.4 we discuss the possibile dynamical scenarios to originate the diffuse emission and its classification. Throughout this work we assume a ΛCDM cosmology, with $H_0 = 70$ km s^{-1} Mpc^{-1}, $\Omega_m = 0.3$, and $\Omega_\Lambda = 0.7$. With these assumptions, at the average distance of the A2061-A2067 system (z$\sim$ 0.076), $1' = 85$ kpc and the luminosity distance is $D_L = 345$ Mpc.

6.2 Observations and data reduction

6.2.1 Radio data

The two clusters were observed as part of a pointing on the northern part of CSC, therefore the system is distant $\sim$35′ from the pointing center. We observed the CSC with LOFAR HBA using the same setup as LoTSS, that is in the frequency range 120-168 MHz, divided into 244 sub-bands of 64 channels each. The total observing time for CSC North was 32 hours (proposal code: LC014_18, P.I: Vazza), however only 16 hours are not affected by severe ionospheric conditions and used for this analysis.

This observation was carried out in co-observing mode with the LoTSS and the data reduction follows the LoTSS reduction scheme. We summarize below the main steps and refer the reader to Shimwell et al. (2022) and Tasse et al. (2021) for further details. The pipeline performs direction-independent and dependent calibration and imaging of full field of view on CSC North, using `PREFACTOR` (van Weeren et al., 2016a; Mechev et al., 2018; de Gasperin et al., 2019), `KILLMS` (Tasse, 2014; Smirnov and Tasse, 2015) and `DDFACET` (Tasse et al., 2018). To allow flexible re-imaging limited to the target of interest, we then performed the so-called 'extraction' procedure (van Weeren et al., 2021), where the direction-dependent solutions are used to subtract all sources outside a box of approximately 0.8° radius around the target. As a final step, additional cycles of phase self-calibration in the extracted field are performed, followed by several rounds of amplitude calibration using a longer solution interval. After this last refinement, we used the final calibrated, extracted visibilities of the target to image at different resolutions with `WSClean v3.1` (Offringa, McKinley, Hurley-Walker, et al., 2014).

We produced a final primary beam corrected image at the central frequency of 144 MHz, at a resolution of $8'' \times 5''$ (p.a. 90°) with a rms noise of $\sigma_{\rm rms} = 80$ μJy beam^{-1}, shown in Fig. 6.2 (left panel). From the high-resolution image, it is already possible to see the diffuse emission from the radio halo and relic in A2061, and a hint of emission connecting them. Since we are particularly interested in the diffuse emission in the field, we produced a high-resolution image excluding baselines shorter than $\sim 760\lambda$ (i.e. emission on scales more extended than $\sim 4.5' \simeq 380$ kpc) to recover only the compact sources, and then subtracted their components from the visibilities. Finally, a $80''$ resolution, source-subtracted image of the target field with a rms noise of $\sigma_{\rm rms} = 0.4$ mJy beam^{-1} is shown in Fig. 6.2 (right panel). In the A2067 field, no diffuse emission is revealed other than residuals from extended sources, such as the tailed Active-Galactic-Nuclei (AGN) visible in Fig. 6.2 (left panel). In the A2061 field, the low-resolution image shows the presence of the radio halo and relic in A2061, detected at high significance. Additionally, we detect the trail of emission connecting the radio halo and relic, and reveal filamentary diffuse emission extending over ~ 800 kpc from the radio halo in A2061 towards A2067, which we label as 'NE extension' in Fig. 6.1 and Fig. 6.2.

6.2.2 X-ray data

The galaxy cluster A2061 has been observed with XMM-Newton (Obs. id: 0721740101) and it also belongs to the Cluster HEritage project with *XMM-Newton* - Mass Assembly and Thermodynamics at the Endpoint of structure formation (CHEX-MATE, CHEX-MATE Collaboration et al., 2021) project sample. For the aim of this study, it is useful to compare the properties of the thermal and non-thermal emission in A2061.

The X-ray data on A2061 were processed using the CHEX-MATE pipeline as detailed by Bartalucci et al. (2023) and Rossetti et al. (2024). Below, we summarize the main steps involved.

Observations were conducted with the European Photon Imaging Camera (EPIC, a set of three X-ray CCD cameras, Turner et al., 2001; Strüder et al., 2001) and the datasets were then reprocessed using the Extended-Science Analysis System E-SAS, Snowden et al. (2008). Flare events were filtered out by excluding time intervals with count rates exceeding 3σ above the mean count rate. Point sources were also excluded from the analysis based on the methodology presented in Ghirardini et al. (2019) and Bartalucci et al. (2023). The scientific images of the cluster are generated from each camera's photon-count images in the [0.7-1.2] keV band, which optimizes the signal-to-noise ratio for cluster thermal emission (Ettori et al., 2010). Exposure and background maps are also created. The X-ray background consists of a sky component (i.e. the local Galactic emission and the Cosmic X-ray background) and an instrumental component introduced by the interaction between high-energy particles and the detector. Following Ghirardini et al. (2019) and Bartalucci et al. (2023), the instrumental background component was then mitigated and the sky component described by a constant profile component. Finally, to maximize statistics, the images, exposure maps, and background maps from the three cameras were merged (Bartalucci et al., 2023) and used for the following analysis.

6.3 Results and discussion

In the next sections, we present and discuss the analysis on the radio and X-ray data performed primarily on the NE extension of diffuse emission discovered in A2061. We also discuss the several diffuse sources found in this cluster, whose discovery has been already reported in dedicated papers (see Sec. 6.1). We present the properties of these sources and add complementary information that we obtained with our new data.

6.3.1 Radial profiles

Radio

The most interesting source of diffuse emission in A2061 is the filamentary emission that is connected to the radio halo and extends in the direction of A2067, creating a bridge of emission between the two R_{500}. In order to investigate the nature of the emission from the radio halo and the extended feature, we computed a radial profile using the radio map from our 144 MHz observations. The surface brightness profile of the radio halo in A2061 was already investigated in Botteon et al. (2022) as part of the Planck (PSZ2 catalog, Planck Collaboration et al. 2016) clusters sample covered

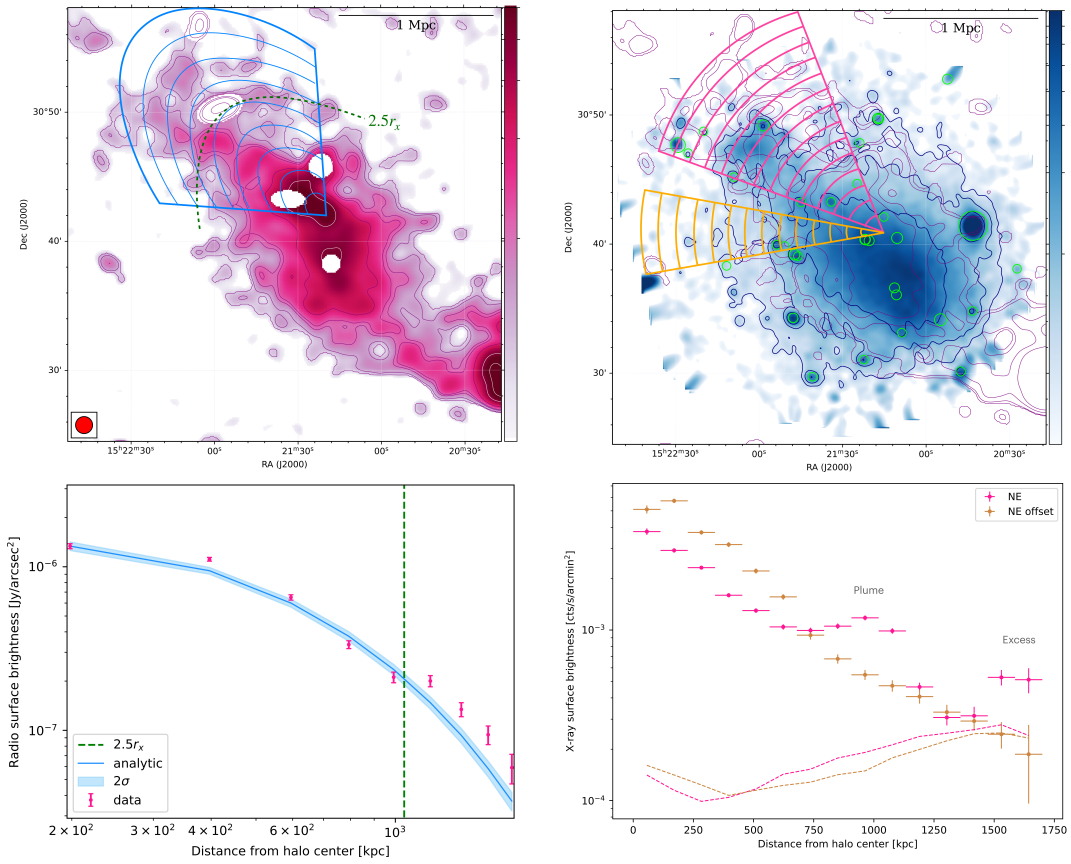

FIGURE 6.3: Radio and X-ray surface brightness profile of A2061. *Top left panel*: the 80″ radio map at 144 MHz with residual sources masked is shown in pink colourscale. We show the $2, 3, 5, 10 - \sigma_{rms}$ contour levels in purple, and the $20, 30 - \sigma_{rms}$ contours level in white. The mean radio brightness is computed inside the blue region. The width of the elliptical annuli along the major axis is $\sim$ 2 times the beam size (80″). The $2.5r_x$ area is delimited by the dashed green line. *Bottom left panel*: comparison between the average surface brightness measured in each blue bin (the magenta data points, with 1σ uncertainties) with the model profile from the best-fit analysis performed with `HALO-FDCA` (solid cyan line, with 2σ uncertainties). Beyond $\sim$ $2.5r_x$ (dashed green line) the average surface brightness is persistently higher than the best fit radio halo model, due to the NE extension. *Top right panel*: the smoothed *XMM-Newton* X-ray map is shown in blue colourscale. The contour-levels from the radio emission are overlaid in purple and the X-ray point sources (green circles) are masked. The X-ray surface brightness is computed inside the magenta slices, centered on the radio halo and covering the NE extension. We compare this sector with the yellow slice, in an offset direction from the extension. The width of the circular sectors is one beam size (80″). *Bottom right panel*: The two profiles extracted from the different sectors are shown in magenta and yellow points. In the NE direction, we note a bump in the profile associated with the X-ray plume, that is followed by an excess at larger radii. On the contrary, there is no evidence of excess at the same distances from the center in the yellow sector. The background level in each sector is shown with magenta and yellow dashed lines.

by the LoTSS-DR2. The radio profile was studied with the use of the Halo-Flux Density CAlculator (HALO-FDCA[1]; Boxelaar, van Weeren, and Botteon 2021). This code fits the two-dimensional brightness profile using Bayesian inference. The Markov Chain Monte Carlo (MCMC) algorithm is perfomed to determine the best-fit parameters and associated uncertainties. We repeat the analysis on A2061 on our 80″ radio map, with additional masking of the residuals from poorly subtracted bright diffuse sources which differs from the masking performed in Botteon et al. (2022). The extension emission is fitted as part of the radio halo. Typically, radio halos brightness profiles are fitted by an exponential law of the form:

$$I_{\mathbf{r}} = I_0\, e^{-G(\mathbf{r})} \tag{6.1}$$

where I_0 is the central radio surface brightness (Murgia et al., 2009), $G(\mathbf{r})$ is a function that describes the model morphology (i.e. circular, elliptical, or skewed) and $\mathbf{r}$ is the positional vector. The radio halo in A2061 was fitted with a rotated ellipse morphology that allows for a rotation ϕ with respect to the coordinate system centered in (x_0, y_0) (Boxelaar, van Weeren, and Botteon, 2021). Therefore $G(r)$ becomes:

$$G(\mathbf{r}) = \left[\left(\frac{X_\phi(\mathbf{r})}{r_x}\right)^2 + \left(\frac{Y_\phi(\mathbf{r})}{r_y}\right)^2\right]^{0.5} \tag{6.2}$$

where X_ϕ, Y_ϕ represent the coordinate transformation, and r_x and r_y represent the two e-folding radii in the direction of the major and minor axis. This model has six free parameters: I_0, x_0, y_0, r_x, r_y, and ϕ. The best-fit parameters and their uncertainties are reported in Table 6.2. The residual from the fitting procedure are shown Fig. 6.4. In Fig. 6.3, we show the radial profile of the halo brightness at 144 MHz. We have computed the mean of the radio surface brightness and its error within an elliptical annuli having a width $\sim 2.3'$ that covers the NE extension. The masked pixels are excluded when calculating the surface brightness. We compare the measured data with the analytical profile evaluated for the same annuli, computed with the model parameters. The best-fit parameters are Monte Carlo resampled 500 times inside their uncertainties, and the final analytical mean radio brightness and its standard deviation are shown in Fig. 6.3 (left panels). The data and the model profile show overall good agreement, with small deviations at small radii. The discrepancy between real and model data when fitting the radio halo with a single exponential profile were already noted in recent works (see e.g. Cuciti et al., 2021; Botteon et al., 2022). For disturbed merging clusters as is the case of A2061, Botteon et al. (2023) showed that, especially in the central regions, these deviations are likely related to the presence of substructure in the brightness distribution of the real halo. We note that after $\sim 2.5 r_x$, i.e. over the NE extension, the data points show a systematic excess of emission with respect to the radio halo profile. This result questions on the

[1] https://github.com/JortBox/Halo-FDCA

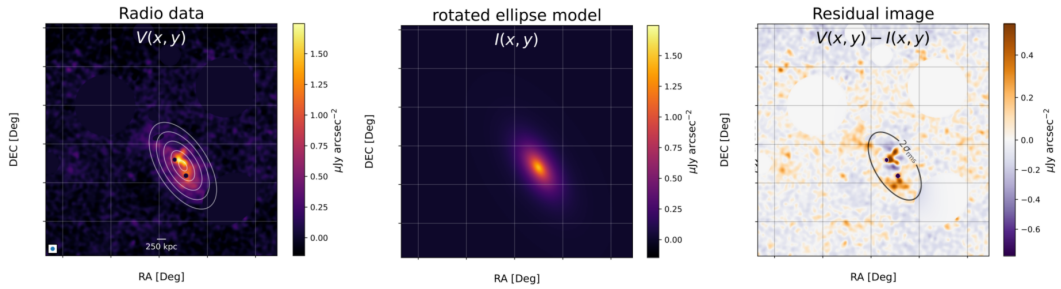

FIGURE 6.4: Result from the fitting procedure performed by `Halo-FDCA` on the radio halo in A2061. The residual from the extended radio emission in the NE extension is visible in the bottom panel.

I_0 [μJy arcsec^2]	x_0 [deg]	y_0 [deg]	r_x [kpc]	r_y [kpc]	ϕ [rad]
1.82	230.33	30.68	418.7	212.7	2.14
0.03	0.0015	0.0017	8.2	4.4	0.018

TABLE 6.2: `Halo-FDCA` best fit parameters (top row) and uncertainties (bottom row) for the radio halo in A2061. The model assumed to fit the radio halo is a rotated ellipse, which has six free parameters. The reduced χ^2 of the best fit is 1.1.

origin of the extended emission. The measured excess might indicate that the emission we observe in the NE extension has a different origin than the radio halo, and could be classified as a radio bridge. We will investigate these possibilities using X-ray data.

X-ray

We perform a similar study of the X-ray profile of A2061 with *XMM-Newton* data to check whether there is an excess emission corresponding to the radio excess.

We extracted the X-ray profile following the radio emission, starting from the same center as the radio halo and covering the X-ray plume. *XMM-Newton* observations field of view extends beyond the X-ray plume, allowing a comparison between the radio emission and the X-ray in the NE extension. We extract the X-ray profile also in a different sector, slightly offset from the plume and reaching the same distance from the center. The extracted X-ray band radial profile is shown in Fig. 6.3 (right panels). We note how the profile extracted in the NE extension shows an evident 'bump' at a distance of $\sim 11'$ from the halo center, which corresponds to the emission from of the X-ray plume. Interestingly, beyond the X-ray plume the profile shows an excess of emission with respect to the background level at larger radii. Compared with another sector, we find that in an offset direction from the NE extension the X-ray profile is monotonically decreasing and, at the same radii, is consistent with the background level. In the scenario where the X-ray plume is

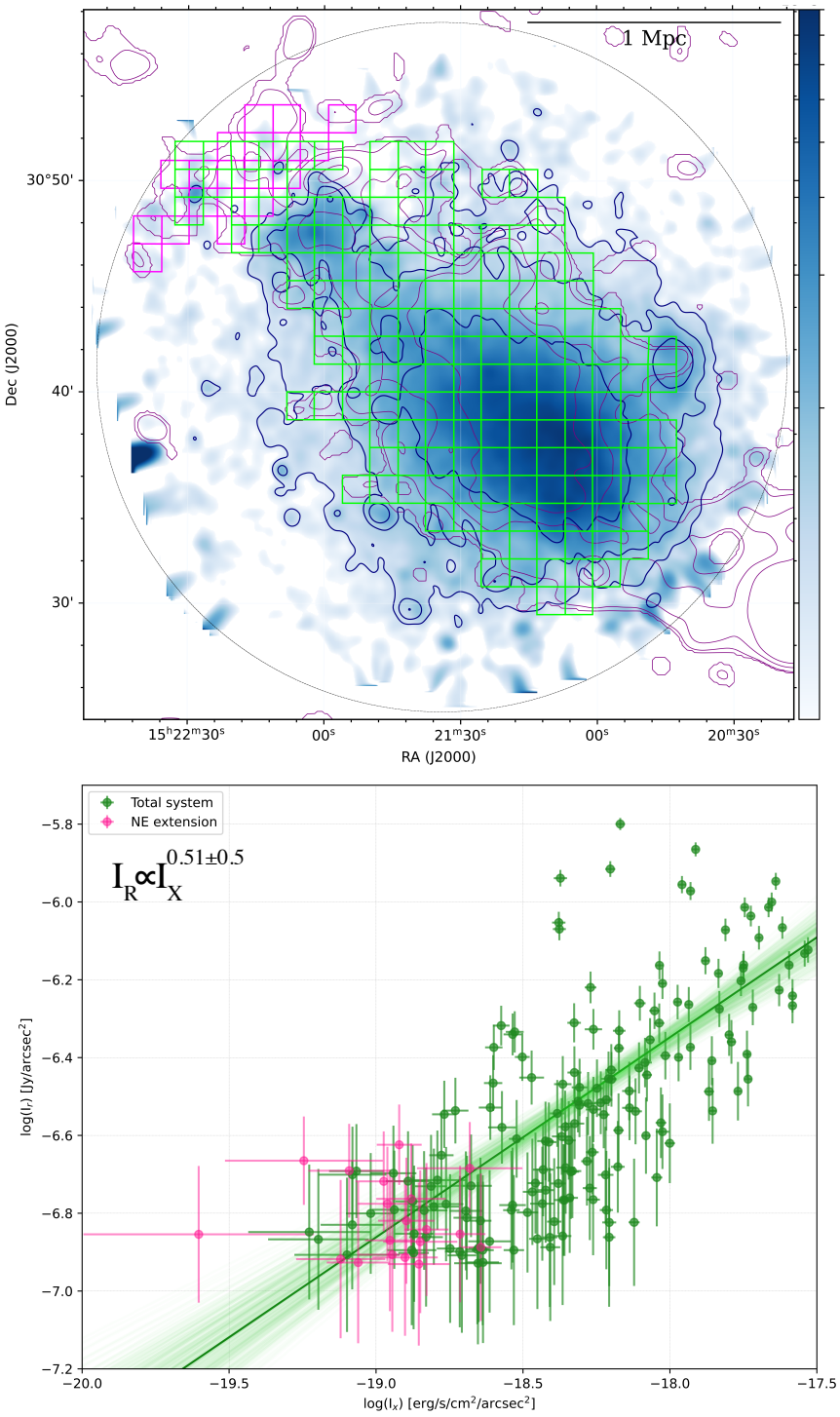

FIGURE 6.5: Point-to-point I_R/I_X correlation for A2061. *Top panel*: Colourscale is the *XMM-Newton* surface brightness smoothed image, after subtraction of point-sources. Radio contours at 144 MHz (80″ resolution) are shown in purple. The regions used to extract the surface brightness for the I_R/I_X correlation are 80″ wide boxes. The green boxes cover the entire object, while magenta boxes are only over the radio emission beyond the X-ray plume. *Bottom panel*: Radio/X-ray surface brightness correlation. The green solid line indicates the best-fit power-law relation for the green points. The slope of the green correlation is reported in the top right corner. The magenta points, relative to the NE extension, show no correlation.

residual thermal gas left behind by an infalling group (Marini et al., 2004), the radial profile shows that the excess is likely not connected with this gas, since we see a clear drop of the emission brightness between the plume and the extension. This excess might instead indicate the presence of thermal filamentary gas, however the limited field of view of the X-ray image does not allow to investigate the properties of the emission at larger distances from the center. An additional *XMM-Newton* pointing covering the separation between the two cluster, will help with a definitive conclusion on the nature of this trend. The infalling group-scenario will be further discussed in Sec. 7.4.

6.3.2 Point-to-point analysis

We are interested in studying the link between the diffuse radio emission and X-ray emission of the thermal plasma, that are found to be spatially aligned at the center of galaxy clusters. Past works have shown that this link can be described by a correlation of the form $I_R \propto I_X^b$ (e.g. Govoni et al., 2001; Rajpurohit et al., 2021b). The slope of this correlation between the X-ray and the radio surface brightness of diffuse emission in galaxy clusters provides important information on the acceleration mechanism at work (for a review, see Feretti et al., 2012; Brunetti and Jones, 2014). Moreover, the spatial distribution of the correlation can reveal the presence of different environments and emission powered by different physical mechanism, as shown in Bonafede et al. (2022) for the radio halo in the Coma cluster, in Rajpurohit et al. (2023) for Abell 2256 and in Biava et al. (2021) for the mini-halo in RXC J1720+2638. Several studies investigated disturbed galaxy clusters, where generally the correlation results to be sub-linear (see e.g., Hoang et al., 2019; Bonafede et al., 2022; Riseley et al., 2022; Riseley et al., 2024), implying a stronger decline of the X-ray emission than the non-thermal surface brightness. In the case of A2061, we can extend the investigation of the correlation to the NE extension.

In order to investigate the correlation, we used the $80''$ resolution, compact source-subtracted radio maps at 144 MHz and the point source-subtracted *XMM-Newton* image. We covered the entire *XMM-Newton* field-of-view of A2061 with a grid of square boxes of $80''$, therefore covering the cluster and the NE extension. We only consider the boxes where the radio surface brightness is above the $2\sigma_{rms}$ level. For comparison, we also perform the analysis over the NE extension area only. The result for the I_R / I_X correlation are shown in Fig. 6.5.

In the case of the total system, the two components appear mildly correlated, with Spearman (r_S) and Pearson (r_P) coefficients of $r_S = 0.73$ and $r_P = 0.71$, respectively. Considering the NE extension region, where we only have 19 points, we do not find evidence of correlation, with $r_S = r_P = -0.06$. We can quantify the slope of the correlation in the entire system fitting a power-law relation in log-log space in the form:

$$\log(I_R) = a + b \log(I_X). \tag{6.3}$$

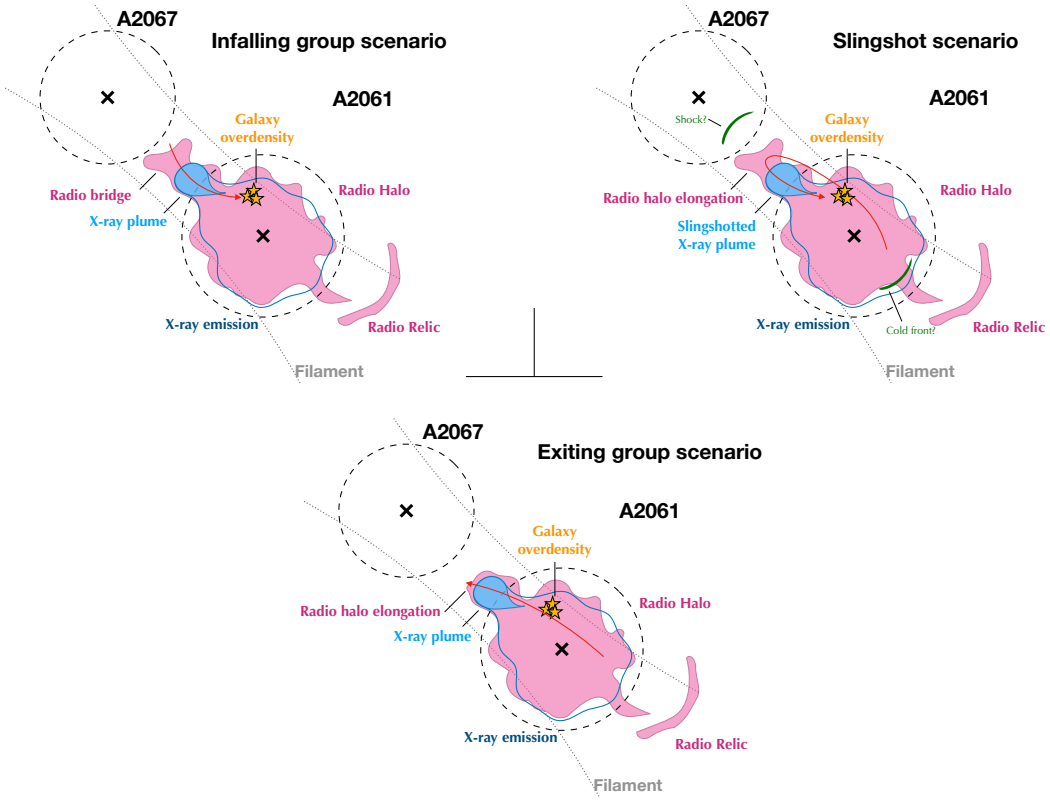

FIGURE 6.6: Schematic representation of the three different dynamical scenarios investigated in this work to explain the NE extension emission.

To perform the fit we use the Bayesian regression MCMC method implemented in `Linmix` (Kelly, 2007) as recently done in, e.g., Riseley et al. (2024); Riseley et al. (2022); Rajpurohit et al. (2021); Rajpurohit et al. (2021). The fitting procedure yields a best-fit slope of $b = 0.51 \pm 0.05$, showing an overall sub-linear correlation. If we remove the points over the NE extension from the total system, we find very similar correlation and best fit, with a slope of $b = 0.54 \pm 0.05$. The connection between thermal and non-thermal emission over the NE extension area remains unclear. It is possible that a better X-ray coverage of the inter-cluster region could reveal a mild correlation. We discuss these findings in relation of three different scenarios to explain the NE extension emission.

6.3.3 The radio halo and the NE extension

The LOFAR observations presented in this work are able to detect both the giant radio halo, the radio relic and the trail in A2061, recently confirmed in Botteon et al. (2022), with the additional detection of large-scale diffuse emission extending towards A2067. In Farnsworth et al. (2013), they observe diffuse emission in A2067 offset from the X-ray peak, tentatively classified as a radio relic, that is connected to the radio halo in A2061 with a filamentary feature. The elongation is present also in Botteon et al. (2022) images. Our new LOFAR observations confirm the presence

of such emission, extending for $\sim$ 800 kpc between the radio halo in A2061 and A2067, of which an additional $\sim$ 350 kpc component in the NE direction is unveiled with respect to the previous LoTSS observations (Botteon et al., 2022). However, this emission does not fully connect the two galaxy clusters. The low resolution ($570'' \times 560''$) and limited sensitivity of the GBT-NVSS observations most likely resulted in a blending of the tails of unresolved radio sources present in A2067 - that were not included in the NVSS subtraction process - which was interpreted as a radio relic. We are able to resolve the sources, and the residual tails of the AGN are also shown in our maps, but there is no evidence of other extended emission in this cluster. Even re-convolving our images to the GBT resolution, the filamentary emission is still not connecting the two galaxy clusters.

Here, we discuss three possible scenarios to explain the NE extension emission (see Fig. 6.6):

- **Infalling group scenario:** initially, the extension towards the NE was interpreted as possibly related to the X-ray plume. According to Marini et al. (2004), the plume can be attributed to a group of galaxies arriving from the NE, infalling in A2061. As a consequence of the impact, the galaxies of the group precede its intracluster medium, and are observed as an overdensity in the bidimensional galaxy distribution (see Fig. 6.7, also Marini et al., 2004). In this case, the NE extension could be classified as a radio bridge.

- **Slingshot scenario:** a slingshot X-ray tail can be formed as a (secondary) sub-halo moves away from the (primary) cluster center toward the apocenter of its orbit (Poole et al., 2006; Markevitch and Vikhlinin, 2007; Sheardown et al., 2019). In this scenario, a galaxy group might have already completed a first passage, and it is now approaching for a second infall from NE. Therefore, in this case the X-ray plume can be explained as the slingshotted gas tail of the re-entering group, and the NE extension as an elongation of the radio halo caused by the passage of the group. There are only few examples of observational features in galaxy clusters that can be explained by the slingshot effect, for example in Abell 168 (Hallman and Markevitch, 2004), in the Fornax Cluster (Sheardown et al., 2018), and in the Coma Cluster (Lyskova et al., 2019; Lal et al., 2022). In this scenario, simulations presented in Sheardown et al. (2019) predict the possible presence of a shock at large distances behind the secondary tail, and/or the presence of a cold front in the primary cluster, attributed to the sloshing in the core caused by the passage of the secondary (Akamatsu et al., in prep.).

- **Exiting group scenario:** in this case, a sub-halo might be moving from the South-West direction, crossing the cluster and causing the elongated shape in the radio halo as it exits on the opposite side (see e.g. Donnert et al., 2013; Beduzzi et al., 2024). From simulations results, in this scenario the extended

radio emission from the radio halo would be, at best, completely co-spatial with the X-ray plume.

Our observations, compared with X-ray maps, show that the radio emission is far more extended towards A2067, beyond the X-ray plume, as seen both by ROSAT (Fig. 6.1) and *XMM-Newton* (Fig. 6.3, right panels), disfavouring the exiting group scenario. The radio surface brightness profiles presented in Sec. 6.3.1 show that the surface brightness measured outside 2.5 e-folding radii in the NE direction significantly deviates from the analytical radio halo profile (Fig. 6.3, left panels). While some deviations between model and real data in disturbed radio halos are expected (Botteon et al., 2023), the excess appears to be systematic at large radii. Moreover, the X-ray radial profile in the same direction (Sec. 6.3.1) shows a similar trend beyond the X-ray plume location, where a significant excess over the background is detected (Fig. 6.3, right panels). Theoretically, in the early stages of a merger, we can expect enhancements of the gas density between approaching clusters, which, in turn, could be detected as an X-ray excess (Machado et al., 2024). Since this source extends along the merger axis, it may be related to the underlying filament connecting the two galaxy clusters. The filament volume can undergo a significant level of Fermi II re-acceleration by solenoidal turbulence motions injected in the early stages of the merger process, provided that the medium hosts a pool of mildly relativistic electrons ($\gamma \sim 10^3$), which is supported by recent simulations (Beduzzi et al., 2023). We have observational evidence of radio bridges between galaxy clusters in the early stages of merger (Botteon et al., 2018; Botteon et al., 2020; Govoni et al., 2019; de Jong et al., 2022; Pignataro et al., 2024a; Pignataro et al., 2024c), where the dynamics of the collapse drives transonic turbulence in the compressed intercluster gas (Brunetti and Vazza, 2020; Nishiwaki et al., 2024). The same acceleration processes could be at play in this case, with the additional amplification of turbulence brought by the merger of groups (Brunetti and Vazza, 2020), as we would expect in the infalling group scenario.

The case in which one of the two clusters does not host a radio halo, opens up a question on the definition of radio bridge. In the two most spectacular cases of radio bridges (Govoni et al., 2019; Botteon et al., 2020), the bridge fully connects the two radio halos at the center of the galaxy clusters. In this scenario, the lack of a radio halo in A2067 is likely the reason we observe a 'gap' of emission between the two clusters. Nonetheless, these system properties, such as the projected separation and the average emissivity of the diffuse emission, closely resembles the other two discovered bridges, as summarized in Table 6.3. In this view, the emerging population of low-surface brightness bridges might represent a more ubiquitous phenomena in merging clusters of galaxies, compared to the appearance of classical radio halos in their clusters. In fact, radio halos additionally require the presence of mergers within clusters (Brunetti and Lazarian, 2007; Brunetti et al., 2009; van Weeren et al., 2019), on top of the large-scale accretion motions that instead may power the radio emission in bridges (Brunetti and Vazza, 2020).

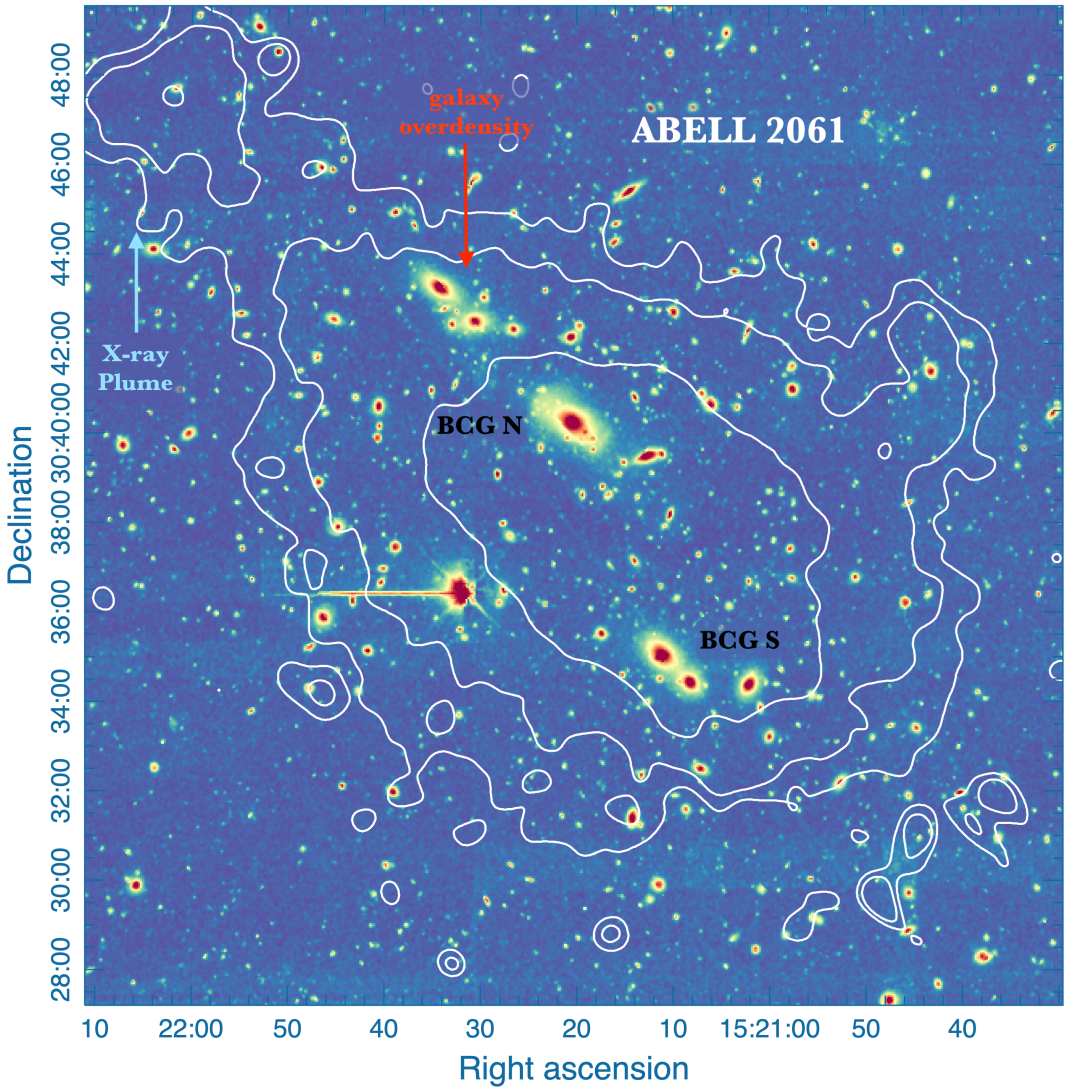

FIGURE 6.7: Optical image of A2061. Colourscale is Dark Energy Spectroscopic Instrument (DESI) Legacy Survey optical image of the galaxies in A2061. *XMM-Newton* contours are overlaid in white. In black we mark the location of the two BCGs, in red the location of a galaxy overdensity attributed to the infall of a group of galaxies (Marini et al., 2004), and in cyan the location of the X-ray plume.

System	$\langle z \rangle$	$\langle \epsilon_{144} \rangle$ [erg s^{-1} Hz^{-1}cm^{-3}]	$D_{centers}$ [Mpc]	M_{tot} [$M_\odot$]
A2061-A2067	0.076	4.5×10^{-43}	2.5	5×10^{14}
A399-A401	0.07	8.6×10^{-43}	3	1.5×10^{15}
A1758N-S	0.28	4.1×10^{-43}	2	3×10^{15}

TABLE 6.3: Comparison between the radio bridges discovered in A399-A401 (Govoni et al., 2019) and A1758N-S (Botteon et al., 2020) and the properties of the NE extension emission between A2061 and A2067. The first column is the average redshift of the system, the second column is the average radio emissivity at 144 MHz, computed assuming a cylindrical volume between the two clusters, the third column is the projected distance between the centers of the clusters, and the last column is the total mass of the system.

However, the radio/X-ray correlation investigated in Sec. 6.3.2 does not provide conclusive evidence. The similar scaling found including and excluding the NE extension emission seems to indicate a trend where the emission traces an extension of the radio halo, which could be the case in the slingshot scenario. In contrast, in the scenario of filamentary gas, we would expect a level of X-ray/radio correlation, as it has been found for the radio bridges in A399-A401 (de Jong et al., 2022) and A1758N-S (Botteon et al., 2020). In both cases, the X-ray observations allowed a full coverage of the bridge, and they are able to create a more extended grid in the bridge region. They both showed good correlation over the bridge, and nearly flat slopes for the correlation ($b \sim 0.25$, de Jong et al., 2022). In this case the limited field of view of the *XMM-Newton* observation does not allow to reach a firm conclusion on the presence and nature of thermal gas in the inter-cluster region. Additionally, assuming a slingshot scenario, for a system that has likely underwent a history of merger with more than one sub-halo, as it is suggested by the disturbed morphology and the presence of multiple BCGs in A2061 (Fig. 6.7, Hill and Oegerle 1998), it is not straightforward to attribute all dynamical features in the primary core to only a secondary halo (Sheardown et al., 2019).

As a result of our current analysis, we are not able to firmly favour the infall group scenario or the slingshot scenario. Therefore, the classification of the NE extension remains open, as it could be described either as a radio bridge or a natural extension of the radio halo. For the NE extension, outside A2061 R_{500} we measure an integrated flux density of $S_{144}^{2\sigma} = 52 \pm 5.0$ mJy. To confirm the classification, it would require a spectral analysis with multifrequency radio detections, and a complementary X-ray/radio point-to-point analysis with a X-ray pointing covering the entire inter-cluster separation, as well as simulations that can help distinguish between the two most likely dynamical scenarios.

6.3.4 The radio relic and trail

Finally, we discuss the other sources of diffuse emission in A2061, the radio relic and the trail.

The presence of the radio relic was confirmed by WSRT observations at 1.38 and 1.7 GHz (van Weeren et al., 2011). In their work, they fit the spectrum of the radio relic with a single power-law between 327 MHz, 1.38 and 1.7 GHz. However, the 327 MHz flux measurement is uncertain (Rudnick and Lemmerman, 2009). To better constrain the spectral index, we measure the flux density of the radio relic at 144 MHz from our observations. We used an image at resolution of 30″, similar to the resolution of the high frequency images (32″ × 15″). At this resolution, we measure for the relic a largest-linear-size (LLS) of $\sim$ 790 kpc inside the $5\sigma_{rms}$ level. The integrated flux density of the relic was computed in the same polygonal region encompassing the 3σ contour of the diffuse emission at 1.38 GHz used in van Weeren et al. (2011). We measure a flux density of $S_{144} = 220 \pm 22$ mJy, and find a spectral index $\alpha = 0.92 \pm 0.05$, consistent with the one derived by van Weeren et al. (2011).

Another interesting source of diffuse emission in this system is the 'trail' of emission connecting the radio halo to the radio relic. This feature is extended with a LLS$\sim$ 700 kpc. Similar features of connected diffuse emission were also detected in several systems, most recently in A1550 (Pasini et al., 2022), in A3667 (Carretti et al., 2013; de Gasperin et al., 2022), and others (see e.g. Kim et al., 1989; van Weeren et al., 2012c; Rajpurohit et al., 2018; Bonafede et al., 2018; de Gasperin et al., 2020b). The most striking example of diffuse emission connecting a radio halo and a radio relic is the Coma cluster bridge (Bonafede et al., 2021), with a LLS of 940 kpc. These trails of diffuse emission are probably related to post-merger generated turbulence that re-accelerates particles previously accelerated by shocks (van Weeren et al., 2016b; Bonafede et al., 2021; Pasini et al., 2022). It is likely that the trail of emission in this system could have the same origin. For the trail between the radio halo and the relic in A2061 we measure an integrated flux density of $S^{2\sigma}_{144} = 49 \pm 5$ mJy inside the $2\sigma_{rms}$ contour level. All the radio quantities measured in this work for the sources in A2061 and the bridge are summarized in Table 6.4.

6.4 Conclusions

Using deep LOFAR HBA observations, we detected diffuse extended emission at 144 MHz between the dynamically interacting galaxy clusters A2061 and A2067, inside the Corona Borealis Supercluster. A2061 is a highly dynamically disturbed system, showing several sources of diffuse emission. The radio halo and the radio relic were already classified with previous radio observations (Farnsworth et al., 2013; van Weeren et al., 2011; Botteon et al., 2022). With new 16 hours of observations at 144 MHz, we are able to detect a source of emission extending for $\sim$ 800 kpc from the radio halo in A2061 towards A2067. We find no evidence of a radio halo in A2067.

	LLS [kpc]	Flux [mJy]	P_{144} [W/Hz]	Spectral index* [α]
NE extension	800	52±5.0	(8.1±0.8)e23	1.4
Radio Halo	1300	265±26	(4.1±0.4)e24	1.3
Radio Relic	790	220±22	(3.3±0.3)e24	0.92±0.05
Trail	760	49±5.0	(7.5±0.8)e23	1.4

TABLE 6.4: Summary of the radio quantities measured for the diffuse sources in A2061. The NE extension and trail quantities are measured on the $2\sigma_{rms}$ contours of the 80″ resolution map. The radio halo quantities are measured on the $6\sigma_{rms}$ contours of the 80″ resolution map. The radio relic quantities are measured on the 30″ resolution map (see text). *Value of the spectral index assumed for the radio power calculation (except the radio relic, which is derived in Sec. 6.3.4). The assumed value for the bridge and trail is based on literature works (Pignataro et al., 2024a; Bonafede et al., 2021).

The results of our radio and X-ray analysis on the NE extension can be summarized as follows:

- From the study of the radio surface brightness radial profile, we find that the NE extension emission deviates from the analytical model for the radio halo in A2061.
- From the study of the X-ray surface brightness radial profile, we find an excess of emission over the background level, which is co-spatial with the radio emission in the extension. This excess is not measured in a different direction, at the same radii, where we measure the expected decline of the X-ray profile.
- From the point-to-point radio-X correlation, we find mild correlation between thermal and non-thermal emission, measured over the total system. The NE extension only does not show any clear correlation.

From these results, we investigate three different dynamical scenarios that can help classify the emission in the NE extension. In the exiting group and slingshot scenario, the diffuse emission can be classified as an elongation of the radio halo, while in the infalling group scenario, the emission can be classified as a radio bridge. Our analysis disfavour the exiting group scenario, while can not firmly confirm the infalling group or slingshot scenarios. The system closely resembles the two other systems were the presence of a radio bridge is confirmed (Govoni et al., 2019; Botteon et al., 2020), yet the absence of a radio halo in one of the two clusters makes this cluster pair unique at the moment. Further analysis will help clarify the on-going dynamical processes in A2061, and therefore understand the nature of the diffuse emission between the two galaxy clusters.

Chapter 7

Detection of Magnetic Fields in Superclusters of Galaxies

7.1 Introduction

In Chapter 1, we have explained how the matter distribution of the Universe on megaparsec scale is not uniform and random, but it is ordered inside the Cosmic Web (Bond, Kofman, and Pogosyan, 1996), in a network of nodes and low density filaments. In recent years, several studies tried to constrain the strength of magnetic fields in filaments with different approaches, as overviewed in Sec. 1.3.2. All these studies are of key importance for understanding the magnetogenesis scenarios for our Universe (Durrer and Neronov, 2013; Subramanian, 2016), because the filaments environment still preserves the memory of the initial conditions, while being more detectable than voids (Vazza et al., 2017; Mtchedlidze et al., 2022). The investigation of low-density environments magnetic fields can help distinguish between two main models: primordial scenarios and astrophysical scenarios (see Sec. 2.3.1). One way to identify the location of filaments is to search for supercluster of galaxies: these are nested within the Cosmic Web, creating a coherent structure of galaxy clusters embedded in a network of filaments spanning up to hundreds of Mpc (Lietzen et al., 2016; Bagchi et al., 2017).

In Chapter 2, we have reviewed the physics of polarization and how we can use the Faraday RM of background polarized sources to infer the magnetic properties of the medium crossed by the polarized emission. In this work, we define a robust method to exploit the currently available RM Grids and catalogs of superclusters of galaxies to investigate the nature of the magnetic fields in the lower-density environments inside the supercluster boundaries.

7.2 Observations and dataset

In this section, we describe the different datasets that were used in this work.

Name	MSCC-ID	RA, Dec [deg, deg]	$< z >$	N_{mem}	N_{Cl}	V_{box} [$10^3\ h_{70}^{-3}$ Mpc^3]	V_{fil}/V_{box} [%]
Corona Borealis	463	232.18, 30.42	0.073	226	14	959.2	1.1
Leo	278	169.37, 28.34	0.033	115	6	459.3	1.6
Hercules	474	241.56, 16.22	0.036	90	5	343.8	0.9

TABLE 7.1: MSCC superclusters properties. We list the superclusters selected for this study (1) names, (2) their MSCC-ID (Chow-Martínez et al., 2014) , (3) their coordinates (J2000), (4) the mean redshift, (5) the total number of members, (6) the number of Abell/ACO clusters, (7) the volume of the box containing the SDSS galaxies, and (8) the filling factor of filaments as found in Santiago-Bautista et al. (2020).

7.2.1 Selection of superclusters of galaxies

This work is based on the selection of polarized sources for which we have an RM value, in the line of sight of superclusters of galaxies. We based this study on the LoTSS RM Grid (O'Sullivan et al., 2023), which is sensitive to small RM, therefore we select nearby ($z \leq 0.1$) superclusters in the Northern sky that are covered, at least partially, by LoTSS observations. We chose to analyse three rich superclusters: *Corona Borealis*, *Leo*, and *Hercules*. These three superclusters are part of the all-sky Main SuperCluster Catalogue (MSCC, Chow-Martínez et al., 2014), which is a catalogue of 601 superclusters created with the combination of a compilation of the rich Abell clusters (Andernach et al., 2005) and spectroscopic redshifts for galaxies in the SDSS-DR7 (Abazajian et al., 2009). With a tunable Friends-of-Friends algorithm, Chow-Martínez et al. (2014) are able to provide a full list of the cluster members with their redshift, coordinates and supercluster membership out to a redshift of z=0.15. This catalogue was further expanded by the analysis of Santiago-Bautista et al. (2020), where they select 46 MSCC clusters to map the elongated structures of low relative density inside each supercluster and they employ optical galaxies with spectroscopic redshifts from the SDSS-DR13 (Albareti et al., 2017). The SDSS galaxies are selected inside a volume of a box with 'walls' set to a distance of 20 h_{70}^{-1} Mpc from the center of the farthest clusters in each direction, for each supercluster (Santiago-Bautista et al., 2020). Therefore, with this catalogue we are able to map the galaxy density over the supercluster volume as well as to recover the redshift, virial radius, and location of each supercluster member (clusters and groups of galaxies). The properties of the selected superclusters, as reported in Santiago-Bautista et al. (2020), are summarized in Table 7.1, and the nominal location of each supercluster member on the sky is shown in Fig. 7.1.

7.2.2 RM Grids

Faraday rotation measure grids are a valuable tool to study the origin and evolution of cosmic magnetism, in particular by measuring the properties of extragalactic magnetic fields (Vernstrom et al., 2019; O'Sullivan et al., 2019). In this particular framework, we observe linearly polarized radio sources across a particular area of

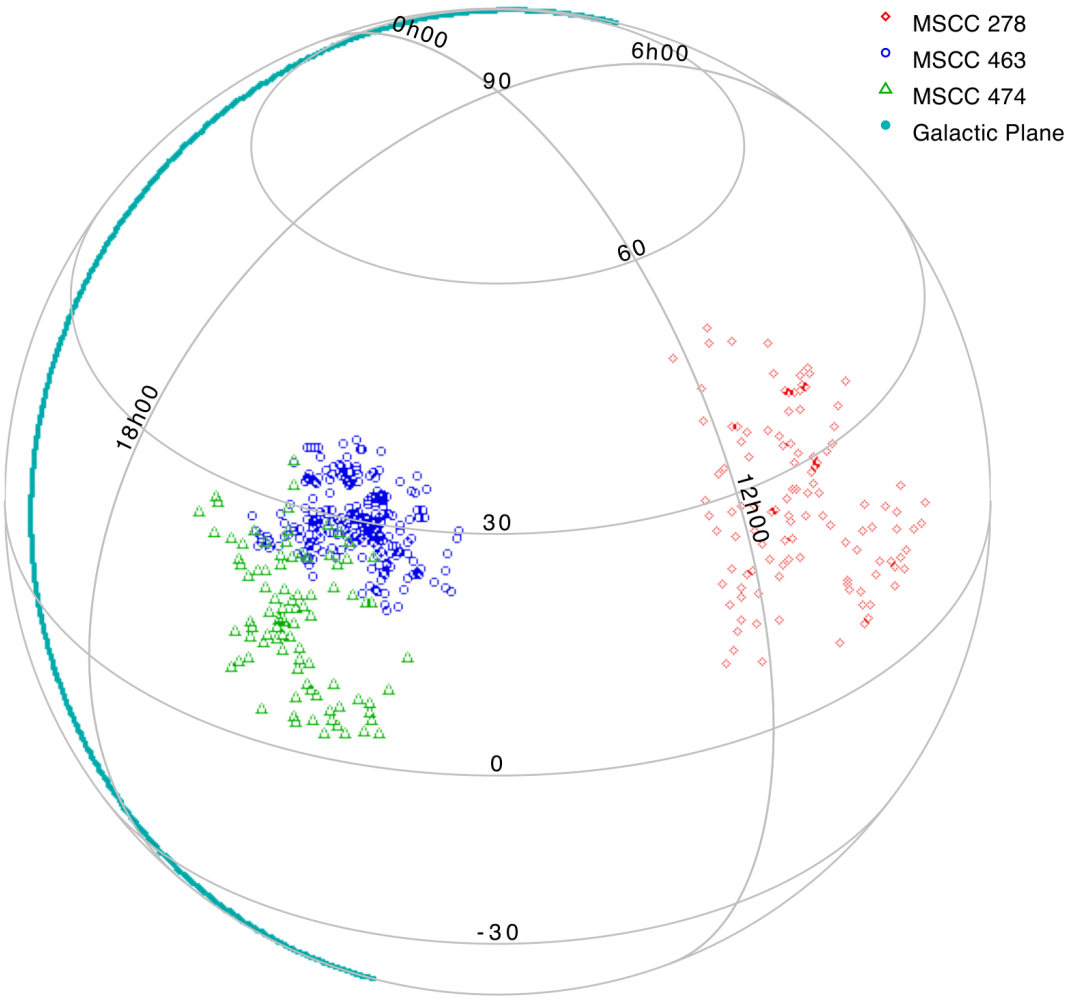

FIGURE 7.1: Sky distribution of the supercluster members in each supercluster in equatorial reference system.

the sky, covered by the extension of a nearby supercluster, to investigate the Faraday rotation properties of the low-density, large-scale environments. To do this, we are mainly interested in the RM variance generated by the variations of the Faraday rotating medium along different lines of sight, either due to the intergalactic or local media. To isolate this component, it is necessary to remove the Galactic contribution from the Milky Way, and the errors introduced by the measurements. The RM variance has been investigated extensively with the 37543 RM values from the NRAO VLA Sky Survey data (NVSS, Condon et al., 1998; Taylor, Stil, and Sunstrum, 2009) at 1.4 GHz, to characterize both the Milky-Way properties (e.g. Purcell et al., 2015; Hutschenreuter and Enßlin, 2020), and to isolate the RM variance contribution local to the source itself (Rudnick and Blundell, 2003; O'Sullivan et al., 2013; Anderson et al., 2018; Banfield et al., 2019; Knuettel et al., 2019).

RM studies at metre wavelengths offer a significant advantage over centimetre wavelength observations due to a better RM accuracy and sensitivity to low RM values. The accuracy of Faraday rotation measurements is directly related to the wavelength-squared coverage, thus RM studies at metre wavelengths provide substantially higher accuracy for individual RM measurements (Neld et al., 2018; O'Sullivan et al., 2018; Van Eck et al., 2018). Despite this, identifying linearly polarized sources at long wavelengths presents its own challenges, primarily requiring high angular resolution and high sensitivity to counteract the significant effects of Faraday depolarization which results in a smaller fraction of radio sources exhibiting detectable polarization levels (e.g., Farnsworth, Rudnick, and Brown, 2011; Bernardi et al., 2013; Lenc et al., 2017). LOFAR is addressing these challenges effectively with its capability to produce high-fidelity images at high angular resolution (Morabito et al., 2016; Jackson et al., 2016; Harris et al., 2019; Sweijen et al., 2022). Additionally, the LOFAR wide field of view and large instantaneous bandwidth facilitate the efficient surveying of large sky areas, aiding the detection of numerous linearly polarized sources and their RM values. The LoTSS-DR2 RM Grid (O'Sullivan et al., 2013) has produced a catalogue of 2461 extragalactic high-precision RM values. The integration of RM Grid catalogues from both metre and centimetre wavelengths is crucial for a more comprehensive understanding of the various contributors to Faraday rotation along the line of sight. We are interested in this combined approach, and we use of both the NVSS and LoTSS RM Grids to identify sources in the line of sight of our selected superclusters. The three superclusters have different extensions on the sky. We select all sources inside a circle of radius 19° centered on each supercluster position. We check for duplicates between NVSS and LoTSS RM sources, and also take into account the slight overlap between Corona Borealis and Hercules on the plane of the sky, which could introduce a number of additional duplicates. The duplicated RM were removed from the NVSS catalogue and kept in LoTSS catalogue, leaving us with 3679 RM values from the NVSS and 579 RM values from the LoTSS DR2 Grid. For the 3679 NVSS RMs, we recompute their overestimated errors σ_{RM}^{NVSS} reported in Taylor, Stil, and Sunstrum (2009), following the equation of

Vernstrom et al. (2019)

$$\sigma_{RM}^{NVSS} = 150 \frac{\sqrt{2}\sigma_P}{P} \text{ rad m}^{-2}, \tag{7.1}$$

where P is the polarized intensity of the source and σ_P the associated error.

7.2.3 Source selection from non-DR2 fields

The selected superclusters are very extended across the sky, in particular Hercules (ID 474) and Leo (ID 278) can reach a Declination as low as $+3°$ (see Fig. 7.1). The LoTSS-DR2 sky area imaged in polarization covers 5720 deg^2 and it is split between two fields centred at 0^h and 13^h respectively, down to a Declination of approximately $+15°$ (Shimwell et al., 2019a; O'Sullivan et al., 2023). Therefore, part of these superclusters are not covered by the DR2. To improve the statistics and to find additional linearly polarized sources to probe the supercluster environments, we analysed an additional 177 LoTSS pointings not included the publicly available DR2 sky area. These RMs will form part of the LoTSS DR3 RM Grid data release. The analysis of the additional pointings follow the same procedure used to create the LoTSS-DR2 RM Grid, as reported in O'Sullivan et al. (2023). Here, we report the main steps:

- We used Stokes Q and U image cubes at $20''$ resolution and the Stokes I $20''$ resolution images and source catalogues (Williams et al., 2019; Shimwell et al., 2022a) from the LoTSS initial data products (Shimwell et al., 2019a; Tasse et al., 2021);
- The RM synthesis technique (Burn, 1966; Brentjens and de Bruyn, 2005) was applied on the Q and U images using `PYRMSYNTH`[1] with uniform weighting, for pixels where the $20''$ total intensity was greater than 1 mJy beam^{-1}. Initially, it is necessary to define a 'leakage' exclusion range between ± 3 rad m^{-2} to remove the contamination of the instrumental polarization. The leakage peak occurs intrinsically at 0 rad m^{-2} with a degree of polarization of $<\sim$ 1% of the Stokes I intensity (Shimwell et al., 2022a), but it is shifted by the ionospheric RM correction by 1 rad m^{-2}(Sotomayor-Beltran et al., 2013). Outside this range, we identify the peak polarized intensity for each pixel in the output cube of the Faraday dispersion function (FDF) or Faraday depth spectrum.
- We estimated the noise σ_{QU} and initially consider the Faraday depth (i.e. the RM) value corresponding the polarized intensity peaks in the FDF larger than $5.5\sigma_{QU}$ from the rms of the wings of the real and imaginary parts of the FDF ($\phi < -100$ rad m^{-2} and $\phi > 100$ rad m^{-2}). Finally, an RM image, a polarized intensity image and a degree of polarization map were created. From the polarized intensity image, all pixels within a box of 20×20 pixels and above the selected noise threshold, were grouped together. The highest signal to noise pixel in this group is the catalogued RM value and sky position of this source component.

[1] https://github.com/mrbell/pyrmsynth

An initial review of the catalogued sources revealed that many bright sources detected at small Faraday depths with very low degree of polarization were likely instrumental peaks extending beyond the previously excluded leakage range. Consequently, to eliminate many of these sources we extended the leakage range to -5 rad m^{-2} $< \phi <$ $+5$ rad m^{-2} and excluded those sources falling in this range with fractional polarization smaller $p < 2\%$, or very high values $p > 30\%$. To be conservative, an $8\sigma_{QU}$ threshold was then applied following what is expected from false detection rates, which is as low as 10^{-4} at $8\sigma_{QU}$, against a possible 4% at $5\sigma_{QU}$ (George, Stil, and Keller, 2012). After these additional cuts, we inspected the Faraday spectra of the remaining sources. From the visual inspection of the FDF and the signal-to-noise ratio (SNR) it is possible to find some unreliable RM values that fell out the cuts. In particular, we inspect the FDF of sources very close-to-the-acceptance threshold of $8\sigma_{QU}$, and check also the degree of polarization. An example of accepted and rejected source after the visual inspection of the Faraday spectrum is shown in Fig. 7.2. In this case, the rejected source satisfies the $8\sigma_{QU}$ criterium but the FDF shows the presence of several other peaks at a similar SNR level, making the detection unreliable.

The preliminary catalogue was then revised, and we noticed that some fields contained a high number of sources with very similar RM values and low polarization fraction. This is likely to be attributed to a '*transfer*' of polarized flux from a bright (> 10 mJy beam^{-1}) polarized source in the field, as it was noticed in the original compilation of the LoTSS-DR2 RM Grid (O'Sullivan et al., 2023). We therefore checked each field for this effect, and removed a total of 876 unreliable candidates from all fields.

After this step, we inspected also the maps produced after running the RM synthesis, and for each source we produced cut-outs to compare the RM map, the polarized intensity image, the degree of polarization map together with the Faraday spectrum and the NVSS 45″-resolution Stokes I and polarized intensity contours (see Fig. 7.3). In this last step of inspection, we excluded sources with very complex Faraday spectrum where the peak is not clearly identified and/or is located at a pixel clearly outside the source, as well as sources with highly inconsistent LoTSS-NVSS degree of polarization. This procedure excluded a few more sources. Finally, we removed duplicate sources from the NVSS, as done for the LoTSS-DR2 fields, keeping the RM value with higher SNR for LoTSS-LoTSS duplicates and LoTSS RM value for LoTSS-NVSS duplicates ($\sim$ 108 new LoTSS sources were also in the NVSS catalogue). The final non-DR2 catalogue contains 239 polarized source components, that are added to the analysis. Averaging together the three superclusters fields, we have a final catalog[2] with 3679 RM values from NVSS and 818 from LoTSS, for a total of 4497 polarized background sources.

[2]The catalog will be made available through Vizier.

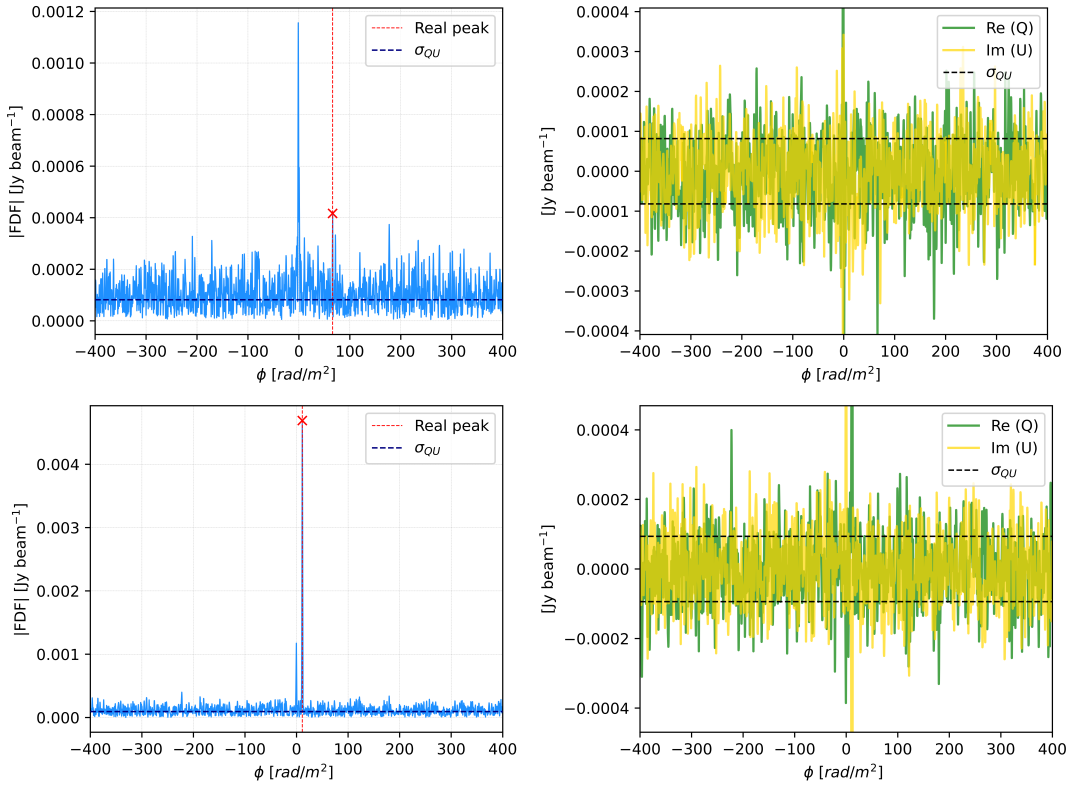

FIGURE 7.2: We show the absolute value of the Faraday spectrum (FDF, blue solid line) and the real (Q, green solid line) and imaginary (U, yellow solid line) components of the FDF, for two example polarized source components. The Q,U plots have restricted range on the y-axis, to better visualize the noise. The 'real' peak, i.e. the highest signal-to-noise polarized component outside the leakage range, is marked with a red cross. The leakage peak is noticeable in both cases at $\phi \sim 0$ rad m^{-2}. The rms noise (σ_{QU}) level is shown as a dashed line. After inspection, the top source at SNR$\sim$ 8 is excluded, while the bottom source, at SNR$\sim$ 40 is accepted.

7.3 Methods

7.3.1 Density maps

We used the final catalogue of polarized sources to study the supercluster medium by measuring the RM variance.

The RM variance is dependent on the free electron density, the line-of-sight magnetic field strength, and the magnetic field reversals that happen along the length of the path crossed by the radiation. Therefore, it is useful to relate the measured RM values to the density of the medium in the supercluster, and investigate which combinations of parameters will yield the observed variance. To limit the supercluster extent and estimate the density in each region, we have used the gas density profile of each supercluster member. For this work, we chose to use the Universal gas density profile for galaxy clusters presented in Pratt et al. (2022). Using XMM-Newton observations, they derive an average intracluster medium density profile

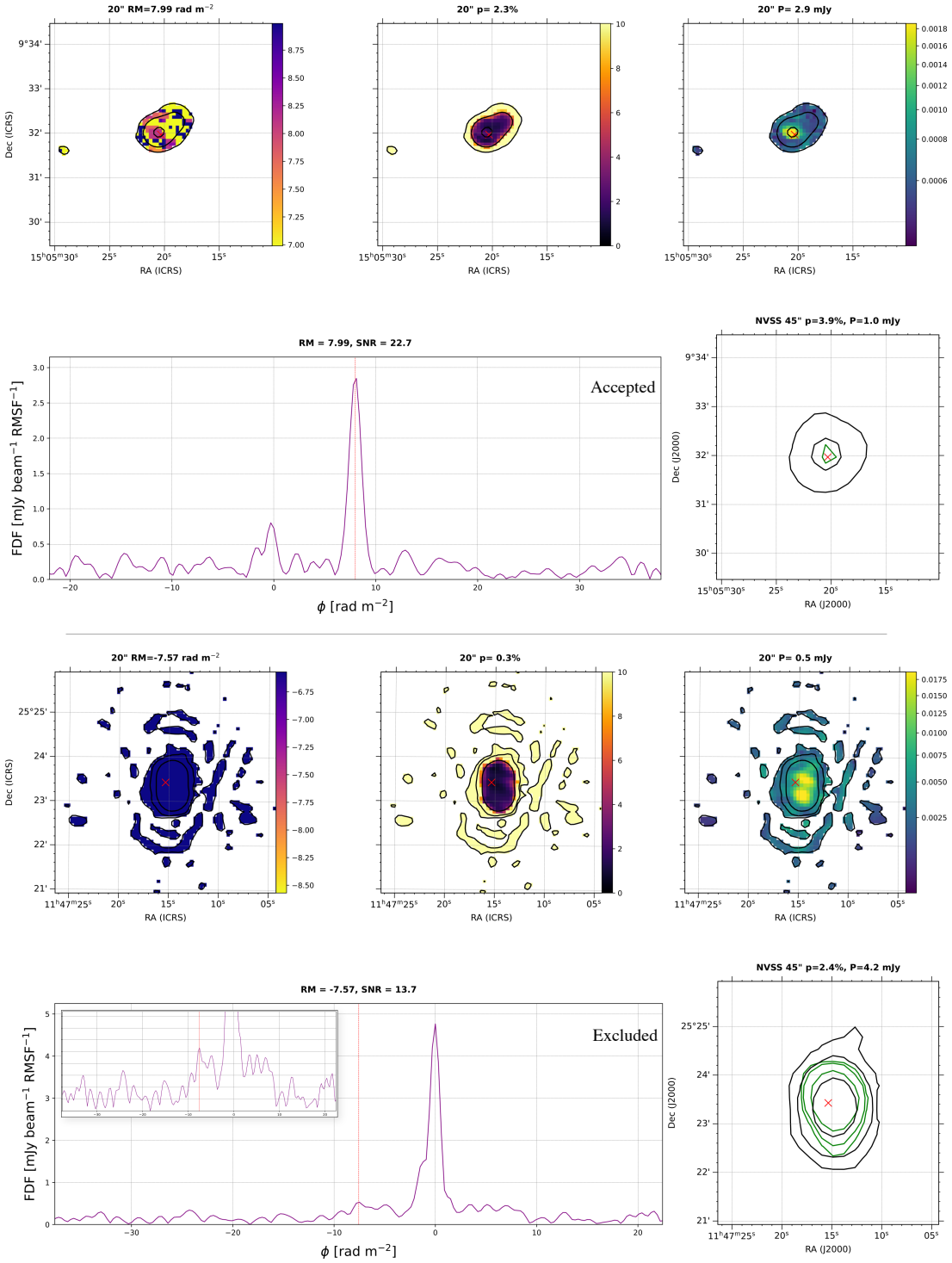

FIGURE 7.3: Inspection maps to evaluate the catalogued polarized source component. *Top row*: we show the LoTSS 20″ resolution RM map, degree of polarization map, and the polarized intensity map for the catalogued source inside the Stokes I contours (black). *Bottom row*: we show the FDF with the catalogued RM value and SNR for the peak, and the NVSS 45″ resolution Stokes I (black) and polarized intensity (green) contours for comparison. For the bottom source, the zoomed-in panel show the complexity of the spectrum around the selected peak. After inspection, the top source is accepted, while the bottom source is excluded.

for a sample of 93 Sunyaev-Zeldovich effect -selected systems and determine its scaling with mass and redshift. The median radial profile is a function of a scaled radius $x = R/R_{500}$, and is expressed as the product between a normalisation that can vary with the redshift z and the mass M_{500} (i.e. the total mass within the radius R_{500}, i.e. when the mean matter density is 500 times the critical density of the Universe):

$$\rho_m(x, z, M_{500}) = N(z, M500)\, f(x), \tag{7.2}$$

where $f(x)$ has the shape of a generalised Navarro-Frenk-White (GNFW) model (Nagai, Kravtsov, and Vikhlinin, 2007):

$$f(x) = \frac{f_0}{\left(\frac{x}{x_s}\right)^{\alpha}\left[1+\left(\frac{x}{x_s}\right)^{\gamma}\right]^{\frac{3\beta-\alpha}{\gamma}}} \tag{7.3}$$

where x_s is the scaling radius, and the parameters α, β, γ are the slopes at $x \ll x_s$, at $x \gg x_s$, and at $x \sim x_s$, respectively. The normalisation is given by the product of f_0 and

$$N(z, M_{500}) = E(z)^{\alpha_z}\left[\frac{M_{500}}{5\times 10^{14} M_{\odot}}\right]^{\alpha_M}, \tag{7.4}$$

where $E(z)$ is the evolution of the Hubble parameter with redshift in a flat cosmology. A complete description of the fitting procedure to the 93 SZ-selected system can be found in Pratt et al. (2022), while here we only report the best-fit model parameters:

$$\begin{aligned} f_0 &= 1.20 \pm 0.15, \\ x_s &= 0.28 \pm 0.01, \\ \alpha &= 0.42 \pm 0.06, \\ \beta &= 0.78 \pm 0.03, \\ \gamma &= 1.52 \pm 0.16, \\ \alpha_z &= 2.09 \pm 0.02, \text{ and} \\ \alpha_M &= 0.22 \pm 0.01. \end{aligned} \tag{7.5}$$

The deprojected density profile with the best-fit parameters is applied to each supercluster member and computed radially for each element in a 3D cube of axis (RA, Dec and z). We zero-padded the density profile at distances $\geq 10\ R_{500}$ from each cluster center. With this approximation, we are treating all members as galaxy clusters, including small groups of galaxies down to five members; in this way, while the contribution of the smallest systems will be of low impact on the density at large distances from their centers, it helps trace the large-scale structure of the supercluster. We are not implementing an additional density component for the filaments between clusters (see Sec. 7.4).

A schematic representation of the output density cube for a supercluster is shown in Fig. 7.4. The construction of the density cubes for each supercluster allows us to

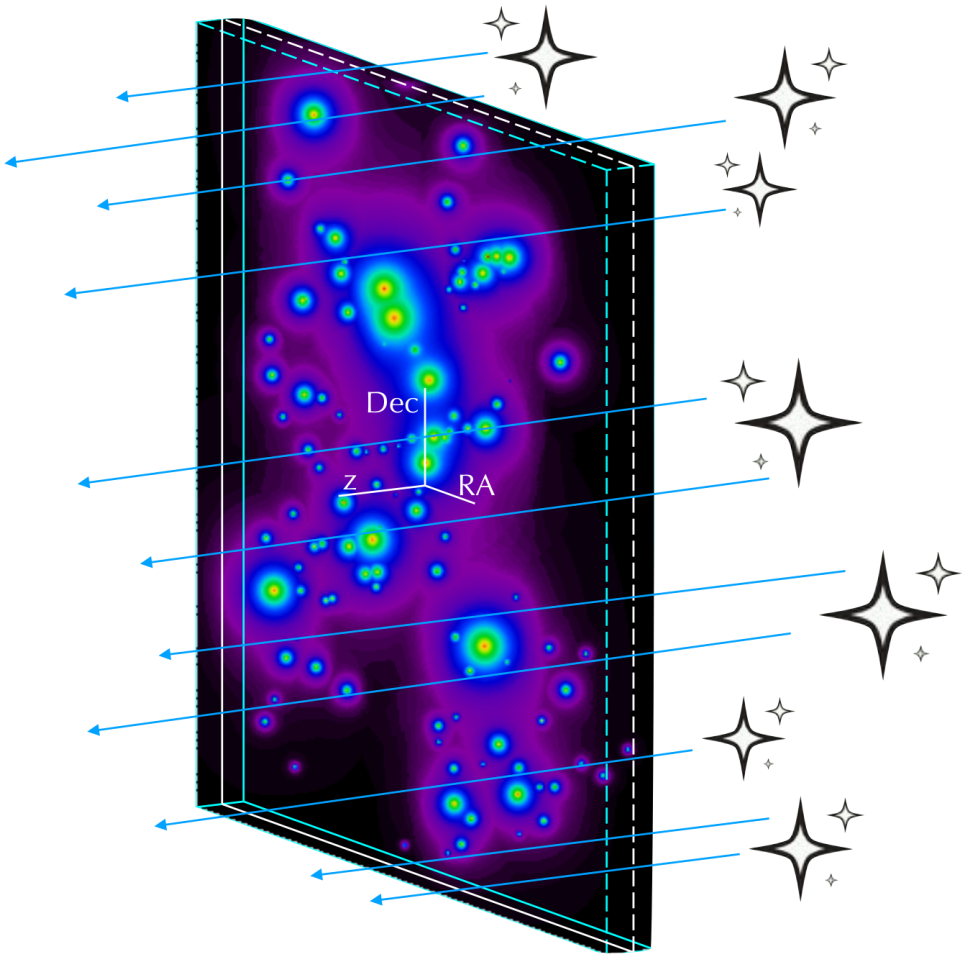

FIGURE 7.4: Simulated 3D density cube with a schematic representation of the background sources.

describe the boundaries of the supercluster and investigate whether the radiation from the selected polarized background sources is crossing regions of high or low mean density, inside or outside the supercluster. Therefore, we computed a mean density $\overline{\rho}$ along the direction of each radio source, averaged over the redshift interval of each cube, that allows us to bin the sources in different density regimes. A two-dimensional representation of the density maps for each supercluster is shown in Fig. 7.5, Fig. 7.6, and Fig. 7.7. It is noticeable how the sources found at 144 MHz have a smaller areal number density (0.43 deg^{-2}, O'Sullivan et al. 2023) with respect to the ones found at 1.4 GHz ($>$ 1 deg^{-2}, Taylor, Stil, and Sunstrum 2009). At both frequencies, sources are rarer in the highest density regions, with $\sim$ 10% and $\sim$ 13% of the total number of sources found at mean densities $>\sim 10^{-27.5}$ g cm^{-3}, at 144 MHz and 1.4 GHz respectively (see Sec. 7.4.1). This is to be expected, due to the strong effect of Faraday depolarization in galaxy clusters that is more important at lower frequencies (O'Sullivan et al., 2019; Carretti et al., 2022).

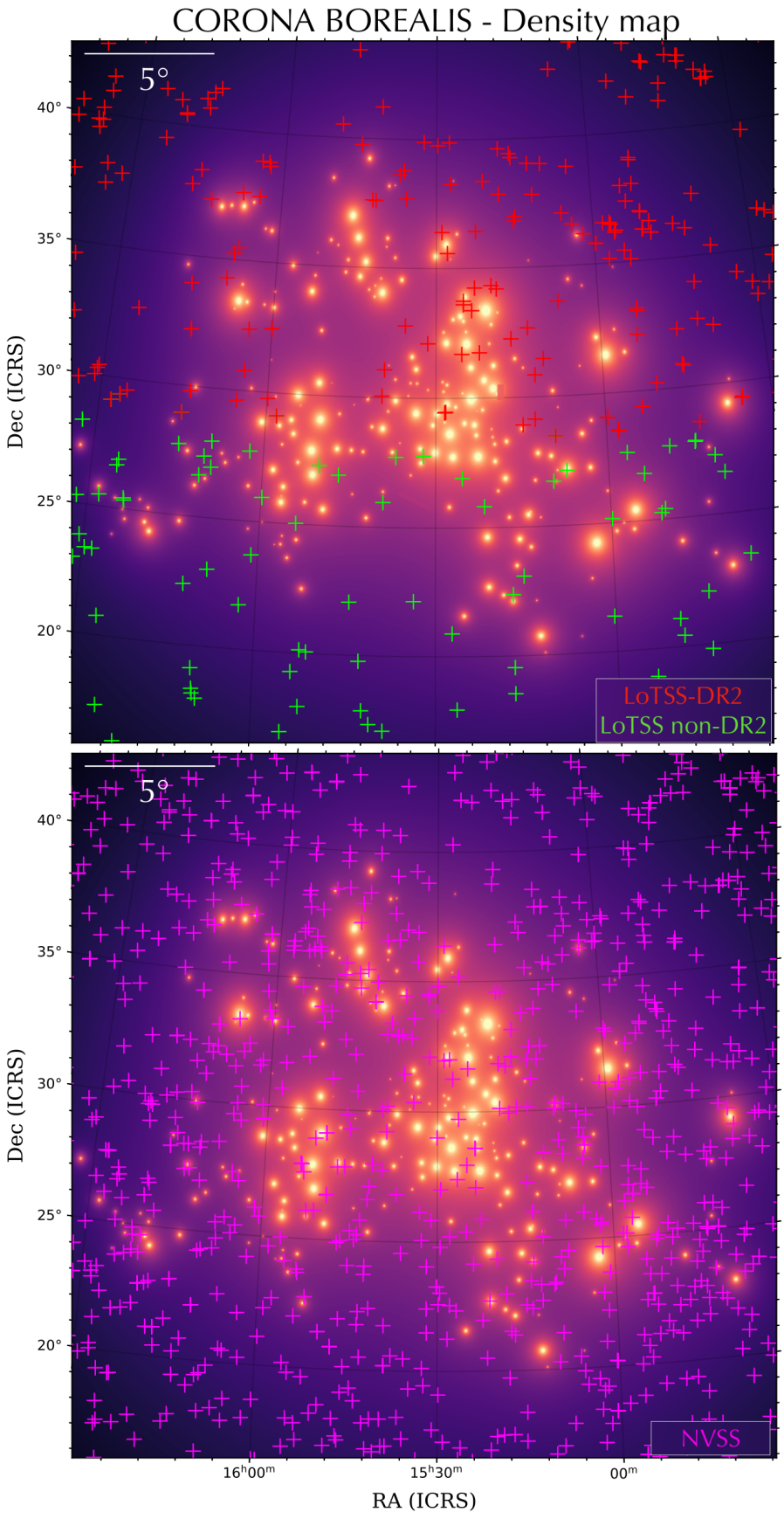

FIGURE 7.5: Two-dimensional density map for Corona Borealis supercluster, assuming that each member is on the same redshift plane. The location of the RM sources is shown in red for LoTSS-DR2, green for LoTSS non-DR2 and magenta for NVSS.

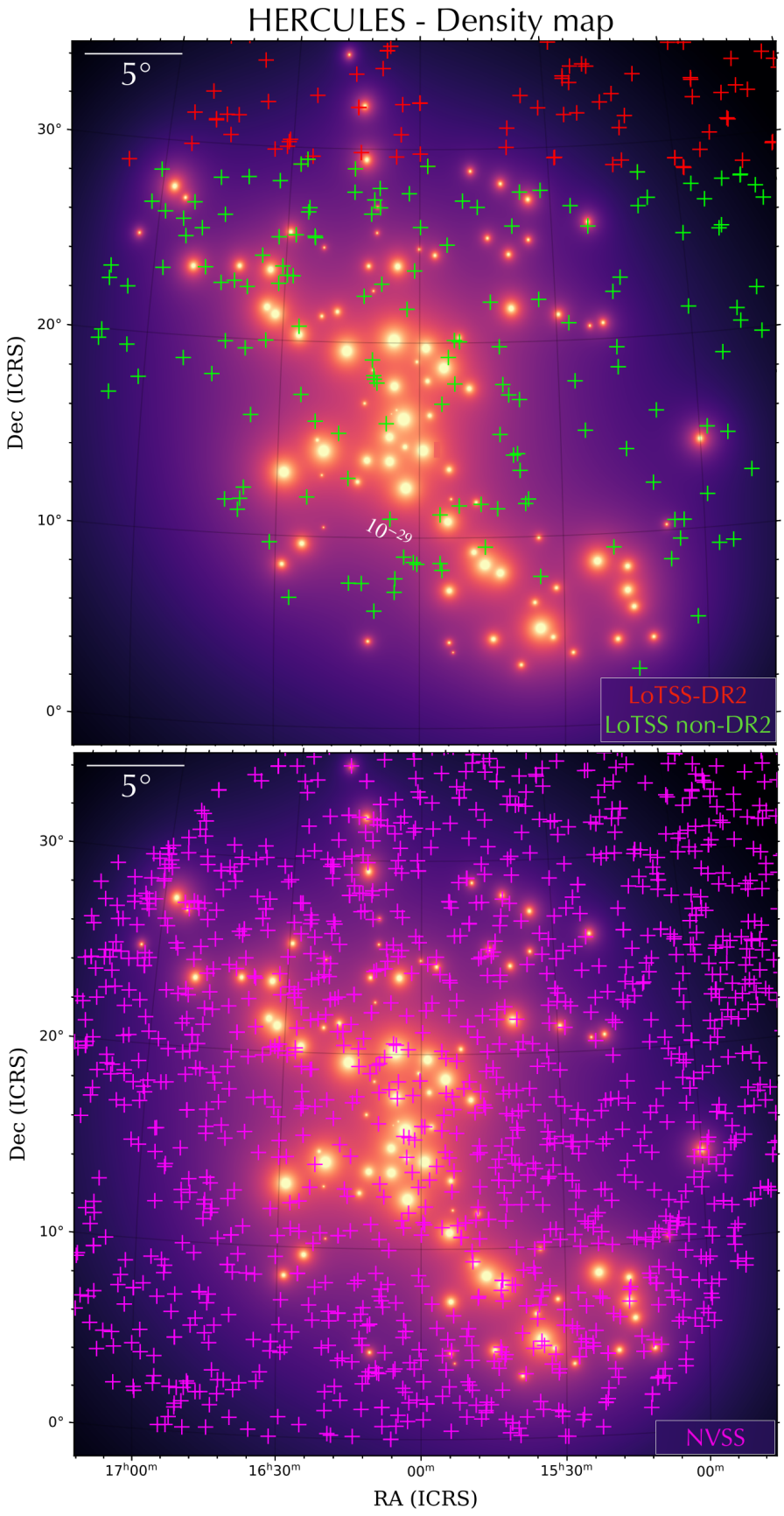

FIGURE 7.6: Same as Fig. 7.5, but for the Hercules supercluster.

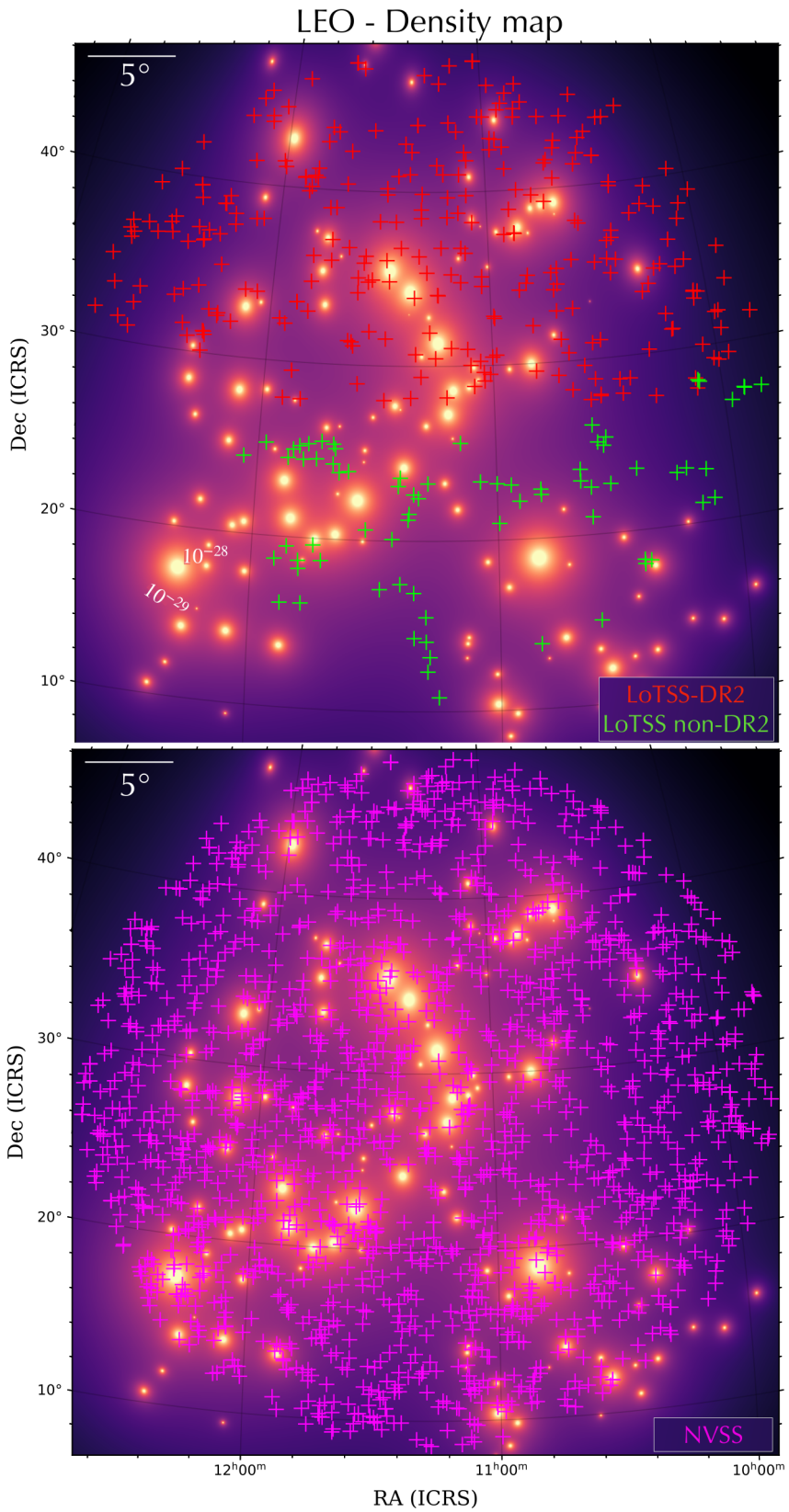

FIGURE 7.7: Same as Fig. 7.5, but for the Leo supercluster.

With this selection, we are also probing the regions outside supercluster boundaries; the sources in the line-of-sight of very low density environments serve as a control sample that allows us to quantify how the supercluster structure is contributing to the RM variance of the higher density regions sources.

7.3.2 Statistics of the RM population

The accuracy with which we can isolate the effects of the supercluster structure on the RMs of the background sources depends on the size of our sample and the dispersion of the RM distribution. The measured RM is the combination of the Galactic RM (GRM) component, the extragalactic component (RM_{ext}) and a noise term. We are mainly interested in the extragalactic component, that can be either attributed to the medium local to the source (Laing et al., 2008), or to the foreground intergalactic medium. Therefore, we subtract off the GRM component to be left with a residual RM (RRM):

$$\mathrm{RRM} = \mathrm{RM} - \mathrm{GRM}, \tag{7.6}$$

where the GRM is estimated as the median of a disc of radius of 0.5° centred at the source position from the GRM map by Hutschenreuter et al. (2022) from several extragalactic source RM catalogues, including LoTSS and NVSS. We can estimate the RRM spread of the population, for example, with a median absolute deviation (MAD) statistic, which is less sensitive to outliers in a distribution. The MAD can be used analogously as the standard deviation (see, e.g., Stuardi et al. 2021) to measure the dispersion of the distribution, by introducing a constant scale factor:

$$\sigma_{MAD} = k \cdot \mathrm{MAD} \approx 1.48 \cdot \mathrm{MAD} \tag{7.7}$$

where the value of k is taken assuming normally distributed data. Therefore, the intrinsic RRM MAD variance is obtained by subtracting the squared total noise term, consisting of the measurement term ($\sigma^2_{RM,err}$) and the GRM error ($\sigma^2_{GRM,err}$), from the observed RRM variance:

$$\sigma^{2_{RRM}}_{MAD} = \sigma^{2_{RRM,obs}}_{MAD} - \sigma^2_{RM,err} - \sigma^2_{GRM,err}. \tag{7.8}$$

As an indication, the typical measurement error for the RM in the selected LoTSS sources is ~ 0.06 rad m^{-2}, as opposed to ~ 10 rad m^{-2} for the NVSS sources, while the average GRM error is ~ 0.7 rad m^{-2}. The combination of the LoTSS RM Grid and NVSS RM catalogue can achieve a better sensitivity for the purpose of investigating the magnetic field strength and structure in superclusters. However, the different variances of the populations, for example, due to different survey sensitivities, frequency, foreground screens and background source properties must be properly weighted for them to be combined in the most effective manner (Rudnick, 2019). In particular, we aim to give more weight to the sources that are better probes

of the foreground medium in the supercluster, while minimizing the local RM variations. One useful proxy of small RM scatter is the fractional polarization of a radio source, which is dependent on both the intrinsic degree of order of the magnetic field and the Faraday depth structure across the emission region. Additionally, the presence of fluctuations on the small scale can cause Faraday depolarization from the mixing of different polarization vector orientations within the beam, which will reduce the fractional polarization. The RM variance is directly linked to the Faraday depolarization, as expressed in (Burn, 1966) for an external screen:

$$p(\lambda) = p(\lambda = 0)e^{-2\lambda^4\sigma^2_{RM}}. \tag{7.9}$$

This will result in a correlation between fractional polarization and depolarization (e.g. Stuardi et al., 2020). Higher fractional polarization implies smaller RM variations due to the medium local to the source, and also smaller scatter in the RM distribution (Lamee et al., 2016). LoTSS detections are already preferentially selecting low depolarization sources with minimum Faraday complexity (O'Sullivan et al., 2023), which are excellent probes for our aim. However, the NVSS RM sources show more complexity and different polarization structure due to the nature of the host galaxy (O'Sullivan et al., 2017). To reduce the effect of low fractional polarization sources on the extragalactic RM variance, we can separate the NVSS sources into two populations, based on the median degree of polarization of the sources in the NVSS RM catalogue ($\sim 5\%$). Therefore, we will weigh differently three populations: LoTSS sources (population a), NVSS sources with high degree of polarization (population b, $p > 5\%$) and NVSS sources with low degree of polarization (population c, $p < 5\%$). Following Rudnick (2019), each population can be described with its own intrinsic RRM variance σ^2_i and a corresponding uncertainty, δ_i, calculated as:

$$\delta_i = \sqrt{\frac{2}{N_i}}\sigma^2_i, \tag{7.10}$$

where N_i is the number of sources of each population. We obtained the variance of the whole sample as the inverse-variance-weighted average of the variance of the three populations:

$$\sigma^2_{MAD,tot}(RRM) = \frac{\left(\frac{\sigma^2_{MAD,a}}{\delta^2_a} + \frac{\sigma^2_{MAD,b}}{\delta^2_b} + \frac{\sigma^2_{MAD,c}}{\delta^2_c}\right)}{\left(\frac{1}{\delta^2_a} + \frac{1}{\delta^2_b} + \frac{1}{\delta^2_c}\right)}, \tag{7.11}$$

and the total uncertainty

$$\delta_{tot} = \frac{1}{\sqrt{\left(\frac{1}{\delta^2_a} + \frac{1}{\delta^2_b} + \frac{1}{\delta^2_c}\right)}}. \tag{7.12}$$

Under this choice, the LoTSS sample will be weighted more than the NVSS sample.

7.4 Results and discussion

7.4.1 RRM variance vs. density

We want to investigate the trend between the variations in the RRM distribution of the populations of sources through the line-of-sight of superclusters of galaxies, and the density of the medium crossed by the polarized emission. As explained in Sec. 7.3.1 and Sec. 7.3.2, with the construction of the 3D density we are able to associate a mean value of density to each source in the field of the each supercluster, and we combine the different populations through a weighted average, where we specifically down-weight the sources we expect to have a large RM variance in their local environments. Therefore, we can maximize the resulting accuracy of any possible RM signature from the superclusters by binning all the sources from the three superclusters in three main density regimes, thereby improving the MAD statistics.

The task of identifying and describing the cosmic web components has been undertaken through numerical simulations and observations with several different methods, both investigating the global pattern in a statistical way (see e.g. Peacock, 1999; Hoyle et al., 2002; Colberg, 2007), and segmenting the structure into its morphological components: voids, filaments, and clusters (e.g. Stoica, Martínez, and Saar, 2007; Stoica, Martínez, and Saar, 2010; Genovese et al., 2010; González and Padilla, 2010; Cautun, van de Weygaert, and Jones, 2013). We can base our investigation of supercluster density regimes on the density distribution across cosmic environments presented in Cautun et al. (2014), where they show that various structures are characterized by different density values. The node regions, where clusters reside, are typically of the highest density ($\rho/\rho_c \geq 100$) and filaments also represent overdense regions spanning a wide range of density values ($\rho/\rho_c \sim 1-10$), while voids are very underdense ($\rho/\rho_c \leq 1/10$). Although it is difficult to precisely define a density range to describe exactly the supercluster environments, we use these density regimes to define the bin ranges for our sources. Specifically, the RRMs that have lines of sight inside the virial radii of the galaxy clusters (nodes) and those with line of sight through the low-density gas inside the supercluster boundaries but outside the virial radii of clusters (filaments). We compare with the sources that fall outside the supercluster boundaries, assuming their RRMs can be attributed to typical extragalactic background. We can use their RRMs to identify the contribution of the supercluster and investigate the magnetic fields in these regions.

We define three starting bins based on the previous considerations: $10^{-31} < \rho_{gas} < 10^{-29}$ g cm^{-3} ($0.01 < \rho/\rho_c < 1$) for sources that can be considered outside supercluster boundaries, $10^{-29} < \rho_{gas} < 10^{-27.5}$ g cm^{-3} ($1 < \rho/\rho_c < 30$) for sources that are falling inside supercluster boundaries but outside galaxy clusters, and finally $10^{-27.5} < \rho_{gas} < 10^{-26}$ g cm^{-3} ($30 < \rho/\rho_c < 1000$) for sources that are inside galaxy clusters virial radii. For each bin, we compute the weighted MAD standard deviation of RRMs from LoTSS, NVSS high-degree of polarization, and NVSS low-degree of polarization source populations (see Sec. 7.3.2). We show the

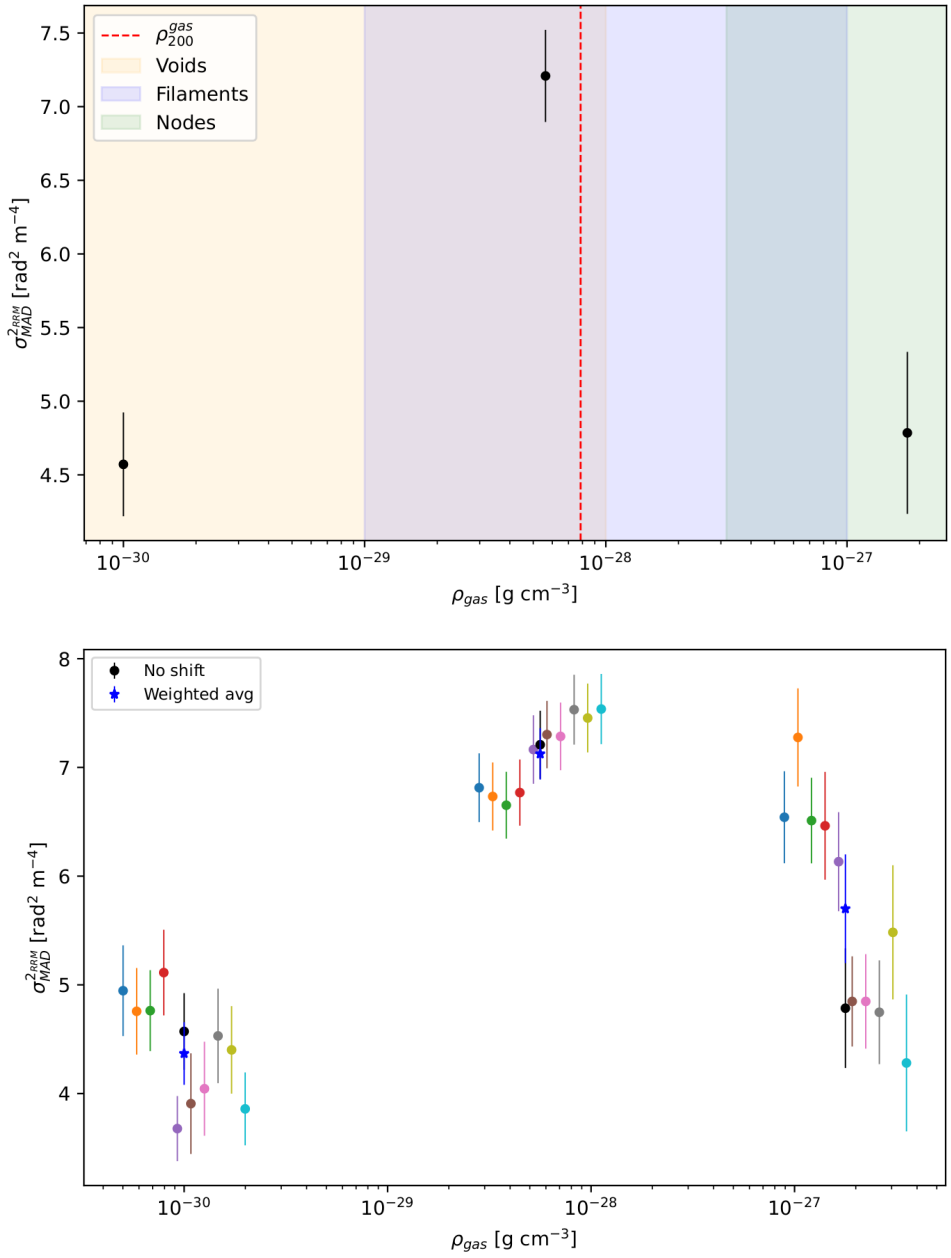

FIGURE 7.8: Total weighted RRM MAD variance $\left(\sigma^{2_{RRM}}_{MAD}\right)$ trend with gas density in superclusters of galaxies. *Top panel:* The plot shows the resulting variance from binning the sources in different gas density regimes. The background is divided between the ranges of densities that are typically related to voids (yellow), filaments (blue), and nodes (green) (Cautun et al., 2014). The red dashed line represents where the gas ρ_{200} limit would approximately be, to highlight the density trend outside galaxy clusters. We measure an excess in the RRM variance between the first and second density bins, that can be attributed to the contribution of the low-density magnetised gas in the supercluster structure. *Bottom panel*: Same as top panel, but varying the bins edges with steps of 0.03 (-0.03) with respect the original chosen value. The different resulting MAD variances and their uncertainties are show in different colors. The weighted average of these results in each bin is shown in blue, consistent with the original value shown in black.

resulting total weighted MAD cariance $\left(\sigma^{2_{RRM}}_{MAD}\right)$ as a function of the gas density in Fig. 7.8 (top panel). If we consider the RRMs variations of sources falling outside supercluster boundaries (first bin) to be mostly caused by the medium local to the source, then we can subtract the local contribution to the variance in the second bin to isolate the effect of the supercluster low density regions. Between the first and second bin, we measure an excess RRM variance of $\Delta\sigma^{2_{RRM}}_{MAD} = 2.5 \pm 0.5$ rad^2 m^{-4}.

To investigate the effect of the choice of bin boundaries in this detection, we can vary the bin edges to shift the boundaries of different quantities and see the effect on the resulting variance. We choose to introduce a shift between 0.0 and 0.3 (-0.3) in 10 equal logarithmic step. The result of this test are shown in Fig. 7.8 (bottom panel), where the results of each shift are marked in a different color. The bin that is most affected by the choice of bin edges is the highest density one, that exhibit very different results. It can be noted that moving the bin edge towards higher density values (i.e. toward galaxy cluster centers), the variance gets lower. This is consistent with the presence of only few sources near cluster centers with low variance that survive depolarization effects. In general, this bin shows higher uncertainty due to the smaller number of sources (only 564 RMs, while 1195 and 2738 RMs in the first two bins) found at higher densities for depolarization effects (see e.g. Bonafede et al. 2011; Böhringer, Chon, and Kronberg 2016; Osinga et al. 2022), and therefore we will not be considering these regions for the purpose of this analysis. If we compute the weighted average of the resulting σ_{MAD} and their uncertainties, we find that the first two bin results are in agreement with the starting value.

7.4.2 Constraints on supercluster magnetic fields

With the detection of an excess in RRM variance that can be attributed to the supercluster structure, we attempt to estimate the required field strength permeating the low-density environments crossed by the polarized emission. The variance of the RRM distribution (σ^2_{th}) for a single-scale model of a randomly oriented field structure can be described by a simple model (Murgia et al., 2004):

$$\sigma^{2_{RRM}}_{th} = 0.812^2 \left(\frac{\Lambda_c}{\mathrm{pc}}\right) \int \left(\frac{n_e}{\mathrm{cm}^{-3}} \frac{B_{||}}{\mu\mathrm{G}}\right)^2 \frac{\mathrm{d}l}{\mathrm{pc}}, \tag{7.13}$$

where Λ_c is the magnetic field reversal scale, n_e is the gas electron number density, and $B_{||}$ is the magnetic field over any line-of-sight through the supercluster over a path length L. The model $\sigma^{2_{RRM}}_{th}$ can be computed as Eq.7.13 for different values of the parameters $(\Lambda_c,\ B_{||}, L)$ and compared with the measured $\sigma^2_{MAD}(RRM)$ at the densities in the first two bins as derived in Sec. 7.4.1.

We adopt a Bayesian Monte Carlo sampling (e.g. Monte Carlo Markov Chain, MCMC) approach to explore the likelihood surface and reconstruct the posterior distribution of the free parameters: $(\Lambda_c,\ B_{||}, L)$. In the modeling framework, we call the data **d** and the model parameters **m**, so we can write the Bayes theorem (up to a

constant) as:

$$P(\mathbf{m} \mid \mathbf{d}) \propto \mathcal{L}(\mathbf{d} \mid \mathbf{m})\Pi, \tag{7.14}$$

that relates the posterior probability function of the parameters $P(\mathbf{m} \mid \mathbf{d})$ to the likelihood function $\mathcal{L}(\mathbf{d} \mid \mathbf{m})$, that we would like to maximize, and the prior Π, that encodes existing knowledge of parameter values. In our case, we can write the likelihood function of detecting the observed $\sigma^{2RRM}_{MAD}(n_e)$ for a medium of density n_e as

$$\mathcal{L}\left(\sigma^{2RRM}_{MAD} \mid \mathbf{m}\right) \propto \exp\left[-\frac{1}{2}\sum_i \left(\frac{\sigma^{2RRM}_{MAD}(n_{e,i}) - \sigma^{2RRM}_{th}(n_{e,i}, \mathbf{m})}{\delta(n_{e,i})}\right)^2\right], \tag{7.15}$$

where δ is the uncertainty on the i-th measured values of σ^{RRM}_{MAD} and $\mathbf{m} = (\Lambda_c, B_{||}, L)$. For the parameters, we assume flat priors in ranges $0 \leq B_{||} \leq 2$ μG, $5 \leq \Lambda_c \leq 500$ kpc, and $5 \leq L \leq 70$ Mpc. While the choice of the parameters ranges is arbitrary given the limited information on supercluster environments, it is dictated by some reasonable considerations: the magnetic field strength is investigated up to values found in galaxy clusters (few μG, e.g. Bonafede et al. 2010; Govoni et al. 2017); the magnetic field will fluctuate on a range of scales, therefore we will investigate out to a large outer scale of $\Lambda_c = 500$ kpc (Enßlin and Vogt, 2003; Murgia et al., 2004; Vacca et al., 2010); finally, the maximum path length through the supercluster is computed following as the average of the three superclusters box size ($\sim$ 70 Mpc) defined in Santiago-Bautista et al. (2020) that enclose each supercluster structure (see Table 7.1).

The distribution is then sampled with MCMC using `emcee` (Foreman-Mackey et al., 2013). Fig. 7.9 shows the posterior probability distributions, marginalized into one and two dimensions, for the model parameters. The distributions for each parameter are plotted along the diagonal and covariances between them under the diagonal. The shape of the covariance indicate the correlation between the parameters, namely a circular or diffuse covariance means no correlation, while elongated shapes can show correlation. As expected from Eq. 7.13, the path length L and the reversal scale Λ_c are essentially unconstrained within the prior range. The posterior distribution of the magnetic field shows correlation with both other parameters but, once marginalized over them, shows a Gaussian-like behavior, though skewed towards high values. As shown in Fig. 7.10, we can constrain $B_{||} = 19^{+50}_{-8}$ nG, different from zero with a confidence level larger than 95%.

This result for the magnetic field in low density regions of superclusters is in agreement with what is found with different methods investigating the filaments of the cosmic web (Carretti et al., 2022; Carretti et al., 2023; Vernstrom et al., 2023) and preliminary studies on superclusters with Faraday RMs (Xu et al., 2006; Sankhyayan and Dabhade, 2024). Moreover,some early works on simulations have investigated the contribution of large scale structure filaments to the RM of background sources. These simulations suggest that the magnetic field intensity in filaments could range from 10 nG to 100 nG (Ryu et al., 2008; Cho and Ryu, 2009; Akahori and Ryu, 2010; Vazza et al., 2015), which still is in agreement with our findings.

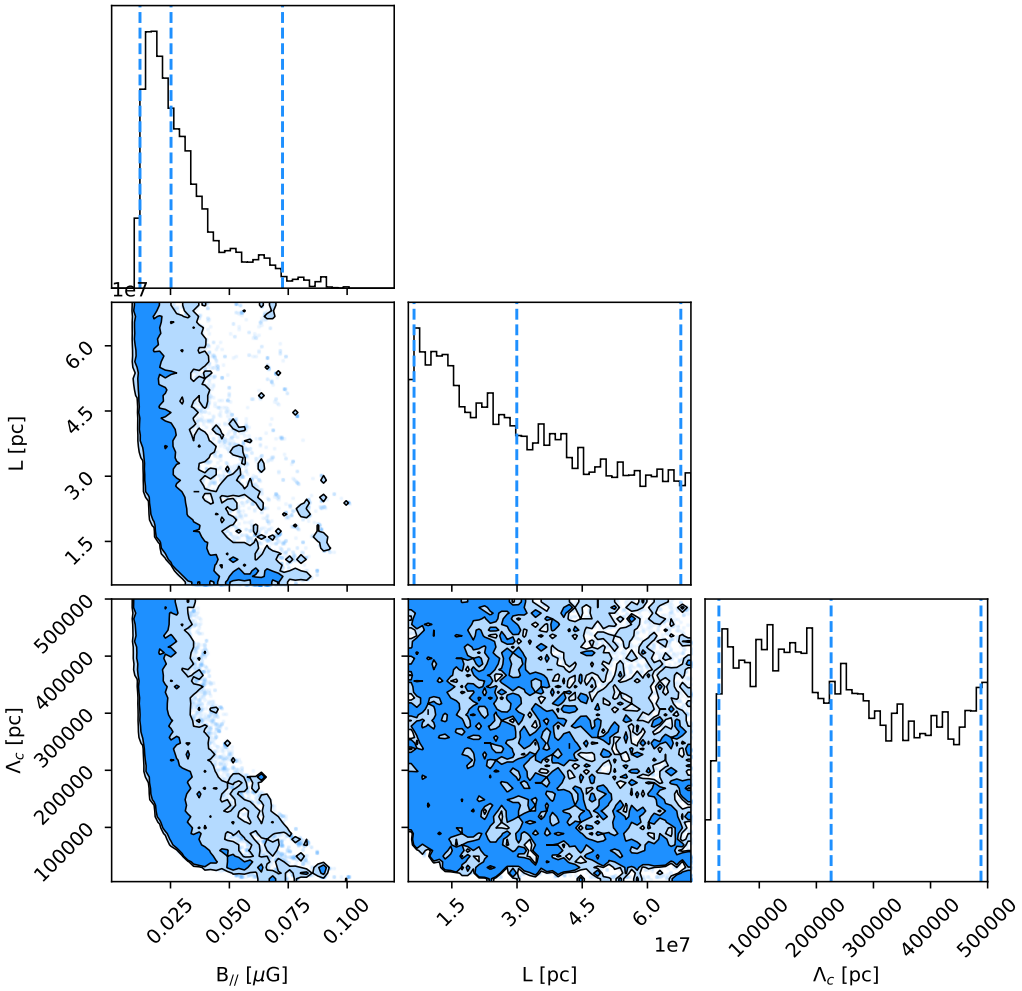

FIGURE 7.9: Posterior probability distribution, marginalized into one and two dimensions, for the parameters $B_{||}$, L, and Λ_c. Dark- and light-blue shaded areas indicate the 68 and 95% confidence regions. The one-dimensional projection for each parameters is shown at the top. The dashed blue lines represent (from left to right) the 2.5th, 50th and 97.5th percentiles.

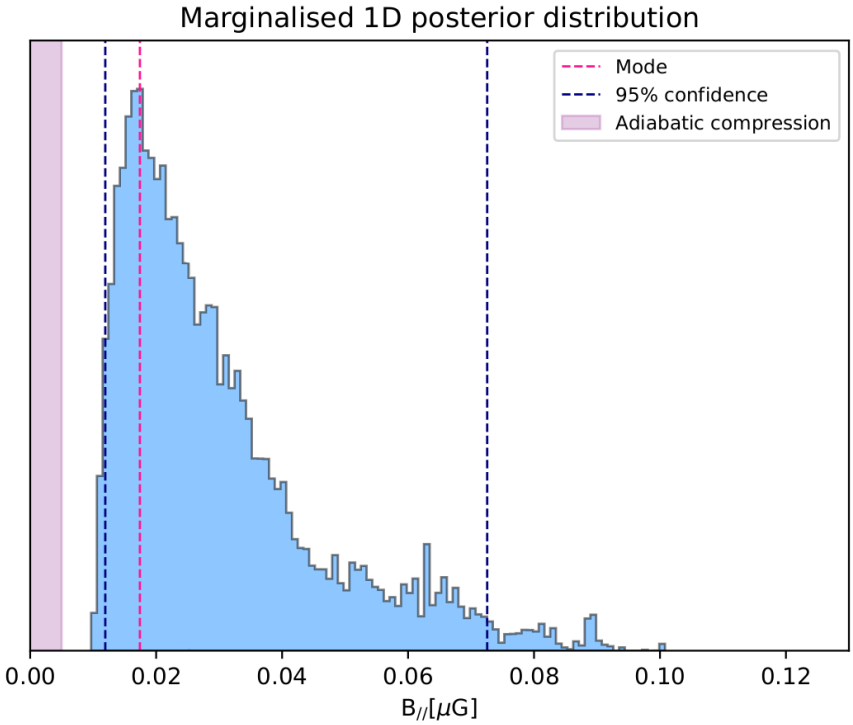

FIGURE 7.10: Magnetic field marginalised posterior distribution, zoomed-in from Fig. 7.9. The distribution is skewed towards small values. The 95% confidence levels of the distribution are shown in dashed blue. The most likely value is shown in dashed red. The resulting adiabatic compression level is shown in purple.

In our analysis we are considering the density contribution from supercluster members only, therefore neglecting the possible filament contribution and, in turn, overestimating the magnetic field intensity. While a better approach may be to compare directly with simulations of the RM variations from supercluster structures, we can estimate the effect of including an additional density component by increasing the density of the second bin (see Fig. 7.8) with a 20% excess from filaments, as recently measured with profiles of the SZ signal from stacked galaxy pairs (de Graaff et al., 2019). The resulting magnetic field is consistent with the initial finding, and therefore still comparable with works of LSS filaments.

Constraints on the magnetic field strength in cosmic structures are of key importance to investigate magnetogenesis scenarios. For this purpose, ad-hoc cosmological simulation of superclusters are needed but not available yet. However, we can compute a preliminary estimate of the predicted adiabatic compression-only effect on a primordial seed and compare with our results. For adiabatic compression, the magnetic field strength scales with density as $B = B_0(n/n_0)^{2/3}$. With an initial seed of cosmological origin, as derived from the analysis of CMB anisotropies (i.e. $B_0 \sim 2$ nG, Planck Collaboration et al., 2016) compression seems enough to explain the magnetic field strength derived in this analysis. However, recent LOFAR RRM measurements in IGM filaments suggest magnetic field seeds more than an order of magnitude below the limit derived with CMB (Neronov et al., 2024). Assuming an

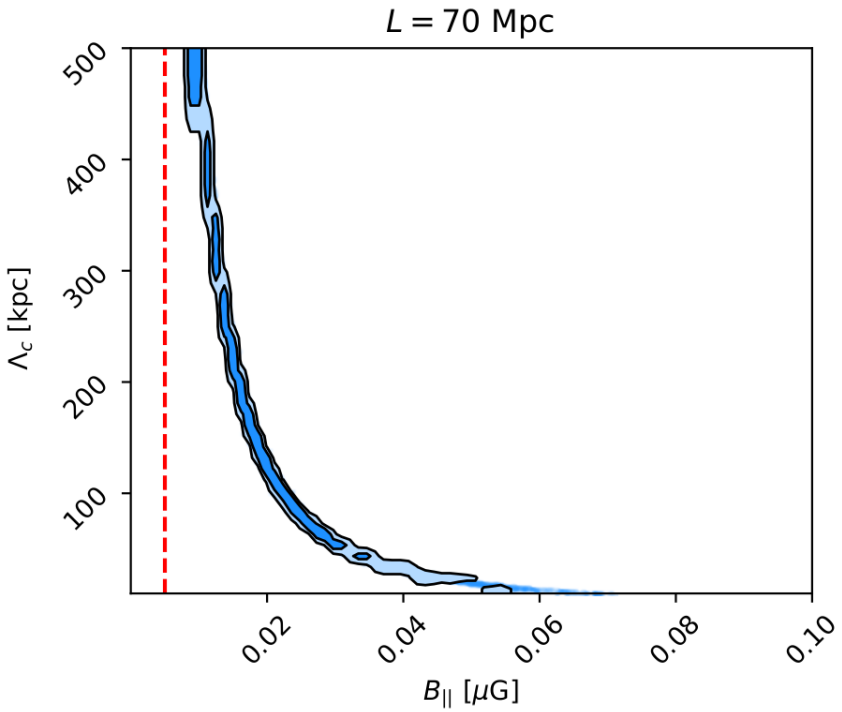

FIGURE 7.11: Covariance plot between the magnetic field strength ($B_{||}$) and reversal scale (Λ_c), fixing the path length to $L = 70$ Mpc. The distribution 1- and 2-σ contour levels are shown in black. The dashed red line represent the magnetic field resulting from adiabatic compression only.

initial seed of $B_0 \sim 0.11$ nG (Carretti et al., 2023) at mean critical barionic density of $n_0 \sim 4 \cdot 10^{-31}$ g cm^{-3}, the adiabatic compression to the density $n \sim 5 \cdot 10^{-29}$ gr cm^{-3} as in our case, would yield $B \sim 3.5$ nG, and $B_{||} = B/\sqrt{3} \sim 2$ nG. Comparing the adiabiatic compression effect to the resulting $B_{||}$ from our analysis (see Fig. 7.10), it suggests that in superclusters of galaxies may be at play different mechanism such as dynamo amplification or AGN feedback, to further amplify the magnetic fields from $\sim$ 2 nG to the measured $\sim$20 nG. Another possible amplification mechanism is the presence of accretion strong shocks surrounding the filaments of the cosmic web, as observed in Vernstrom et al. (2023).

Since our result is dependent on the chosen Λ_c parameter range, we can try to set an additional constrain on the reversal scale length by fixing the path length to $L = 70$, the largest value considered for the parameter range. In this way, to reproduce the same RRM variance, we would minimize the magnetic field. The contour plot in Fig. 7.11 shows the two dimensional posterior distribution between $B_{||}$ and Λ_c once L is fixed to 70 Mpc. In the case of the maximum path length through the superclusters, the magnetic field is still larger than what is predicted by adiabatic-compression only for all values of Λ_c. A strong constrain on Λ_c would result in the minimum line-of-sight magnetic field component in the supercluster environment.

7.5 Conclusions

The Faraday rotation measure signal from distant polarized sources is a sensitive probe of foreground, extragalactic low-density gas that permeates the large scale structure, otherwise difficult to detect. In this work, we have made use of the NVSS and LoTSS RM catalogs, combining the large number of sources found at cm-wavelengths with the highest precision of the sources detected at m-wavelengths, to investigate the rarefied environments of three major superclusters of galaxies in the northern sky: Corona Borealis, Hercules, and Leo. Our findings can be summarized as follows:

- For each supercluster we built a density 3D map (RA, DEC, z), computing the universal gas density profile (Pratt et al., 2022) for each member.
- We created a catalog of 4497 polarized sources fund in the background of the three superclusters. Among these, 3697 RM values are from the NVSS (Taylor, Stil, and Sunstrum, 2009), and 818 are from LoTSS (O'Sullivan et al., 2023). At the location of each source, we compute the mean gas density crossed by the polarized emission passing through the supercluster. We subtract the Galactic contribution, to investigate the extragalactic component. We then have for each source a pair of RRM and associated density values.
- We computed the MAD variance of the RRM distribution in three different density regimes: voids, filaments and nodes. While the highest density bin (inside galaxy cluster virial radii) is difficult to interpret due to several depolarization effects at play and to the low-number statistics, we detect an excess RRM variance of $\Delta\sigma^{2_{RRM}}_{MAD} = 2.5 \pm 0.5$ rad^2 m^{-4}. between the lowest density region (outside the supercluster boundaries) and the low-density region inside the supercluster. We attribute this excess to the intervening medium of the filaments in the supercluster.
- We estimate the required magnetic field strength permeating the low-density environments crossed by the polarized emission through a Bayesian approach. We infer a line-of-sight magnetic field strength of $B_{||} = 19^{+50}_{-8}$ nG, while other quantities such as the path-length and the magnetic field reversal scale remain unconstrained. Our result is in line with other work conducted on the filaments of the large scale structure (e.g. Vernstrom et al., 2021; Carretti et al., 2022; Carretti et al., 2023). Assuming only the effect of adiabatic compression from a primordial seed field consistent with current upper limits from LOFAR RRM measurements in IGM filaments (Neronov et al., 2024), would give $B_{||} \sim 2$ nG. Our result suggests that in superclusters of galaxies different mechanisms of magnetic field amplification may be at play, such as dynamo amplification or AGN/galaxy feedback, or that an additional primordial seed should be considered.

Chapter 8

Thesis Conclusions

8.1 Conclusions

The advent of cutting-edge low frequency radio observatories has revolutionized the study of the large scale structure by enabling the discovery of new types of diffuse radio sources. Among these are Mpc-scale diffuse radio emissions found in merging galaxy clusters, including new phenomena such as radio bridges and megahalos. The detection and the study of these sources, through observations and numerical simulations, provide a new and powerful way to probe the universe on the largest scales.

This Thesis is dedicated to the study of cosmic rays interacting in magnetic fields in the environments of bridges and filaments. For the first time, their spectral characteristics, magnetic field properties, and occurrence have been thoroughly investigated.

Starting from the most spectacular example of detected radio bridges, in A399-A401, we have analysed new systems basing our search on Recent X-ray and SZ observations, that have detected thermal emission between early-stage merging galaxy clusters. In Chapter 4, we focused on A399-A401 and A21-PSZ2 G114.9, two unique cluster pairs found in an interacting state, identified through the detection of inter-cluster thermal plasma with Planck. We analysed new high-sensitivity, wideband (250-500 MHz) uGMRT data of these two systems and we developed an injection procedure to place limits on the spectrum of A399-A401 and on the radio emission between A21-PSZ2 G114.9. In fact, in both cases, the low-surface-brightness diffuse emission is not detected in Band 3 (250-500 MHz). The methods that we proposed for the limits on the radio emission in the A21-PSZ2 G114.9 system represent a first step towards a systematic study of these sources. This work also provided a constraint on the spectrum in the bridge A399-A401 that disfavours shock acceleration as the main mechanism for the radio emission. This is extensively investigated in Chapter 5, where we present follow-up observations at 60 MHz to constrain the spectral index of the bridge, which so far has only been detected at 140 and 144 MHz. We conducted a multi-frequency study with LOFAR HBA data at 144 MHz and uGMRT

data at 400 MHz. Assuming second-order Fermi mechanisms for the re-acceleration of relativistic electrons driven by turbulence in the radio bridge regions, we compared the observed radio spectrum with theoretical synchrotron models. For the first time, we produced spectral index and related uncertainties maps for a radio bridge. We produce a radio spectrum, which show significant steepening between 144 and 400 MHz. The steepening of the spectrum above 144 MHz can be explained in a turbulent re-acceleration framework, constraining the acceleration timescales to $\sim$ 200 Myr, and the magnetic field to the order of $\sim$ 0.3 μG. Thus, this detection at low frequencies provides important information on the models of particle acceleration and magnetic field structure on very extended scales. This study showed the importance of characterizing the spectral properties derived from observations at different radio frequencies, that allows us to constrain the theoretical models.

To refine our understanding of the mechanism at play in this emerging population of bridges, we investigated more promising merging systems. In Chapter 6, we present the clusters Abell 2061 and Abell 2067 in the Corona Borealis supercluster, which have been studied at different radio frequencies and are both known to host diffuse radio emission. This dynamically interacting, pre-merger system closely resembles the two other cluster pairs where radio bridges connecting the radio halos on Megaparsecs scales have been detected. The system is observed at 144 MHz to follow up on the possible inter-cluster filament suggested by previous 1.4 GHz observations. We report the detection of diffuse radio emission on an 800 kpc scale, which is more extended than previously known, reaching beyond the radio halo in Abell 2061 towards Abell 2067 and over the separation outside the two clusters R_{500} radii. However, in this unique case, the absence of the radio halo in Abell 2067 creates a 'gap' between the two clusters, and makes the classification of the filamentary emission challenging. We investigated the radial profiles and the point-to-point surface-brightness correlation of the emission in Abell 2061 with radio and X-ray observations, to describe the nature of the diffuse emission and compared the observed features with the predictions of three different dynamical scenarios to explain the nature of the diffuse emission. While the classification of the emission remains unclear, this study represent an important step towards a detailed spectral and dynamical analysis of the candidate radio bridge.

Finally, we also explore the population of longer filaments, that connect the nodes of the Cosmic Web. In fact, the magnetic fields in the unprocessed gas in filaments of the large-scale structure, far beyond galaxy clusters, are still poorly explored. In particular, superclusters of galaxies are an ideal laboratory to investigate the filament environments that are not easily identified, given the low signals and densities involved. In fact, superclusters are a coherent structure of clusters embedded in a network of filaments, which have higher densities with respect to the cosmic filaments. In Chapter 7, we use the observed Faraday rotation measure of polarized sources in the line-of-sight of superclusters to constrain the magnetic field properties

in these extended environments. We selected three rich and nearby ($z < 0.1$) superclusters of galaxies in the northern sky: Corona Borealis, Hercules and Leo. We constructed a catalog of 4497 polarized background sources with the existing NVSS and LoTSS RM grids, plus additional new sources detected in the latest LoTSS data, yet to be published. For each supercluster, we created a 3D density cube, to have associated RM- density pairs and investigated how variations in the RM distribution are linked to the mean density crossed by the polarized emission. Three separate density regimes are investigated: we detect an excess of variation between the lowest density regions (outside supercluster boundaries) and the low-density region inside the supercluster. We attribute this excess to the intervening medium of the filaments in the supercluster. We estimate the magnetic field strength permeating the low-density environments, required to produce this excess. With a Bayesian approach, we estimate a magnetic field $B_{||} = 19^{+50}_{-8}$ nG, while other quantities such as the path-length and the magnetic field reversal scale remain unconstrained. Our findings are consistent with other several works conducted on the filaments of the large scale structure, and suggest that the adiabatic compression of a primordial magnetic field seed is not the only mechanism at play in superclusters of galaxies to reproduce the observed magnetic field strength. This indicates that other processed, such as the small-scale dynamo, are amplifying the magnetic field also in these rarefied environments.

Overall, the results presented in this Thesis highlight the crucial role that low-frequency radio observations, both in total intensity and polarization, play in advancing our understanding of cosmic filaments. By probing their non-thermal properties, the work conducted during the PhD has strengthened our knowledge on the interplay between cosmic rays and magnetic fields in the large-scale structure.

8.2 Future prospects

In the future, further advances in understanding cosmic filament will rely on next-generation radio observatories. For example, the higher resolution and improved calibration capabilities of LOFAR 2.0 will enable more detailed mapping of the spectral properties of diffuse radio emissions. Together with the Square Kilometre Array (SKA), and in particular SKA-LOW, these facilities will provide unprecedented sensitivity to discover more systems and trace the complex interactions between cosmic rays and magnetic fields in environments like radio bridges and filaments, extending the work presented in this Thesis. Moreover, the Polarization Sky Survey of the Universe's Magnetism (POSSUM) and the Very Large Array Sky Survey (VLASS) will provide high-resolution polarization data that will be instrumental in mapping the magnetic field structure in low density environments through detailed Faraday rotation measurements. Finally, the observational capabilities of these upcoming facilities combined with advanced numerical simulations will allow us to compare

detailed predictions of the radio, X-ray, and SZ signatures of filaments. These comparisons can be used for testing theoretical models of cosmic ray acceleration and magnetogenesis on the largest scales.

Acknowledgements

At the end of my PhD, I would like to sincerely thank my supervisors, Annalisa and Gianni, for patiently guiding me and creating such a friendly and stimulating environment for me to learn and work with a clear mind.

Annalisa, you have been not only a brilliant mentor for me, but also an inspiring example of how a woman can excel at the top of her field while remaining kind and respectful to all. I will forever be your biggest fan (. . . Queen!).

I would also like to thank my office mate Filippo, for all the fun stuff he showed me to lighten the mood when we were both tired already at 11am. And, of course, Francesco, who not only endured many (and I mean *many*) of my coding rants, but also consistently offered a positive outlook to calm my worries about the future. And for those times I was *really* stressed, thank you, Villiam, for all the fun late-night gossip sessions.

Thanks to my family, who believed in me even when I doubted myself.
And I will be forever grateful to Lorenzo, who supported my every need even during the most intense time of all: planning a wedding and writing this Thesis at the same time.

I carry the love of my grandparents with me as I complete this journey, grateful to be surrounded by such incredible people.

Bibliography

Abazajian, Kevork N. et al. (June 2009). "The Seventh Data Release of the Sloan Digital Sky Survey". In: 182.2, pp. 543–558. DOI: 10.1088/0067-0049/182/2/543. arXiv: 0812.0649 [astro-ph].

Ackermann, M. et al. (Nov. 2010). "Fermi LAT observations of cosmic-ray electrons from 7 GeV to 1 TeV". In: 82.9, 092004, p. 092004. DOI: 10.1103/PhysRevD.82.092004. arXiv: 1008.3999 [astro-ph.HE].

Ackermann, M. et al. (May 2014). "Search for Cosmic-Ray-induced Gamma-Ray Emission in Galaxy Clusters". In: 787.1, 18, p. 18. DOI: 10.1088/0004-637X/787/1/18. arXiv: 1308.5654 [astro-ph.HE].

Ackermann, M. et al. (Mar. 2016). "Search for Gamma-Ray Emission from the Coma Cluster with Six Years of Fermi-LAT Data". In: 819.2, 149, p. 149. DOI: 10.3847/0004-637X/819/2/149. arXiv: 1507.08995 [astro-ph.HE].

Akahori, Takuya and Dongsu Ryu (Nov. 2010). "Faraday Rotation Measure Due to the Intergalactic Magnetic Field". In: 723.1, pp. 476–481. DOI: 10.1088/0004-637X/723/1/476. arXiv: 1009.0570 [astro-ph.CO].

Akamatsu, H. et al. (Sept. 2017). "Properties of the cosmological filament between two clusters: A possible detection of a large-scale accretion shock by Suzaku". In: 606, A1, A1. DOI: 10.1051/0004-6361/201730497. arXiv: 1704.05843 [astro-ph.HE].

Albareti, Franco D. et al. (Dec. 2017). "The 13th Data Release of the Sloan Digital Sky Survey: First Spectroscopic Data from the SDSS-IV Survey Mapping Nearby Galaxies at Apache Point Observatory". In: 233.2, 25, p. 25. DOI: 10.3847/1538-4365/aa8992. arXiv: 1608.02013 [astro-ph.GA].

Allen, Steven W., August E. Evrard, and Adam B. Mantz (Sept. 2011). "Cosmological Parameters from Observations of Galaxy Clusters". In: 49.1, pp. 409–470. DOI: 10.1146/annurev-astro-081710-102514. arXiv: 1103.4829 [astro-ph.CO].

Almeida, Andrés et al. (Aug. 2023). "The Eighteenth Data Release of the Sloan Digital Sky Surveys: Targeting and First Spectra from SDSS-V". In: 267.2, 44, p. 44. DOI: 10.3847/1538-4365/acda98. arXiv: 2301.07688 [astro-ph.GA].

Amaral, A. D., T. Vernstrom, and B. M. Gaensler (May 2021). "Constraints on large-scale magnetic fields in the intergalactic medium using cross-correlation methods". In: 503.2, pp. 2913–2926. DOI: 10.1093/mnras/stab564. arXiv: 2102.11312 [astro-ph.CO].

Andernach, H. et al. (June 2005). "Redshifts and Distribution of ACO Clusters of Galaxies". In: *Nearby Large-Scale Structures and the Zone of Avoidance*. Ed. by Anthony P. Fairall and Patrick A. Woudt. Vol. 329. Astronomical Society of the Pacific Conference Series, pp. 283–287. DOI: 10.48550/arXiv.astro-ph/0407097. arXiv: astro-ph/0407097 [astro-ph].

Anderson, C. S. et al. (Mar. 2018). "Broadband Radio Polarimetry of Fornax A. I. Depolarized Patches Generated by Advected Thermal Material from NGC 1316". In: 855.1, 41, p. 41. DOI: 10.3847/1538-4357/aaaec0. arXiv: 1802.04812 [astro-ph.HE].

Arieli, Yinon, Yoel Rephaeli, and Michael L. Norman (June 2010). "Hydrodynamical Simulations of Galaxy Clusters with Galcons". In: 716.2, pp. 918–928. DOI: 10.1088/0004-637X/716/2/918. arXiv: 1004.3839 [astro-ph.CO].

Arshakian, Tigran G. and Rainer Beck (Dec. 2011). "Optimum frequency band for radio polarization observations". In: 418.4, pp. 2336–2342. DOI: 10.1111/j.1365-2966.2011.19623.x. arXiv: 1101.2631 [astro-ph.CO].

Bagchi, Joydeep et al. (July 2017). "Saraswati: An Extremely Massive ∼200 Megaparsec Scale Supercluster". In: 844.1, 25, p. 25. DOI: 10.3847/1538-4357/aa7949. arXiv: 1707.03082 [astro-ph.CO].

Banfield, J. K. et al. (Feb. 2019). "Faraday rotation study of NGC 612 (PKS 0131-36): a hybrid radio source and its magnetized circumgalactic environment". In: 482.4, pp. 5250–5258. DOI: 10.1093/mnras/sty3108. arXiv: 1811.06266 [astro-ph.HE].

Bartalucci, I. et al. (June 2023). "CHEX-MATE: Constraining the origin of the scatter in galaxy cluster radial X-ray surface brightness profiles". In: 674, A179, A179. DOI: 10.1051/0004-6361/202346189. arXiv: 2305.03082 [astro-ph.CO].

Batiste, Merida and David J. Batuski (Dec. 2013). "A dynamical analysis of the Corona Borealis supercluster". In: 436.4, pp. 3331–3340. DOI: 10.1093/mnras/stt1810. arXiv: 1310.0429 [astro-ph.CO].

Beduzzi, L. et al. (Oct. 2023). "Exploring the origins of mega radio halos". In: 678, L8, p. L8. DOI: 10.1051/0004-6361/202346784. arXiv: 2306.03764 [astro-ph.HE].

Beduzzi, Luca et al. (June 2024). "Cosmological simulations of the generation of cluster-scale radio emission from turbulent re-acceleration". In: *arXiv e-prints*, arXiv:2406.09859, arXiv:2406.09859. DOI: 10.48550/arXiv.2406.09859. arXiv: 2406.09859 [astro-ph.HE].

Bell, M. R. et al. (Mar. 2013). "Improved CLEAN reconstructions for rotation measure synthesis with maximum likelihood estimation". In: 551, L7, p. L7. DOI: 10.1051/0004-6361/201220771. arXiv: 1211.5105 [astro-ph.IM].

Bernardi, G. et al. (July 2013). "A 189 MHz, 2400 deg^2 Polarization Survey with the Murchison Widefield Array 32-element Prototype". In: 771.2, 105, p. 105. DOI: 10.1088/0004-637X/771/2/105. arXiv: 1305.6047 [astro-ph.CO].

Bernardi, G. et al. (Feb. 2016). "KAT-7 observations of an unbiased sample of mass-selected galaxy clusters". In: 456.2, pp. 1259–1268. DOI: 10.1093/mnras/stv2589. arXiv: 1511.01022 [astro-ph.CO].

Bertone, Serena, Corina Vogt, and Torsten Enßlin (July 2006). "Magnetic field seeding by galactic winds". In: 370.1, pp. 319–330. DOI: 10.1111/j.1365-2966.2006.10474.x. arXiv: astro-ph/0604462 [astro-ph].

Biava, N. et al. (Dec. 2021). "The ultra-steep diffuse radio emission observed in the cool-core cluster RX J1720.1+2638 with LOFAR at 54 MHz". In: 508.3, pp. 3995–4007. DOI: 10.1093/mnras/stab2840. arXiv: 2110.01629 [astro-ph.GA].

Blandford, Roger and David Eichler (Oct. 1987). "Particle acceleration at astrophysical shocks: A theory of cosmic ray origin". In: 154.1, pp. 1–75. DOI: 10.1016/0370-1573(87)90134-7.

Böhringer, Hans, Gayoung Chon, and Philipp P. Kronberg (Nov. 2016). "The Cosmic Large-Scale Structure in X-rays (CLASSIX) Cluster Survey. I. Probing galaxy cluster magnetic fields with line of sight rotation measures". In: 596, A22, A22. DOI: 10.1051/0004-6361/201628873. arXiv: 1610.02887 [astro-ph.CO].

Bonafede, A. et al. (Sept. 2009). "Revealing the magnetic field in a distant galaxy cluster: discovery of the complex radio emission from MACS J0717.5 +3745". In: 503.3, pp. 707–720. DOI: 10.1051/0004-6361/200912520. arXiv: 0905.3552 [astro-ph.CO].

Bonafede, A. et al. (Sept. 2010a). "Galaxy cluster magnetic fields from radio polarized emission". In: *arXiv e-prints*, arXiv:1009.1233, arXiv:1009.1233. DOI: 10.48550/arXiv.1009.1233. arXiv: 1009.1233 [astro-ph.CO].

Bonafede, A. et al. (Apr. 2010b). "The Coma cluster magnetic field from Faraday rotation measures". In: 513, A30, A30. DOI: 10.1051/0004-6361/200913696. arXiv: 1002.0594 [astro-ph.CO].

— (Apr. 2010c). "The Coma cluster magnetic field from Faraday rotation measures". In: 513, A30, A30. DOI: 10.1051/0004-6361/200913696. arXiv: 1002.0594 [astro-ph.CO].

Bonafede, A. et al. (June 2011). "Fractional polarization as a probe of magnetic fields in the intra-cluster medium". In: 530, A24, A24. DOI: 10.1051/0004-6361/201016298. arXiv: 1103.0277 [astro-ph.CO].

Bonafede, A. et al. (Oct. 2012). "Discovery of radio haloes and double relics in distant MACS galaxy clusters: clues to the efficiency of particle acceleration". In: 426.1, pp. 40–56. DOI: 10.1111/j.1365-2966.2012.21570.x. arXiv: 1206.6102 [astro-ph.CO].

Bonafede, A. et al. (Aug. 2013). "Measurements and simulation of Faraday rotation across the Coma radio relic". In: 433.4, pp. 3208–3226. DOI: 10.1093/mnras/stt960. arXiv: 1305.7228 [astro-ph.CO].

Bonafede, A. et al. (Apr. 2014). "Evidence for Particle Re-acceleration in the Radio Relic in the Galaxy Cluster PLCKG287.0+32.9". In: 785.1, 1, p. 1. DOI: 10.1088/0004-637X/785/1/1. arXiv: 1402.1492 [astro-ph.CO].

Bonafede, A. et al. (Sept. 2017). "On the absence of radio haloes in clusters with double relics". In: 470.3, pp. 3465–3475. DOI: 10.1093/mnras/stx1475. arXiv: 1706.04203 [astro-ph.CO].

Bonafede, A. et al. (Aug. 2018). "LOFAR discoveryof radio emission in MACS J0717.5+3745". In: 478.3, pp. 2927–2938. DOI: 10.1093/mnras/sty1121. arXiv: 1805.00473 [astro-ph.GA].

Bonafede, A. et al. (Jan. 2021). "The Coma Cluster at LOw Frequency ARray Frequencies. I. Insights into Particle Acceleration Mechanisms in the Radio Bridge". In: 907.1, 32, p. 32. DOI: 10.3847/1538-4357/abcb8f. arXiv: 2011.08856 [astro-ph.CO].

Bonafede, A. et al. (July 2022). "The Coma Cluster at LOFAR Frequencies. II. The Halo, Relic, and a New Accretion Relic". In: 933.2, 218, p. 218. DOI: 10.3847/1538-4357/ac721d. arXiv: 2203.01958 [astro-ph.HE].

Bond, J. Richard, Lev Kofman, and Dmitry Pogosyan (Apr. 1996). "How filaments of galaxies are woven into the cosmic web". In: 380.6575, pp. 603–606. DOI: 10.1038/380603a0. arXiv: astro-ph/9512141 [astro-ph].

Bonjean, V. et al. (Jan. 2018). "Gas and galaxies in filaments between clusters of galaxies. The study of A399-A401". In: 609, A49, A49. DOI: 10.1051/0004-6361/201731699. arXiv: 1710.08699 [astro-ph.CO].

Botteon, A. et al. (July 2016). "A shock at the radio relic position in Abell 115". In: 460.1, pp. L84–L88. DOI: 10.1093/mnrasl/slw082. arXiv: 1604.07823 [astro-ph.HE].

Botteon, A. et al. (July 2018). "LOFAR discovery of a double radio halo system in Abell 1758 and radio/X-ray study of the cluster pair". In: 478.1, pp. 885–898. DOI: 10.1093/mnras/sty1102. arXiv: 1804.09187 [astro-ph.CO].

Botteon, A. et al. (Dec. 2020). "A giant radio bridge connecting two galaxy clusters in Abell 1758". In: 499.1, pp. L11–L15. DOI: 10.1093/mnrasl/slaa142. arXiv: 2008.09613 [astro-ph.GA].

Botteon, A. et al. (Apr. 2022). "The Planck clusters in the LOFAR sky. I. LoTSS-DR2: New detections and sample overview". In: 660, A78, A78. DOI: 10.1051/0004-6361/202143020. arXiv: 2202.11720 [astro-ph.CO].

Botteon, Andrea et al. (June 2023). "Surface brightness discontinuities in radio halos. Insights from the MeerKAT Galaxy Cluster Legacy Survey". In: 674, A53, A53. DOI: 10.1051/0004-6361/202346150. arXiv: 2302.07881 [astro-ph.CO].

Boxelaar, J. M., R. J. van Weeren, and A. Botteon (Apr. 2021). "A robust model for flux density calculations of radio halos in galaxy clusters: Halo-FDCA". In: *Astronomy and Computing* 35, 100464, p. 100464. DOI: 10.1016/j.ascom.2021.100464. arXiv: 2103.08554 [astro-ph.CO].

Brentjens, M. A. and A. G. de Bruyn (Oct. 2005). "Faraday rotation measure synthesis". In: 441.3, pp. 1217–1228. DOI: 10.1051/0004-6361:20052990. arXiv: astro-ph/0507349 [astro-ph].

Briggs, D. S. (Dec. 1995a). "High Fidelity Interferometric Imaging: Robust Weighting and NNLS Deconvolution". In: *American Astronomical Society Meeting Abstracts*. Vol. 187. American Astronomical Society Meeting Abstracts, 112.02, p. 112.02.

Briggs, D. S. and T. J. Cornwell (Jan. 1992). "An Alternative Interpretation for the Physical Basis of CLEAN". In: *Astronomical Data Analysis Software and Systems*

I. Ed. by Diana M. Worrall, Chris Biemesderfer, and Jeannette Barnes. Vol. 25. Astronomical Society of the Pacific Conference Series, p. 170.

Briggs D., S. (Aug. 1995b). "PhD thesis, "High fidelity deconvolution of moderately resolved sources". In: *PhD thesis, "High fidelity deconvolution of moderately resolved sources, New Mexico Institute of Mining Technology, Socorro, New Mexico, USA*.

Brown, S. et al. (July 2017). "Limiting magnetic fields in the cosmic web with diffuse radio emission". In: 468.4, pp. 4246–4253. DOI: 10.1093/mnras/stx746. arXiv: 1703.07829 [astro-ph.CO].

Brüggen, M., R. J. van Weeren, and H. J. A. Röttgering (Sept. 2012). "Simulating the toothbrush: evidence for a triple merger of galaxy clusters". In: 425.1, pp. L76–L80. DOI: 10.1111/j.1745-3933.2012.01304.x. arXiv: 1206.6118 [astro-ph.CO].

Brunetti, G. and A. Lazarian (June 2007). "Compressible turbulence in galaxy clusters: physics and stochastic particle re-acceleration". In: 378.1, pp. 245–275. DOI: 10.1111/j.1365-2966.2007.11771.x. arXiv: astro-ph/0703591 [astro-ph].

— (Apr. 2011). "Particle reacceleration by compressible turbulence in galaxy clusters: effects of a reduced mean free path". In: 412.2, pp. 817–824. DOI: 10.1111/j.1365-2966.2010.17937.x. arXiv: 1011.1198 [astro-ph.CO].

— (May 2016). "Stochastic reacceleration of relativistic electrons by turbulent reconnection: a mechanism for cluster-scale radio emission?" In: 458.3, pp. 2584–2595. DOI: 10.1093/mnras/stw496. arXiv: 1603.00458 [astro-ph.HE].

Brunetti, G. et al. (Jan. 2001). "Particle reacceleration in the Coma cluster: radio properties and hard X-ray emission". In: 320.3, pp. 365–378. DOI: 10.1046/j.1365-8711.2001.03978.x. arXiv: astro-ph/0008518 [astro-ph].

Brunetti, G. et al. (Oct. 2008). "A low-frequency radio halo associated with a cluster of galaxies". In: 455.7215, pp. 944–947. DOI: 10.1038/nature07379. arXiv: 0810.4288 [astro-ph].

Brunetti, G. et al. (Nov. 2009). "On the evolution of giant radio halos and their connection with cluster mergers". In: 507.2, pp. 661–669. DOI: 10.1051/0004-6361/200912751. arXiv: 0909.2343 [astro-ph.CO].

Brunetti, Gianfranco and Thomas W. Jones (Mar. 2014). "Cosmic Rays in Galaxy Clusters and Their Nonthermal Emission". In: *International Journal of Modern Physics D* 23.4, 1430007-98, pp. 1430007–98. DOI: 10.1142/S0218271814300079. arXiv: 1401.7519 [astro-ph.CO].

Brunetti, Gianfranco and Franco Vazza (Feb. 2020). "Second-order Fermi Reacceleration Mechanisms and Large-Scale Synchrotron Radio Emission in Intracluster Bridges". In: 124.5, 051101, p. 051101. DOI: 10.1103/PhysRevLett.124.051101. arXiv: 2001.07718 [astro-ph.HE].

Bruno, L. et al. (Oct. 2023). "A three-component giant radio halo: The puzzling case of the galaxy cluster Abell 2142". In: 678, A133, A133. DOI: 10.1051/0004-6361/202347245. arXiv: 2308.07603 [astro-ph.CO].

Buote, David A. (May 2001). "On the Origin of Radio Halos in Galaxy Clusters". In: 553.1, pp. L15–L18. DOI: 10.1086/320500. arXiv: astro-ph/0104211 [astro-ph].

Burn, B. J. (Jan. 1966). "On the depolarization of discrete radio sources by Faraday dispersion". In: 133, p. 67. DOI: 10.1093/mnras/133.1.67.

Caprioli, Damiano, Horace Zhang, and Anatoly Spitkovsky (June 2018). "Diffusive shock re-acceleration". In: *Journal of Plasma Physics* 84.3, 715840301, p. 715840301. DOI: 10.1017/S0022377818000478. arXiv: 1801.01510 [astro-ph.HE].

Carilli, C. L. and G. B. Taylor (Jan. 2002). "Cluster Magnetic Fields". In: 40, pp. 319–348. DOI: 10.1146/annurev.astro.40.060401.093852. arXiv: astro-ph/0110655 [astro-ph].

Carlstrom, John E., Gilbert P. Holder, and Erik D. Reese (Jan. 2002). "Cosmology with the Sunyaev-Zel'dovich Effect". In: 40, pp. 643–680. DOI: 10.1146/annurev.astro.40.060401.093803. arXiv: astro-ph/0208192 [astro-ph].

Carretti, E. et al. (Apr. 2013). "Detection of a radio bridge in Abell 3667". In: 430.2, pp. 1414–1422. DOI: 10.1093/mnras/stt002. arXiv: 1205.1082 [astro-ph.CO].

Carretti, E. et al. (Jan. 2023). "Magnetic field evolution in cosmic filaments with LOFAR data". In: 518.2, pp. 2273–2286. DOI: 10.1093/mnras/stac2966. arXiv: 2210.06220 [astro-ph.CO].

Carretti, Ettore et al. (May 2022). "Magnetic field strength in cosmic web filaments". In: 512.1, pp. 945–959. DOI: 10.1093/mnras/stac384. arXiv: 2202.04607 [astro-ph.CO].

Cassano, R. et al. (Oct. 2010). "On the Connection Between Giant Radio Halos and Cluster Mergers". In: 721.2, pp. L82–L85. DOI: 10.1088/2041-8205/721/2/L82. arXiv: 1008.3624 [astro-ph.CO].

Cassano, R. et al. (Nov. 2013). "Revisiting Scaling Relations for Giant Radio Halos in Galaxy Clusters". In: 777.2, 141, p. 141. DOI: 10.1088/0004-637X/777/2/141. arXiv: 1306.4379 [astro-ph.CO].

Cassano, R. et al. (Apr. 2023). "The Planck clusters in the LOFAR sky. IV. LoTSS-DR2: Statistics of radio haloes and re-acceleration models". In: 672, A43, A43. DOI: 10.1051/0004-6361/202244876. arXiv: 2301.08052 [astro-ph.CO].

Cautun, Marius, Rien van de Weygaert, and Bernard J. T. Jones (Feb. 2013). "NEXUS: tracing the cosmic web connection". In: 429.2, pp. 1286–1308. DOI: 10.1093/mnras/sts416. arXiv: 1209.2043 [astro-ph.CO].

Cautun, Marius et al. (July 2014). "Evolution of the cosmic web". In: 441.4, pp. 2923–2973. DOI: 10.1093/mnras/stu768. arXiv: 1401.7866 [astro-ph.CO].

Cavaliere, A. and R. Fusco-Femiano (May 1976). "X-rays from hot plasma in clusters of galaxies". In: *Astronomy and Astrophysics* 49, pp. 137–144. ISSN: 0004-6361. URL: http://adsabs.harvard.edu/abs/1976A%26A....49..137C (visited on 09/28/2020).

Chandra, P., A. Ray, and S. Bhatnagar (Sept. 2004). "The Late-Time Radio Emission from SN 1993J at Meter Wavelengths". In: 612.2, pp. 974–987. DOI: 10.1086/422675. arXiv: astro-ph/0405448 [astro-ph].

CHEX-MATE Collaboration et al. (June 2021). "The Cluster HEritage project with XMM-Newton: Mass Assembly and Thermodynamics at the Endpoint of structure formation. I. Programme overview". In: 650, A104, A104. DOI: 10.1051/0004-6361/202039632. arXiv: 2010.11972 [astro-ph.CO].

Chisari, Nora Elisa et al. (June 2019). "Modelling baryonic feedback for survey cosmology". In: *The Open Journal of Astrophysics* 2.1, 4, p. 4. DOI: 10.21105/astro.1905.06082. arXiv: 1905.06082 [astro-ph.CO].

Cho, Jungyeon and Dongsu Ryu (Nov. 2009). "Characteristic Lengths of Magnetic Field in Magnetohydrodynamic Turbulence". In: 705.1, pp. L90–L94. DOI: 10.1088/0004-637X/705/1/L90. arXiv: 0908.0610 [astro-ph.CO].

Chow-Martínez, M. et al. (Dec. 2014). "Two new catalogues of superclusters of Abell/ACO galaxy clusters out to redshift 0.15". In: 445.4, pp. 4073–4085. DOI: 10.1093/mnras/stu1961. arXiv: 1409.5152 [astro-ph.CO].

Clark, B. G. (Sept. 1980). "An efficient implementation of the algorithm 'CLEAN'". In: 89.3, p. 377.

Colberg, Jörg M. (Feb. 2007). "Quantifying cosmic superstructures". In: 375.1, pp. 337–347. DOI: 10.1111/j.1365-2966.2006.11312.x. arXiv: astro-ph/0611641 [astro-ph].

Coles, Peter and Francesco Lucchin (2002). *Cosmology: The Origin and Evolution of Cosmic Structure, Second Edition*.

Condon, J. J. et al. (May 1998). "The NRAO VLA Sky Survey". In: 115.5, pp. 1693–1716. DOI: 10.1086/300337.

Condon, James J. (1988). "Radio sources and cosmology." In: *Galactic and Extragalactic Radio Astronomy*. Ed. by K. I. Kellermann and G. L. Verschuur, pp. 641–678.

Cooray, Suchetha et al. (Jan. 2021). "An iterative reconstruction algorithm for Faraday tomography". In: 500.4, pp. 5129–5141. DOI: 10.1093/mnras/staa3580. arXiv: 2011.10840 [astro-ph.IM].

Cornwell, T. J. (Aug. 1988). "Radio-interferometric imaging of very large objects." In: 202, pp. 316–321.

Cornwell, T. J., K. Golap, and S. Bhatnagar (Dec. 2005). "W Projection: A New Algorithm for Wide Field Imaging with Radio Synthesis Arrays". In: *Astronomical Data Analysis Software and Systems XIV*. Ed. by P. Shopbell, M. Britton, and R. Ebert. Vol. 347. Astronomical Society of the Pacific Conference Series, p. 86.

Cornwell, T. J. and R. A. Perley (Nov. 1992). "Book-Review - Radio Interferometry - Theory Techniques and Applications". In: *Science* 258, p. 1017.

Cornwell, T. J., M. A. Voronkov, and B. Humphreys (Oct. 2012). "Wide field imaging for the square kilometre array". In: *Image Reconstruction from Incomplete Data VII*. Ed. by Philip J. Bones, Michael A. Fiddy, and Rick P. Millane. Vol. 8500. Society of Photo-Optical Instrumentation Engineers (SPIE) Conference Series, 85000L, p. 85000L. DOI: 10.1117/12.929336. arXiv: 1207.5861 [astro-ph.IM].

Cotton, W. D. and J. M. Uson (Oct. 2008). "Pixelization and dynamic range in radio interferometry". In: 490.1, pp. 455–460. DOI: 10.1051/0004-6361:20079104. arXiv: 0809.1447 [astro-ph].

Cowie, L. L. and A. Songaila (Apr. 1977). "Thermal evaporation of gas within galaxies by a hot intergalactic medium". In: *Nature* 266, pp. 501–503. DOI: 10.1038/266501a0. URL: http://adsabs.harvard.edu/abs/1977Natur.266..501C (visited on 09/18/2020).

Cuciti, V. et al. (Aug. 2015). "Occurrence of radio halos in galaxy clusters. Insight from a mass-selected sample". In: 580, A97, A97. DOI: 10.1051/0004-6361/201526420. arXiv: 1506.03209 [astro-ph.CO].

Cuciti, V. et al. (Mar. 2021). "Radio halos in a mass-selected sample of 75 galaxy clusters. II. Statistical analysis". In: 647, A51, A51. DOI: 10.1051/0004-6361/202039208. arXiv: 2101.01641 [astro-ph.CO].

Cuciti, V. et al. (Sept. 2022). "Galaxy clusters enveloped by vast volumes of relativistic electrons". In: 609.7929, pp. 911–914. DOI: 10.1038/s41586-022-05149-3. arXiv: 2209.13617 [astro-ph.CO].

Dallacasa, D. et al. (July 2009). "Deep 1.4 GHz Follow-up of the Steep Spectrum Radio Halo in A521". In: 699.2, pp. 1288–1292. DOI: 10.1088/0004-637X/699/2/1288. arXiv: 0905.0588 [astro-ph.CO].

de Gasperin, F. et al. (Nov. 2014). "A new double radio relic in PSZ1 G096.89+24.17 and a radio relic mass-luminosity relation". In: 444.4, pp. 3130–3138. DOI: 10.1093/mnras/stu1658. arXiv: 1408.2677 [astro-ph.CO].

de Gasperin, F. et al. (Nov. 2015). "A powerful double radio relic system discovered in PSZ1 G108.18-11.53: evidence for a shock with non-uniform Mach number?" In: 453.4, pp. 3483–3498. DOI: 10.1093/mnras/stv1873. arXiv: 1508.02901 [astro-ph.HE].

de Gasperin, F. et al. (Aug. 2018). "The effect of the ionosphere on ultra-low-frequency radio-interferometric observations". In: 615, A179, A179. DOI: 10.1051/0004-6361/201833012. arXiv: 1804.07947 [astro-ph.IM].

de Gasperin, F. et al. (Feb. 2019). "Systematic effects in LOFAR data: A unified calibration strategy". In: 622, A5, A5. DOI: 10.1051/0004-6361/201833867. arXiv: 1811.07954 [astro-ph.IM].

de Gasperin, F. et al. (Mar. 2020a). "Cassiopeia A, Cygnus A, Taurus A, and Virgo A at ultra-low radio frequencies". In: 635, A150, A150. DOI: 10.1051/0004-6361/201936844. arXiv: 2002.10431 [astro-ph.HE].

de Gasperin, F. et al. (Oct. 2020b). "Reaching thermal noise at ultra-low radio frequencies. Toothbrush radio relic downstream of the shock front". In: 642, A85, A85. DOI: 10.1051/0004-6361/202038663. arXiv: 2007.16043 [astro-ph.HE].

de Gasperin, F. et al. (Apr. 2021). "The LOFAR LBA Sky Survey. I. Survey description and preliminary data release". In: 648, A104, A104. DOI: 10.1051/0004-6361/202140316. arXiv: 2102.09238 [astro-ph.IM].

de Gasperin, F. et al. (Mar. 2022). "MeerKAT view of the diffuse radio sources in Abell 3667 and their interactions with the thermal plasma". In: 659, A146, A146. DOI: 10.1051/0004-6361/202142658. arXiv: 2111.06940 [astro-ph.CO].

de Gasperin, F. et al. (May 2023). "The LOFAR LBA Sky Survey. II. First data release". In: 673, A165, A165. DOI: 10.1051/0004-6361/202245389. arXiv: 2301.12724 [astro-ph.IM].

de Graaff, Anna et al. (Apr. 2019). "Probing the missing baryons with the Sunyaev-Zel'dovich effect from filaments". In: 624, A48, A48. DOI: 10.1051/0004-6361/201935159. arXiv: 1709.10378 [astro-ph.CO].

de Jong, J. M. G. H. J. et al. (Sept. 2022). "A deep study of A399-401: An application for wide-field facet calibration". In: *arXiv e-prints*, arXiv:2209.13930, arXiv:2209.13930. arXiv: 2209.13930 [astro-ph.HE].

De Rubeis, E. et al. (Aug. 2024). "Magnetic fields in the outskirts of PSZ2 G096.88+24.18 from depolarization analysis of radio relics". In: *arXiv e-prints*, arXiv:2408.08603, arXiv:2408.08603. DOI: 10.48550/arXiv.2408.08603. arXiv: 2408.08603 [astro-ph.CO].

Di Gennaro, G. et al. (Oct. 2021). "A LOFAR-uGMRT spectral index study of distant radio halos". In: 654, A166, A166. DOI: 10.1051/0004-6361/202141510. arXiv: 2108.10562 [astro-ph.CO].

Dolag, K., A. M. Bykov, and A. Diaferio (Feb. 2008). "Non-Thermal Processes in Cosmological Simulations". In: 134.1-4, pp. 311–335. DOI: 10.1007/s11214-008-9319-2. arXiv: 0801.1048 [astro-ph].

Dolag, K. et al. (Aug. 2006). "Simulating the physical properties of dark matter and gas inside the cosmic web". In: 370.2, pp. 656–672. DOI: 10.1111/j.1365-2966.2006.10511.x. arXiv: astro-ph/0511357 [astro-ph].

Dolag, Klaus et al. (Dec. 2004). "Magnetic Field in the Local Universe and the Propagation of UHECRS". In: *Journal of Korean Astronomical Society* 37.5, pp. 427–431. DOI: 10.5303/JKAS.2004.37.5.427.

Domínguez-Fernández, P. et al. (June 2019). "Dynamical evolution of magnetic fields in the intracluster medium". In: 486.1, pp. 623–638. DOI: 10.1093/mnras/stz877. arXiv: 1903.11052 [astro-ph.CO].

Donnert, J. et al. (Jan. 2009). "Cluster magnetic fields from galactic outflows". In: 392.3, pp. 1008–1021. DOI: 10.1111/j.1365-2966.2008.14132.x. arXiv: 0808.0919 [astro-ph].

Donnert, J. et al. (Mar. 2013). "Rise and fall of radio haloes in simulated merging galaxy clusters". In: 429.4, pp. 3564–3569. DOI: 10.1093/mnras/sts628. arXiv: 1211.3337 [astro-ph.CO].

Donnert, J. et al. (Dec. 2018). "Magnetic Field Amplification in Galaxy Clusters and Its Simulation". In: 214.8, 122, p. 122. DOI: 10.1007/s11214-018-0556-8. arXiv: 1810.09783 [astro-ph.CO].

Duchesne, S. W. et al. (Apr. 2022). "The merging galaxy cluster Abell 3266 at low radio frequencies". In: 511.3, pp. 3525–3535. DOI: 10.1093/mnras/stac335. arXiv: 2201.09629 [astro-ph.CO].

Durrer, Ruth and Andrii Neronov (June 2013). "Cosmological magnetic fields: their generation, evolution and observation". In: 21, 62, p. 62. DOI: 10.1007/s00159-013-0062-7. arXiv: 1303.7121 [astro-ph.CO].

Ebeling, H. et al. (Dec. 1998). "The ROSAT Brightest Cluster Sample - I. The compilation of the sample and the cluster log N-log S distribution". In: 301.4, pp. 881–914. DOI: 10.1046/j.1365-8711.1998.01949.x. arXiv: astro-ph/9812394 [astro-ph].

Eckert, D. et al. (Sept. 2016). "A shock front at the radio relic of Abell 2744". In: 461.2, pp. 1302–1307. DOI: 10.1093/mnras/stw1435. arXiv: 1603.02272 [astro-ph.HE].

Einasto, J., M. Joeveer, and E. Saar (Nov. 1980). "Structure of superclusters and supercluster formation". In: 193, pp. 353–375. DOI: 10.1093/mnras/193.2.353.

Einasto, J. et al. (Dec. 1975). "Superclusters of galaxies". In: *Astronomicheskij Tsirkulyar* 895, pp. 2–4.

Einasto, J. et al. (Feb. 1984). "Structure of superclusters and supercluster formation - III. Quantitative study of the Local Supercluster." In: 206, pp. 529–558. DOI: 10.1093/mnras/206.3.529.

Einasto, J. et al. (Feb. 2007). "Superclusters of galaxies from the 2dF redshift survey. II. Comparison with simulations". In: 462.2, pp. 397–410. DOI: 10.1051/0004-6361:20065501. arXiv: astro-ph/0604539 [astro-ph].

Einasto, Maret et al. (May 2021). "The Corona Borealis supercluster: connectivity, collapse, and evolution". In: 649, A51, A51. DOI: 10.1051/0004-6361/202040200. arXiv: 2103.02326 [astro-ph.CO].

Ekers, R. D. and A. H. Rots (Jan. 1979). "Short Spacing Synthesis from a Primary Beam Scanned Interferometer". In: *IAU Colloq. 49: Image Formation from Coherence Functions in Astronomy*. Ed. by C. van Schooneveld. Vol. 76. Astrophysics and Space Science Library, p. 61. DOI: 10.1007/978-94-009-9449-2_7. arXiv: 1212.3311 [astro-ph.IM].

Enßlin, T. A. and C. Vogt (Apr. 2003). "The magnetic power spectrum in Faraday rotation screens". In: 401, pp. 835–848. DOI: 10.1051/0004-6361:20030172. arXiv: astro-ph/0302426 [astro-ph].

Ensslin, Torsten A. et al. (Apr. 1998). "Cluster radio relics as a tracer of shock waves of the large-scale structure formation". In: 332, pp. 395–409. DOI: 10.48550/arXiv.astro-ph/9712293. arXiv: astro-ph/9712293 [astro-ph].

Ettori, S. and F. Brighenti (June 2008). "On the evolution of cooling cores in X-ray galaxy clusters". en. In: *Monthly Notices RAS* 387.2, pp. 631–638. ISSN: 0035-8711, 1365-2966. DOI: 10.1111/j.1365-2966.2008.13054.x. URL: https://academic.oup.com/mnras/article-lookup/doi/10.1111/j.1365-2966.2008.13054.x (visited on 09/22/2020).

Ettori, S. et al. (Dec. 2010). "Mass profiles and c-M_{DM} relation in X-ray luminous galaxy clusters". In: 524, A68, A68. DOI: 10.1051/0004-6361/201015271.

Farnsworth, Damon, Lawrence Rudnick, and Shea Brown (June 2011). "Integrated Polarization of Sources at $\lambda \sim 1$ m and New Rotation Measure Ambiguities". In:

141.6, 191, p. 191. DOI: 10.1088/0004-6256/141/6/191. arXiv: 1103.4149 [astro-ph.CO].

Farnsworth, Damon et al. (Dec. 2013). "Discovery of Megaparsec-scale, Low Surface Brightness Nonthermal Emission in Merging Galaxy Clusters Using the Green Bank Telescope". In: 779.2, 189, p. 189. DOI: 10.1088/0004-637X/779/2/189. arXiv: 1311.3313 [astro-ph.CO].

Feretti, L. and G. Giovannini (Jan. 1996). "Diffuse Cluster Radio Sources (Review)". In: *Extragalactic Radio Sources*. Ed. by Ron D. Ekers, C. Fanti, and L. Padrielli. Vol. 175. IAU Symposium, p. 333.

Feretti, Luigina et al. (May 2012). "Clusters of galaxies: observational properties of the diffuse radio emission". In: 20, 54, p. 54. DOI: 10.1007/s00159-012-0054-z. arXiv: 1205.1919 [astro-ph.CO].

Fermi, ENRICO (1949). "On the Origin of the Cosmic Radiation". In: *Phys. Rev.* 75 (8), pp. 1169–1174. DOI: 10.1103/PhysRev.75.1169. URL: https://link.aps.org/doi/10.1103/PhysRev.75.1169.

Foreman-Mackey, Daniel et al. (Mar. 2013). "emcee: The MCMC Hammer". In: 125.925, p. 306. DOI: 10.1086/670067. arXiv: 1202.3665 [astro-ph.IM].

Frick, P. et al. (Jan. 2010). "Wavelet-based Faraday rotation measure synthesis". In: 401.1, pp. L24–L28. DOI: 10.1111/j.1745-3933.2009.00778.x. arXiv: 0911.0261 [astro-ph.GA].

Fujita, Yutaka et al. (Apr. 1996). "The X-Ray Structure of A399 and A401: A Pre-Merging Cluster Pair". In: 48, pp. 191–200. DOI: 10.1093/pasj/48.2.191. arXiv: astro-ph/9602059 [astro-ph].

Fujita, Yutaka et al. (Jan. 2008). "High Metallicity of the X-Ray Gas Up to the Virial Radius of a Binary Cluster of Galaxies: Evidence of Galactic Superwinds at High-Redshift". In: 60, S343. DOI: 10.1093/pasj/60.sp1.S343. arXiv: 0705.2017 [astro-ph].

Genovese, Christopher R. et al. (Mar. 2010). "The Geometry of Nonparametric Filament Estimation". In: *arXiv e-prints*, arXiv:1003.5536, arXiv:1003.5536. DOI: 10.48550/arXiv.1003.5536. arXiv: 1003.5536 [math.ST].

George, Samuel J., Jeroen M. Stil, and Ben W. Keller (Oct. 2012). "Detection Thresholds and Bias Correction in Polarized Intensity". In: 29.3, pp. 214–220. DOI: 10.1071/AS11027. arXiv: 1106.5362 [astro-ph.IM].

Ghirardini, V. et al. (Jan. 2019). "Universal thermodynamic properties of the intracluster medium over two decades in radius in the X-COP sample". In: 621, A41, A41. DOI: 10.1051/0004-6361/201833325. arXiv: 1805.00042 [astro-ph.CO].

Giovannini, G., L. Feretti, and C. Stanghellini (Dec. 1991). "The Coma cluster radio source 1253+275, revisited." In: 252, pp. 528–537.

Gitti, M., R. Piffaretti, and S. Schindler (Sept. 2007). "Mass distribution in the most X-ray-luminous galaxy cluster RX J1347.5-1145 studied with *XMM-Newton*". en. In: *A&A* 472.2, pp. 383–394. ISSN: 0004-6361, 1432-0746. DOI: 10.1051/0004-6361:

20077580. URL: http://www.aanda.org/10.1051/0004-6361:20077580 (visited on 09/22/2020).

Gitti, Myriam, Fabrizio Brighenti, and Brian R. McNamara (Jan. 2012). *Evidence for AGN Feedback in Galaxy Clusters and Groups*. en. Review Article. ISSN: 1687-7969 Pages: e950641 Publisher: Hindawi Volume: 2012. DOI: https://doi.org/10.1155/2012/950641. URL: https://www.hindawi.com/journals/aa/2012/950641/ (visited on 09/16/2020).

González, Roberto E. and Nelson D. Padilla (Sept. 2010). "Automated detection of filaments in the large-scale structure of the Universe". In: 407.3, pp. 1449–1463. DOI: 10.1111/j.1365-2966.2010.17015.x. arXiv: 0912.0006 [astro-ph.CO].

Gorkom, J. H. van (Aug. 2003). "Interaction of Galaxies with the ICM". In: *arXiv:astro-ph/0308209*. arXiv: astro-ph/0308209. URL: http://arxiv.org/abs/astro-ph/0308209 (visited on 09/18/2020).

Govoni, F. et al. (Apr. 2001). "A comparison of radio and X-ray morphologies of four clusters of galaxies containing radio halos". In: 369, pp. 441–449. DOI: 10.1051/0004-6361:20010115. arXiv: astro-ph/0101418 [astro-ph].

Govoni, F. et al. (July 2017). "Sardinia Radio Telescope observations of Abell 194. The intra-cluster magnetic field power spectrum". In: 603, A122, A122. DOI: 10.1051/0004-6361/201630349. arXiv: 1703.08688 [astro-ph.CO].

Govoni, F. et al. (June 2019). "A radio ridge connecting two galaxy clusters in a filament of the cosmic web". In: *Science* 364.6444, pp. 981–984. DOI: 10.1126/science.aat7500. arXiv: 1906.07584 [astro-ph.GA].

Gunn, James E. and J. Richard Gott (Aug. 1972). "On the Infall of Matter Into Clusters of Galaxies and Some Effects on Their Evolution". en. In: *The Astrophysical Journal* 176, p. 1. ISSN: 0004-637X. DOI: 10.1086/151605. URL: https://ui.adsabs.harvard.edu/abs/1972ApJ...176....1G/abstract (visited on 09/18/2020).

Gupta, Y. et al. (Aug. 2017). "The upgraded GMRT: opening new windows on the radio Universe". In: *Current Science* 113.4, pp. 707–714. DOI: 10.18520/cs/v113/i04/707-714.

Ha, Ji-Hoon, Dongsu Ryu, and Hyesung Kang (Apr. 2018). "Properties of Merger Shocks in Merging Galaxy Clusters". In: 857.1, 26, p. 26. DOI: 10.3847/1538-4357/aab4a2. arXiv: 1706.05509 [astro-ph.CO].

Hales, C. A. et al. (Aug. 2012). "Analytic detection thresholds for measurements of linearly polarized intensity using rotation measure synthesis". In: 424.3, pp. 2160–2172. DOI: 10.1111/j.1365-2966.2012.21372.x. arXiv: 1205.5310 [astro-ph.IM].

Hallman, Eric J. and Maxim Markevitch (Aug. 2004). "Chandra Observation of the Merging Cluster A168: A Late Stage in the Evolution of a Cold Front". In: 610.2, pp. L81–L84. DOI: 10.1086/423449. arXiv: astro-ph/0406322 [astro-ph].

Hamaker, J. P., J. D. Bregman, and R. J. Sault (May 1996). "Understanding radio polarimetry. I. Mathematical foundations." In: 117, pp. 137–147.

Hardcastle, M. J. and J. H. Croston (June 2020). "Radio galaxies and feedback from AGN jets". In: 88, 101539, p. 101539. DOI: 10.1016/j.newar.2020.101539. arXiv: 2003.06137 [astro-ph.HE].

Hardcastle, M. J. et al. (Feb. 2019). "Radio-loud AGN in the first LoTSS data release. The lifetimes and environmental impact of jet-driven sources". In: 622, A12, A12. DOI: 10.1051/0004-6361/201833893. arXiv: 1811.07943 [astro-ph.GA].

Harris, D. E. et al. (Mar. 2019). "LOFAR Observations of 4C+19.44: On the Discovery of Low-frequency Spectral Curvature in Relativistic Jet Knots". In: 873.1, 21, p. 21. DOI: 10.3847/1538-4357/ab01ff. arXiv: 1903.06824 [astro-ph.GA].

Harrison, E. R. (Jan. 1973). "Origin of Magnetic Fields in the Early Universe". In: 30.5, pp. 188–190. DOI: 10.1103/PhysRevLett.30.188.

Heald, George (Apr. 2009). "The Faraday rotation measure synthesis technique". In: *Cosmic Magnetic Fields: From Planets, to Stars and Galaxies*. Ed. by Klaus G. Strassmeier, Alexander G. Kosovichev, and John E. Beckman. Vol. 259. IAU Symposium, pp. 591–602. DOI: 10.1017/S1743921309031421.

Heald, George et al. (July 2020). "Magnetism Science with the Square Kilometre Array". In: *Galaxies* 8.3, 53, p. 53. DOI: 10.3390/galaxies8030053. arXiv: 2006.03172 [astro-ph.GA].

Hill, G. J. et al. (Oct. 2008). "The Hobby-Eberly Telescope Dark Energy Experiment (HETDEX): Description and Early Pilot Survey Results". In: *Panoramic Views of Galaxy Formation and Evolution*. Ed. by T. Kodama, T. Yamada, and K. Aoki. Vol. 399. Astronomical Society of the Pacific Conference Series, p. 115. DOI: 10.48550/arXiv.0806.0183. arXiv: 0806.0183 [astro-ph].

Hill, John M. and William R. Oegerle (Oct. 1998). "Dynamics of cD Clusters of Galaxies. III. Redshift Data for 11 Abell Clusters". In: 116.4, pp. 1529–1540. DOI: 10.1086/300575.

Hincks, Adam D. et al. (Mar. 2022). "A high-resolution view of the filament of gas between Abell 399 and Abell 401 from the Atacama Cosmology Telescope and MUSTANG-2". In: 510.3, pp. 3335–3355. DOI: 10.1093/mnras/stab3391. arXiv: 2107.04611 [astro-ph.CO].

Hindson, L. et al. (Nov. 2014). "The First Murchison Widefield Array low-frequency radio observations of cluster scale non-thermal emission: the case of Abell 3667". In: 445.1, pp. 330–346. DOI: 10.1093/mnras/stu1669. arXiv: 1408.3167 [astro-ph.GA].

Hoang, D. N. et al. (Oct. 2017). "Deep LOFAR observations of the merging galaxy cluster CIZA J2242.8+5301". In: 471.1, pp. 1107–1125. DOI: 10.1093/mnras/stx1645. arXiv: 1706.09903 [astro-ph.GA].

Hoang, D. N. et al. (Aug. 2018). "Radio observations of the double-relic galaxy cluster Abell 1240". In: 478.2, pp. 2218–2233. DOI: 10.1093/mnras/sty1123. arXiv: 1804.11352 [astro-ph.HE].

Hoang, D. N. et al. (Feb. 2019). "Radio observations of the merging galaxy cluster Abell 520". In: 622, A20, A20. DOI: 10.1051/0004-6361/201833900. arXiv: 1811.09713 [astro-ph.HE].

Hoeft, M. et al. (Oct. 2021). "Abell 1430: A merging cluster with exceptional diffuse radio emission". In: 654, A68, A68. DOI: 10.1051/0004-6361/202039725. arXiv: 2010.10331 [astro-ph.CO].

Högbom, J. A. (June 1974). "Aperture Synthesis with a Non-Regular Distribution of Interferometer Baselines". In: 15, p. 417.

Holdaway, M. A. (Jan. 1999). "Mosaicing with Interferometric Arrays". In: *Synthesis Imaging in Radio Astronomy II*. Ed. by G. B. Taylor, C. L. Carilli, and R. A. Perley. Vol. 180. Astronomical Society of the Pacific Conference Series, p. 401.

Hoyle, Fiona et al. (Dec. 2002). "Two-dimensional Topology of the Sloan Digital Sky Survey". In: 580.2, pp. 663–671. DOI: 10.1086/343734. arXiv: astro-ph/0206146 [astro-ph].

Huchra, John P., Michael S. Vogeley, and Margaret J. Geller (Apr. 1999). "The CFA Redshift Survey: Data for the South Galactic CAP". In: 121.2, pp. 287–368. DOI: 10.1086/313194.

Huchra, John P. et al. (Apr. 2012). "The 2MASS Redshift Survey—Description and Data Release". In: 199.2, 26, p. 26. DOI: 10.1088/0067-0049/199/2/26. arXiv: 1108.0669 [astro-ph.CO].

Humphreys, B and T Cornwell (2011). "Memo 132, analysis of convolutional resampling algorithm performance". In: *Square Kilometre Array, Tech. Rep* 11.

Hutschenreuter, S. et al. (Jan. 2022). "The Galactic Faraday rotation sky 2020". In: 657, A43, A43. DOI: 10.1051/0004-6361/202140486. arXiv: 2102.01709 [astro-ph.GA].

Hutschenreuter, Sebastian and Torsten A. Enßlin (Jan. 2020). "The Galactic Faraday depth sky revisited". In: 633, A150, A150. DOI: 10.1051/0004-6361/201935479. arXiv: 1903.06735 [astro-ph.GA].

Iapichino, L. et al. (July 2011). "Turbulence production and turbulent pressure support in the intergalactic medium". In: 414.3, pp. 2297–2308. DOI: 10.1111/j.1365-2966.2011.18550.x. arXiv: 1102.3352 [astro-ph.CO].

Iapichino, Luigi and Marcus Brüggen (July 2012). "Magnetic field amplification by shocks in galaxy clusters: application to radio relics". In: 423.3, pp. 2781–2788. DOI: 10.1111/j.1365-2966.2012.21084.x. arXiv: 1204.2455 [astro-ph.CO].

Ideguchi, Shinsuke, Yoshimitsu Miyashita, and George Heald (Dec. 2018). "Faraday Tomography Tutorial". In: *Galaxies* 6.4, 140, p. 140. DOI: 10.3390/galaxies6040140.

Intema, H. T. et al. (July 2009). "Ionospheric calibration of low frequency radio interferometric observations using the peeling scheme. I. Method description and first results". In: 501.3, pp. 1185–1205. DOI: 10.1051/0004-6361/200811094. arXiv: 0904.3975 [astro-ph.IM].

Intema, H. T. et al. (Feb. 2017). "The GMRT 150 MHz all-sky radio survey. First alternative data release TGSS ADR1". In: 598, A78, A78. DOI: 10.1051/0004-6361/201628536. arXiv: 1603.04368 [astro-ph.CO].

Intema, Huib T. (Aug. 2014). *SPAM: Source Peeling and Atmospheric Modeling*. Astrophysics Source Code Library, record ascl:1408.006. ascl: 1408.006.

Jackson, N. et al. (Nov. 2016). "LBCS: The LOFAR Long-Baseline Calibrator Survey". In: 595, A86, A86. DOI: 10.1051/0004-6361/201629016. arXiv: 1608.02133 [astro-ph.IM].

Johnston-Hollitt, Melanie (July 2003). "Detection of magnetic fields and diffuse radio emission in Abell 3667 and other rich southern clusters of galaxies". PhD thesis. University of Adelaide, Australia.

Jones, A. et al. (Dec. 2023). "The Planck clusters in the LOFAR sky. VI. LoTSS-DR2: Properties of radio relics". In: 680, A31, A31. DOI: 10.1051/0004-6361/202245102. arXiv: 2301.07814 [astro-ph.CO].

Kahniashvili, Tina, Axel Brandenburg, and Alexander G. Tevzadze (Oct. 2016). "The evolution of primordial magnetic fields since their generation". In: 91.10, 104008, p. 104008. DOI: 10.1088/0031-8949/91/10/104008. arXiv: 1507.00510 [astro-ph.CO].

Kahniashvili, Tina, Alexander G. Tevzadze, and Bharat Ratra (Jan. 2011). "Phase Transition Generated Cosmological Magnetic Field at Large Scales". In: 726.2, 78, p. 78. DOI: 10.1088/0004-637X/726/2/78. arXiv: 0907.0197 [astro-ph.CO].

Kahniashvili, Tina et al. (Oct. 2010). "Primordial magnetic field limits from cosmological data". In: 82.8, 083005, p. 083005. DOI: 10.1103/PhysRevD.82.083005. arXiv: 1009.2094 [astro-ph.CO].

Kale, R. et al. (Sept. 2013). "The Extended GMRT Radio Halo Survey. I. New upper limits on radio halos and mini-halos". In: 557, A99, A99. DOI: 10.1051/0004-6361/201321515. arXiv: 1306.3102 [astro-ph.CO].

Kale, R. et al. (Sept. 2015). "Brightest cluster galaxies in the extended GMRT radio halo cluster sample. Radio properties and cluster dynamics". In: 581, A23, A23. DOI: 10.1051/0004-6361/201526341. arXiv: 1506.05612 [astro-ph.GA].

Kang, Hyesung, Dongsu Ryu, and T. W. Jones (Sept. 2012). "Diffusive Shock Acceleration Simulations of Radio Relics". In: 756.1, 97, p. 97. DOI: 10.1088/0004-637X/756/1/97. arXiv: 1205.1895 [astro-ph.HE].

Kang, Hyesung et al. (June 2014). "Injection of κ-like Suprathermal Particles into Diffusive Shock Acceleration". In: 788.2, 142, p. 142. DOI: 10.1088/0004-637X/788/2/142. arXiv: 1405.0557 [astro-ph.HE].

Kelly, Brandon C. (Aug. 2007). "Some Aspects of Measurement Error in Linear Regression of Astronomical Data". In: 665.2, pp. 1489–1506. DOI: 10.1086/519947. arXiv: 0705.2774 [astro-ph].

Kempner, Joshua C. and Craig L. Sarazin (Feb. 2001). "Radio Halo and Relic Candidates from the Westerbork Northern Sky Survey". In: 548.2, pp. 639–651. DOI: 10.1086/319024. arXiv: astro-ph/0010251 [astro-ph].

Kim, K. T. et al. (Oct. 1989). "Discovery of intergalactic radio emission in the Coma-A1367 supercluster". In: 341.6244, pp. 720–723. DOI: 10.1038/341720a0.

King, Ivan (Oct. 1962). "The structure of star clusters. I. an empirical density law". In: *The Astronomical Journal* 67, p. 471. DOI: 10.1086/108756. URL: http://adsabs.harvard.edu/abs/1962AJ.....67..471K (visited on 09/22/2020).

Klypin, Anatoly A., Sebastian Trujillo-Gomez, and Joel Primack (Oct. 2011). "Dark Matter Halos in the Standard Cosmological Model: Results from the Bolshoi Simulation". In: 740.2, 102, p. 102. DOI: 10.1088/0004-637X/740/2/102. arXiv: 1002.3660 [astro-ph.CO].

Knuettel, S. et al. (Feb. 2019). "The magnetic field strength of the Faraday screen surrounding the radio galaxy Coma A". In: 482.4, pp. 4606–4616. DOI: 10.1093/mnras/sty3018. arXiv: 1811.02844 [astro-ph.GA].

Kravtsov, Andrey V. and Stefano Borgani (Sept. 2012). "Formation of Galaxy Clusters". In: 50, pp. 353–409. DOI: 10.1146/annurev-astro-081811-125502. arXiv: 1205.5556 [astro-ph.CO].

Krymskii, G. F. (June 1977). "A regular mechanism for the acceleration of charged particles on the front of a shock wave". In: *Akademiia Nauk SSSR Doklady* 234, pp. 1306–1308.

Laing, R. A. et al. (Dec. 2008). "Structures of the magnetoionic media around the Fanaroff-Riley Class I radio galaxies 3C31 and Hydra A". In: 391.2, pp. 521–549. DOI: 10.1111/j.1365-2966.2008.13895.x. arXiv: 0809.2411 [astro-ph].

Lal, D. V. et al. (Aug. 2022). "High-resolution, High-sensitivity, Low-frequency uGMRT View of Coma Cluster of Galaxies". In: 934.2, 170, p. 170. DOI: 10.3847/1538-4357/ac7a9b. arXiv: 2207.06624 [astro-ph.GA].

Lamee, Mehdi et al. (Sept. 2016). "Magnetic Field Disorder and Faraday Effects on the Polarization of Extragalactic Radio Sources". In: 829.1, 5, p. 5. DOI: 10.3847/0004-637X/829/1/5. arXiv: 1607.04914 [astro-ph.GA].

Large, M. I., D. S. Mathewson, and C. G. T. Haslam (June 1959). "A High-Resolution Survey of the Coma Cluster of Galaxies at 408 Mc./s." In: 183.4676, pp. 1663–1664. DOI: 10.1038/1831663a0.

Lawler, J. M. and B. Dennison (Jan. 1982). "On intracluster Faraday rotation. II - Statistical analysis." In: 252, pp. 81–91. DOI: 10.1086/159536.

Lenc, E. et al. (Sept. 2017). "The Challenges of Low-Frequency Radio Polarimetry: Lessons from the Murchison Widefield Array". In: 34, e040, e040. DOI: 10.1017/pasa.2017.36. arXiv: 1708.05799 [astro-ph.IM].

Lietzen, H. et al. (Apr. 2016). "Discovery of a massive supercluster system at z ~0.47". In: 588, L4, p. L4. DOI: 10.1051/0004-6361/201628261. arXiv: 1602.08498 [astro-ph.CO].

Lin, Yen-Ting, Joseph J. Mohr, and S. Adam Stanford (July 2003). "Near-Infrared Properties of Galaxy Clusters: Luminosity as a Binding Mass Predictor and the State of Cluster Baryons". In: *The Astrophysical Journal* 591, pp. 749–763. DOI: 10.1086/375513. URL: http://adsabs.harvard.edu/abs/2003ApJ...591..749L (visited on 09/17/2020).

Locatelli, N. et al. (Aug. 2021). "New constraints on the magnetic field in cosmic web filaments". In: 652, A80, A80. DOI: 10.1051/0004-6361/202140526. arXiv: 2101.06051 [astro-ph.CO].

Lovisari, L., T. H. Reiprich, and G. Schellenberger (Jan. 2015). "Scaling properties of a complete X-ray selected galaxy group sample". In: 573, A118, A118. DOI: 10.1051/0004-6361/201423954. arXiv: 1409.3845 [astro-ph.CO].

Lovisari, Lorenzo et al. (Sept. 2017). "X-Ray Morphological Analysis of the Planck ESZ Clusters". In: 846.1, 51, p. 51. DOI: 10.3847/1538-4357/aa855f. arXiv: 1708.02590 [astro-ph.CO].

Lyskova, N. et al. (May 2019). "Close-up view of an ongoing merger between the NGC 4839 group and the Coma cluster - a post-merger scenario". In: 485.2, pp. 2922–2934. DOI: 10.1093/mnras/stz597. arXiv: 1811.07944 [astro-ph.HE].

Macario, G. et al. (July 2010). "The very steep spectrum radio halo in Abell 697". In: 517, A43, A43. DOI: 10.1051/0004-6361/201014109. arXiv: 1004.1515 [astro-ph.CO].

Machado, Rubens E. G. et al. (2024). *Simulating the arrival of the southern substructure in the galaxy cluster Abell 1758*. arXiv: 2405.20497 [astro-ph.CO].

Malkov, M. A. and L. O'C. Drury (Apr. 2001). "Nonlinear theory of diffusive acceleration of particles by shock waves". In: *Reports on Progress in Physics* 64.4, pp. 429–481. DOI: 10.1088/0034-4885/64/4/201.

Marinacci, Federico et al. (Nov. 2015). "The large-scale properties of simulated cosmological magnetic fields". In: 453.4, pp. 3999–4019. DOI: 10.1093/mnras/stv1692. arXiv: 1506.00005 [astro-ph.CO].

Marini, F. et al. (Oct. 2004). "BeppoSAX temperature maps of galaxy clusters in the Corona Borealis supercluster: A2061, A2067 and A2124". In: 353.4, pp. 1219–1230. DOI: 10.1111/j.1365-2966.2004.08148.x. arXiv: astro-ph/0406538 [astro-ph].

Markevitch, M. et al. (July 2005). "Bow Shock and Radio Halo in the Merging Cluster A520". In: 627.2, pp. 733–738. DOI: 10.1086/430695. arXiv: astro-ph/0412451 [astro-ph].

Markevitch, Maxim, Craig L. Sarazin, and Alexey Vikhlinin (Aug. 1999). "Physics of the Merging Clusters Cygnus A, A3667, and A2065". In: 521.2, pp. 526–530. DOI: 10.1086/307598. arXiv: astro-ph/9812005 [astro-ph].

Markevitch, Maxim and Alexey Vikhlinin (May 2007). "Shocks and cold fronts in galaxy clusters". In: 443.1, pp. 1–53. DOI: 10.1016/j.physrep.2007.01.001. arXiv: astro-ph/0701821 [astro-ph].

Martin-Alvarez, Sergio, Susana Planelles, and Vicent Quilis (May 2017). "On the interplay between cosmological shock waves and their environment". In: 362.5, 91, p. 91. DOI: 10.1007/s10509-017-3066-3.

McMullin, J. P. et al. (Oct. 2007). "CASA Architecture and Applications". In: *Astronomical Data Analysis Software and Systems XVI*. Ed. by R. A. Shaw, F. Hill, and D. J. Bell. Vol. 376. Astronomical Society of the Pacific Conference Series, p. 127.

McNamara, B. R. and P. E. J. Nulsen (Sept. 2007). "Heating Hot Atmospheres with Active Galactic Nuclei". In: 45.1, pp. 117–175. DOI: 10.1146/annurev.astro.45.051806.110625. arXiv: 0709.2152 [astro-ph].

Mechev, A. P. et al. (July 2018). "Pipeline Collector: Gathering performance data for distributed astronomical pipelines". In: *Astronomy and Computing* 24, 117, p. 117. DOI: 10.1016/j.ascom.2018.06.005. arXiv: 1807.05733 [astro-ph.IM].

Mevius, Maaijke (June 2018). *RMextract: Ionospheric Faraday Rotation calculator*. Astrophysics Source Code Library, record ascl:1806.024.

Miniati, Francesco (Feb. 2014). "The Matryoshka Run: A Eulerian Refinement Strategy to Study the Statistics of Turbulence in Virialized Cosmic Structures". In: 782.1, 21, p. 21. DOI: 10.1088/0004-637X/782/1/21. arXiv: 1310.2951 [astro-ph.CO].

— (Feb. 2015). "The Matryoshka Run. II. Time-dependent Turbulence Statistics, Stochastic Particle Acceleration, and Microphysics Impact in a Massive Galaxy Cluster". In: 800.1, 60, p. 60. DOI: 10.1088/0004-637X/800/1/60. arXiv: 1409.3576 [astro-ph.CO].

Morabito, Leah K. et al. (Sept. 2016). "LOFAR VLBI studies at 55 MHz of 4C 43.15, a z = 2.4 radio galaxy". In: 461.3, pp. 2676–2687. DOI: 10.1093/mnras/stw1501. arXiv: 1606.06741 [astro-ph.GA].

Mtchedlidze, Salome et al. (Apr. 2022). "Evolution of Primordial Magnetic Fields during Large-scale Structure Formation". In: 929.2, 127, p. 127. DOI: 10.3847/1538-4357/ac5960. arXiv: 2109.13520 [astro-ph.CO].

Murgia, M. et al. (May 1999). "Synchrotron spectra and ages of compact steep spectrum radio sources". In: 345, pp. 769–777.

Murgia, M. et al. (Sept. 2004). "Magnetic fields and Faraday rotation in clusters of galaxies". In: 424, pp. 429–446. DOI: 10.1051/0004-6361:20040191. arXiv: astro-ph/0406225 [astro-ph].

Murgia, M. et al. (June 2009). "Comparative analysis of the diffuse radio emission in the galaxy clusters A1835, A2029, and Ophiuchus". In: 499.3, pp. 679–695. DOI: 10.1051/0004-6361/200911659. arXiv: 0901.1943 [astro-ph.CO].

Murgia, M. et al. (Jan. 2010). "A double radio halo in the close pair of galaxy clusters Abell 399 and Abell 401". In: 509, A86, A86. DOI: 10.1051/0004-6361/200913414. arXiv: 0911.3594 [astro-ph.CO].

Murphy, Tara et al. (Mar. 2010). "The Australia Telescope 20 GHz Survey: the source catalogue". In: 402.4, pp. 2403–2423. DOI: 10.1111/j.1365-2966.2009.15961.x. arXiv: 0911.0002 [astro-ph.GA].

Nadathur, Seshadri and Robert Crittenden (Oct. 2016). "A Detection of the Integrated Sachs-Wolfe Imprint of Cosmic Superstructures Using a Matched-filter Approach". In: 830.1, L19, p. L19. DOI: 10.3847/2041-8205/830/1/L19. arXiv: 1608.08638 [astro-ph.CO].

Nagai, Daisuke, Andrey V. Kravtsov, and Alexey Vikhlinin (Oct. 2007). "Effects of Galaxy Formation on Thermodynamics of the Intracluster Medium". In: 668.1, pp. 1–14. DOI: 10.1086/521328. arXiv: astro-ph/0703661 [astro-ph].

Neld, A. et al. (Oct. 2018). "Reliable detection and characterization of low-frequency polarized sources in the LOFAR M51 field". In: 617, A136, A136. DOI: 10.1051/0004-6361/201732157. arXiv: 1807.09240 [astro-ph.GA].

Nelson, Dylan et al. (June 2024). "Introducing the TNG-Cluster simulation: Overview and the physical properties of the gaseous intracluster medium". In: 686, A157, A157. DOI: 10.1051/0004-6361/202348608. arXiv: 2311.06338 [astro-ph.GA].

Neronov, A. et al. (2024). *Revision of upper bound on volume-filling intergalactic magnetic fields with LOFAR*. arXiv: 2412.14825 [astro-ph.CO]. URL: https://arxiv.org/abs/2412.14825.

Neyrinck, Mark C. (June 2008). "ZOBOV: a parameter-free void-finding algorithm". In: 386.4, pp. 2101–2109. DOI: 10.1111/j.1365-2966.2008.13180.x. arXiv: 0712.3049 [astro-ph].

Nishiwaki, Kosuke et al. (Jan. 2024). "Efficiency of Turbulent Reacceleration by Solenoidal Turbulence and Its Application to the Origin of Radio Megahalos in Cluster Outskirts". In: 961.1, 15, p. 15. DOI: 10.3847/1538-4357/ad11ce. arXiv: 2312.01120 [astro-ph.HE].

Noordam, Jan E. (Oct. 2004). "LOFAR calibration challenges". In: *Ground-based Telescopes*. Ed. by Jr. Oschmann Jacobus M. Vol. 5489. Society of Photo-Optical Instrumentation Engineers (SPIE) Conference Series, pp. 817–825. DOI: 10.1117/12.544262.

Nunhokee, C. D. et al. (Feb. 2023). "Radio multifrequency observations of galaxy clusters. The Abell 399−401 pair". In: *arXiv e-prints*, arXiv:2102.02900, arXiv:2102.02900. arXiv: 2102.02900 [astro-ph.CO].

Oegerle, William R. and John M. Hill (Dec. 2001). "Dynamics of cD Clusters of Galaxies. IV. Conclusion of a Survey of 25 Abell Clusters". In: 122.6, pp. 2858–2873. DOI: 10.1086/323536.

Offringa, A. R., B. McKinley, Hurley-Walker, et al. (2014). "WSClean: an implementation of a fast, generic wide-field imager for radio astronomy". In: *MNRAS* 444.1, pp. 606–619. DOI: 10.1093/mnras/stu1368.

Offringa, A. R., J. J. van de Gronde, and J. B. T. M. Roerdink (Mar. 2012). "A morphological algorithm for improving radio-frequency interference detection". In: 539, A95, A95. DOI: 10.1051/0004-6361/201118497. arXiv: 1201.3364 [astro-ph.IM].

Osinga, E. et al. (Sept. 2022). "The detection of cluster magnetic fields via radio source depolarisation". In: 665, A71, A71. DOI: 10.1051/0004-6361/202243526. arXiv: 2207.09717 [astro-ph.CO].

Osinga, Erik et al. (Aug. 2024). "Probing cluster magnetism with embedded and background radio sources in Planck clusters". In: *arXiv e-prints*, arXiv:2408.07178, arXiv:2408.07178. DOI: 10.48550/arXiv.2408.07178. arXiv: 2408.07178 [astro-ph.CO].

O'Sullivan, S. P. et al. (Apr. 2012). "Complex Faraday depth structure of active galactic nuclei as revealed by broad-band radio polarimetry". In: 421.4, pp. 3300–3315. DOI: 10.1111/j.1365-2966.2012.20554.x. arXiv: 1201.3161 [astro-ph.CO].

O'Sullivan, S. P. et al. (Feb. 2013). "Thermal Plasma in the Giant Lobes of the Radio Galaxy Centaurus A". In: 764.2, 162, p. 162. DOI: 10.1088/0004-637X/764/2/162. arXiv: 1301.1400 [astro-ph.CO].

O'Sullivan, S. P. et al. (Aug. 2017). "Broad-band, radio spectro-polarimetric study of 100 radiative-mode and jet-mode AGN". In: 469.4, pp. 4034–4062. DOI: 10.1093/mnras/stx1133. arXiv: 1705.00102 [astro-ph.GA].

O'Sullivan, S. P. et al. (Feb. 2019). "The intergalactic magnetic field probed by a giant radio galaxy". In: 622, A16, A16. DOI: 10.1051/0004-6361/201833832. arXiv: 1811.07934 [astro-ph.HE].

O'Sullivan, S. P. et al. (Mar. 2023). "The Faraday Rotation Measure Grid of the LOFAR Two-metre Sky Survey: Data Release 2". In: 519.4, pp. 5723–5742. DOI: 10.1093/mnras/stac3820. arXiv: 2301.07697 [astro-ph.CO].

O'Sullivan, Shane P. et al. (Nov. 2018). "Untangling Cosmic Magnetic Fields: Faraday Tomography at Metre Wavelengths with LOFAR". In: *Galaxies* 6.4, 126, p. 126. DOI: 10.3390/galaxies6040126. arXiv: 1811.12732 [astro-ph.HE].

Paoletti, D. et al. (Dec. 2022). "Constraints on primordial magnetic fields from their impact on the ionization history with Planck 2018". In: 517.3, pp. 3916–3927. DOI: 10.1093/mnras/stac2947. arXiv: 2204.06302 [astro-ph.CO].

Pasini, T. et al. (July 2022). "Particle re-acceleration and diffuse radio sources in the galaxy cluster Abell 1550". In: 663, A105, A105. DOI: 10.1051/0004-6361/202243833. arXiv: 2205.12281 [astro-ph.CO].

Peacock, John A. (1999). *Cosmological Physics*.

Pearce, C. J. J. et al. (Aug. 2017). "VLA Radio Observations of the HST Frontier Fields Cluster Abell 2744: The Discovery of New Radio Relics". In: 845.1, 81, p. 81. DOI: 10.3847/1538-4357/aa7e2f. arXiv: 1708.03367 [astro-ph.CO].

Pearson, David W., Merida Batiste, and David J. Batuski (June 2014). "The largest gravitationally bound structures: the Corona Borealis supercluster - mass and bound extent". In: 441.2, pp. 1601–1614. DOI: 10.1093/mnras/stu693. arXiv: 1404.1308 [astro-ph.CO].

Perley, Richard A. (Jan. 1989). "Wide Field Imaging II: Imaging with Non-Coplanar Arrays". In: *Synthesis Imaging in Radio Astronomy*. Ed. by Richard A. Perley, Frederic R. Schwab, and Alan H. Bridle. Vol. 6. Astronomical Society of the Pacific Conference Series, p. 259.

Perley, Richard A., Frederic R. Schwab, and Alan H. Bridle, eds. (Jan. 1989). *Synthesis imaging in radio astronomy : a collection of lectures from the third NRAO synthesis imaging summer school*. Vol. 6. Astronomical Society of the Pacific Conference Series.

Petrosian, Vahé (Aug. 2001). "On the Nonthermal Emission and Acceleration of Electrons in Coma and Other Clusters of Galaxies". In: 557.2, pp. 560–572. DOI: 10.1086/321557. arXiv: astro-ph/0101145 [astro-ph].

Piffaretti, R. et al. (Oct. 2011). "The MCXC: a meta-catalogue of x-ray detected clusters of galaxies". In: 534, A109, A109. DOI: 10.1051/0004-6361/201015377. arXiv: 1007.1916 [astro-ph.CO].

Pignataro, G. V. et al. (May 2024a). "Abell 0399-Abell 0401 radio bridge spectral index: First multi-frequency detection". In: 685, L10, p. L10. DOI: 10.1051/0004-6361/202450051. arXiv: 2405.00772 [astro-ph.CO].

Pignataro, G. V. et al. (Sept. 2024b). "Mind the Gap between A2061 and A2067: Unveiling new diffuse large-scale radio emission". In: *arXiv e-prints*, arXiv:2409.15412, arXiv:2409.15412. DOI: 10.48550/arXiv.2409.15412. arXiv: 2409.15412 [astro-ph.CO].

Pignataro, G. V. et al. (Feb. 2024c). "Probing diffuse radio emission in bridges between galaxy clusters with uGMRT". In: 682, A105, A105. DOI: 10.1051/0004-6361/202346243. arXiv: 2311.09287 [astro-ph.CO].

Planck Collaboration et al. (Dec. 2011). "Planck early results. I. The Planck mission". In: 536, A1, A1. DOI: 10.1051/0004-6361/201116464. arXiv: 1101.2022 [astro-ph.IM].

Planck Collaboration et al. (Feb. 2013). "Planck intermediate results. VIII. Filaments between interacting clusters". In: 550, A134, A134. DOI: 10.1051/0004-6361/201220194. arXiv: 1208.5911 [astro-ph.CO].

Planck Collaboration et al. (Sept. 2016). "Planck 2015 results. XXII. A map of the thermal Sunyaev-Zeldovich effect". In: 594, A22, A22. DOI: 10.1051/0004-6361/201525826. arXiv: 1502.01596 [astro-ph.CO].

Planck Collaboration et al. (Sept. 2020). "Planck 2018 results. VII. Isotropy and statistics of the CMB". In: 641, A7, A7. DOI: 10.1051/0004-6361/201935201. arXiv: 1906.02552 [astro-ph.CO].

Planelles, S., D. R. G. Schleicher, and A. M. Bykov (2016). "Large-Scale Structure Formation: From the First Non-linear Objects to Massive Galaxy Clusters". In: *Multi-scale Structure Formation and Dynamics in Cosmic Plasmas*. Ed. by Andre Balogh et al. Vol. 51, pp. 93–139. DOI: 10.1007/978-1-4939-3547-5_4.

Poole, Gregory B. et al. (Dec. 2006). "The impact of mergers on relaxed X-ray clusters - I. Dynamical evolution and emergent transient structures". In: 373.3, pp. 881–905. DOI: 10.1111/j.1365-2966.2006.10916.x. arXiv: astro-ph/0608560 [astro-ph].

Pratt, G. W. et al. (Sept. 2022). "Linking a universal gas density profile to the core-excised X-ray luminosity in galaxy clusters up to z $\sim$ 1.1". In: 665, A24, A24. DOI: 10.1051/0004-6361/202243074. arXiv: 2206.06656 [astro-ph.CO].

Purcell, C. R. et al. (May 2015). "A Radio-Polarisation and Rotation Measure Study of the Gum Nebula and Its Environment". In: 804.1, 22, p. 22. DOI: 10.1088/0004-637X/804/1/22. arXiv: 1502.06296 [astro-ph.GA].

Radiconi, Federico et al. (Dec. 2022). "The thermal and non-thermal components within and between galaxy clusters Abell 399 and Abell 401". In: 517.4, pp. 5232–5246. DOI: 10.1093/mnras/stac3015. arXiv: 2206.04697 [astro-ph.CO].

Rajpurohit, K. et al. (Jan. 2018). "Deep VLA Observations of the Cluster 1RXS J0603.3+4214 in the Frequency Range of 1-2 GHz". In: 852.2, 65, p. 65. DOI: 10.3847/1538-4357/aa9f13. arXiv: 1712.01327 [astro-ph.GA].

Rajpurohit, K. et al. (Oct. 2020). "A perfect power-law spectrum even at the highest frequencies: The Toothbrush relic". In: 642, L13, p. L13. DOI: 10.1051/0004-6361/202039165. arXiv: 2008.02694 [astro-ph.CO].

Rajpurohit, K. et al. (Oct. 2021a). "Dissecting nonthermal emission in the complex multiple-merger galaxy cluster Abell 2744: Radio and X-ray analysis". In: 654, A41, A41. DOI: 10.1051/0004-6361/202141060. arXiv: 2104.05690 [astro-ph.CO].

Rajpurohit, K. et al. (Feb. 2021b). "Physical insights from the spectrum of the radio halo in MACS J0717.5+3745". In: 646, A135, A135. DOI: 10.1051/0004-6361/202039591. arXiv: 2012.14373 [astro-ph.GA].

Rajpurohit, K. et al. (Feb. 2021c). "Understanding the radio relic emission in the galaxy cluster MACS J0717.5+3745: Spectral analysis". In: 646, A56, A56. DOI: 10.1051/0004-6361/202039428. arXiv: 2011.14436 [astro-ph.GA].

Rajpurohit, K. et al. (Mar. 2022). "Deep Low-frequency Radio Observations of A2256. I. The Filamentary Radio Relic". In: 927.1, 80, p. 80. DOI: 10.3847/1538-4357/ac4708. arXiv: 2111.04449 [astro-ph.CO].

Rajpurohit, K. et al. (Jan. 2023). "Deep low-frequency radio observations of Abell 2256. II. The ultra-steep spectrum radio halo". In: 669, A1, A1. DOI: 10.1051/0004-6361/202244925. arXiv: 2209.03288 [astro-ph.CO].

Rengelink, R. B. et al. (Aug. 1997). "The Westerbork Northern Sky Survey (WENSS), I. A 570 square degree Mini-Survey around the North Ecliptic Pole". In: 124, pp. 259–280. DOI: 10.1051/aas:1997358.

Ricker, Paul M. and Craig L. Sarazin (Nov. 2001). "Off-Axis Cluster Mergers: Effects of a Strongly Peaked Dark Matter Profile". In: 561.2, pp. 621–644. DOI: 10.1086/323365. arXiv: astro-ph/0107210 [astro-ph].

Rines, Kenneth and Antonaldo Diaferio (Sept. 2006). "CIRS: Cluster Infall Regions in the Sloan Digital Sky Survey. I. Infall Patterns and Mass Profiles". In: 132.3, pp. 1275–1297. DOI: 10.1086/506017. arXiv: astro-ph/0602032 [astro-ph].

Riseley, C. J. et al. (Sept. 2022). "Radio fossils, relics, and haloes in Abell 3266: cluster archaeology with ASKAP-EMU and the ATCA". In: 515.2, pp. 1871–1896. DOI: 10.1093/mnras/stac1771. arXiv: 2208.00395 [astro-ph.GA].

Riseley, C. J. et al. (June 2024). "A "MeerKAT-meets-LOFAR" study of the complex multi-component (mini-)halo in the extreme sloshing cluster Abell 2142". In: 686, A44, A44. DOI: 10.1051/0004-6361/202348944. arXiv: 2403.00414 [astro-ph.CO].

Roettiger, Kurt, Jack O. Burns, and James M. Stone (June 1999). "A Cluster Merger and the Origin of the Extended Radio Emission in Abell 3667". In: 518.2, pp. 603–612. DOI: 10.1086/307327. arXiv: astro-ph/9902115 [astro-ph].

Rossetti, M. et al. (Feb. 2024). "CHEX-MATE: Robust reconstruction of temperature profiles in galaxy clusters with XMM-Newton". In: *arXiv e-prints*, arXiv:2402.18653, arXiv:2402.18653. DOI: 10.48550/arXiv.2402.18653. arXiv: 2402.18653 [astro-ph.CO].

Rottgering, H. J. A. et al. (Sept. 1997). "The extended radio emission in the luminous X-ray cluster A3667". In: 290.4, pp. 577–584. DOI: 10.1093/mnras/290.4.577.

Rudnick, Lawrence (Jan. 2019). "Optimizing Faraday Background Grids". In: *arXiv e-prints*, arXiv:1901.09074, arXiv:1901.09074. DOI: 10.48550/arXiv.1901.09074. arXiv: 1901.09074 [astro-ph.GA].

Rudnick, Lawrence and Katherine M. Blundell (May 2003). "Lowering Inferred Cluster Magnetic Field Strengths: The Radio Galaxy Contributions". In: 588.1, pp. 143–154. DOI: 10.1086/373891. arXiv: astro-ph/0301260 [astro-ph].

Rudnick, Lawrence and Jeffrey A. Lemmerman (June 2009). "An Objective Survey of Mpc-scale Radio Emission in 0.03 < z < 0.3 Bright X-ray Clusters". In: 697.2, pp. 1341–1357. DOI: 10.1088/0004-637X/697/2/1341. arXiv: 0903.0335 [astro-ph.CO].

Ryu, D. et al. (May 2012). "Magnetic Fields in the Large-Scale Structure of the Universe". In: 166.1-4, pp. 1–35. DOI: 10.1007/s11214-011-9839-z. arXiv: 1109.4055 [astro-ph.CO].

Ryu, Dongsu et al. (Aug. 2003). "Cosmological Shock Waves and Their Role in the Large-Scale Structure of the Universe". In: 593.2, pp. 599–610. DOI: 10.1086/376723. arXiv: astro-ph/0305164 [astro-ph].

Ryu, Dongsu et al. (May 2008). "Turbulence and Magnetic Fields in the Large-Scale Structure of the Universe". In: *Science* 320.5878, p. 909. DOI: 10.1126/science.1154923. arXiv: 0805.2466 [astro-ph].

Sabater, J. et al. (Apr. 2021). "The LOFAR Two-meter Sky Survey: Deep Fields Data Release 1. II. The ELAIS-N1 LOFAR deep field". In: 648, A2, A2. DOI: 10.1051/0004-6361/202038828. arXiv: 2011.08211 [astro-ph.GA].

Sanderson, Alastair J. R., Ewan O'Sullivan, and Trevor J. Ponman (May 2009). "A statistically selected Chandra sample of 20 galaxy clusters - II. Gas properties and cool core/non-cool core bimodality". In: 395.2, pp. 764–776. DOI: 10.1111/j.1365-2966.2009.14613.x. arXiv: 0902.1747 [astro-ph.CO].

Sankhyayan, Shishir and Pratik Dabhade (July 2024). "Search and analysis of giant radio galaxies with associated nuclei (SAGAN). IV. Interplay with the Supercluster environment". In: 687, L8, p. L8. DOI: 10.1051/0004-6361/202450011. arXiv: 2405.19154 [astro-ph.GA].

Santiago-Bautista, Iris et al. (May 2020). "Identification of filamentary structures in the environment of superclusters of galaxies in the Local Universe". In: 637, A31, A31. DOI: 10.1051/0004-6361/201936397. arXiv: 2002.03446 [astro-ph.GA].

Sarazin, C. L. (Dec. 1988). "Book-Review - X-Ray Emissions from Clusters of Galaxies". In: 76, p. 639.

Sarazin, Craig L. (Jan. 1986). "X-ray emission from clusters of galaxies". In: *Reviews of Modern Physics* 58.1, pp. 1–115. DOI: 10.1103/RevModPhys.58.1.

Scaife, Anna M. M. and George H. Heald (June 2012). "A broad-band flux scale for low-frequency radio telescopes". In: 423.1, pp. L30–L34. DOI: 10.1111/j.1745-3933.2012.01251.x. arXiv: 1203.0977 [astro-ph.IM].

Schnitzeler, D. H. F. M. (Feb. 2018). "Finding a complex polarized signal in wide-band radio data". In: 474.1, pp. 300–312. DOI: 10.1093/mnras/stx2754. arXiv: 1710.10274 [astro-ph.IM].

Schnitzeler, D. H. F. M. and K. J. Lee (Apr. 2017). "Finding a faint polarized signal in wide-band radio data". In: 466.1, pp. 378–391. DOI: 10.1093/mnras/stw3104. arXiv: 1611.09865 [astro-ph.IM].

Sheardown, Alex et al. (Oct. 2018). "The Recent Growth History of the Fornax Cluster Derived from Simultaneous Sloshing and Gas Stripping: Simulating the Infall of NGC 1404". In: 865.2, 118, p. 118. DOI: 10.3847/1538-4357/aadc0f. arXiv: 1809.02134 [astro-ph.GA].

Sheardown, Alex et al. (Apr. 2019). "A New Class of X-Ray Tails of Early-type Galaxies and Subclusters in Galaxy Clusters: Slingshot Tails versus Ram Pressure Stripped Tails". In: 874.2, 112, p. 112. DOI: 10.3847/1538-4357/ab0c06. arXiv: 1903.00482 [astro-ph.GA].

Shimwell, T. W. et al. (Feb. 2017). "The LOFAR Two-metre Sky Survey. I. Survey description and preliminary data release". In: 598, A104, A104. DOI: 10.1051/0004-6361/201629313. arXiv: 1611.02700 [astro-ph.IM].

Shimwell, T. W. et al. (Feb. 2019a). "The LOFAR Two-metre Sky Survey. II. First data release". In: 622, A1, A1. DOI: 10.1051/0004-6361/201833559. arXiv: 1811.07926 [astro-ph.GA].

— (Feb. 2019b). "The LOFAR Two-metre Sky Survey. II. First data release". In: 622, A1, A1. DOI: 10.1051/0004-6361/201833559. arXiv: 1811.07926 [astro-ph.GA].

Shimwell, T. W. et al. (Mar. 2022a). "The LOFAR Two-metre Sky Survey. V. Second data release". In: 659, A1, A1. DOI: 10.1051/0004-6361/202142484. arXiv: 2202.11733 [astro-ph.GA].

— (Mar. 2022b). "The LOFAR Two-metre Sky Survey. V. Second data release". In: 659, A1, A1. DOI: 10.1051/0004-6361/202142484. arXiv: 2202.11733 [astro-ph.GA].

Shimwell, Timothy W. et al. (May 2015). "Another shock for the Bullet cluster, and the source of seed electrons for radio relics". In: 449.2, pp. 1486–1494. DOI: 10.1093/mnras/stv334. arXiv: 1502.01064 [astro-ph.HE].

Simmons, J. F. L. and B. G. Stewart (Jan. 1985). "Point and interval estimation of the true unbiased degree of linear polarization in the presence of low signal-to-noise ratios". In: 142.1, pp. 100–106.

Skrutskie, M. F. et al. (Feb. 2006). "The Two Micron All Sky Survey (2MASS)". In: 131.2, pp. 1163–1183. DOI: 10.1086/498708.

Smirnov, O. M. and C. Tasse (May 2015). "Radio interferometric gain calibration as a complex optimization problem". In: 449.3, pp. 2668–2684. DOI: 10.1093/mnras/stv418. arXiv: 1502.06974 [astro-ph.IM].

Smith, Randall K. and John P. Hughes (July 2010). "IONIZATION EQUILIBRIUM TIMESCALES IN COLLISIONAL PLASMAS". en. In: *ApJ* 718.1, pp. 583–585. ISSN: 0004-637X, 1538-4357. DOI: 10.1088/0004-637X/718/1/583. URL: https:

//iopscience.iop.org/article/10.1088/0004-637X/718/1/583 (visited on 09/22/2020).

Snowden, S. L. et al. (Feb. 2008). "A catalog of galaxy clusters observed by XMM-Newton". In: 478.2, pp. 615–658. DOI: 10.1051/0004-6361:20077930. arXiv: 0710.2241 [astro-ph].

Sokoloff, D. D. et al. (Aug. 1998). "Depolarization and Faraday effects in galaxies". In: 299.1, pp. 189–206. DOI: 10.1046/j.1365-8711.1998.01782.x.

Sotomayor-Beltran, C. et al. (Apr. 2013). "Calibrating high-precision Faraday rotation measurements for LOFAR and the next generation of low-frequency radio telescopes". In: 552, A58, A58. DOI: 10.1051/0004-6361/201220728. arXiv: 1303.6230 [astro-ph.IM].

Spergel, D. N. et al. (Sept. 2003). "First Year Wilkinson Microwave Anisotropy Probe (WMAP) Observations: Determination of Cosmological Parameters". In: *ASTROPHYS J SUPPL S* 148.1. arXiv: astro-ph/0302209, pp. 175–194. ISSN: 0067-0049, 1538-4365. DOI: 10.1086/377226. URL: http://arxiv.org/abs/astro-ph/0302209 (visited on 09/18/2020).

Springel, Volker et al. (June 2005). "Simulations of the formation, evolution and clustering of galaxies and quasars". In: 435.7042, pp. 629–636. DOI: 10.1038/nature03597. arXiv: astro-ph/0504097 [astro-ph].

Springel, Volker et al. (Mar. 2018). "First results from the IllustrisTNG simulations: matter and galaxy clustering". In: 475.1, pp. 676–698. DOI: 10.1093/mnras/stx3304. arXiv: 1707.03397 [astro-ph.GA].

Stoica, R. S., V. J. Martínez, and E. Saar (Aug. 2007). "A three-dimensional object point process for detection of cosmic filaments." In: *Journal of the Royal Statistical Society: Series C (Applied Statistics) 56 (4* 56, p. 1. DOI: 10.1111/j.1467-9876.2007.00587.x.

— (Feb. 2010). "Filaments in observed and mock galaxy catalogues". In: 510, A38, A38. DOI: 10.1051/0004-6361/200912823. arXiv: 0912.2021 [astro-ph.CO].

Stokes, G. G. (Jan. 1851). "On the Composition and Resolution of Streams of Polarized Light from different Sources". In: *Transactions of the Cambridge Philosophical Society* 9, p. 399.

Strüder, L. et al. (Jan. 2001). "The European Photon Imaging Camera on XMM-Newton: The pn-CCD camera". In: 365, pp. L18–L26. DOI: 10.1051/0004-6361:20000066.

Stuardi, C. et al. (June 2020). "The LOFAR view of intergalactic magnetic fields with giant radio galaxies". In: 638, A48, A48. DOI: 10.1051/0004-6361/202037635. arXiv: 2004.05169 [astro-ph.GA].

Stuardi, C. et al. (Apr. 2021). "The intracluster magnetic field in the double relic galaxy cluster Abell 2345". In: 502.2, pp. 2518–2535. DOI: 10.1093/mnras/stab218. arXiv: 2101.09302 [astro-ph.GA].

Subramanian, Kandaswamy (July 2016). "The origin, evolution and signatures of primordial magnetic fields". In: *Reports on Progress in Physics* 79.7, 076901, p. 076901. DOI: 10.1088/0034-4885/79/7/076901. arXiv: 1504.02311 [astro-ph.CO].

Sunyaev, R. A., M. L. Norman, and G. L. Bryan (Dec. 2003). "On the Detectability of Turbulence and Bulk Flows in X-ray Clusters". In: *Astronomy Letters* 29, pp. 783–790. DOI: 10.1134/1.1631411. arXiv: astro-ph/0310041 [astro-ph].

Sunyaev, R. A. and Ya. B. Zeldovich (Nov. 1972). "The Observations of Relic Radiation as a Test of the Nature of X-Ray Radiation from the Clusters of Galaxies". In: *Comments on Astrophysics and Space Physics* 4, p. 173.

Sweijen, F. et al. (Jan. 2022). "Deep sub-arcsecond wide-field imaging of the Lockman Hole field at 144 MHz". In: *Nature Astronomy* 6, pp. 350–356. DOI: 10.1038/s41550-021-01573-z. arXiv: 2202.01608 [astro-ph.IM].

Tanaka, Masayuki et al. (Aug. 2007). "A huge filamentary structure at z = 0.55 and star formation histories of galaxies at z < 1". In: 379.4, pp. 1546–1556. DOI: 10.1111/j.1365-2966.2007.12062.x. arXiv: 0706.0783 [astro-ph].

Tanimura, H. et al. (Nov. 2020). "First detection of stacked X-ray emission from cosmic web filaments". In: 643, L2, p. L2. DOI: 10.1051/0004-6361/202038521. arXiv: 2011.05343 [astro-ph.CO].

Tasse, C. (June 2014). "Nonlinear Kalman filters for calibration in radio interferometry". In: 566, A127, A127. DOI: 10.1051/0004-6361/201423503. arXiv: 1403.6308 [astro-ph.IM].

Tasse, C. et al. (Apr. 2018). "Faceting for direction-dependent spectral deconvolution". In: 611, A87, A87. DOI: 10.1051/0004-6361/201731474. arXiv: 1712.02078 [astro-ph.IM].

Tasse, C. et al. (Apr. 2021). "The LOFAR Two-meter Sky Survey: Deep Fields Data Release 1. I. Direction-dependent calibration and imaging". In: 648, A1, A1. DOI: 10.1051/0004-6361/202038804. arXiv: 2011.08328 [astro-ph.IM].

Taylor, A. R., J. M. Stil, and C. Sunstrum (Sept. 2009). "A Rotation Measure Image of the Sky". In: 702.2, pp. 1230–1236. DOI: 10.1088/0004-637X/702/2/1230.

Taylor, A. R. et al. (Sept. 2007). "Radio Polarimetry of the ELAIS N1 Field: Polarized Compact Sources". In: 666.1, pp. 201–211. DOI: 10.1086/519786. arXiv: 0705.2736 [astro-ph].

Thierbach, M., U. Klein, and R. Wielebinski (Jan. 2003). "The diffuse radio emission from the Coma cluster at 2.675 GHz and 4.85 GHz". In: 397, pp. 53–61. DOI: 10.1051/0004-6361:20021474. arXiv: astro-ph/0210147 [astro-ph].

Tribble, Peter C. (Nov. 1991). "Radio emission in random magnetic field : radio haloes and the structure of the magnetic field in the Coma cluster." In: 253, p. 147. DOI: 10.1093/mnras/253.1.147.

Turner, M. J. L. et al. (Jan. 2001). "The European Photon Imaging Camera on XMM-Newton: The MOS cameras". In: 365, pp. L27–L35. DOI: 10.1051/0004-6361:20000087. arXiv: astro-ph/0011498 [astro-ph].

Urry, C. Megan and Paolo Padovani (Sept. 1995). "Unified Schemes for Radio-Loud Active Galactic Nuclei". In: 107, p. 803. DOI: 10.1086/133630. arXiv: astro-ph/9506063 [astro-ph].

Vacca, V. et al. (May 2010). "The intracluster magnetic field power spectrum in Abell 665". In: 514, A71, A71. DOI: 10.1051/0004-6361/200913060.

Vacca, V. et al. (Sept. 2018). "Observations of a nearby filament of galaxy clusters with the Sardinia Radio Telescope". In: 479.1, pp. 776–806. DOI: 10.1093/mnras/sty1151. arXiv: 1804.09199 [astro-ph.CO].

Vallés-Pérez, David, Susana Planelles, and Vicent Quilis (June 2021). "Troubled cosmic flows: turbulence, enstrophy, and helicity from the assembly history of the intracluster medium". In: 504.1, pp. 510–527. DOI: 10.1093/mnras/stab880. arXiv: 2103.13449 [astro-ph.CO].

Van der Tol, Sebastiaan (Jan. 2009). "Bayesian estimation for ionospheric calibration in radio astronomy". PhD thesis. Technical University of Delft, Netherlands.

van Diepen, Ger, Tammo Jan Dijkema, and André Offringa (Apr. 2018). *DPPP: Default Pre-Processing Pipeline*. Astrophysics Source Code Library, record ascl:1804.003.

Van Eck, C. L. et al. (June 2018). "Polarized point sources in the LOFAR Two-meter Sky Survey: A preliminary catalog". In: 613, A58, A58. DOI: 10.1051/0004-6361/201732228. arXiv: 1801.04467 [astro-ph.GA].

van Haarlem, M. P. et al. (Aug. 2013). "LOFAR: The LOw-Frequency ARray". In: 556, A2, A2. DOI: 10.1051/0004-6361/201220873. arXiv: 1305.3550 [astro-ph.IM].

van Weeren, R. J. et al. (Sept. 2011). "Radio continuum observations of new radio halos and relics from the NVSS and WENSS surveys. Relic orientations, cluster X-ray luminosity, and redshift distributions". In: 533, A35, A35. DOI: 10.1051/0004-6361/201117149. arXiv: 1107.5597 [astro-ph.CO].

van Weeren, R. J. et al. (July 2012a). "First LOFAR observations at very low frequencies of cluster-scale non-thermal emission: the case of Abell 2256". In: 543, A43, A43. DOI: 10.1051/0004-6361/201219154. arXiv: 1205.4730 [astro-ph.CO].

van Weeren, R. J. et al. (Oct. 2012b). "The "toothbrush-relic": evidence for a coherent linear 2-Mpc scale shock wave in a massive merging galaxy cluster?" In: 546, A124, A124. DOI: 10.1051/0004-6361/201219000. arXiv: 1209.2196 [astro-ph.CO].

— (Oct. 2012c). "The "toothbrush-relic": evidence for a coherent linear 2-Mpc scale shock wave in a massive merging galaxy cluster?" In: 546, A124, A124. DOI: 10.1051/0004-6361/201219000. arXiv: 1209.2196 [astro-ph.CO].

van Weeren, R. J. et al. (Mar. 2016a). "LOFAR Facet Calibration". In: 223.1, 2, p. 2. DOI: 10.3847/0067-0049/223/1/2. arXiv: 1601.05422 [astro-ph.IM].

van Weeren, R. J. et al. (Feb. 2016b). "LOFAR, VLA, and Chandra Observations of the Toothbrush Galaxy Cluster". In: 818.2, 204, p. 204. DOI: 10.3847/0004-637X/818/2/204. arXiv: 1601.06029 [astro-ph.HE].

van Weeren, R. J. et al. (Feb. 2019). "Diffuse Radio Emission from Galaxy Clusters". In: 215.1, 16, p. 16. DOI: 10.1007/s11214-019-0584-z. arXiv: 1901.04496 [astro-ph.HE].

van Weeren, R. J. et al. (July 2021). "LOFAR observations of galaxy clusters in HETDEX. Extraction and self-calibration of individual LOFAR targets". In: 651, A115, A115. DOI: 10.1051/0004-6361/202039826. arXiv: 2011.02387 [astro-ph.CO].

van Weeren, Reinout J. et al. (Oct. 2010). "Particle Acceleration on Megaparsec Scales in a Merging Galaxy Cluster". In: *Science* 330.6002, p. 347. DOI: 10.1126/science.1194293. arXiv: 1010.4306 [astro-ph.CO].

van Weeren, Reinout J. et al. (Jan. 2017). "The case for electron re-acceleration at galaxy cluster shocks". In: *Nature Astronomy* 1, 0005, p. 0005. DOI: 10.1038/s41550-016-0005. arXiv: 1701.01439 [astro-ph.HE].

Vazza, F., G. Brunetti, and C. Gheller (May 2009). "Shock waves in Eulerian cosmological simulations: main properties and acceleration of cosmic rays". In: 395.3, pp. 1333–1354. DOI: 10.1111/j.1365-2966.2009.14691.x. arXiv: 0808.0609 [astro-ph].

Vazza, F. et al. (June 2006). "Turbulent velocity fields in smoothed particle hydrodynamics simulated galaxy clusters: scaling laws for the turbulent energy". In: 369.1, pp. L14–L18. DOI: 10.1111/j.1745-3933.2006.00164.x. arXiv: astro-ph/0602247 [astro-ph].

Vazza, F. et al. (Sept. 2009). "Turbulent motions and shocks waves in galaxy clusters simulated with adaptive mesh refinement". In: 504.1, pp. 33–43. DOI: 10.1051/0004-6361/200912535. arXiv: 0905.3169 [astro-ph.CO].

Vazza, F. et al. (Apr. 2012). "Why are central radio relics so rare?" In: 421.3, pp. 1868–1873. DOI: 10.1111/j.1365-2966.2011.20160.x. arXiv: 1111.1720 [astro-ph.CO].

Vazza, F. et al. (Dec. 2014). "On the amplification of magnetic fields in cosmic filaments and galaxy clusters". In: 445.4, pp. 3706–3722. DOI: 10.1093/mnras/stu1896. arXiv: 1409.2640 [astro-ph.CO].

Vazza, F. et al. (Aug. 2015). "Forecasts for the detection of the magnetised cosmic web from cosmological simulations". In: 580, A119, A119. DOI: 10.1051/0004-6361/201526228. arXiv: 1503.08983 [astro-ph.CO].

Vazza, F. et al. (Dec. 2017). "Simulations of extragalactic magnetic fields and of their observables". In: *Classical and Quantum Gravity* 34.23, 234001, p. 234001. DOI: 10.1088/1361-6382/aa8e60. arXiv: 1711.02669 [astro-ph.CO].

Vazza, F. et al. (Nov. 2018). "The turbulent pressure support in galaxy clusters revisited". In: 481.1, pp. L120–L124. DOI: 10.1093/mnrasl/sly172. arXiv: 1809.02690 [astro-ph.CO].

Vazza, F. et al. (July 2019). "Detecting shocked intergalactic gas with X-ray and radio observations". In: 627, A5, A5. DOI: 10.1051/0004-6361/201935439. arXiv: 1903.04166 [astro-ph.CO].

Venturi, T. et al. (June 2008). "GMRT radio halo survey in galaxy clusters at z = 0.2-0.4. II. The eBCS clusters and analysis of the complete sample". In: 484.2, pp. 327–340. DOI: 10.1051/0004-6361:200809622. arXiv: 0803.4084 [astro-ph].

Venturi, T. et al. (July 2017). "The two-component giant radio halo in the galaxy cluster Abell 2142". In: 603, A125, A125. DOI: 10.1051/0004-6361/201630014. arXiv: 1703.06802 [astro-ph.CO].

Venturi, T. et al. (Apr. 2022). "Radio footprints of a minor merger in the Shapley Supercluster: From supercluster down to galactic scales". In: 660, A81, A81. DOI: 10.1051/0004-6361/202142048. arXiv: 2201.04887 [astro-ph.CO].

Vernstrom, T. et al. (June 2017). "Low-frequency radio constraints on the synchrotron cosmic web". In: 467.4, pp. 4914–4936. DOI: 10.1093/mnras/stx424. arXiv: 1702.05069 [astro-ph.CO].

Vernstrom, T. et al. (June 2019). "Differences in Faraday Rotation between Adjacent Extragalactic Radio Sources as a Probe of Cosmic Magnetic Fields". In: 878.2, 92, p. 92. DOI: 10.3847/1538-4357/ab1f83. arXiv: 1905.02410 [astro-ph.CO].

Vernstrom, T. et al. (Aug. 2021). "Discovery of magnetic fields along stacked cosmic filaments as revealed by radio and X-ray emission". In: 505.3, pp. 4178–4196. DOI: 10.1093/mnras/stab1301. arXiv: 2101.09331 [astro-ph.CO].

Vernstrom, Tessa et al. (Feb. 2023). "Polarized accretion shocks from the cosmic web". In: *Science Advances* 9.7, eade7233, eade7233. DOI: 10.1126/sciadv.ade7233. arXiv: 2302.08072 [astro-ph.CO].

Vikhlinin, A. et al. (Feb. 2009). "Chandra Cluster Cosmology Project. II. Samples and X-Ray Data Reduction". In: 692.2, pp. 1033–1059. DOI: 10.1088/0004-637X/692/2/1033. arXiv: 0805.2207 [astro-ph].

Vogelsberger, Mark et al. (Oct. 2014). "Introducing the Illustris Project: simulating the coevolution of dark and visible matter in the Universe". In: 444.2, pp. 1518–1547. DOI: 10.1093/mnras/stu1536. arXiv: 1405.2921 [astro-ph.CO].

Voigt, L. M. and A. C. Fabian (May 2006). "Galaxy cluster mass profiles". In: *Monthly Notices of the Royal Astronomical Society* 368.2. arXiv: astro-ph/0602373, pp. 518–533. ISSN: 0035-8711, 1365-2966. DOI: 10.1111/j.1365-2966.2006.10199.x. URL: http://arxiv.org/abs/astro-ph/0602373 (visited on 09/28/2020).

Voronkov, M. A. and M. H. Wieringa (Apr. 2004). "The Cotton-Schwab Clean At Ultra-High Dynamic Range". In: *Experimental Astronomy* 18.1-3, pp. 13–29. DOI: 10.1007/s10686-005-9000-7.

White, S. D. M. and M. J. Rees (May 1978). "Core condensation in heavy halos: a two-stage theory for galaxy formation and clustering." In: 183, pp. 341–358. DOI: 10.1093/mnras/183.3.341.

Widrow, Lawrence M. et al. (May 2012). "The First Magnetic Fields". In: 166.1-4, pp. 37–70. DOI: 10.1007/s11214-011-9833-5. arXiv: 1109.4052 [astro-ph.CO].

Wilber, A. et al. (Jan. 2018). "LOFAR discovery of an ultra-steep radio halo and giant head-tail radio galaxy in Abell 1132". In: 473.3, pp. 3536–3546. DOI: 10.1093/mnras/stx2568. arXiv: 1708.08928 [astro-ph.GA].

Williams, W. L. et al. (Feb. 2019). "The LOFAR Two-metre Sky Survey. III. First data release: Optical/infrared identifications and value-added catalogue". In: 622, A2, A2. DOI: 10.1051/0004-6361/201833564. arXiv: 1811.07927 [astro-ph.GA].

Williams, W. L. et al. (Nov. 2021). "The LOFAR LBA Sky Survey: Deep Fields. I. The Boötes Field". In: 655, A40, A40. DOI: 10.1051/0004-6361/202141745. arXiv: 2109.14865 [astro-ph.GA].

Willson, M. A. G. (Jan. 1970). "Radio observations of the cluster of galaxies in Coma Berenices - the 5C4 survey." In: 151, p. 1. DOI: 10.1093/mnras/151.1.1.

Xie, C. et al. (Apr. 2020). "The discovery of radio halos in the frontier fields clusters Abell S1063 and Abell 370". In: 636, A3, A3. DOI: 10.1051/0004-6361/201936953. arXiv: 2001.04725 [astro-ph.HE].

Xu, Hao et al. (June 2009). "Turbulence and Dynamo in Galaxy Cluster Medium: Implications on the Origin of Cluster Magnetic Fields". In: 698.1, pp. L14–L17. DOI: 10.1088/0004-637X/698/1/L14. arXiv: 0905.2196 [astro-ph.CO].

Xu, Yongzhong et al. (Jan. 2006). "A Faraday Rotation Search for Magnetic Fields in Large-scale Structure". In: 637.1, pp. 19–26. DOI: 10.1086/498336. arXiv: astro-ph/0509826 [astro-ph].

Zeldovich, Ia. B., J. Einasto, and S. F. Shandarin (Dec. 1982). "Giant voids in the Universe". In: 300.5891, pp. 407–413. DOI: 10.1038/300407a0.